Imperial College London
Department of Mathematics

Novel applications of complex analysis to effective parameter quantification in transport theory

Hiroyuki Miyoshi

Submitted in part fulfilment of the requirements
for the degree of Doctor of Philosophy at
Imperial College London, August 2023

I certify that this thesis, and the research to which it refers, is the product of my own work, and that any ideas or quotations from the work of other people, published or otherwise, are fully acknowledged in accordance with the standard referencing practices of the discipline.

Hiroyuki Miyoshi (2023)

Abstract

This thesis proposes the application of complex analysis to the calculation of effective parameters of transport problems in multiply connected domains. This can be done by using special functions called Schottky-Klein prime functions. The effective parameters focused on in this thesis are electrical resistivity, electrical capacity, and slip lengths of channels. The prime function is a powerful mathematical function invented by Crowdy for solving problems in multiply connected domains including transport problems governed by Laplace's equation and Poisson's equation in domains with multiple boundaries. The functional properties of the prime function make it possible to analyse effective parameters in multiply connected domains.

First, a new method for solving a new class of boundary value problems in multiply connected domains is explained. An explicit solution can be derived by multiplying of the boundary data with a radial slit map written in terms of the prime functions.

We then focus on two electrical transport problems called "the van der Pauw method" and "electrical capacity". For the van der Pauw method, the prime function allows us to derive new formulas for calculating the resistivity of holey samples. A new method for the electrical capacity of multiply connected domains is formulated by coupling the prime function with asymptotic matching.

We next construct explicit solutions for flows through superhydrophobic surfaces in periodic channels and calculate the slip length of these channels. We end the thesis by mentioning that the new methodology gives accurate estimates for so-called "accessory parameter problems" associated with conformal maps of multiply connected domains.

Acknowledgements

First, I deeply appreciate my supervisor Prof. Darren Crowdy, who always encourages me to dive into the new world of Mathematics. During my master course at the University of Tokyo and my PhD at Imperial College London, he always gave me a deep insight into complex analysis and conformal mappings. Because of his continuous help, I could continue to study these subjects with passion.

Second, I appreciate my former supervisor Prof. Takaaki Nara at the University of Tokyo. He taught me fundamentals of research. My adventure started with his kind recommendation for me to go to the PhD to study complex analysis. I appreciate Prof. Koji Ikuta and Prof. Kumiko Morimura, who have always encouraged me to study abroad.

I advanced my research through the meetings with Prof. Demetrios Papageorgiou, Prof. Marc Hodes, Dr. Eric Keaveny, Dr. Michael Mayer, and Dr. Toby Kirk. Research meetings with them always gave me new ideas for my research topics.

I also have to say thank you to my family. My parents Kazuhiko and Mariko, who had been a teacher, always support me both financially and mentally. My grandparents, Kaname and Chiyoe, who had been a farmer, kept telling me the importance of hard works since I was in elementary school. My two brothers, Toshiyuki and Takayuki, always supported me. With their support and their passion, I always did my best in college.

Through my PhD, I was happy to be surrounded by great colleagues at the Department of Mathematics at Imperial College London, Henry Putley, Anna Katsiavria, Karina, Jamie, Sara, Thivan, Connor, Tobias, Beth, Bo, Jian. I deeply appreciate the research group members, Anna Curran and Henry Rodriguez-Broadbent, who helped me every time to understand mathematics and culture in the UK. I cannot name everyone, but thanks to everyone involved, I was able to write my doctoral dissertation. I also say thank you to my flatmate Hana, who taught me a new tool and technique for drawing figures.

I must thank my sponsor "Nakajima Foundation" in Japan, who supported me with 2-years full tuition for the Department of Mathematics at Imperial College London and 4-years living expenses. Without the funding, I could not have completed my PhD.

Finally, without my wife, Yuka, my thesis is meaningless. She has always supported me throughout my PhD. I am happy that we could complete our PhDs at the same time and I am officially "part of your world". I hope we can share our dreams from now on.

Dedicated to my wife, Yuka Miyoshi.

Contents

List of Tables

List of Figures

Chapter 1

Introduction

1.1 Background

Transport theory focuses on the transport of physical quantities such as heat, gas, water, and mass, and its aim is to quantify these flows. Transport theory dates back to research on heat flow by Fourier. In 1822, Fourier found that the heat flux through materials was proportional to the negative gradient of the temperature field; this is now called Fourier's law (see [59]). Four years later, Ohm found his famous law, which is an electrical analogue of Fourier's law. Ohm's law states that electrical current is proportional to voltage gradient.

Transport theory appears in many areas [22]. For example, it has applications in electrical engineering, such as the study of electrical power systems, measurement of the electrical conductivity of molten salts, signal processing and machine learning, engineering, and research in a wide variety of fields such as, porous media, intelligent transport systems, and infrastructure. Duderstadt and Martin' book on transport theory covers topics such as radiation transport, plasma physics, and gas dynamics [53].

The theory of fluid dynamics can also be interpreted in terms of transport theory [133]. Fluid flows transport energy, mass, heat, and gas. For example, flows in a heat sink transport heat in order to cool down machines in industry [151]. Similar to electrical current, a pressure-driven flow is caused by the pressure difference between the inlet and outlet of tubes or channels. It is noteworthy that different transport phenomena share the same physical model and hence important quantities, such as the total heat flux, electrical conductivity, and diffusion rates can be calculated by solving these mathematical models.

The main purpose of the analysis of transport phenomena is to evaluate the important effective parameters, which characterize the material, the flow, and the industrial performance. Here we choose three parameters as important examples arising in the transport theory.

1.2 Effective parameters arising in transport theory

In this section, we provide detailed explanations of three important parameters associated with physical flows in transport theory. These parameters extensively investigated in this thesis are electrical conductivity (or resistivity), electrical capacitance (or capacity), and slip lengths of fluid flows.

1.2.1 Electrical conductivity/ resistivity

Materials are classified according to their electrical conductivity as insulators, semiconductors, metals, superconductors, etc. Electrical conductivity is a fundamental quantity that determines the properties of metals and has a very long history since Ohm's experimental measurement of resistance.

As is well known, the resistance R of a uniform conductor of length l and cross-sectional area A, as shown in Figure 1.1, is expressed as follows:

$$R = \frac{V}{I} = \sigma \frac{l}{A}. \tag{1.1}$$

The coefficient σ is called resistivity and its inverse is called conductivity.

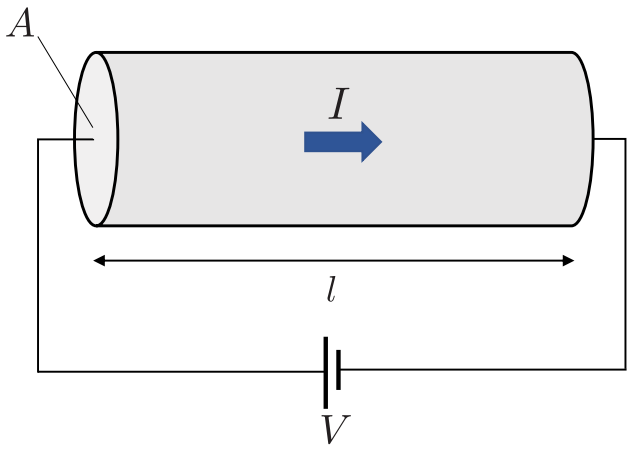

Figure 1.1: Normal setting for measuring electrical resistivity. The current I flows through the material due to the induced voltage V.

Electrical conductivity varies greatly depending on the type of metal, temperature, and impurities inside metals. For example, resistivity is very high for insulators such as quartz but very small for metals. Therefore, laboratory experiments require a technique to measure resistivity easily and accurately. Some research on resistivity measurement in laboratories includes the measurement of the temperature dependence of the electrical conductivity of diamond [54], the electrical conductivity of perovskiteoxide heterostructures

for two-dimensional electron gases [163], resistivity of metals and alloys [125], and even water content or fluid composition of soil [130].

Methods for accurate measurement of electrical conductivity are required in many situations and thus several methods have been proposed. In particular, the two-point method, which involves measuring the voltage difference and current between two electrodes, is a basic method for measuring the resistivity of metals. Wenner used the two-point method for measuring the resistivity of Earth [157]. However, the two-point method is known to be susceptible to contact resistances. Instead of this method, the four-point method is commonly used due to the fact that the method is not affected by contact resistance [148]. The following review paper discusses the various four-point methods in detail [96].

Another famous method for measuring electrical resistivity of samples is the van der Pauw method. Van der Pauw's method is a simple method for measuring the resistivity of flat thin samples, and was invented in 1958 by Van der Pauw [117, 118]. One of the most important advantages of the method is that it can be used to measure resistivity of arbitrary shaped materials. In order to use the method, the sample must satisfy the following conditions [154]:

- The sample must have a flat shape of uniform thickness.
- The sample must not have any isolated holes.
- The sample must be homogeneous and isotropic.

The van der Pauw setup is illustrated in Figure 1.2. Here we assume that the contact size is small and all contacts Ω_a, Ω_b, Ω_z, and Ω_w are located at the edge. The van der Pauw method needs two voltage measurements, V_{zw} and V_{zb}, with the following setups. The first measurement is the voltage difference between Ω_z and Ω_w with current J_{ab} flowing from Ω_a to Ω_b. The second measurement is the voltage difference between Ω_z and Ω_b with current J_{aw} flowing from Ω_a to Ω_w. The important quantities R_{ab}^{zw}, R_{aw}^{zb} are measured resistances defined by

$$R_{ab}^{zw} \equiv \frac{V_{zw}}{J_{ab}}, \quad R_{aw}^{zb} \equiv \frac{V_{zb}}{J_{aw}}. \tag{1.2}$$

Then the sheet resistivity σ is known to satisfy the famous van der Pauw equation [118]:

$$\exp\left(-\frac{\pi d R_{ab}^{zw}}{\sigma}\right) + \exp\left(-\frac{\pi d R_{aw}^{zb}}{\sigma}\right) = 1, \tag{1.3}$$

where d is the thickness of the sample.

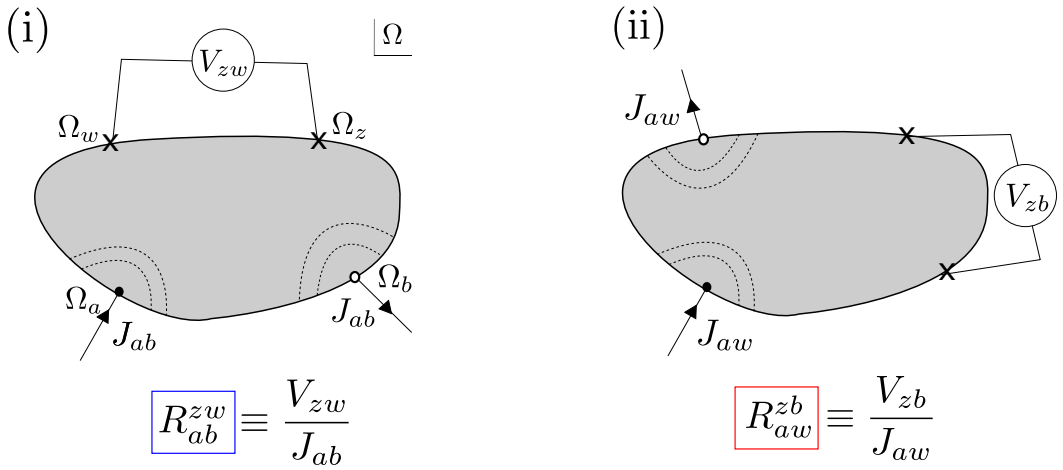

Figure 1.2: Normal van der Pauw setup. The van der Pauw method needs two voltage measurements. The first measurement is the voltage difference between Ω_z and Ω_w with current J_{ab} flowing from Ω_a to Ω_b. The second measurement is the voltage difference between Ω_z and Ω_b with current J_{aw} flowing from Ω_a to Ω_w. The simple two measurements determine the resistivity of the material.

Because of its simplicity, the van der Pauw method is used in many laboratory experiments. In particular, it is used for the resistivity measurement for superconducting materials, due to the fact that it is a convenient and accurate method for measuring the sheet resistivity of square-shaped samples [158, 159].

In recent years, the van der Pauw method has been widely studied for samples with an isolated hole [12, 137, 139]. Szymański *et. al* studied a sample with a single isolated hole whose boundary comprises more than a single point as the natural first case to study. [137, 139]. By conducting both numerical and laboratory experiments Szymański *et al.* showed that the van der Pauw equation (1.3) does not hold for a sample with a hole but conjectured that the data instead satisfy the inequality [137]

$$\exp\left(-\frac{\pi d R_{ab}^{zw}}{\sigma}\right) + \exp\left(-\frac{\pi d R_{aw}^{zb}}{\sigma}\right) \leq 1. \tag{1.4}$$

The same inequality has been proposed in series of papers [112, 138]. Those authors state that a rigorous proof of this conjecture has not been given.

They also find that the pair of measured resistance $(R_{ab}^{zw}, R_{aw}^{zb})$ satisfies another inequality which they dubbed a "lower envelope" – a phrase we also adopt – and they proposed a method to measure the resistivity based on the existence of this envelope [138]. By conjecturing that the shape of the lower envelope depends only on a Riemann modulus ρ, they applied a standard fitting technique for pairs of measurements $(R_{ab}^{zw}, R_{aw}^{zb})$ lying on

this envelope and consequently were able to determine the sample resistivity. They did not, however, succeed in finding a mathematical representation for this lower envelope. The mathematical construction of the van der Pauw method for holey samples is one of the main purposes of the thesis.

1.2.2 Electrical capacity

Here we focus on another quantity associated with electrical engineering, called electrical capacity. To accurately measure the performance of a complex circuit such as interdigitated circuits or MOSFET VLSIs, it is essential to measure their electrical properties, i.e., how current flows in the circuit [55]. Among these, one of the most important quantity to be measured is a capacity of the circuit. As the capacity of the MOS gate determines its delay time, much research has been done in order to measure the capacity of electrically interconnected circuits [50].

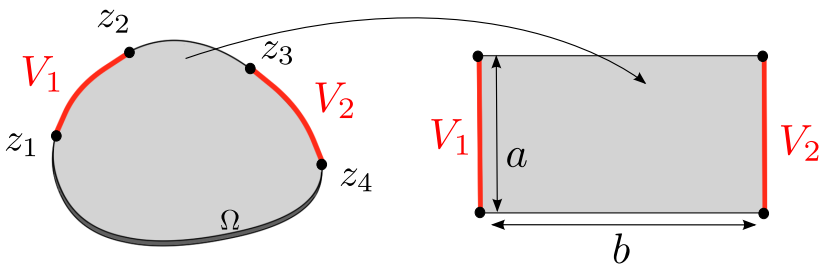

Figure 1.3: Setup for the capacity problem considered by Papamichael [114]. The voltages V_1 and V_2 are set along the portions $\{z_1, z_2\}$ and $\{z_2, z_4\}$, respectively. The capacity of the domain can be calculated by the conformal map to a rectangle.

The classical way to understand two-dimensional capacity is given by Papamichael [114]. First, we explain the capacity in simply connected domains. As shown in Figure 1.3, four points z_i, $i = 1, 2, 3, 4$ around the plate Ω with the unit conductivity are chosen on the boundary of a simply connected (no-hole) sample and constant voltages V_1 and V_2 are applied to the boundary segment (z_1, z_2) and (z_3, z_4), respectively. The other segments (z_2, z_3) and (z_4, z_1) are insulated, i.e., no current flux flows into or out of these boundaries. The thickness of the sample is assumed to be uniform and thin compared to the width of the sample. The problem now is to determine the resistance

$$r = \frac{V_2 - V_1}{I}, \tag{1.5}$$

where I is the current passing through the plate. According to Gaier [60], this resistance is

related to the capacity of the domain

$$C = \frac{I}{4\pi}, \tag{1.6}$$

where V_2 is set to unit voltage and V_1 is grounded in this case.

Mathematically, the problem for finding the capacity of the domain can be formulated by considering the following 2D potential problem:

$$\nabla^2\phi(x,y) = 0, \qquad (x,y) \in \Omega, \tag{1.7}$$

$$\phi(x,y) = 1, \qquad (x,y) \in (z_1, z_2), \tag{1.8}$$

$$\phi(x,y) = 0, \qquad (x,y) \in (z_3, z_4), \tag{1.9}$$

$$\frac{\partial\phi}{\partial n} = 0, \qquad (x,y) \in (z_2, z_3),\ (z_4, z_1), \tag{1.10}$$

and the total current passing through the plate is calculated by the integral along the segment (z_1, z_2) defined by

$$I \equiv \int_{z_1}^{z_2} \frac{\partial\phi}{\partial n} ds, \tag{1.11}$$

where ds is the element of arclength and $\partial\phi/\partial n$ is the outward normal derivative to the domain.

In this thesis, we use a special mathematical property called "conformal invariance" to solve potential problems. Here conformal invariance is used to express the following fact [1, 114]. For a 2D potential ϕ, there is a complex conjugate ψ of the function ϕ. With these functions, we define a complex potential $f(z) \equiv \phi + \mathrm{i}\psi$, where $z \equiv x + \mathrm{i}y$. By the Riemann mapping theorem, there is a conformal map $z = g(\zeta)$ to the original domain Ω_z in z-plane from another domain Ω_ζ in ζ-plane with the same connectivity [107]. Note that the boundaries of the domain, $\partial\Omega_\zeta$, are mapped to the boundaries of the original domain, $\partial\Omega_z$. Now define $\phi + \mathrm{i}\psi = f(g(\zeta)) \equiv F(\zeta)$. Conformal invariance means that equipotential lines, i.e., $\phi =$ const correspond to equipotential lines in Ω_ζ, and streamlines , i.e., $\psi =$ const correspond to streamlines in Ω_ζ.

Due to the conformal invariance of the potential problem above, the mixed boundary value problem (1.7)–(1.10) can be solved by a conformal mapping approach [1, 114]. As shown in Figure 1.3, once we find the conformal map from Ω to a rectangle domain, the total current and capacity are obtained by

$$I = m(Q)^{-1}(V_2 - V_1), \quad C = \frac{1}{4\pi m(Q)}. \tag{1.12}$$

Here $m(Q) = b/a$ is called the conformal modulus of $Q = \{\Omega, (z_1, z_2, z_3, z_4)\}$. The conformal

modulus is one of the important conformal invariants and described in detail in [3].

It is important to note that the expression for the capacity (1.12) is different from equation (2) given by Gaier [60]. This is because he considered different potential problem which satisfies the following conditions:

$$\nabla^2\phi(x,y) = 0, \qquad (x,y) \in \Omega, \tag{1.13}$$

$$\phi(x,y) = 1, \qquad (x,y) \in (z_1, z_2), \tag{1.14}$$

$$\phi(x,y) = 0, \qquad (x,y) \in (z_2, z_3),\ (z_3, z_4),\ (z_4, z_1). \tag{1.15}$$

In this case he obtained the explicit expression for the capacity by the Fourier series expansion:

$$C = \frac{2}{\pi^2} \sum_{n=1,3,5,\cdots}^{\infty} \frac{1}{\sinh(n\pi m(Q))}. \tag{1.16}$$

Due to the complexity of the geometry, most capacities are calculated by numerical approaches. Much research has been done to calculate the capacity of circuits based on numerical schemes that find harmonic functions with certain boundary conditions. Some numerical calculations such as the finite element method are explained in detail in [23].

In recent years, the capacity in multiply connected domains has been studied from both mathematical and engineering perspectives. Interconnected digital circuits have multiple voltage domains with grounded lines in general, whose geometry consists of multiply connected domains [6]. It is therefore essential to be able to calculate the capacity of multiply connected geometries.

Mathematically, the electrical capacity is the same definition as conformal capacity, which has been studied extensively since the 20th century. The rigorous mathematical definition of capacity is given by Pölya and Szegö [120]. Following the book on the conformal capacity and symmetrization given by Dubinin [52], the conformal capacity of a domain $\mathcal{G}$ containing a subset E is defined by the extremal value of the integral

$$\mathrm{cap}(\mathcal{G}, E) = \inf_{\phi} \int_{\mathcal{G}} |\nabla\phi|^2 dxdy, \tag{1.17}$$

where $\phi(x,y)$ is a harmonic function with $\phi(x,y) \geq 1$ for all $(x,y) \in E$ and $\phi(x,y) \to 0$ as $(x,y) \to \partial\mathcal{G}$. It is known that the extremal function ϕ satisfies

$$\nabla^2\phi(x,y) = 0, \qquad (x,y) \in \mathcal{G}/E, \tag{1.18}$$

with the following boundary conditions

$$\phi(x, y) = 0, \qquad (x, y) \in \partial\mathcal{G}, \tag{1.19}$$

$$\phi(x, y) = 1, \qquad (x, y) \in \partial E. \tag{1.20}$$

Here E is the union of the voltage areas and $\mathcal{G}$ is the union of the grounded areas. The simplest example is where $\mathcal{G}$ is taken as the unit disc with centre at the origin and E is a concentric disc of radius ρ, $0 < \rho < 1$. In this case, the capacity is known to be

$$\mathrm{cap}(\mathcal{G}, E) = \frac{2\pi}{\log(1/\rho)}. \tag{1.21}$$

The shapes of E and $\mathcal{G}$ are generally circular regions or slits. Much research has relied on numerical methods because the geometries have multiple disconnected boundaries (see [92], who calculated the capacity of ring capacitors with four electrodes). Due to the conformal invariance of the capacity, the capacity can be calculated by finding a conformal map of a multiply connected domain to a canonical target domain. Conformal mappings, such as the Schwarz-Christoffel mapping or the polycircular arc mapping [40], require finding the unknown parameters called "accessory parameters". This makes it difficult to obtain explicit formulas for the conformal capacities. Therefore, research into the study of capacities uses the finite element method due to the lack of fast mathematical methods for solving the potential problem in the multiply connected domains. An illustration of these techniques is given in Figure 1.4.

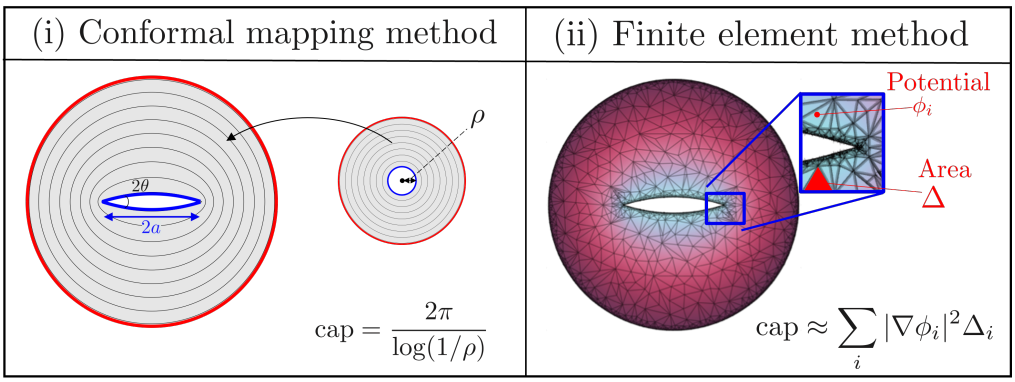

Figure 1.4: (i) Capacity calculation by the conformal mapping approach. In order to obtain the capacity, it is necessary to compute the inner radius ρ. (ii) Finite element method for the capacity calculation. A fine mesh is required to obtain accurate numerical results.

There has been research into obtaining explicit formulas for electrical capacity. Chang obtained analytical formulas for a single IC metal line capacity [25] from Schwarz-Christoffel mappings. Palmer also used the Schwarz-Christoffel map to calculate parallel plate

capacity [113] and the result was verified by Chen *et. al.* [26]. These formulas explained above are all explicit, although geometries in which the capacity can be explicitly calculated are limited. This means that almost all electrical capacities cannot be written in an explicit formula. A new framework is needed to derive estimates of capacities. The main objective of the research presented here is to present a new methodology to obtain explicit simple formulas for electrical capacity of multiply connected domains.

1.2.3 Slip lengths

Another effective parameter is the "slip length" associated with fluid flows. Fluid flows exhibit complex behaviour such as slip at the interface between fluids and solid surfaces. At the micro scale, the interaction between fluid and interface is still unclear but at the macro scale the flow slips at the interface. According to [122], the slip length in fluid flow is influenced by a number of factors such as the degree of hydrophobicity, surface roughness, and the presence of interstitial lubricating layers, the polymer molecular weight, and the applied shear rate.

In classic work, Navier first proposed the concept of slip length in fluid flow; it quantifies the slipperiness of the flow [106]. He found that the slippage at the interface is proportional to a frictional force to the fluid velocity relative to the surfaces [108]. Navier then introduced the concept of flow satisfying partial slip boundary conditions at the interface and defined the slip length as the constant of proportionality.

For flow in a bounded channel with a partial slip boundary condition, the slip length is quantified by equating the total flux of the actual flow and the flow satisfying the Navier slip condition on the walls [82]. The Navier slip condition imposed on the boundary is

$$w = \lambda \frac{\partial w}{\partial \boldsymbol{n}}, \tag{1.22}$$

where w is a velocity of a pressure-driven flow and $\partial/\partial n$ is the Neumann derivative to the surfaces.

Figure 1.5 (i) shows a diagram of slip lengths. The slip length λ is zero (centre of the figure) when the flow has no slip at the interface. The slip length becomes positive when a partial slip occurs at the interfaces. When $\lambda = \infty$, which is called 'perfect slip', the velocity at the wall is equal to the velocity in the bulk. Figure 1.5 (ii) shows a diagram of the slip length of a bounded channel flow. The slip length of the fluid flowing above the wall containing no-shear slots is evaluated by imposing the Navier slip condition on the entire wall.

A review article shows how to measure the slip length of fluid flow in confined geometries such as microfluidic devices [90, 108]. Maxwell was the first to measure the slip length of

(i) Semi-infinite channel

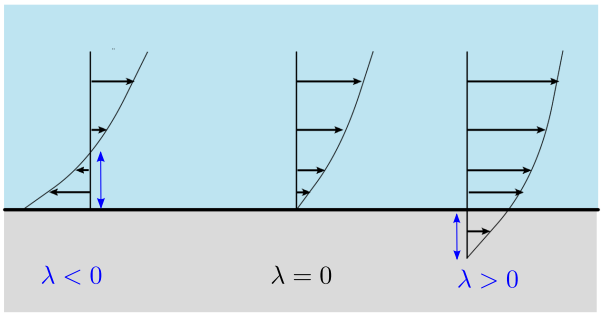

(ii) Bounded channel

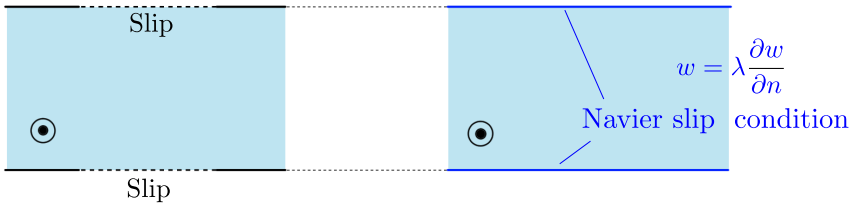

Figure 1.5: Slip length for semi-infinite channels and bounded channel. (i) Slip length of (1.22) is defined by the distance between the boundary and the height where the flow velocity vanishes. (ii) Slip length λ is calculated to satisfy the condition that the total flux of the actual channel flow is equal to the total flux of the right channel with Navier slip condition.

gas flowing past a solid surface [126]. Microscopic slip lengths are measured experimentally using a capillary rheometer at four different temperatures [91]. The velocity profile around the interface is measured directly by particle image velocimetry experiments [111, 145].

Recently, the slip length of fluid flowing through a channel with a superhydrophobic surface has been actively studied, because the fluid slips at the boundary of the superhydrophobic channel, which reduces the friction of the fluid and allows more fluid to flow with less pressure [82]. Because the superhydrophobic surface is slippery, a channel with a superhydrophobic surface can be designed to have applications to anti-corrosion, anti-icing, and drag reduction [116].

When calculating the slip length of a superhydrophobic surface, the no-slip condition is imposed on the wall and the partial slip or perfect slip condition is imposed on the meniscus. Meniscus is the upward or downward curve at the boundary of a liquid produced

by a surface tension. Mathematically, the fluid satisfies a mixed boundary condition with different boundary conditions at the walls and the meniscus. Philip was the first to calculate the slip length of longitudinal flows in a semi-infinite and a bounded channel with periodic superhydrophobic surfaces using a conformal mapping approach [119]. He obtained an explicit formulas for the slip length of a semi-infinite $2L$-periodic channel flow as shown in (i) of Figure 1.6:

$$\lambda = \frac{2L}{\pi} \log \sec \left(\frac{\pi c}{2L} \right), \tag{1.23}$$

where the length of no-shear slots is $2c$, $0 < c < L$. This formula is not only simple but good for approximating the slip length of a bounded channel of finite height [76]. Philip also found a formula for calculating the slip length of a bounded superhydrophobic channel with slots on one side and a wall on the other [119] as shown in (iii) of Figure 1.6.

On the superhydrophobic surface, the meniscus can move into the groove due to pressure fluctuation and gas transfer [72]. When the movement proceeds, the meniscus reaches the bottom of the groove and the friction between the walls becomes high. This transition is called the Cassie state to Wenzel state transition, which is known to decrease the slipperiness of the superhydrophobic surfaces [109].

Crowdy was the first to evaluate the slip length of the longitudinal flow of a semi-infinite channel with superhydrophobic surfaces with partially invaded grooves. The slip length formula is similar to the Philip's case (i) in Figure 1.6 and given by

$$\lambda = \frac{2L}{\pi} \log \operatorname{cosech} \left(\frac{\pi H}{2L} \right), \tag{1.24}$$

where the baseline of the slip length measured here is the top of the gratings [41].

The results described above can be summarised in Figure 1.6. For longitudinal flow in the semi-infinite periodic channel shown in (i), Philip found an explicit formula for the slip length. Philip also found an explicit representation for the periodic channel flows with superhydrophobic slots on one side and a wall on the other as shown in (iii). For the semi-infinite channel with partially invaded grooves, Crowdy found an analytical formula (ii) for the flow and calculated the slip length of the channel [41]. An analytical expression for a bounded periodic channel flow with partially invaded grooves has not, to our knowledge, been given. In Chapter 6, we derive an analytical expression for the flow and this is one of the main contributions of the thesis.

(i) Semi-infinite periodic channel (Philip, 1972)

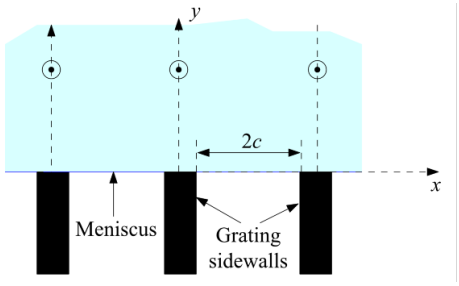

$$\lambda = \frac{2L}{\pi} \log \sec\left(\frac{\pi c}{2L}\right)$$

(ii) Semi-infinite periodic channel with partially invaded grooves (Crowdy, 2021)

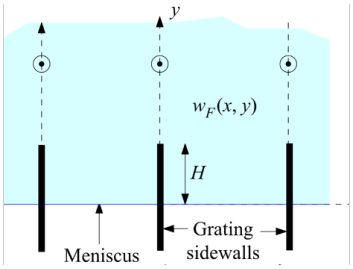

$$\lambda = \frac{2L}{\pi} \log \operatorname{cosech}\left(\frac{\pi H}{2L}\right)$$

(iii) Bounded periodic channel (Philip, 1972)

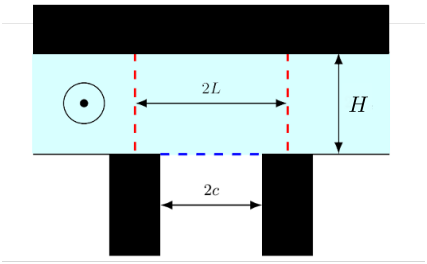

$$\lambda = \frac{H \int_{-c}^{c} \hat{w}_1(x,0)dx}{H^2 L - \int_{-c}^{c} \hat{w}_1(x,0)dx}$$

(iv) Bounded periodic channel with partially invaded grooves

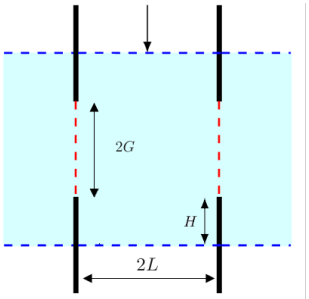

Figure 1.6: Summary of the slip length formulas. The figures (i) and (ii) are copies of Figure 1 of the paper [41]. (i) Semi-infinite periodic channel. (ii) Semi-infinite periodic channel with partially invaded grooves. (iii) Bounded superhydrophobic channel with slots on one side and a wall on the other. (iv) Bounded periodic channel with partially invaded grooves.

1.3 Mathematical techniques

The transport of flows is generally governed by two- or three-dimensional partial differential equations, such as the Laplace, Poisson, and Helmholtz equations, etc, with some boundary conditions. In most cases, numerical techniques are required to evaluate the flows. The Finite Element Method (FEM) is a well-known numerical scheme to perform a finite element analysis of any given physical phenomena. It involves discretizing the problem space into discrete elements, usually triangles for 2D geometries and tetrahedra for 3D geometries, which gives the discretized type of differential equations. The FEM is widely used in engineering and mathematical modelling for fields such as structural analysis, heat transfer, fluid flow, mass transport and electromagnetic potential [124].

The difficulty in solving partial differential equations is often attributed to the inhomogeneity present in the domain. This can manifest itself in various ways such as the presence of internal holes within a sample when measuring resistivity, which increases the computational time. Another example is the evaluation of superhydrophobic surfaces where channels with superhydrophobic surfaces have mixed boundary conditions, including a no-slip condition and a no-shear condition. These mixed boundary conditions can sometimes lead to numerical inaccuracy. The FEMs used for mixed boundary conditions require a large number of mesh points around the boundary where the conditions change, further increasing the computational complexity. These challenges require careful consideration in order to develop accurate and efficient computational models for inhomogeneous domains.

Also, in order to find a geometry that optimises the slip length or capacities, it is necessary to change the geometries one by one to find the optimal parameters that meet the requirements. This procedure has a clear numerical cost when using FEMs. Therefore, analytical formulas for these quantities are desirable to carry out the optimisation.

Another method of solving transport problems is complex analysis. The complex analysis techniques are powerful tool for solving 2D potential problems by using conformal maps. Conformal maps are one-to-one maps from simple domains to physical target regions that have the same connectivity. Conformal mapping is a powerful technique for solving PDEs in complicated 2D domains. Due to the conformal invariance of complex potentials, the potential problems can be solved immediately after finding the appropriate conformal mapping. Moreover, the existence of the conformal mapping is guaranteed by the famous Riemann mapping theorem [107]. Some recent research focuses on extending the conformal mapping theory to other transport problems such as diffusion equations and Helmholtz equations [18,51]. Engineering applications of conformal mapping approaches are discussed in detail in [132]. In order to solve nonlinear partial differential equations in the planar domain, Fokas and Kapaev derived a new transform method, called the Fokas method [58]. Crowdy extended the Fokas method to more general domains consisting of circular arcs and straight lines [38]. The transform method for solving the Helmholtz equation is proposed in [64].

Crowdy has developed a theoretical framework for solving problems in multiply connected domains [40]. Using a special function called the "Schottky-Klein prime function", henceforth simply "prime function", it is possible to derive analytical formulas for the flows. Throughout this thesis we formulate analytical solutions for PDEs based on this special function and we show that the various problems in multiply connected domains can be solved in a closed form.

Another importance of using the complex analysis approach is that the harmonic extension of the field is also calculated. The purpose of solving the fields in the target

domain is usually to evaluate effective parameters explained in the previous section. Using the Cauchy-Riemann equations, the harmonic extension of the field is useful for evaluating the integral along boundaries. We use this technique to calculate effective parameters in Chapter 5 and 6.

1.4 Overview

This section gives an overview of the thesis and the main results of each section. This thesis solves important problems for electrical potentials and fluid mechanics in domains with multiply connected domains and calculates physical quantities appearing in transport theory. The key mathematical tool for solving these problems is the prime function [40].

Chapter 2

This chapter defines an important mathematical tool developed by Crowdy [40] called the Schottky-Klein prime function. The prime function is a special function in multiply connected domains and it is computed uniquely according to the positions and radii of inner circles. Mathematical analysis in multiply connected domains can be done using this function. The properties of the prime function are introduced and the main conformal maps used throughout this thesis are explained in this chapter. The maps described in this chapter are described in detail in [40], but for the sake of completeness they are briefly explained here.

The prime function is also important for solving boundary value problems. In the last section we see that the Schwarz integral formulas with the prime function are used to solve the famous boundary value problems called Dirichlet problems proposed by [40].

Chapter 3

Chapter 3 proposes a new method for solving mixed boundary value problems in multiply connected domains. The boundary value problem we consider in this chapter is one where the boundary data is of a different type on each component of the boundary, e.g. a Dirichlet condition on one boundary and a Neumann condition on the other. This new method is necessary to solve the problems in Chapters 5. In multiply connected domains, one method for solving boundary value problems is the Schwarz integral. This is a method of reconstructing a harmonic function given the real part on the boundary. However, in certain problems, the type of boundary conditions (boundary value or its Neumann derivative) can be different for each boundary, and it is an open question how to solve it specifically for multiply connected domains. In this chapter we propose an integral formula, the generalised Schwarz integral, which gives a specific solution for problems where the boundary conditions are different for each boundary. By using a radial slit map computed for each multiply connected region, the types of boundary conditions are unified,

and by using the Schwarz integral and the single-valuedness condition, an explicit solution is constructed. The solution obtained contains several parameters which are uniquely determined based on the single-valuedness condition. The content of this chapter addresses on the open problem explained in [31] and the results have been published in [98].

Chapter 4

Chapter 4 focuses on the van der Pauw method. While the conventional van der Pauw method can easily measure sheet resistivity, it can only be applied when there are no holes in the sample. This chapter attempts to extend the van der Pauw method to the simplest multiply connected region, the annulus. This can be done by exploiting the fact that the potential is described by the prime function and the van der Pauw equation corresponds to the cross ratio. First, the van der Pauw equation for the annulus is proposed. The equation has a new parameter k which is not included in the conventional van der Pauw equation. By considering the integral with respect to this parameter k, a mathematical proof is given for the existence of the two envelopes predicted by a number of previous authors [112, 138] and a new method for measuring sheet resistivity is proposed. The results of this chapter have been published in [99, 100].

Chapter 5

Continuing with the main topic of electrical transport theory, we study the electrical capacity of multiply connected domains. Similar to Chapter 4, the electrical potential of doubly or multiply connected domains is considered using the prime function introduced in Chapter 2. The aim of this chapter is to propose a new method for estimating the electrical capacity of multiply connected domains. This can be done by matched asymptotic expansions as discussed by Tuck [146] and Van Dyke [150]. We show that matched asymptotic expansions give simple formulas and good estimates for the electrical capacity in multiply connected domains. This research is based on a paper accepted in an IMA Lighthill-Thwaites special issue [97].

Chapter 6

Chapter 6 calculates flow in a channel involving superhydrophobic surfaces and proposes a specific formula for calculating the slip length of such surfaces. In this chapter, an explicit formula for the flow of a superhydrophobic channel with a partially invaded groove is derived and a method for calculating the slip length is proposed. The content of this chapter corresponds to the author's published paper [102].

Chapter 7

In this chapter, a new mathematical technique is given for calculating estimates of so-called "accessory parameters". The new methodology presented here proposes accurate estimates for these parameters by using matched asymptotic expansions proposed in

Chapter 5. This research is partly based on a paper accepted in an IMA Lighthill-Thwaites special issue [97].

Chapter 8

In Chapter 8, the conclusions of the thesis are explained and a short summary for each chapter is given.

Chapter 2

The Schottky-Klein prime function

In this chapter, a special function called the Schottky-Klein prime function is introduced. Throughout this thesis the prime function is a fundamental mathematical tool, so it is instructive to explain the important properties of it here.

The Schottky-Klein prime function is a transcendental function, which was first documented by Baker's book [15] and appeared again in [65]. The physical importance of the prime function was discovered by Crowdy in 2005 to calculate the Schwarz-Christoffel mapping for multiply connected domains [29]. Crowdy also applies this function to solve physical problems which include multiple boundaries. The monograph [40] focuses extensively on how to build solutions for physical problems such as fluid dynamics and heat transfer in multiply connected domains with the use of the prime function.

We first explain the definition of the prime functions. With the use of the prime function the important examples of conformal maps are introduced in the Section 2.3. In Section 2.4 we present an explicit solution for the Dirichlet boundary value problem with multiple boundaries.

The prime function is easily computable and numerically stable after solving some parameters. The parameters of the prime function associated to domains can be obtained by a simple collocation point method [46]. There is also a github code for the evaluation of the prime function, which is accessible when one can use Matlab [9]. Throughout this thesis, many solutions for physical transport problems are calculated numerically by evaluating the prime function.

2.1 The definition of the prime functions

Following [40], the definition of the prime function is described here. Let D_ζ be a multiply connected circular domain consisting the unit disc with M inner circles separated each other, where $M \geq 1$. Let C_0 be the boundary of the unit circle and C_j, $j = 1, \ldots, M$ be

the boundaries of circular discs with centres $\{\delta_j \in \mathbb{C} | j = 1, \ldots, M\}$, and radii $\{q_j \in \mathbb{R} | j = 1, \ldots, M\}$. An example of the geometry when $M = 3$ is illustrated in Figure 2.1.

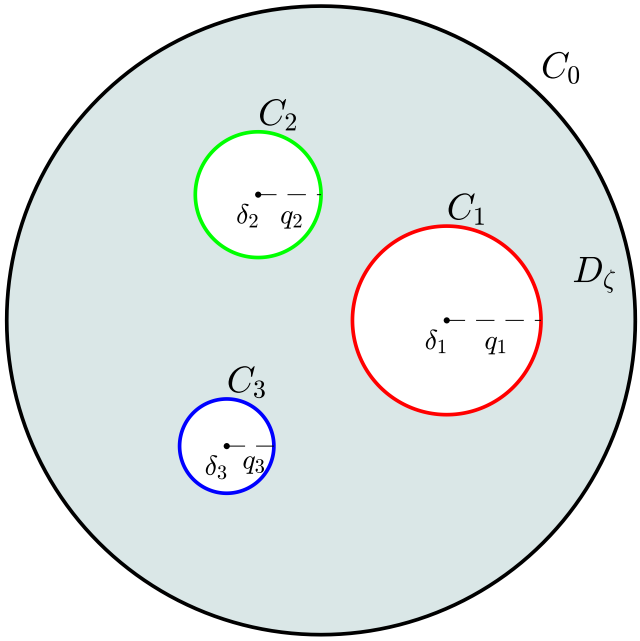

Figure 2.1: A quadruply connected circular domain D_ζ with boundary circles. The outer circle is C_0 and the inner circles are C_1, C_2, and C_3. The centres of the circle C_j are δ_j with radii q_j, $j = 1, 2, 3$.

First the Möbius map θ_j associated with C_j is defined by

$$\theta_j(\zeta) \equiv \delta_j + \frac{q_j^2 \zeta}{1 - \overline{\delta_j} \zeta}, \quad j = 1, \ldots, M. \tag{2.1}$$

Let C_j' be the circle with the centre δ_j' and the radius q_j' which is the reflection of circle C_j in C_0. Also let D_ζ' be the region which is the reflection of D_ζ in C_0. It is easy to see that C_j' is the image of C_j by the Möbius map θ_j. The union of D_ζ and D_ζ' is called the fundamental region associated with the Möbius maps $\{\theta_j | j = 1, \ldots, M\}$ and their inverses. The set of Möbius map is called the Schottky group Θ, defined to be the infinite free group of mappings generated by compositions of the M basic Möbius maps $\{\theta_j | j = 1, \ldots, M\}$ and their inverses $\{\theta_j | j = 1, \ldots, M\}$ and including the identity map [46]. The union of D_ζ and D_ζ' is defined as F and it is explained in [46, 62] that the region F can be viewed as a model of the two "sides" of a compact (symmetric) Riemann surface associated with D_ζ known as its Schottky double. The genus of this compact Riemann surface is M. An

illustration of the fundamental region for $M = 3$ is given in Figure 2.2.

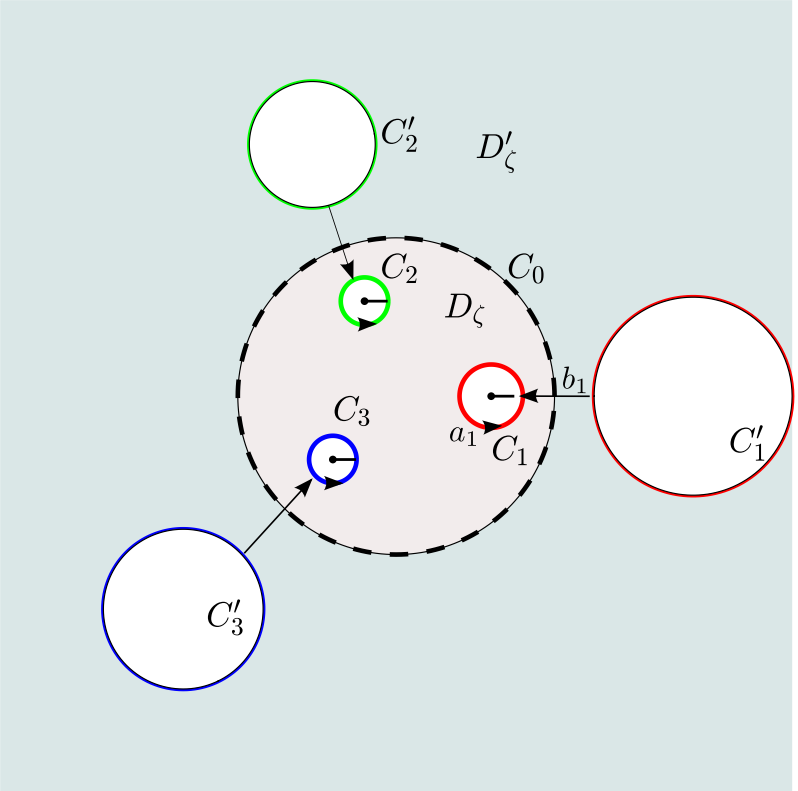

Figure 2.2: A quadruply connected circular domain D_ζ with boundary circles. The circles C_j' are the reflection of the circles C_j in C_0. The a-cycle and b-cycle associated with each circle are illustrated.

It is known that any compact Riemann surface of genus M has exactly M holomorphic differential dv_j, $j = 1, \ldots, M$ [56]. The function $v_j(\zeta)$ is an integral of the first kind and satisfies the following properties around a-cycles and b-cycles as shown in Figure 2.2:

$$\oint_{a_k} dv_j = \delta_{jk}, \qquad \oint_{b_k} dv_j = \tau_{jk}, \quad \tau_{jk} \in \mathbb{C}, \quad j, k = 1, \ldots, M, \tag{2.2}$$

where δ_{jk} is a Kronecker's delta. It is important to mention that these functions are analytic everywhere in D_ζ, but $\mathrm{Re}[v_j]$ is not single-valued around C_j and C_0 because of a logarithmic branch cut between them. An illustration of $v_1(\zeta)$ and $v_2(\zeta)$ for a triply connected domain is given in Figure 2.3.

With $v_j(\zeta)$ and τ_{jk} defined above, Hejhal constructed a function $X(\zeta, \gamma)$ in his

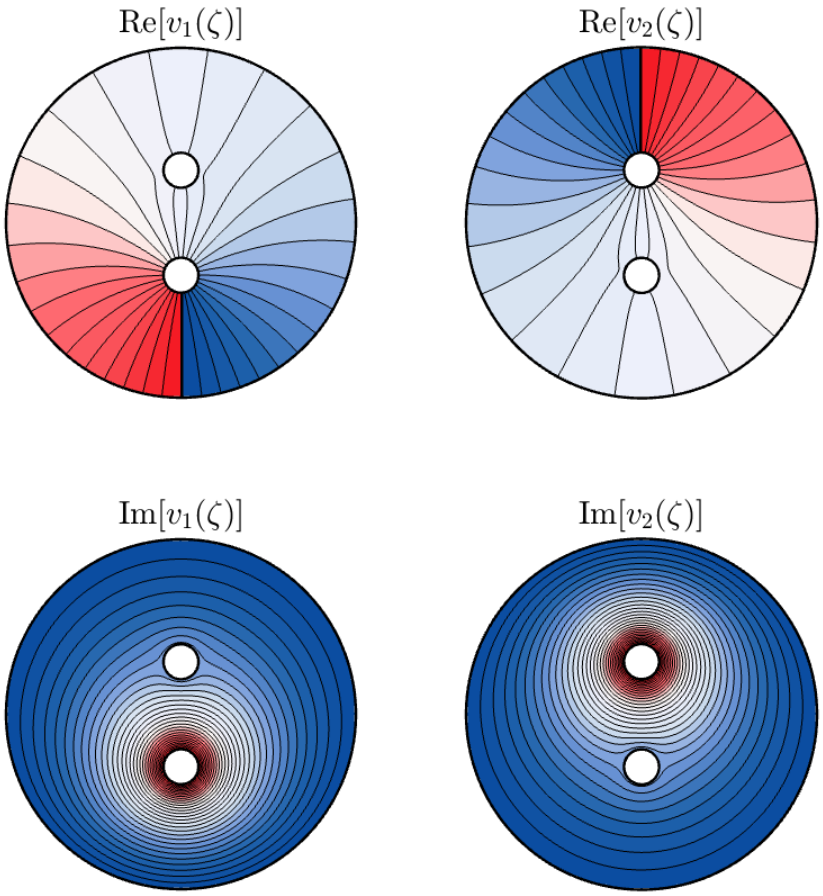

Figure 2.3: Visualization of the functions $v_1(\zeta)$ and $v_2(\zeta)$ of triply connected doamins.

monograph [65] based on the following theorem:

Theorem There is a unique function $X(\zeta, \gamma)$ having the following properties:

- $X(\zeta, \gamma)$ is a single-valued analytic function everywhere in the fundamental region F associated with the Schottky group of D_ζ.
- $\lim_{\zeta \to \gamma} X(\zeta, \gamma)/(\zeta - \gamma)^2 = 1$.
- For $j = 1, 2, \ldots, M$, $X(\zeta, \gamma)$ satisfies

$$X(\theta_j(\zeta), \gamma) = \exp(-2\pi \mathrm{i}(2(v_j(\zeta) - v_j(\gamma)) + \tau_{jj}) \frac{d\theta_j}{d\zeta} X(\zeta, \gamma). \tag{2.3}$$

- $X(\zeta, \gamma)$ has second-order zeros at the set of points $\{\theta(\gamma) |\ \theta \in \Theta''\}$.

Here Θ'' is defined to be the subgroup of Θ with the inverse composition maps and the identity element excluded.

With $X(\zeta,\gamma)$, the Schottky-Klein prime function $\omega(\zeta,\gamma)$ is defined by

$$\omega(\zeta,\gamma) = (X(\zeta,\gamma))^{1/2}, \tag{2.4}$$

where the branch cut of the function is chosen so that $\omega(\zeta,\gamma) \to (\zeta-\gamma)$ as $\zeta \to \gamma$.

The prime function $\omega(\zeta,\gamma)$ has the following properties [40]:

- $\omega(\zeta,\gamma)$ has a simple zero at $\zeta=\gamma$, (2.5)
- $\omega(\gamma,\zeta) = -\omega(\zeta,\gamma)$, (2.6)
- $\overline{\omega}(1/\zeta,1/\gamma) = -\dfrac{1}{\zeta\gamma}\omega(\zeta,\gamma)$, (2.7)
- $\omega(\theta_j(\zeta),\gamma) = -\dfrac{q_j}{1-\overline{\delta}_j\zeta}e^{-2\pi\mathrm{i}(v_j(\zeta)-v_j(\gamma)+\tau_{jj}/2)}\omega(\zeta,\gamma)$. (2.8)

2.2 The prime function for the concentric annulus

In the doubly connected domain, i.e., $M=1$, the prime function is related to one-dimensional theta functions, and can be represented in closed form. Here we consider an eccentric annulus, which is the unit disc with an inner circular hole with radius r_1 and center c_1. The eccentric annulus in the z-plane is mapped to the concentric annulus with inner radius ρ in z'-plane by the simple Möbius transformation [40]:

$$z' = \frac{z-a}{1-az}, \quad a = \frac{1+c_1^2-r_1^2-\sqrt{(1+c_1^2-r_1^2)^2-4c_1^2}}{2c_1}, \quad \rho = \frac{r_1+c_1-a}{1-a(r_1+c_1)}. \tag{2.9}$$

Hence it is enough to consider the prime function in the concentric annulus. The prime function $\omega(\zeta,c)$ for the annulus $\rho<|\zeta|<1$ is a function of two complex variables, ζ and c say, which can be defined explicitly in this case by the formula [40]:

$$\omega(\zeta,c) = -\frac{c}{\hat{P}(1)}P(\zeta/c,\rho), \tag{2.10}$$

where

$$P(\zeta,\rho) \equiv (1-\zeta)\hat{P}(\zeta,\rho), \qquad \hat{P}(\zeta,\rho) \equiv \prod_{n=1}^{\infty}(1-\rho^{2n}\zeta)(1-\rho^{2n}/\zeta). \tag{2.11}$$

It is easy to show, directly from these definitions via an infinite product, that $P(\zeta,\rho)$ satisfies the following functional relations

$$\begin{aligned} P(\zeta^{-1},\rho) &= (1-\zeta^{-1})\prod_{n=1}^{\infty}(1-\rho^{2n}\zeta^{-1})(1-\rho^{2n}\zeta) \\ &= -\zeta^{-1}(1-\zeta)\prod_{n=1}^{\infty}(1-\rho^{2n}\zeta^{-1})(1-\rho^{2n}\zeta) = -\zeta^{-1}P(\zeta,\rho), \end{aligned} \tag{2.12}$$

and

$$\begin{aligned} P(\rho^2\zeta,\rho) &= (1-\rho^2\zeta)\prod_{n=1}^{\infty}(1-\rho^{2(n+1)}\zeta)(1-\rho^{2(n-1)}\zeta^{-1}) \\ &= (1-\zeta^{-1})\prod_{n=1}^{\infty}(1-\rho^{2n}\zeta)(1-\rho^{2n}\zeta^{-1}) = -\zeta^{-1}P(\zeta,\rho). \end{aligned} \tag{2.13}$$

For notational brevity, we write $P(\zeta)$ even though this function *also* depends on the parameter ρ as is clear from its definition (2.11). The reader should bear in mind this additional parametric dependence. We will also need the function $K(\zeta)$ and $L(\zeta)$ defined by

$$K(\zeta) \equiv \zeta\frac{\partial}{\partial\zeta}\log P(\zeta), \tag{2.14}$$

and

$$L(\zeta) \equiv \zeta\frac{\partial K}{\partial\zeta}. \tag{2.15}$$

This logarithmic derivative of the prime function is also an important function in the general function theory on multiply connected domains [40]. By direct calculation,

$$K(\zeta) = -\frac{\zeta}{1-\zeta} - \sum_{n=1}^{\infty}\left(\frac{\rho^{2n}\zeta}{1-\rho^{2n}\zeta} - \frac{\rho^{2n}\zeta^{-1}}{1-\rho^{2n}\zeta^{-1}}\right), \tag{2.16}$$

$$L(\zeta) = -\frac{\zeta}{(\zeta-1)^2} - \sum_{n=1}^{\infty}\left[\frac{\rho^{2n}\zeta}{(1-\rho^{2n}\zeta)^2} + \frac{\rho^{2n}\zeta^{-1}}{(1-\rho^{2n}\zeta^{-1})^2}\right], \tag{2.17}$$

and hence, it is easily shown that $K(\zeta)$ and $L(\zeta)$ satisfy the functional relations

$$K(\zeta^{-1}) = 1 - K(\zeta), \qquad K(\rho^2\zeta) = K(\zeta) - 1, \tag{2.18}$$

and

$$L(\zeta^{-1}) = L(\zeta), \qquad L(\rho^2\zeta) = L(\zeta). \tag{2.19}$$

These mathematical relationships are used extensively in Chapter 4.

2.3 Numerical computation of the prime function for $M > 1$

For $M > 1$, the prime function cannot be written in a simple form like $M = 1$, so a numerical method is necessary for evaluating it. The most numerically efficient method is to make use of freely available MATLAB codes that compute $\omega(.,.)$ for any user-specified circular domain akin to D_ζ [9, 40, 46]. These codes are based on a numerical algorithm described in detail in [46], and which extends an earlier algorithm proposed by Crowdy and Marshall [49]. These methods use Laurent series representations.

For a triply connected domain, it is also known (see Chapter 14 of [40]) that the infinite product representation

$$\omega(z,\zeta) = (z-\zeta)\prod_{\theta\in\Theta''}\frac{(\theta(z)-\zeta)(\theta(\zeta)-z)}{(\theta(z)-z)(\theta(\zeta)-\zeta)}, \tag{2.20}$$

is convergent; here each function θ lies in the set of Möbius maps Θ'' which denotes all elements of the free Schottky group generated by the basic Möbius maps $\{\theta_j, \theta_j^{-1} : j = 1, 2\}$, except for the identity and excluding all inverses [40, 46, 49]. For numerical purposes of evaluation it is necessary to truncate this product, and the natural way to do so is to include all Möbius maps up to a chosen *level*: see [49] for more details. Use of this infinite product is perfectly feasible for most channel geometries. Also, it has been verified that the numerical results from the infinite product representation matches the Laurent series expression when $M = 2$ [49]. However, maintaining a required degree of accuracy requires truncation at increasingly high levels as the radii of C_1 and C_2 get larger, resulting in the convergence of the product becoming unacceptably slow. In such cases, use of the MATLAB code from [9] is preferred and advised.

When $M > 2$ the convergence of the infinite product is an open question (see [31]). Also, even if the series expression is convergent, the convergence becomes very slow as the inner circle approaches each other. In this case, it is recommended to use the github code to calculate the prime function [9].

2.4 Examples of conformal maps

Throughout this thesis, conformal mappings from multiply connected domains are used to solve boundary value problems in two-dimensional domains with multiple boundaries. Here two types of important conformal mappings are introduced. The expressions for these maps are simple rational functions of the prime functions associated to multiply connected

domains D_ζ.

As mentioned in the previous section, the prime function $\omega(\zeta,\gamma)$ is analytic everywhere inside the domain, has a simple zero at $\zeta=\gamma$, and satisfies the functional relations (2.5)–(2.8). Various formulas in terms of the prime function yield several important conformal maps.

2.4.1 Radial slit map

Consider

$$w = w_1(\zeta) = \frac{\omega(\zeta,a)\omega(\zeta,1/\overline{a})}{\omega(\zeta,b)\omega(\zeta,1/\overline{b})}, \tag{2.21}$$

where a and b are two distinct points inside D_ζ. This map has a simple zero at $\zeta=a$ and a simple pole at $\zeta=b$. For $\zeta\in C_0$, i.e., $\overline{\zeta}=1/\zeta$, it is easy to obtain

$$\overline{w_1(\zeta)} = \frac{\overline{\omega}(\overline{\zeta},\overline{a})\overline{\omega}(\overline{\zeta},1/a)}{\overline{\omega}(\overline{\zeta},\overline{b})\overline{\omega}(\overline{\zeta},1/b)} = \frac{\overline{\omega}(1/\zeta,\overline{a})\overline{\omega}(1/\zeta,1/a)}{\overline{\omega}(1/\zeta,\overline{b})\overline{\omega}(1/\zeta,1/b)} = \left(\frac{\overline{a}b}{a\overline{b}}\right) w_1(\zeta), \tag{2.22}$$

where the functional relation (2.7) is used. For $\zeta\in C_j$, $j=1,2,\ldots,M$, by using $\overline{\zeta}=\overline{\theta_j}(1/\zeta)$, it can be shown that

$$\overline{w_1(\zeta)} = \frac{\overline{\omega}(\overline{\zeta},\overline{a})\overline{\omega}(\overline{\zeta},1/a)}{\overline{\omega}(\overline{\zeta},\overline{b})\overline{\omega}(\overline{\zeta},1/b)} = \frac{\overline{\omega}(\overline{\theta_j}(1/\zeta),\overline{a})\overline{\omega}(\overline{\theta_j}(1/\zeta),1/a)}{\overline{\omega}(\overline{\theta_j}(1/\zeta),\overline{b})\overline{\omega}(\overline{\theta_j}(1/\zeta),1/b)} \tag{2.23}$$

$$= \left(\frac{\overline{a}b}{a\overline{b}}\right) e^{-2\pi\mathrm{i}(\overline{v_j(a)}-\overline{v_j(b)}+\overline{v_j(1/\overline{a})}-\overline{v_j(1/\overline{b})})} w, \tag{2.24}$$

where the following property of the prime function is used:

$$\begin{aligned}\overline{\omega(\zeta,a)} = \overline{\omega}(\overline{\theta_j}(1/\zeta),\overline{a}) &= -\frac{q_j}{1-\delta_1/\zeta} e^{2\pi\mathrm{i}(\overline{v_j}(1/z)-\overline{v_j(a)}+\tau_{jj}/2)}\overline{\omega}(1/\zeta,\overline{a}) \\ &= -\frac{q_j}{1-\delta_j/\zeta} e^{2\pi\mathrm{i}(\overline{v_j}(1/z)-\overline{v_j(a)}+\tau_{jj}/2)} \cdot \left(-\frac{\overline{a}}{\zeta}\right)\cdot\omega(\zeta,1/\overline{a}).\end{aligned} \tag{2.25}$$

Thus, it is concluded that the arguments of w are constant on C_j, $j=0,1,\ldots,M$. This map is called a radial slit map because each circular boundary is mapped to a radial slit emanating from the origin. An example of radial slit maps in a quadruply connected domain is illustrated in Figure 2.4.

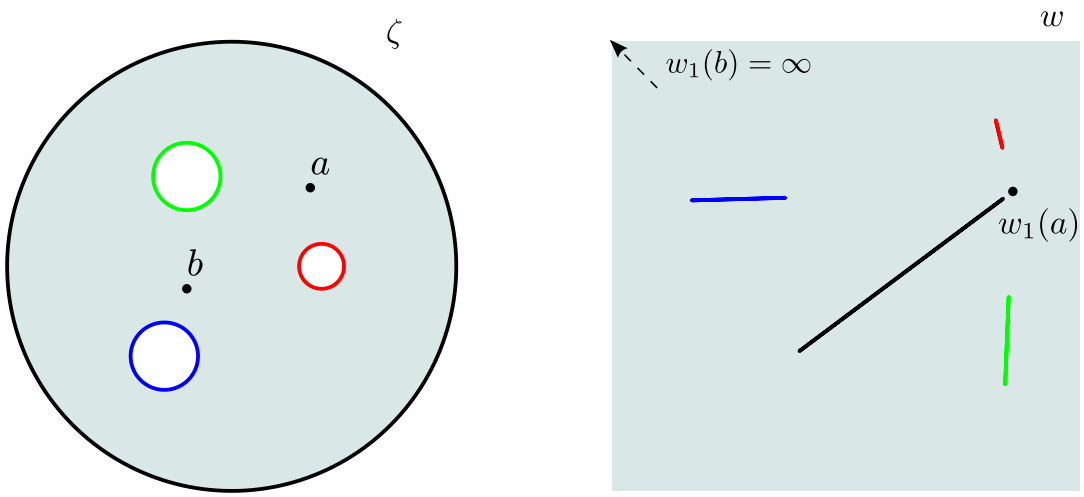

Figure 2.4: (Left) A quadruply connected circular domain D_ζ with boundary circles and inner points a and b. (Right) An example of a radial slit map. The point a and b are mapped to the origin and ∞, respectively.

2.4.2 Horizontal slit map

Consider

$$w = w_2(\zeta) = \frac{1}{2\pi \mathrm{i}} \log\left(\frac{\omega(\zeta, a)}{|a|\omega(\zeta, 1/\overline{a})}\right), \qquad a \in D_\zeta. \tag{2.26}$$

Note that the function $w_2(\zeta)$ has a branch cut between a to $1/\overline{a}$. This function is called the (modified) Green's function associated with the domain D_ζ [40]. It can be shown that, on C_0,

$$\overline{w_2(\zeta)} = -\frac{1}{2\pi \mathrm{i}} \log\left(\frac{\overline{\omega(\zeta, a)}}{|a|\overline{\omega(\zeta, 1/\overline{a})}}\right) = -\frac{1}{2\pi \mathrm{i}} \log\left(\frac{\overline{\omega}(1/\zeta, \overline{a})}{|a|\overline{\omega}(1/\zeta, 1/a)}\right) = w_2(\zeta). \tag{2.27}$$

Also, on C_j, we have

$$\begin{aligned}\overline{w_2(\zeta)} &= -\frac{1}{2\pi \mathrm{i}} \log\left(\frac{\overline{\omega(\zeta, a)}}{|a|\overline{\omega(\zeta, 1/\overline{a})}}\right) = -\frac{1}{2\pi \mathrm{i}} \log\left(\frac{\overline{\omega}(\overline{\theta_j}(1/\zeta), \overline{a})}{|a|\overline{\omega}(\overline{\theta_j}(1/\zeta), 1/a)}\right) \\ &= \overline{v_j(a)} - \overline{v_j}(1/a) + w_2(\zeta),\end{aligned} \tag{2.28}$$

where the functional property (2.25) is used.

Thus, it is concluded that the imaginary part of $w_2(\zeta)$ is constant on each boundary C_j,

$j = 0, 1, \ldots, M$. This map is called a horizontal slit map because each boundary is mapped to a slit parallel to the real axis. An example of horizontal a slit map in a quadruply connected domain is illustrated in Figure 2.5.

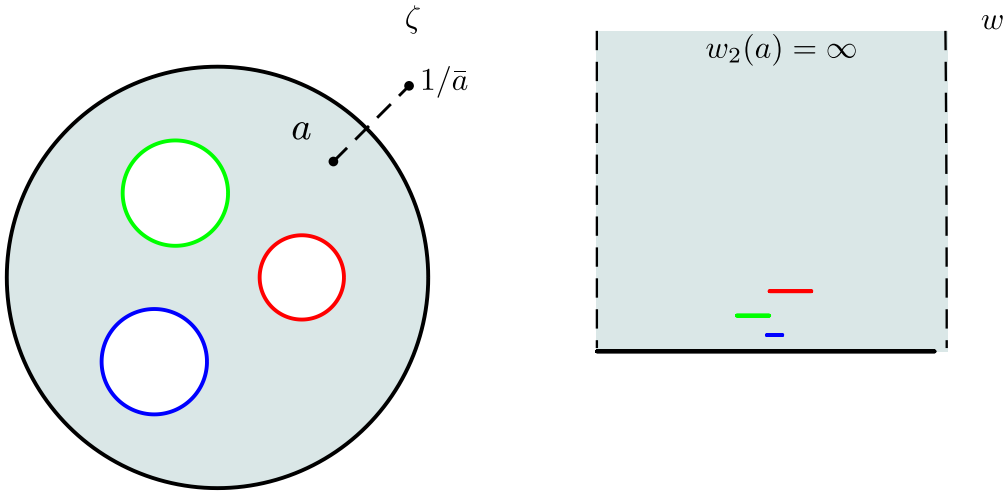

Figure 2.5: (Left) A quadruply connected circular domain D_ζ with boundary circles and a branch cut between $z = a$ and $z = 1/\overline{a}$. (Right) An example of a horizontal slit map.

An important example of the horizontal slit map is the map from a symmetrical triply connected domain with radii $q_1 = q_2 = q$, $q > 0$, and centres $\delta_1 = \overline{\delta_2} = \delta$:

$$w = w_3(\zeta) = \frac{1}{2\pi \mathrm{i}} \log\left(\frac{\omega(\zeta, \theta_1(\infty))}{\omega(\zeta, \theta_2(\infty))}\right), \tag{2.29}$$

where δ is purely imaginary. This map is shown in Figure 2.6. It maps the outer boundary to a slit on the real axis and the two inner circles to lines parallel to the real axis. Because of the symmetry, the function $w_3(\zeta)$ satisfies a special functional relation

$$w_3(-\zeta) = -w_3(\zeta). \tag{2.30}$$

This map is used to solve for a superhydrophobic channel flow in Chapter 6.

2.5 Schwarz integral formulas for multiply connected domains

Another important application of the prime function is presenting the explicit solution for the Dirichlet problem in multiply connected domains, which was discovered by Crowdy [32]. This method is used for solving several boundary value problems in this thesis and used

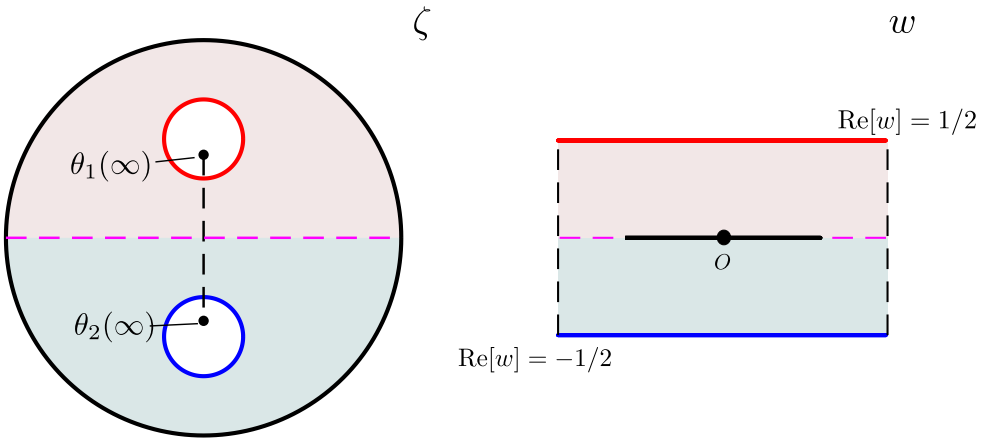

Figure 2.6: (Left) A triply connected circular domain D_ζ with boundary circles with branch cut between two inner circles. (Right) An example of a horizontal slit map.

extensively in Chapter 3, where we propose a new solution for a mixed boundary value problem. Let D_ζ be a multiply connected domain consisting of M inner circles in complex ζ-plane. The Dirichlet problem in D_ζ is to find the solution ϕ satisfying

$$\nabla^2\phi = 0, \qquad \zeta \in D_\zeta, \tag{2.31}$$

with

$$\phi = \Phi_j(\zeta), \qquad \zeta \in C_j,\ j = 0, 1, \ldots, M, \tag{2.32}$$

where $\Phi_j(\zeta)$, $j = 0, 1, \ldots, M$ are continuous real functions around each circle C_j. This problem appears in vast areas of applications, such as irrotational 2D flow and finding electrical potentials [114].

Because ϕ is harmonic it is convenient to define the complex-valued function $f \equiv \phi + \mathrm{i}\psi$, where ψ is the harmonic conjugate of the function ϕ. The problem now is to find a complex function $f(\zeta)$ with boundary conditions

$$\mathrm{Re}[f(\zeta)] = \Phi_j(\zeta), \qquad \zeta \in C_j,\ j = 0, 1, \ldots, M. \tag{2.33}$$

It is important to note that $f(\zeta)$ is not necessary single-valued. This is because any harmonic function can be represented by the real part of an analytic function plus a logarithmic term [152]. The logarithmic function has a continuous real part, but its imaginary part has a branch cut.

The simplest case is when D_ζ is the unit disc, i.e., no inner circle inside it. In this case, the famous integral formula called the Poisson integral formula for the unit disc [1] can recover the analytic function up to an imaginary constant. The function $f(\zeta)$ analytic in the unit disc is given by

$$f(\zeta) = \frac{1}{2\pi \mathrm{i}} \oint_{C_0} \Phi_0(\zeta') \frac{\zeta' + \zeta}{\zeta' - \zeta} \frac{d\zeta'}{\zeta'} + \mathrm{i}c_0, \quad c_0 \in \mathbb{R}. \tag{2.34}$$

A simple proof of the formula is given in [1].

For $M = 1$ and D_ζ taken to be a canonical doubly connected concentric annulus the solution can be expressed in terms of the lesser known, but still arguably classical, Villat integral formulas [40, 149]. Crowdy [32, 40] has shown that the Poisson and Villat integral formulas are special cases of much more general integral formulas valid for any $(M+1)$-connected domain [40] with $M \geq 0$. These formulas were constructed [32, 40] using the prime function associated with any such multiply connected circular domains. Crowdy [32, 40] has shown that $f(\zeta)$ has the representation

$$f(\zeta) = I(\zeta) - \sum_{k=1}^{M} A_k v_k(\zeta) + \mathrm{i}c_0, \qquad c_0 \in \mathbb{R}, \tag{2.35}$$

where the single-valued (in D_ζ) integral $I(\zeta)$ is

$$\begin{aligned} I(\zeta) = &\frac{1}{2\pi \mathrm{i}} \oint_{C_0} \Phi_0(\zeta')(d \log \omega(\zeta, \zeta') + d \log \overline{\omega}(\zeta^{-1}, \zeta'^{-1})) \\ &- \frac{1}{2\pi \mathrm{i}} \sum_{k=1}^{M} \oint_{C_k} \Phi_k(\zeta')(d \log \omega(\zeta, \zeta') + d \log \overline{\omega}(\overline{\theta_k}(\zeta^{-1}), \zeta'^{-1})). \end{aligned} \tag{2.36}$$

The set of constants $\{A_j | j = 1, \ldots, M\}$ is given by

$$A_j = -\left[\int_{C_0} \Phi_0 d\hat{v}_j - \sum_{k=1}^{M} \int_{C_k} \Phi_k d\hat{v}_j \right], \tag{2.37}$$

where $\hat{v}_k$ are linear combinations of v_j, $j = 1, 2, \ldots, M$.

The prime function $\omega(\zeta, \zeta')$ has a simple zero whenever $\zeta = \zeta'$ so (2.36) is also a singular integral formula of Cauchy type. In the simply connected case, or $M = 0$, the relevant prime function is just $\omega(\zeta, \zeta') = (\zeta - \zeta')$ and (2.35) reduces to the familiar Poisson integral formula (3.2).

The existence of the term v_k, $k = 1, \ldots, M$ means that $f(\zeta)$ is no longer a single-valued function except when $A_k = 0$ for $k = 1, \ldots, M$. To ensure that $f(\zeta)$ is single-valued, the

boundary condition $\Phi_j(\zeta)$ should satisfy M conditions:

$$\int_{C_0} \Phi_0 d\hat{v}_k - \sum_{j=1}^{M} \int_{C_j} \Phi_j d\hat{v}_k = 0, \quad k = 1, \ldots, M. \tag{2.38}$$

This is called the single-valuedness condition and it will be shown that the condition is important when we solve mixed boundary problems in multiply connected domains in Chapter 3.

2.6 Conclusions

We have introduced the prime function and presented its important functional properties. Using the prime function, we have shown that important conformal maps such as radial slit maps and horizontal slit maps can be written in terms of it. We also showed that the solution for the Dirichlet boundary value problems in multiply connected domains is expressible in terms of the prime function. In addition, we have noted the single-valuedness conditions for the boundary values.

The horizontal slit map and the Schwarz integral formula presented are shown here to be powerful mathematical tools for solving physical problems. For example, they are used to solve for channel flow over superhydrophobic surfaces with partially invaded grooves in Chapter 5.

In the next Chapter we extend the Schwarz integral formula described in the last section to produce "generalized Schwarz integral formulas", which solve mixed boundary value problems in multiply connected domains. The extension comes from a combination of radial slit maps and the Schwarz integral formula.

Chapter 3

Generalized Schwarz integral formulas for multiply connected domains

This chapter focuses on a generalization of the Schwarz integral formulas in the class of multiply connected circular domains. A Schwarz integral formula retrieves, up to an imaginary constant, an analytic function in a domain given its real part on the boundary. This integral formula corresponds to the solution for the Dirichlet problem in a multiply connected domain. Here we derive an integral formula for solving mixed-type boundary value problems in multiply connected domains. The present chapter combines Schwarz integral formulas with the radial slit conformal mappings introduced in Chapter 2, also expressible in terms of the prime function, to produce integral expressions for analytic functions where more general linear combinations of their real and imaginary parts are specified on the boundary components of a multiply connected domain. We refer to the resulting expressions as generalized Schwarz integral formulas.

3.1 Introduction and background

Consider the problem of finding a function $f(\zeta)$, analytic in some given $(M+1)$-connected two-dimensional domain D in a complex ζ-plane for $M \geq 1$, with the following data specified on its $M+1$ boundary components $\{\partial C_j | j = 0, 1, \ldots, M\}$:

$$\mathrm{Re}[e^{\mathrm{i}\alpha_j} f(\zeta)] = r_j(\zeta), \qquad \zeta \in C_j, \qquad j = 0, 1, \ldots, M, \tag{3.1}$$

for some given set of real constants $\{\alpha_j | j = 0, 1, \ldots, M\}$ and where the set of real-valued functions $\{r_j(\zeta) | j = 0, 1, \ldots, M\}$ is given. This problem arises in a wide range of applied

mathematical applications. It has the advantage of conformal invariance, so that solving it in some canonical class of domains has great value. When $M = 0$ and D is the canonical simply connected unit disc, (3.1) is just the classical Schwarz problem whose solution was already given in Chapter 2 as

$$e^{\mathrm{i}\alpha_0} f(\zeta) = \frac{1}{2\pi \mathrm{i}} \oint_{|\zeta'|=1} \frac{d\zeta'}{\zeta'} \frac{\zeta' + \zeta}{\zeta' - \zeta} r_0(\zeta') + \mathrm{i}c_0, \qquad c_0 \in \mathbb{R}. \tag{3.2}$$

When $\alpha_j = 0$ for all values of j, and D is taken as a circular domain D_ζ in a complex ζ plane comprising the unit disc with outer boundary C_0 and M smaller circular discs with boundaries $\{C_j | j = 1, \ldots, M\}$ excised, Crowdy [32, 40] has shown that $f(\zeta)$ has the representation as introduced in Chapter 2:

$$f(\zeta) = I(\zeta) - \sum_{k=1}^{M} A_k v_k(\zeta) + \mathrm{i}c_0, \qquad c_0 \in \mathbb{R}, \tag{3.3}$$

where the single-valued (in D_ζ) integral $I(\zeta)$ is given by the equation (2.36).

In the special case where the data on the right hand side of (3.1) is also a set of constants on each boundary component, Crowdy [33] used the prime function to derive formulas for the solutions of (3.1) for any values of the parameters $\{\alpha_j | j = 0, 1, \ldots, M\}$. Those formulas are not integral formulas of Cauchy type, but are akin to those found to describe Schwarz-Christoffel conformal mapping formulas to multiply connected polygons [13, 29, 30]. This is because the special piecewise-constant nature of the data allows use of conformal slit mappings expressible in terms of the prime function to deduce expressions for the functional form of the derivative $df/d\zeta$ up to a finite set of accessory parameters.

To summarize, problem (3.1) is known to admit explicit formulas for its solution in terms of the prime function in (at least) the two cases where: (i) all the constants $\{\alpha_j | j = 0, 1, \ldots, M\}$ are equal, but with no restrictions on the data $\{r_j(\zeta) | j = 0, 1, \ldots, M\}$; (ii) when the data $\{r_j | j = 0, 1, \ldots, M\}$ are constants but with no restrictions on $\{\alpha_j | j = 0, 1, \ldots, M\}$.

A natural question arises: can integral formulas in terms of the prime function be found for the solution, when it exists, of problem (3.1) when there are no restrictions on either the constants $\{\alpha_j | j = 0, 1, \ldots, M\}$ or the data $\{r_j(\zeta) | j = 0, 1, \ldots, M\}$?

The answer, as we show here, it is in the affirmative and is again use of conformal slit mappings – here we use the class of radial slit mappings [40, 48] – that provides the key to the construction.

3.2 The construction of solution: radial slit map approach

In this section we provide a general scheme to solve the boundary value problem (3.1).

(i) Doubly connected domain

To illustrate the essential idea, take D_ζ to be the concentric annulus $\rho < |\zeta| < 1$ in which a single-valued analytic function $f(\zeta)$ must satisfy the boundary conditions

$$\begin{aligned} \mathrm{Re}[f(\zeta)] &= r_0(\zeta), \qquad |\zeta| = 1, \\ \mathrm{Im}[f(\zeta)] &= r_1(\zeta), \qquad |\zeta| = \rho, \end{aligned} \tag{3.4}$$

where $r_0(\zeta)$ and $r_1(\zeta)$ are given real continuous functions on the respective boundaries. This is not a standard Schwarz problem because the real part of $f(\zeta)$ is given on one boundary of the doubly connected domain, and its imaginary part on the other. It corresponds to problem (3.1) with $M = 1$ and $\alpha_0 = 0, \alpha_1 = \pi/2$. Therefore, the standard Schwarz integral formula (2.35) – which, in this case, is equivalent to the Villat integral formula – cannot be used directly here. Consequently, to find $f(\zeta)$, other ideas are needed.

Our solution is to consider the radial slit mapping in Chapter 2:

$$\chi = \eta(\zeta) = c_\eta \frac{\omega(\zeta, a)\omega(\zeta, 1/\overline{a})}{\omega(\zeta, b)\omega(\zeta, 1/\overline{b})}, \quad c_\eta \in \mathbb{C}, \tag{3.5}$$

where, in this case, $\omega(.,.)$ is the prime function of the annulus. The distinct points a and b lie strictly inside D_ζ and can be chosen so that, when viewed as a conformal mapping to a complex χ-plane, the image of the boundary circle $|\zeta| = 1$ is a finite-length slit along the real χ-axis and that of $|\zeta| = \rho$ is a finite-length slit along the imaginary χ-axis. Now introduce

$$X(\zeta) \equiv \eta(\zeta) f(\zeta) \tag{3.6}$$

which is analytic in D_ζ except for a simple pole of unknown residue, B say, at $\zeta = b$. Since $\eta(\zeta)$ takes real values on $|\zeta| = 1$,

$$\mathrm{Re}[X(\zeta)] = \eta(\zeta)\mathrm{Re}[f(\zeta)] = \eta(\zeta) r_0(\zeta), \qquad |\zeta| = 1 \tag{3.7}$$

and since $\eta(\zeta)$ takes purely imaginary values on $|\zeta| = \rho$,

$$\mathrm{Re}[X(\zeta)] = -\frac{\eta(\zeta)}{\mathrm{i}}\mathrm{Im}[f(\zeta)] = \mathrm{i}\eta(\zeta) r_1(\zeta), \qquad |\zeta| = \rho. \tag{3.8}$$

The simple pole of $X(\zeta)$ at b can be subtracted off:

$$\mathrm{Re}\left[X(\zeta) - \frac{B}{\zeta - b}\right] = \begin{cases} \eta(\zeta) r_0(\zeta) - \mathrm{Re}\left[\dfrac{B}{\zeta - b}\right], & |\zeta| = 1, \\ \\ \mathrm{i}\eta(\zeta) r_1(\zeta) - \mathrm{Re}\left[\dfrac{B}{\zeta - b}\right], & |\zeta| = \rho. \end{cases} \tag{3.9}$$

This modified boundary value problem now more closely resembles a standard Schwarz problem in the annulus for the (single-valued, analytic in D_ζ) function in square brackets on the left hand side of (3.9). It does not quite qualify as such, however, as the real part of the function is not completely specified by the right-hand-side of (3.9) because B in unknown. But by pretending it known, the Schwarz integral formula (2.35) can be used to write

$$X(\zeta) = \frac{B}{\zeta - b} + I(\zeta) - A_1 v_1(\zeta) + \mathrm{i}c, \qquad c \in \mathbb{R}, \tag{3.10}$$

where $I(\zeta)$ is given by (2.36). Therefore,

$$f(\zeta) = \frac{1}{\eta(\zeta)} \left[I(\zeta) + \frac{B}{\zeta - b} + \mathrm{i}c \right], \tag{3.11}$$

which contains the unknown parameters B and c. But these must be chosen so that the function in square brackets in (3.11) vanishes at the zero of $\eta(\zeta)$ in D_ζ at $\zeta = a$ in order that $f(\zeta)$ is analytic there. With these parameters so determined, (3.11) is an integral formula for the required solution. It is essentially the Schwarz integral formula from [32, 40] but now with an enmeshed radial slit mapping: notice that $\eta(\zeta)$ appears not only outside the square bracket in (3.11) but also in the integral formula for $I(\zeta)$ owing to its appearance in the right-hand-side data in (3.9). For this reason, we have chosen to refer to it as a *generalized Schwarz integral formula* for the annulus.

(ii) Multiply connected domain

Now we discuss the generalized Schwarz problem for $M+1$-connected domains to find an analytic and single-valued function $f(\zeta)$, which satisfies the following boundary conditions

$$\mathrm{Re}[e^{\mathrm{i}\alpha_j} f(\zeta)] = r_j(\zeta), \qquad \zeta \in C_j, \quad j = 0, \ldots, M. \tag{3.12}$$

The construction of the solution starts by finding the radial slit map $\eta(\zeta)$ which satisfies

$$\arg[\eta(\zeta)] = -\alpha_j, \qquad \zeta \in C_j, \quad j = 0, \ldots, M. \tag{3.13}$$

Considering $\eta(\zeta)f(\zeta)$, and noting that $\eta(\zeta)$ has a pole at $\zeta = b$, we have the following boundary conditions:

$$\mathrm{Re}\left[\eta(\zeta)f(\zeta) - \frac{B}{\zeta - b}\right] = e^{\mathrm{i}\alpha_j}\eta(\zeta)r_j(\zeta) - \mathrm{Re}\left[\frac{B}{\zeta - b}\right] \equiv s_j(\zeta), \quad \zeta \in C_j, \quad j = 0, \ldots, M, \tag{3.14}$$

where $B \in \mathbb{C}$ is an unknown parameter to be found. Then the solution is given by using the Schwarz integral formula as follows:

$$f(\zeta) = \frac{1}{\eta(\zeta)}\left[I(\zeta) + \frac{B}{\zeta - b} + \mathrm{i}c_0\right], \quad c_0 \in \mathbb{R}, \tag{3.15}$$

where $I(\zeta)$ is a Schwarz integral formula for multiply connected domains given in (2.36) with boundary data $s_j(\zeta)$.

The parameters should satisfy the following conditions. First, because $\eta(\zeta)$ has a zero at $\zeta = a$ and $f(\zeta)$ must be analytic at $\zeta = a$, the function in square brackets must vanish at $\zeta = a$, which means

$$I(a) + \frac{B}{a - b} + \mathrm{i}c_0 = 0, \tag{3.16}$$

and because $f(\zeta)$ is single-valued we have M single-valuedness conditions:

$$-\int_{C_0} s_0(\zeta)dv_k(\zeta) + \sum_{j=1}^{M}\int_{C_j} s_j(\zeta)dv_k(\zeta) = 0, \quad k = 1, \ldots, M. \tag{3.17}$$

We have parameters $B \in \mathbb{C}$ and $c_0 \in \mathbb{R}$, which gives 3 real parameters to be found. However, we have M single-valuedness conditions and two conditions due to the fact that $\eta(\zeta)$ has a zero at $\zeta = a$.

When we consider finding an analytic and single-valued function $f(\zeta)$ which satisfies the given boundary data $r_0(\zeta)$, the above argument means that there are $M - 1$ additional conditions on $r_j(\zeta)$. This was first proved mathematically by Vekua [152]. The important result here is that when $M = 1$, i.e., D_ζ is the annular region, there always exists an analytic and single-valued function which satisfies the given regular boundary data $r_0(\zeta)$ and $r_1(\zeta)$. For $M > 1$, it will be seen that these $M - 1$ conditions are necessary for solving the parameters of multi-valued functions in section 3.3.

3.3 Generalized Schwarz integral formulas with multi-valued functions

In this section, we will see how the Schwarz problem in multiply connected domains can be uniquely solved by introducing multi-valued functions. The existence of the term v_k in the solution (3.3) for the Dirichlet problem means that the solution $f(\zeta)$ is analytic but not necessarily single-valued unless $A_k = 0$ for $k = 1, \ldots, M$. Hence, it is clear that the boundary value $r_j(\zeta)$ satisfies the M conditions if we want to find a single-valued analytic function for the Dirichlet problem.

Here we consider the problem of finding an analytic, but not necessarily single-valued function which satisfies the following boundary conditions:

$$\begin{cases} \mathrm{Re}[f(\zeta)] = r_0(\zeta), & \zeta \in C_0 \\ \mathrm{Re}[f(\zeta)] = r_1(\zeta), & \zeta \in C_1 \\ \mathrm{Im}[f(\zeta)] = r_2(\zeta), & \zeta \in C_2. \end{cases} \tag{3.18}$$

The continuities of $r_j(\zeta)$ around the boundary C_j, for $j = 0, 1, 2$, allow us to have a branch cut between C_0 and C_1. This means that real part of $f(\zeta)$ should be continuous around C_0 and C_1, but the imaginary part of $f(\zeta)$ is not necessarily continuous. It is convenient to write

$$f(\zeta) = \hat{f}(\zeta) + \mathrm{i}\beta v_1(\zeta), \quad \beta \in \mathbb{R}, \tag{3.19}$$

where $\hat{f}(\zeta)$ is a single-valued function in D_ζ. Note that the function $v_1(\zeta)$ introduced in Chapter 2 has a branch-cut between C_0 and C_1. By introducing an appropriate radial slit map $\eta(\zeta)$, which satisfies

$$\begin{cases} \arg[\eta(\zeta)] = 0 \text{ or } \pi, & \zeta \in C_0,\ C_1, \\ \arg[\eta(\zeta)] = \dfrac{\pi}{2} \text{ or } -\dfrac{\pi}{2}, & \zeta \in C_2, \end{cases} \tag{3.20}$$

we have the modified Schwarz boundary value problem

$$\mathrm{Re}\left[\eta(\zeta)\hat{f}(\zeta) - \frac{B}{\zeta - b}\right] = \begin{cases} \eta(\zeta)(r_0(\zeta) - \mathrm{Re}[\mathrm{i}\beta v_1(\zeta)]) - \mathrm{Re}\left[\dfrac{B}{\zeta - b}\right] \equiv s_0(\zeta), & \zeta \in C_0, \\ \eta(\zeta)(r_1(\zeta) - \mathrm{Re}[\mathrm{i}\beta v_1(\zeta)]) - \mathrm{Re}\left[\dfrac{B}{\zeta - b}\right] \equiv s_1(\zeta), & \zeta \in C_1, \\ \mathrm{i}\eta(\zeta)(r_2(\zeta) - \mathrm{Im}[\mathrm{i}\beta v_1(\zeta)]) - \mathrm{Re}\left[\dfrac{B}{\zeta - b}\right] \equiv s_2(\zeta), & \zeta \in C_2. \end{cases} \tag{3.21}$$

Thus, we have the solution for the mixed boundary value problem (3.18):

$$f(\zeta) = \frac{1}{\eta(\zeta)} \left[I(\zeta) + \frac{B}{\zeta - b} + \mathrm{i}c_0 \right] + \mathrm{i}\beta v_1(\zeta). \tag{3.22}$$

The problem now is to find the parameters $\beta, c_0 \in \mathbb{R}$, and $A \in \mathbb{C}$. Since $\hat{f}(\zeta)$ is a single-valued function in D_ζ, the boundary data $s_j(\zeta)$, $j = 0, 1, 2$, must satisfy the following single-valuedness conditions

$$-\int_{C_0} s_0(\zeta) dv_k(\zeta) + \sum_{j=1}^{2} \int_{C_j} s_j(\zeta) dv_k(\zeta) = 0, \quad k = 1, 2. \tag{3.23}$$

This gives us two real linear equations. Since the radial slit map $\eta(\zeta)$ has a zero at $\zeta = a$, we also require that the function inside the bracket vanishes at $\zeta = a$, i.e.,

$$I(a) + \frac{B}{a - b} + \mathrm{i}c_0 = 0. \tag{3.24}$$

The real part and the imaginary parts of this equation give two additional conditions. There are the 4 real linear equations for the 4 unknown real parameters, and so the mixed boundary value problem (3.18) can be solved uniquely.

3.4 Products of radial slit mappings

This section focuses on *products* of radial slit maps. The product of N radial slit mappings is defined by

$$\eta(\zeta) \equiv \prod_{n=1}^{N} \eta_k(\zeta) = \hat{c}_\eta \prod_{n=1}^{N} \frac{\omega(\zeta, a_n)\omega(\zeta, 1/\overline{a}_n)}{\omega(\zeta, b_n)\omega(\zeta, 1/\overline{b}_n)}, \quad \hat{c}_\eta \in \mathbb{C}, \tag{3.25}$$

where the parameters a_n, b_n, $n = 1, 2, \ldots, N$ are strictly inside D_ζ. In this section, it is shown that the products of radial slit maps have two advantages for calculating generalized Schwarz integral formulas.

3.4.1 Parameters

It is important to point out that a given radial slit mapping of the form (3.5) contains only three complex adjustable parameters, c_η, a, and b, yet as more boundaries of a multiply connected domain are added this will not be enough adjustable parameters to ensure the function required for our construction has all the requisite properties. The resolution is to consider the products of radial slit maps (3.25) to produce a function with the required properties. It is clear that (3.25) has more adjustable parameters, and also has piecewise

constant argument on all boundaries of the domain having prime function $\omega(.,.)$. By considering the products of radial slit maps instead of (3.5), we can find a suitable function $\eta(\zeta)$ that satisfies the boundary conditions (3.13).

3.4.2 Conditioning

The method proposed in the previous section becomes unstable when the two circles (the outer circle and the inner circle, or two inner circles) approach each other. This is because the radial slit map $\eta(\zeta)$ maps a boundary to an long radial slit when appropriate parameters a or b are chosen. In this section, the resolution for these difficulties is described.

(i) Doubly connected domains

In this section, we solve the following mixed-type boundary value problem:

$$\mathrm{Im}[f(\zeta)] = r_0(\zeta), \quad |\zeta| = 1, \tag{3.26}$$

$$\mathrm{Re}[f(\zeta)] = r_1(\zeta), \quad |\zeta| = \rho. \tag{3.27}$$

The radial slit map $\eta(\zeta)$ in this case can be found explicitly as

$$\eta(\zeta) = \frac{P(\zeta/a)P(\overline{a}\zeta)}{P(\zeta/\overline{a})P(a\zeta)}, \quad a \equiv r\exp\left(\frac{\pi \mathrm{i}}{4}\right), \quad \rho < r < 1. \tag{3.28}$$

Figure 3.1 shows the annulus region with different ρ and the slit map we obtained, where the parameter r is chosen to be $r = \sqrt{\rho}$ so that the lengths of the two slits are equal. It can be seen that as ρ becomes large, the edges of the radial slit map approach 0. Since the generalized Schwarz integral includes the integration of $\eta(\zeta)r_j(\zeta)$ on C_j for $j = 0, 1$ as shown in (3.9), the integral loses information around the edge of $\eta(\zeta)$. This reduces the accuracy of the proposed method.

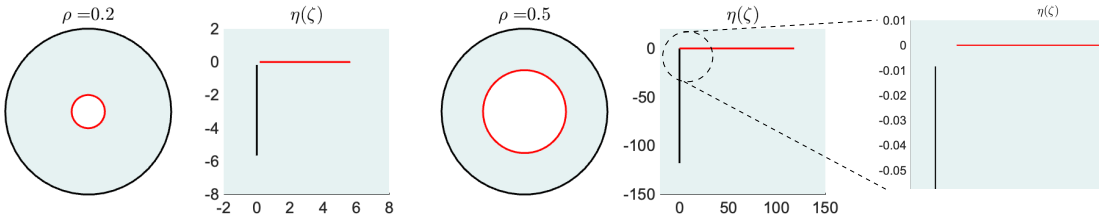

Figure 3.1: Examples of radial slit maps of doubly connected domains. When ρ becomes big the lengths of two radial slits become long, which compromises the accuracy of the radial slit map approach.

Based on the above observation, it is natural to define the condition number of the generalized Schwarz integral, which quantifies the ill-posedness of the problem, as

$$\mathrm{cond}(\eta) \equiv \max_{j=0,\ldots,M} \left(\frac{\max\limits_{\zeta \in C_j} |\eta(\zeta)|}{\min\limits_{\zeta \in C_j} |\eta(\zeta)|} \right). \tag{3.29}$$

Figure 3.2 shows the condition number of the radial slit map in (3.28) with respect to ρ. When ρ becomes large the condition number increases exponentially, which means that the accuracy of the approach becomes worse.

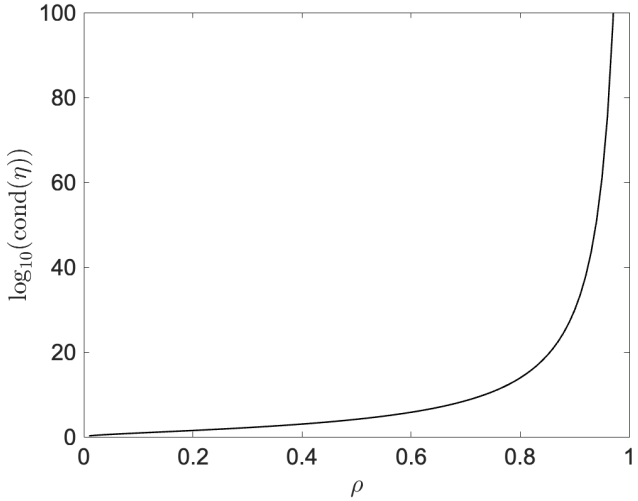

Figure 3.2: Log plot of condition number of the radial slit map defined in (3.29). As the inner radius ρ increases, the condition number increases.

One way to overcome this accuracy problem is to use products of radial slit maps. Consider a product of N radial slit maps as follows:

$$\eta(\zeta) = \prod_{n=1}^{N} \frac{P(\zeta/a_n)P(\overline{a_n}\zeta)}{P(\zeta/\overline{a_n})P(a_n\zeta)}, \tag{3.30}$$

where

$$a_n = \sqrt{\rho} \exp\left[\frac{\pi \mathrm{i}}{N} \left(2(n-1) + \frac{1}{4} \right) \right], \quad n = 1, \ldots, N. \tag{3.31}$$

The value of the function (3.30) for $\rho = 0.7$ is illustrated in Figure 3.3. The number of multiplication is changed from $N = 1$ to $N = 5$. The condition numbers (3.29) of these functions are 3.35×10^8, 1.04×10^4, and 20.7, respectively. This means that the products

of radial slit maps can reduce the condition numbers.

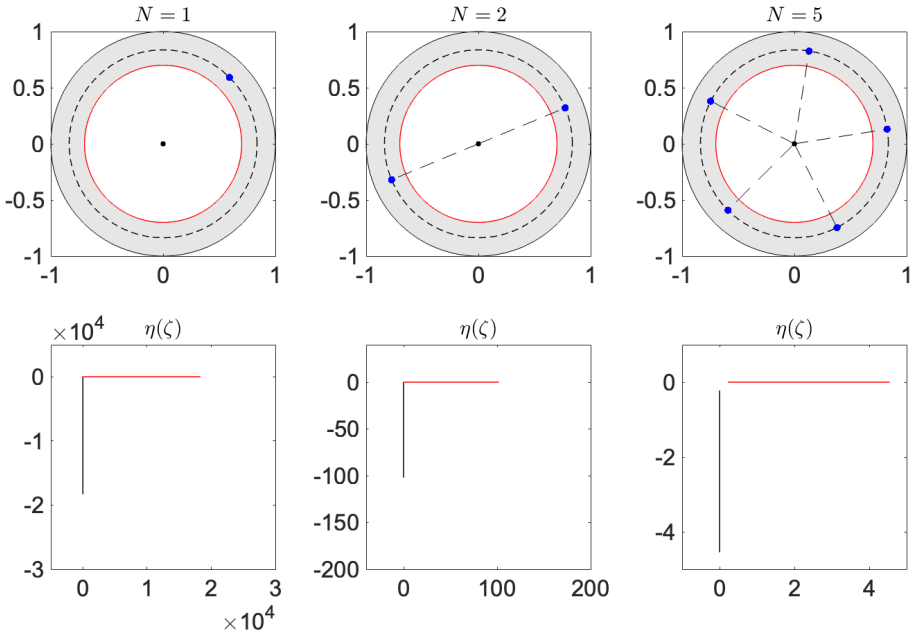

Figure 3.3: The boundary values of the function (3.30). The blue circles are the parameters a_n. The radius of the inner circle ρ is 0.7. The condition numbers for $N = 1$, $N = 2$, and $N = 5$ are 3.35×10^8, 1.04×10^4, and 20.7, respectively.

Now we consider $X(\zeta) \equiv \eta(\zeta) f(\zeta)$. The product of radial slit maps changes the problem slightly, because $\eta(\zeta)$ in (3.30) now has N-simple poles at $\zeta = \overline{a_n}$, $n = 1, \ldots, N$. Hence, we should eliminate the poles at $\zeta = \overline{a_n}$ such that

$$\operatorname{Re}\left[X(\zeta) - \sum_{n=1}^{N} \frac{B_n}{\zeta - \overline{a_n}}\right] = \begin{cases} \mathrm{i}\eta(\zeta) r_0(\zeta) - \operatorname{Re}\left[\displaystyle\sum_{j=1}^{N} \frac{B_n}{\zeta - \overline{a_n}}\right], & |\zeta| = 1, \\ \eta(\zeta) r_1(\zeta) - \operatorname{Re}\left[\displaystyle\sum_{n=1}^{N} \frac{B_n}{\zeta - \overline{a_n}}\right], & |\zeta| = \rho, \end{cases} \tag{3.32}$$

where $B_n \in \mathbb{C}$, $n = 1, 2, \ldots, N$, are parameters to be found. Thus, the solution for the problem with boundary conditions (3.26) and (3.27) is

$$f(\zeta) = \frac{1}{\eta(\zeta)} \left[I(\zeta) + \sum_{n=1}^{N} \frac{B_n}{\zeta - \overline{a_n}} + \mathrm{i}c_0 \right]. \tag{3.33}$$

The new approach increases the number of parameters but we have the same number of additional conditions. Because $\eta(\zeta)$ has simple zeros at $\zeta = a_n$, $n = 1, \ldots, N$, the bracket

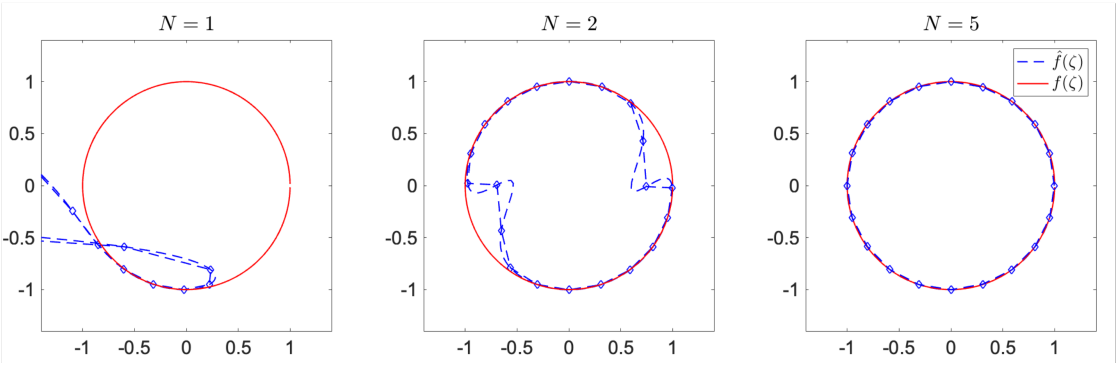

Figure 3.4: The accuracy of the radial slit map approach with respect to the number of products of radial slit maps. We solve the problem with boundary values (3.26) and (3.27) with $\rho = 0.7$. The function is set to be $f(\zeta) = \zeta$. The red lines correspond to the true value on C_0 and the blue dotted lines correspond to the reconstructed values by the radial slit map approach. When $N = 1$ and $N = 2$, there are some errors between the test function and the reconstructed results. In contrast, when $N = 5$ the proposed method is much more accurate than $N = 1$ or $N = 2$. This is due to the condition number defined in (3.29). For numerical integration of the Schwarz integral, alternate trapezoidal rule around C_0 and C_1 with the interval $\pi/3000$ was used.

in (3.33) should vanish at $\zeta = a_n$, for $n = 1, \ldots, N$. This produces the same number of conditions as the additional parameters.

The effect of the change of the condition number is validated numerically in Figure 3.4. In Figure 3.4, we solve the mixed boundary value problem in the annular region D_ζ defined in (3.26) and (3.27) and we set $f(\zeta) = \zeta$.

Figure 3.4 shows the value of $f(\zeta)$ on C_0 in red lines and the function $\hat{f}(\zeta)$ on C_0 calculated by the generalized Schwarz integral in blue dotted lines. Since the condition number for $N = 5$ is small, the proposed method can achieve sufficient accuracy.

One of the advantages of the products is that they do not increase the computational time. To determine B_n, an N-by-N linear system for B_n is created, which can be solved in a straightforward manner. Therefore, it is recommended to reduce the condition number by the products in order to obtain the accuracy.

(ii) Triply connected domain

In this subsection, we consider the mixed boundary value problem in the symmetrical triply connected domain below:

$$\begin{cases} \mathrm{Re}[f(\zeta)] = r_0(\zeta), & \zeta \in C_0, \\ \mathrm{Im}[f(\zeta)] = r_1(\zeta), & \zeta \in C_1, \\ \mathrm{Im}[f(\zeta)] = r_2(\zeta), & \zeta \in C_2. \end{cases} \tag{3.34}$$

The centres of the inner circles are $(-\delta, 0)$ and $(\delta, 0)$, and the radii are both q, where δ is purely imaginary.

Following the argument in Chapter 2, an appropriate map for solving the boundary value problem (3.34) is given by

$$\eta(\zeta) \equiv c_\eta \frac{\omega(z,a)\omega(z,1/\overline{a})}{\omega(z,b)\omega(z,1/\overline{b})}, \qquad c_\eta = \left(\frac{\overline{a}b}{a\overline{b}}\right)^{1/2}, \tag{3.35}$$

where a and b are chosen so that $\eta(\zeta)$ satisfies

$$\begin{cases} \arg[\eta(\zeta)] = 0,\ \pi, & \zeta \in C_0, \\ \arg[\eta(\zeta)] = \pm\dfrac{\pi}{2},, & \zeta \in C_1, \\ \arg[\eta(\zeta)] = \pm\dfrac{\pi}{2}, & \zeta \in C_2. \end{cases} \tag{3.36}$$

It can be shown that the parameters a and b in the radial slit map $\eta(\zeta)$ then satisfy

$$\begin{cases} \overline{v_1(a)} - \overline{v_1(b)} + \overline{v_1(1/\overline{a})} - \overline{v_1(1/\overline{b})} = \dfrac{1}{2},\ \text{or}\ -\dfrac{1}{2}, \\ \overline{v_2(a)} - \overline{v_2(b)} + \overline{v_2(1/\overline{a})} - \overline{v_2(1/\overline{b})} = \dfrac{1}{2},\ \text{or}\ -\dfrac{1}{2}. \end{cases} \tag{3.37}$$

For triply connected domains, there are no explicit expressions for the parameters (a, b) in the radial slit map. Therefore, a non-linear solver such as Newton's method must be used to find these parameters which satisfy the condition (3.36). The candidates for the parameters (a, b) which satisfy the condition (3.36) are visualized in Figure 3.5. The parameter a is shown as red dots and b is illustrated as blue dots. The radii of the two inner circles are $q = 0.2$, and the centres are $(0, 0.4)$ and $(0, -0.4)$. There are several choices of (a, b) and if we choose (a, b) as the cyan circles as shown in the left figure of Figure 3.5, the condition number is 194.96.

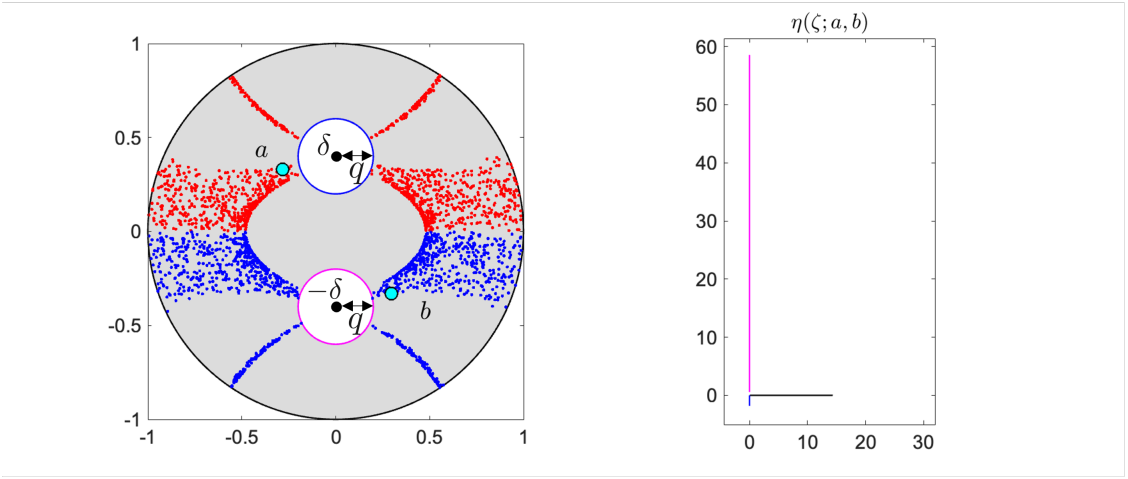

Figure 3.5: The possible candidate of the parameters (a, b), which satisfies the condition (3.36). We have plotted the case where $\mathrm{Im}[a] > 0$ and $\mathrm{Im}[b] < 0$. The parameter a is shown as red dots and b is illustrated as blue dots. The radius of the inner circle is $q = 0.2$, and the centres are $(0, 0.4)$ and $(0, -0.4)$. There are multiple choices of (a, b). If we choose (a, b) as shown in the left figure, the condition number is 194.96.

For triply connected domains, we can also consider products of radial slit maps in order to reduce the condition number as follows:

$$\eta(\zeta) \equiv \hat{c}_\eta \prod_{n=1}^{N} \frac{\omega(z, a_n)\omega(z, 1/\overline{a_n})}{\omega(z, b_n)\omega(z, 1/\overline{b}_n)}, \qquad \hat{c}_\eta \equiv \prod_{n=1}^{N} \left(\frac{\overline{a}_n b_n}{a_n \overline{b}_n} \right)^{1/2}. \tag{3.38}$$

It is observed that the condition number increases as the inner circles approach to the unit circle for any choice of parameters a and b. Therefore, it is recommended to use a product of radial slit maps in order to reduce the condition number.

3.5 Application to hollow vortex wake behind a wedge

In this section, we apply the proposed method to calculate the flow around hollow vortices. The main mathematical tools are the prime function and generalized Schwarz integral formula derived in the previous section. The formula solves the mixed boundary value problems which include parameters of the fluid velocity and the Bernoulli constants. By minimising the cost function, these parameters are optimized and then the shape of the free surfaces is determined. The result we present here show the versatility of the proposed generalized Schwarz integral formulas.

3.5.1 Introduction

The hollow vortex wake behind a wedge object concerns a generalization of the Föppl point vortex pair behind a bluff body, a well-known problem in fluid dynamics [17, 142]. We propose to study a more realistic model in which we smear out those point vortices (in which the vorticity is concentrated in two δ-functions behind the body) to two "hollow vortices". A hollow vortex is a bounded region of constant pressure with a non-zero circulation around it. Hollow vortices are an old vortex model [128] but have recently been the subject of much renewed interest [27, 45, 47, 62]. A hollow vortex wake behind a bluff body has been studied by Batchelor [16], Lin and Landweber [87] and, more recently, by Telib and Zannetti [142]. Following [87] we will study a pair of closed free streamlines, with non-zero circulation of opposite sign, enclosing finite-area constant-pressure regions (these are the hollow vortices) behind an open wedge of finite length. Our methodology is extendible to other geometries; for example, the problem of a hollow vortex in an infinite wedge region has recently received attention [27, 88, 153] and the approach here can be adapted to that case too.

3.5.2 Problem formulation

Consider a wedge obstacle with opening angle $2\pi\phi$ in a complex $z = x + \mathrm{i}y$-plane, where $0 < \phi < \pi/2$, as shown in Figure 3.6. The origin is taken at the wedge apex. Suppose there is an irrotational ideal flow of speed U flowing from left to right in the x direction. There will therefore be an associated complex potential [17] $w(z) = \phi + \mathrm{i}\psi$, where ϕ and ψ are the velocity potential and streamfunction respectively, from which the velocity field (u, v) can be determined from the formula $u - \mathrm{i}v = dw/dz$. Following [87] we assume that two hollow vortices, of identical shape with equal but opposite circulation $\pm\Gamma$, form a steady wake behind the wedge; see Figure 3.6. At the trailing edge, labelled B in Figure 3.6, a Kutta condition is imposed [87, 142].

A hollow vortex is a constant-pressure region of finite area with circulation around it [27]. On the boundary of the hollow vortex, Bernoulli's equation gives

$$p + \frac{(u^2 + v^2)}{2} = \text{constant}, \tag{3.39}$$

where p is pressure on the hollow vortex boundary. The pressure on the hollow vortex is constant, and thus, the Bernoulli condition gives the velocity around the hollow vortex constant.

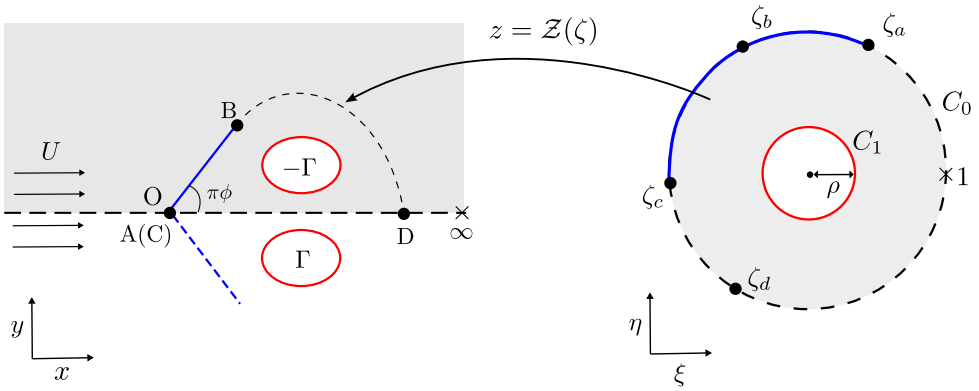

Figure 3.6: A hollow vortex wake behind a wedge in uniform flow and the associated conformal mapping used in the solution scheme.

3.5.3 Complex analysis formulation

The fluid domain here is triply connected. However, by a flow symmetry across the x axis, it is enough to consider the flow in the upper-half region exterior to the wedge and the upper hollow vortex. This domain is doubly connected, making it appropriate to use a parametric annulus $\rho < |\zeta| < 1$ as the preimage domain appropriate; let C_0 and C_1 denote its outer and inner circular boundaries. To solve this free boundary problem we will construct the conformal mapping, $z = \mathcal{Z}(\zeta)$ say, from this concentric annulus to the upper-half flow region. Two prevertices ζ_a and ζ_c indicated in Figure 3.6 are transplanted to the origin (on different "sides" of the wedge) and ζ_b is mapped to the upper trailing edge B. From an analysis of the Föppl point vortex problem, a stagnation point, labelled D, is expected on the x-axis; its preimage will be denoted by ζ_d. We suppose the conformal map has the form,

$$\mathcal{Z}(\zeta) = -\frac{\mathrm{i}s}{\zeta - 1} + \hat{\mathcal{Z}}(\zeta), \qquad s \in \mathbb{R}, \qquad s > 0, \tag{3.40}$$

where $\hat{\mathcal{Z}}(\zeta)$ is analytic in the annulus and where a rotational freedom of the Riemann mapping theorem allows us to choose $\zeta = 1$ as the preimage of $z = \infty$.

Supposing such a conformal mapping can be found, it turns out that a general "calculus" [34, 40] for solving two-dimensional irrotational flow problems of this kind can be used to immediately write down that the complex potential for this flow as [34, 40]

$$W(\zeta) \equiv w(\mathcal{Z}(\zeta)) = -\mathrm{i}UsK(\zeta) + \frac{\mathrm{i}\Gamma}{2\pi}\log\zeta, \tag{3.41}$$

where $K(\zeta)$ is defined in Chapter 2. Note that $K(\zeta)$ has a simple zero at $\zeta = 1$, which

corresponds to the uniform flow U at $z \to \infty$, or $w(z) \to Uz$. The logarithmic term in (3.41) accounts for the required circulation Γ around the hollow vortex.

In the spirit of free streamline theory [17] it is now convenient to write

$$\log\left(\frac{dw}{dz}\right) = \log S(\zeta) + T(\zeta), \tag{3.42}$$

where

$$S(\zeta) \equiv \frac{\hat{S}(\zeta)}{\hat{S}(1)}, \quad \hat{S}(\zeta) \equiv \frac{(\zeta_b - \zeta)(\zeta - \zeta_d)}{\zeta}\left(\frac{\zeta_a - \zeta}{\zeta - \zeta_b}\right)^{\phi}\left(\frac{\zeta_c - \zeta}{\zeta - \zeta_b}\right)^{1-\phi}. \tag{3.43}$$

The job of $\log S(\zeta)$ is to capture all expected singularities of $\log(dw/dz)$ on C_0 and C_1 associated with the corners and edges of the wedge, and any stagnation points, leaving the function $T(\zeta)$ analytic inside the annulus domain D_ζ and up to the boundary. The form of $\hat{S}(\zeta)$ is analytic at $\zeta = \zeta_b$, but some terms are included for numerical convenience. It can be shown to satisfy the boundary value problem

$$\begin{aligned} &\mathrm{Im}[T(\zeta)] = 0, \qquad \zeta \in C_0, \\ &\mathrm{Re}[T(\zeta)] = \log(v_c) - \mathrm{Re}[\log S(\zeta)], \qquad \zeta \in C_1, \end{aligned} \tag{3.44}$$

where v_c is the constant velocity of the hollow vortex. In order to derive the equation (3.43), we used that

$$\log\left(\frac{dw}{dz}\right) = \log\left|\frac{dw}{dz}\right| + \mathrm{i}\arg\left(\frac{dw}{dz}\right). \tag{3.45}$$

Since $dw/dz = u - \mathrm{i}v$, its argument on the wedge is $-\pi\phi$. It is important to mention that at $\zeta = \zeta_a$ the argument of $S(\zeta)$ changes by $-\pi\phi$, and at $\zeta = \zeta_c$ the argument changes by $-(1-\phi)\pi$. In addition, because $S(\zeta)$ consists of products of powers of Cayley maps it can be shown that, from Chapter 7 of [40], $S(\zeta)$ has a piecewise constant argument on $\zeta \in C_0$.

The key point is that this is essentially the same mixed boundary value problem (3.4), falling within in the general class (3.1), whose solution was discussed in the previous section. As such, we can represent its solution using the generalized Schwarz integrals discussed there. The radial slit map used in the generalized Schwarz integral formula in this case is

$$\eta(\zeta) = \frac{P(\zeta/c)P(\overline{c}\zeta)}{P(\zeta/\overline{c})P(c\zeta)}, \qquad c = r\exp\left(\frac{\pi\mathrm{i}}{4}\right), \qquad \rho < r < 1. \tag{3.46}$$

With an expression for dw/dz found as a function of ζ in this way, and with $W(\zeta)$ known

from (3.41), we can reconstruct the shape of hollow vortex by the chain rule:

$$\mathcal{Z}(\zeta) = \int_{\zeta_a}^{\zeta} \frac{d\mathcal{Z}}{d\zeta'} d\zeta' = \int_{\zeta_a}^{\zeta} \frac{dW/d\zeta'}{dw/dz} d\zeta'. \tag{3.47}$$

Given these representations of the solutions, there is still a parameter problem to solve. The parameters ζ_a, ζ_b, ζ_c, and $\log(v_c)$ are determined by ensuring the sides of the wedge have specified length, and by imposing the condition of single-valuedness of the mapping $\mathcal{Z}(\zeta)$, i.e.,

$$\oint_{C'} \mathcal{Z}'(\zeta) d\zeta = 0, \tag{3.48}$$

where C' is any closed circle in the annulus. Other conditions on this problem are that

$$\frac{dW}{d\zeta} = 0, \text{ for } \zeta = \zeta_b,\ \zeta_d, \qquad \left|\frac{dW}{dz}\right| = v_c, \qquad \text{for } |\zeta| = \rho. \tag{3.49}$$

The condition at ζ_d enforces that it is a stagnation point, the condition at ζ_b is the Kutta condition. The second condition on $|dw/dz|$ follows from the Bernoulli theorem and the assumption that the wake vortex is hollow, meaning that the pressure inside it is constant forcing its boundary speed to be constant.

As $\rho \to 0$ the hollow vortex will degenerate to a point vortex, and standard methods can be used to find the equilibrium point in this limit (akin to the standard Föppl vortex pair analysis). The coordinate of the Föppl point vortex (ξ_0, η_0) is given by solving the zero velocity at the vortex and Kutta condition on the edge.

$$\frac{\Gamma}{U} = -\frac{4\pi}{1/\eta_0 - \mathrm{Im}[(d/d\zeta)(\log dz/d\zeta)]}, \tag{3.50}$$

where $z = \mathcal{Z}(\zeta)$ is a conformal map from the upper half region to the upper half region with a half wedge. The Kutta condition is

$$-\frac{U}{\Gamma} = -\frac{\mathrm{i}}{2\pi}\left(\frac{1}{\zeta_b - \zeta_0} - \frac{1}{\zeta - \overline{\zeta_0}}\right), \quad \zeta_0 \equiv \xi_0 + \mathrm{i}\eta_0. \tag{3.51}$$

A continuation method for $\rho > 0$ was then used to determine unique values of the parameters by Newton's method.

The numerical algorithm to find the hollow vortex wake can be summarized as follows.

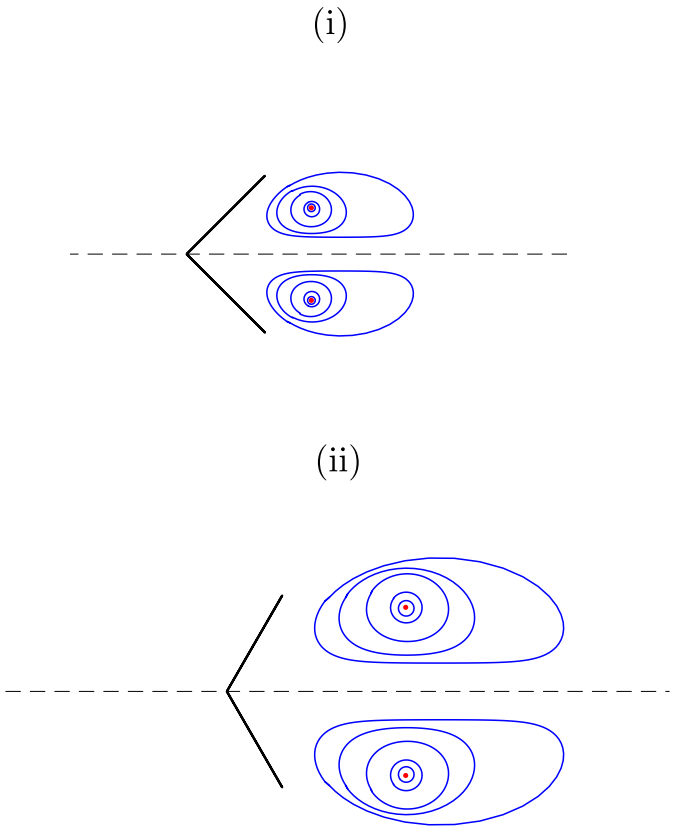

Figure 3.7: Hollow vortex wakes calculated by solving the mixed boundary value problem (3.44). The red point corresponds to the equilibrium point vortices. The innermost line corresponds to the case where $\rho = 0.05$, and blue lines from the inner line corresponds to $\rho = 0.1, 0.25, 0.4, 0.6$. (i) $\Gamma = 6.0$, $\theta = \pi/4$. (ii) $\Gamma = 10.0$, $\theta = \pi/3$.

Algorithm 1 A hollow vortex wake computed using generalized Schwarz integrals

1: Set parameters U, Γ, ρ (these parameters are fixed)
2: Set initial parameters $\zeta_a, \zeta_b, \zeta_c$ and the speed of the hollow vortex v_c. The stagnation point ζ_d is set to be $1/\zeta_b$ because $\frac{dW}{d\zeta}(\zeta_d) = 0$.
3: the cost functions are $|\mathcal{Z}(\zeta_a)| - 1$, $|\mathcal{Z}(\zeta_c)| - 1$, and $\oint_C \frac{d\mathcal{Z}}{d\zeta'} d\zeta' = 0$. (4 in total)
4: **while** The cost function $> \epsilon$ **do**
5: Obtain the value s by enforcing the Kutta condition $\frac{dW}{d\zeta}(\zeta_b) = 0$.
6: Solve for $\frac{d\mathcal{Z}}{d\zeta}$ and calculate the cost function.
7: **end while**
8: Calculate $\mathcal{Z}(\zeta) = \int_{\zeta_a}^{\zeta} \frac{d\mathcal{Z}}{d\zeta'} d\zeta'$ for $\zeta \in C_1$ to obtain the shape of the hollow vortex.

Figure 3.7 shows the shape of hollow vortex wakes for different wedge angles θ and Γ. As ρ increases, the size of the hollow vortex wake becomes larger and there is qualitative

agreement with the earlier calculations of Lin and Landweber [87] who used very different methods (those authors gave no numerical data with which to make a quantitative comparison).

3.6 Application to the longitudinal flow in a heat sink

Based on the generalized Schwarz integral formula proposed in this chapter, an analytical formula for longitudinal flow in heat channels with periodic fins can be derived. Heat sinks or heat channels are devices that is used to transfer heat in order to manage the temperature of electrical devices or elsewhere easily and at low cost [85]. They consist of a sealed container filled with a liquid (such as water or a special fluid) and a finned structure that helps to circulate the liquid and transfer heat. Heat sinks can be used in a variety of applications, such as computer cooling, space heating, and thermal management in electronic devices [70]. They are highly efficient at transferring heat and can operate over a wide temperature range. A review article focuses on microchannel heat transfer [75].

Figure 3.8 shows a typical heat channel with periodic fins. Various numerical methods have been proposed to calculate the flow and the temperature fields in microchannels or pipes with fins [73, 134]. The velocity fields and heat transfer through a tube with equally-spaced fins were calculated by Hu and Chang [69]. Another method was proposed by Masilyah and Nandakumar in order to solve the flow and thermal temperature using an approximate Green's function of cylindrical channels [94]. However, a special case has to be taken around the points adjacent to the top of the fins because the edge of the fin becomes singular for numerical calculations.

In this section, we aim to obtain an analytical solution for the flow in a heat channel. This can be done by using the horizontal map introduced in Chapter 2 and generalized Schwarz integral formulas in the triply connected domain.

3.6.1 Problem formulation

Following the problem formulation described by Sparrow, Baliga, and Patankar [134], a pressure-driven longitudinal flow is considered in the period window consisting of equally-spaced periodic thermal fins. The fins are assumed to be infinite in Z-direction, so the velocity field is $\underline{u} = (0, 0, w(x, y))$. The period window is bounded by a top wall called "shroud" and a bottom wall called "base", which consist of periodic fins. The periodicity of the fins is $2L$ and the height of the fins is H. The distance between the top of the fin and the top wall is c. The total height of the channel is $H + c$.

We define a half period window as D^+ and set the origin as the centre of the bottom line. The geometry is illustrated in the left figure of Figure 3.9. The flow is assumed to be

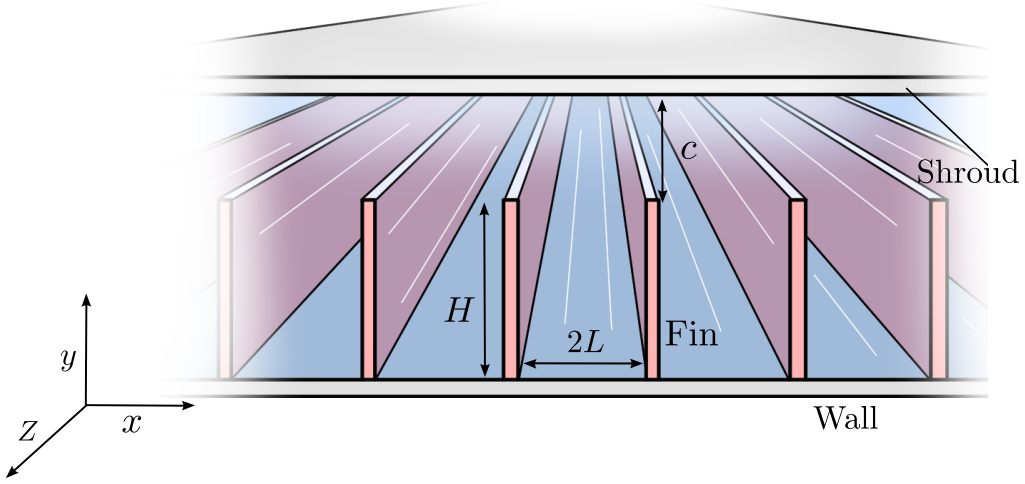

Figure 3.8: Illustration of a periodic heat sink. The heat pipe has periodic fins with height H consisting of top and bottom walls.

fully-developed. The non-dimensional velocity field $w(x, y)$ satisfies

$$\nabla^2 w(x, y) = 1, \qquad (x, y) \in D^+. \tag{3.52}$$

The half period window D^+ is bounded by top and bottom walls. The boundary conditions on the walls and fins are

$$w(x, y) = 0, \qquad 0 \le x \le L, \ y = 0, \ H + c \tag{3.53}$$

$$w(0, y) = 0, \qquad 0 \le y \le H, \quad x = 0. \tag{3.54}$$

Because of the periodicity, the partial derivative of the velocity $w(x, y)$ with respect to x vanishes at the centre line of the period window and the gap between the fins and the upper wall. These conditions are given by

$$\frac{\partial w}{\partial x}(0, y) = 0, \qquad H \le y \le H + c, \tag{3.55}$$

$$\frac{\partial w}{\partial x}(L, y) = 0, \qquad 0 \le y \le H + c. \tag{3.56}$$

This is a mixed boundary value problem. Sparrow used the finite element method to calculate the velocity field [134]. Karamanis *et. al.* also used the discretized mesh to calculate the flow and the temperature field [73]. However, since the flow at the edge of the fins becomes singular, a number of discretized meshes are used to achieve sufficient accuracy. The following analytical solution appears to be new.

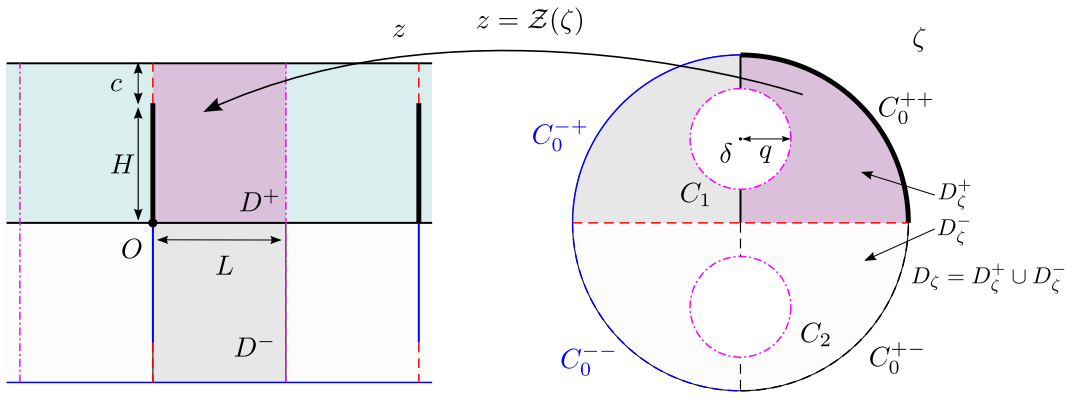

Figure 3.9: The conformal map to the half period window from the upper-left of triply connected domain.

3.6.2 Complex Analysis Formulation

Here a complex analysis formulation is introduced to solve the mixed boundary value problem. We split the flow $w(x, y)$ into two parts:

$$w(x, y) = w_0(x, y) + \hat{w}(x, y), \quad w_0(x, y) \equiv -\frac{y(H + c - y)}{2}, \tag{3.57}$$

where $\hat{w}(x, y)$ is a harmonic function which satisfies

$$\hat{w}(x, y) = 0, \qquad 0 \le x \le L, \ y = 0, \ H + c \tag{3.58}$$

$$\hat{w}(0, y) = \frac{y(H + c - y)}{2}, \qquad 0 \le y \le H, \tag{3.59}$$

$$\frac{\partial \hat{w}}{\partial x}(0, y) = 0, \qquad H < y \le H + c, \tag{3.60}$$

$$\frac{\partial \hat{w}}{\partial x}(L, y) = 0, \qquad 0 < y < H + c. \tag{3.61}$$

Because $\hat{w}(x, y)$ is a harmonic function it is convenient to define $h(z) = \chi + \mathrm{i}\hat{w}$, $z \equiv x + \mathrm{i}y$, where χ is the harmonic extension of $\hat{w}$. On the real axis, i.e., $\overline{z} = z$, we have

$$\overline{h(z)} = \overline{h}(\overline{z}) = \overline{h}(z) = h(z), \tag{3.62}$$

where $\overline{f}(z)$ is a Schwarz conjugate of the function $f(z)$ defined by $\overline{f}(z) \equiv \overline{f(\overline{z})}$. Due to the Schwarz reflection principle, the function $h(z)$ can be analytically extended to the region

D^- and it satisfies

$$h(z) = \overline{h(\overline{z})}, \qquad z \in D^-. \tag{3.63}$$

Hence, from (3.59) and (3.63),

$$\hat{w}(0,y) = \mathrm{Im}[h(z)] = \mathrm{Im}[\overline{h(\overline{z})}] = -\mathrm{Im}[h(\overline{z})] = \frac{y(H+c+y)}{2} \tag{3.64}$$

for $-H-c \leq y \leq 0$. From (3.60), (3.61), and the Cauchy-Riemann equations, it is straightforward to see that χ is constant both on the centre line of the period window and on the gap between the fins and the top surface. Without loss of generality, it suffices to set

$$\chi(0,y) = 0, \quad H \leq y \leq H+c \tag{3.65}$$

$$\chi(L,y) = \chi_0, \quad 0 \leq y \leq H+c, \tag{3.66}$$

where $\chi_0 \in \mathbb{R}$ is an unknown parameter that is solved during the flow calculation.

Now we introduce the conformal mapping to $D = D^+ \cup D^-$ in the z-plane from the upper half unit disc with an inner small circular disc excised; let this region be called D_ζ^+ in the complex ζ-plane. The map is defined by

$$z = \mathcal{Z}(\zeta) = -\frac{H+c}{\pi} \log\left(\frac{\omega(\zeta,\theta_1(\infty))}{\omega(\zeta,\theta_2(\infty))}\right), \tag{3.67}$$

where

$$\theta_1(\zeta) \equiv \delta + \frac{q^2}{1-\overline{\delta}\zeta}, \quad \theta_2(\zeta) \equiv -\delta + \frac{q^2}{1+\overline{\delta}\zeta}, \tag{3.68}$$

and where $\omega(.,.)$ is the prime function associated with D_ζ [40].

The one-to-one map $\mathcal{Z}(\zeta)$ is shown in Figure 3.9. The upper-right semi-circle C_0^{++} is mapped to the fins, the positive real axis inside the circle is mapped to the gap between the top surface and the top of the fins, and the right part of the inner circle is mapped to the centre line of the period window, respectively. This mapping is explicit up to two unknown parameters δ and q. These parameters can be easily obtained by solving a nonlinear system using Newton's method.

Because of the conformal invariance of the analytic function, it is useful to define $\mathcal{H}(\zeta) \equiv h(\mathcal{Z}(\zeta))$. The boundary condition (3.59) on the upper semi-circle becomes

$$\mathrm{Im}[\mathcal{H}(\zeta)] = \frac{y(H+c-y)}{2} = \frac{\mathrm{Im}[\mathcal{Z}(\zeta)](H+c-\mathrm{Im}[\mathcal{Z}(\zeta)])}{2}, \quad \zeta \in C_0^{++}, \tag{3.69}$$

and

$$\mathrm{Im}[\mathcal{H}(\zeta)] = \frac{y(H+c+y)}{2} = \frac{\mathrm{Im}[\mathcal{Z}(\zeta)](H+c+\mathrm{Im}[\mathcal{Z}(\zeta)])}{2}, \quad \zeta \in C_0^{-+}. \tag{3.70}$$

From (3.65) and the fact that the $\mathcal{Z}(\zeta)$ maps the real axis of the ζ-plane to the gap, we have

$$\mathrm{Re}[\mathcal{H}(\zeta)] = 0, \quad \overline{\zeta} = \zeta. \tag{3.71}$$

Using the Schwarz reflection principle, the function $H(\zeta)$ can be analytically extended to the lower half disc outside the inner circle and

$$\mathcal{H}(\zeta) = -\overline{\mathcal{H}(\overline{\zeta})}, \quad \zeta \in D_\zeta^-. \tag{3.72}$$

Thus, combining (3.69), (3.70), and (3.72), we have the following boundary value problem for $\mathcal{H}(\zeta)$ in D_ζ:

$$\mathrm{Im}[\mathcal{H}(\zeta)] = \phi(\zeta), \qquad \zeta \in C_0, \tag{3.73}$$

$$\mathrm{Re}[\mathcal{H}(\zeta)] = \chi_0, \qquad \zeta \in C_1, \tag{3.74}$$

$$\mathrm{Re}[\mathcal{H}(\zeta)] = -\chi_0, \qquad \zeta \in C_2, \tag{3.75}$$

where

$$\phi(\zeta) = \begin{cases} \dfrac{\mathrm{Im}[\mathcal{Z}(\zeta)](H+c-\mathrm{Im}[\mathcal{Z}(\zeta)])}{2}, & \zeta \in C_0^{++},\ C_0^{+-} \\ \dfrac{\mathrm{Im}[\mathcal{Z}(\zeta)](H+c+\mathrm{Im}[\mathcal{Z}(\zeta)])}{2}, & \zeta \in C_0^{-+},\ C_0^{--}. \end{cases} \tag{3.76}$$

This boundary value problem can be solved using the generalized Schwarz integral formula introduced in this Chapter. By introducing a suitable radial slit map $\eta(\zeta)$, which satisfies the conditions such that $\eta(\zeta)$ is purely imaginary on $\zeta \in C_0$ and purely real on $\zeta \in C_1$ and $\zeta \in C_2$. The boundary value problem then becomes

$$\mathrm{Re}\left[\eta(\zeta)\mathcal{H}(\zeta) - \frac{A}{\zeta - b}\right] = \begin{cases} \mathrm{i}\eta(\zeta)f(\zeta) - \mathrm{Re}\left[\dfrac{A}{\zeta-b}\right] \equiv g_0(\zeta), & \zeta \in C_0, \\ \chi_0\eta(\zeta) - \mathrm{Re}\left[\dfrac{A}{\zeta-b}\right] \equiv g_1(\zeta), & \zeta \in C_1, \\ -\chi_0\eta(\zeta) - \mathrm{Re}\left[\dfrac{A}{\zeta-b}\right] \equiv g_2(\zeta), & \zeta \in C_2. \end{cases} \tag{3.77}$$

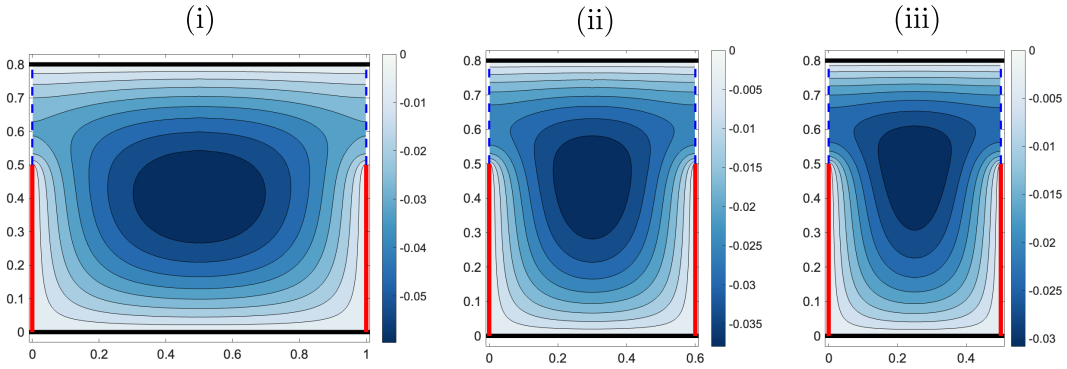

Figure 3.10: Velocity contour plots of $w(x, y)$. The total height of the channel and the height of fins are fixed to 0.8 and 0.5, respectively. (i) $L = 0.5$. (ii) $L = 0.3$. (iii) $L = 0.25$.

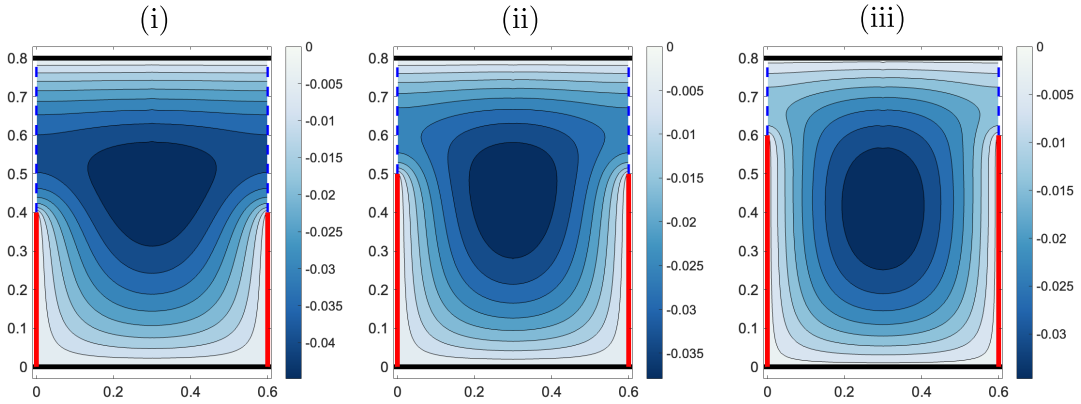

Figure 3.11: Velocity contour plots of $w(x, y)$. The total height of the channel and the space of fins are fixed to 0.8 and 0.6, respectively. (i) $H = 0.4$, $c = 0.4$. (ii) $H = 0.5$, $c = 0.3$. (iii) $H = 0.6$, $c = 0.2$.

The solution for this boundary value problem is given by

$$\mathcal{H}(\zeta) = \frac{X(\zeta)}{\eta(\zeta)}, \qquad X(\zeta) \equiv I(\zeta) + \frac{A}{\zeta - b} + \mathrm{i}c_0, \tag{3.78}$$

where $I(\zeta)$ is a Schwarz integral with the boundary data $g_j = \{g_0(\zeta), g_1(\zeta), g_2(\zeta)\}$. The parameters $\chi_0 \in \mathbb{R}$, $c_0 \in \mathbb{R}$, and $A \in \mathbb{C}$ can be solved uniquely from a linear system obtained by the single-valued conditions around C_1 and C_2 plus the condition $X(a) = 0$.

3.6.3 Numerical evaluations

The solution (3.78) is almost explicit except for the unknown parameters q and δ of D_ζ and the parameters in the radial slit map a and b. The geometric parameters q and δ can

be obtained by solving the following non-linear equations:

$$\begin{cases} \mathcal{Z}(1) = \mathrm{i}H, \\ \mathcal{Z}(\delta + q\mathrm{i}) = L. \end{cases} \tag{3.79}$$

This can be solved by the Newton's method. After solving these parameters, the conformal map and the solution can be constructed by computing the prime function.

Figures 3.10 and 3.11 show typical flows in different geometries. We have compared our data with Sparrow, Baliga, and Patankar given in [134].

It is important to note that this boundary value problem is also solved using Schwarz integral formulas in Chapter 2 by considering

$$w(x, y) = w_P(x, y) + \tilde{w}(x, y), \tag{3.80}$$

where $w_P(x, y)$ satisfies

$$\nabla^2 w_P(x, y) = 1, \tag{3.81}$$

with

$$w_P(0, y) = 0, \quad 0 \le y \le H, \tag{3.82}$$

$$w_P(x, 0) = w(x, H) = 0, \quad 0 \le x \le L, \tag{3.83}$$

$$\frac{\partial w_P}{\partial x}(L, y) = 0, \quad 0 \le y \le H. \tag{3.84}$$

This formulation is explained in detail in [101].

This section has shown how to incorporate the generalized Schwarz integral formulas [98] to solve for flow in microchannels with periodic fins. The solutions are explicit once two parameters, δ and q, have been found by solving two non-linear equations given the geometry of the surface. It is expected that our formulation would be able to deal with the flow in microchannels with staggered fins, previously studied in [74, 160].

3.7 Conclusion

This chapter has shown how to use radial slit mappings (expressed in terms of the prime function of a preimage domain) in conjunction with Schwarz integral formulas (with kernels also expressible in terms of that the same prime function) to find what we have dubbed *generalized Schwarz integral formulas* that solve the class of boundary value problems (3.1) for analytic functions in multiply connected domains. Such problems are ubiquitous in the

applied sciences as we hope to have shown here by showing the new solution method in action in two problems in the physical sciences. The ideas here constitute a flexible new applied mathematical tool for applications.

In implementing the method this chapter has used radial slit mappings which have piecewise constant argument on the boundaries of a given multiply connected circular domain. We could alternatively have used the class of mappings called Cayley-type mappings by Crowdy [40]. They share the property of having piecewise constant argument on the boundaries of the domain, but they have a pole on one of the boundary circles rather than inside the domain (as is the case for the radial slit mappings). This only requires a few minor modifications and, indeed, we solved without difficulty some of the problems in this paper using such Cayley-type mappings.

In the class of problems with boundary conditions (3.1) it has been assumed that a single type of boundary condition holds on the *whole* of boundary portion ∂D_j. But one can easily envisage the boundary condition switching type *on* a given boundary portion ∂D_j. Then it is likely that Schwarz-Christoffel type functions as constructed for multiply connected domains using the prime function in [29, 30, 40] will play the role of the radial slit or Cayley-type mappings used in the present construction. Indeed, those Schwarz-Christoffel type functions were themselves constructed using radial slit and Cayley-type mappings as "building blocks". This matter will be investigated in future work.

Mathematically, we end by mentioning that, if preferred, problem (3.1) can be recast as a special case of a linear Riemann-Hilbert problem in a multiply connected domain. Many methods have been put forward to solve such Riemann-Hilbert problems (e.g. [152]) and new contributions on numerical methods for them continue to emerge [155, 156]. Those methods can, in principle, be adapted to provide alternative schemes to those developed here.

Chapter 4

Van der Pauw method for holey samples: new resistivity measurement

This chapter explains a new approach for measuring the resistivity of holey materials. One method is the van der Pauw method [117, 118], which is commonly used to measure the resistivity of a thin material. The van der Pauw method is simple and accurate but it has the limitation that the sample to be measured should not have any holes in it. We will see that the use of the prime function introduced in Chapter 2 and generalization of the cross-ratio identity gives a new van der Pauw equation for holey samples. This chapter contains one of the important applications of the conformal mapping of multiply connected domains introduced in Chapter 2.

4.1 Introduction and background

Figure 4.1 shows a setup for the original van der Pauw measurement: the four electrical contacts $(\Omega_a, \Omega_b, \Omega_z, \Omega_w)$ are placed on the perimeter of a test sample. If Ω_a and Ω_b are a source and sink of current J_{ab} respectively, then the potential difference V_{zw} between points Ω_z and Ω_w can be measured while this current is flowing. The resistance $R_{ab}^{zw} = V_{zw}/J_{ab}$ is then a measured quantity; a second resistance R_{aw}^{zb} can be measured in exactly the same way. Van der Pauw [118] showed that for any arrangement of four electrical contacts, and given these two resistance measurements R_{ab}^{zw} and R_{aw}^{zb}, the resistivity λ can be found by solving the nonlinear equation:

$$\exp\left(-\frac{R_{ab}^{zw}}{\lambda}\right) + \exp\left(-\frac{R_{aw}^{zb}}{\lambda}\right) = 1. \tag{4.1}$$

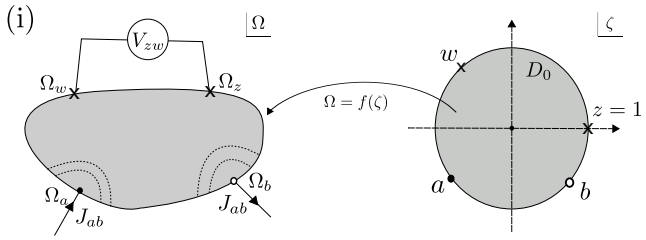

$$R_{ab}^{zw} \equiv \frac{V_{zw}}{J_{ab}} = \lambda \log \frac{\omega(z,a)\omega(w,b)}{\omega(z,b)\omega(w,a)}$$

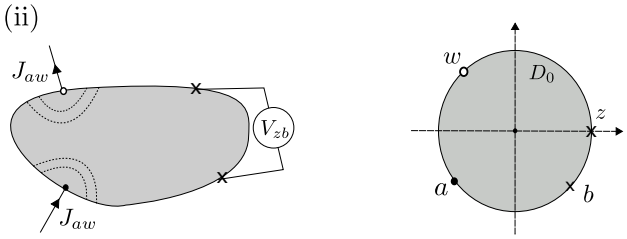

$$R_{aw}^{zb} \equiv \frac{V_{zb}}{J_{aw}} = \lambda \log \frac{\omega(z,a)\omega(b,w)}{\omega(z,w)\omega(b,a)}$$

van der Pauw equation

$$\exp\left(-\frac{R_{ab}^{zw}}{\lambda}\right) + \exp\left(-\frac{R_{aw}^{zb}}{\lambda}\right) = 1$$

Figure 4.1: The original van der Pauw setup. The first measurement is the voltage difference between z and w with a source of current a and a sink of current b. The second measurement is the difference between z and b with a source a and a sink w. These resistances satisfy the van der Pauw equation (4.1) which can be solved for λ. Because the domain is simply connected, the prime function is $\omega(\zeta, c) \equiv \zeta - c$.

In this thesis, this will be referred to as the classical *van der Pauw equation* and it provides the basis for the van der Pauw method. Because this method needs only two resistance measurements, and works for samples of arbitrary shape, the method is widely applied for measuring the resistivity of superconductors or Hall coefficients of materials in laboratory experiments [117, 135]. An efficient numerical method to determine λ is discussed in [28]. In the next section we will see how the van der Pauw method is changed when considering holey samples.

4.2 Two conjectures of the van der Pauw measurements for annular domains

In recent years, the van der Pauw method for samples with a single hole, or even several holes, has been extensively studied [11, 79, 80, 112, 136–141]. It has been reported that the van der Pauw equation (4.1) is inaccurate for samples with several holes [103]. This is to be expected since this formula takes no account of the presence of any holes. Indeed, quite what form the appropriate generalization of the van der Pauw method should take is not currently clear from the extant literature.

A sample with a single isolated hole whose boundary comprises more than a single point is the natural first case to study and has been considered by [137, 139]. Any 2D sample with a single hole is doubly connected and can be transplanted conformally into an annulus [40] where the radius of the inner circle of the annulus depends on the shape of sample [107]. By conducting both numerical and laboratory experiments Szymański et al. [137] showed that the van der Pauw equation (4.1) does not hold for a sample with a hole but conjectured that the data instead satisfies the inequality

$$\exp\left(-\frac{R_{ab}^{zw}}{\lambda}\right)+\exp\left(-\frac{R_{aw}^{zb}}{\lambda}\right)\leq 1. \tag{4.2}$$

The same inequality has been proposed in series of papers [112, 138]. To the best of the authors' knowledge, a rigorous proof of this conjecture has not been given. It is one of the objectives of this chapter to show how the inequality (4.2) can be confirmed mathematically.

For holey samples Szymański et al. proposed some modifications to the van der Pauw setting [138, 139]. Firstly, they proposed a six-point method, which uses six electrical contacts on the perimeter of a sample with a hole, and measures nine pairs of resistances [139]. Because the nine resistances can be expressed explicitly in terms of the coordinates of six electrical contacts on the perimeter of a unit circle, they obtained a well-conditioned equation for the unknown sample resistivity. The method was also validated by some laboratory experiments. Arguably a drawback is that the method requires the measurement of nine resistances to solve seven nonlinear equations.

Szymański et al. [138] also find that the pair of measured resistance $(R_{ab}^{zw}, R_{aw}^{zb})$ satisfies another inequality which they dubbed a "lower envelope" – a phrase we also adopt – and they proposed a method to measure the resistivity based on the existence of this envelope. By conjecturing that the shape of the lower envelope depends only on a Riemann modulus ρ, they applied a standard fitting technique for pairs of measurements $(R_{ab}^{zw}, R_{aw}^{zb})$ lying on this envelope and consequently were able to determine the sample resistivity. They did not, however, succeed in finding a mathematical expression for this lower envelope. This is

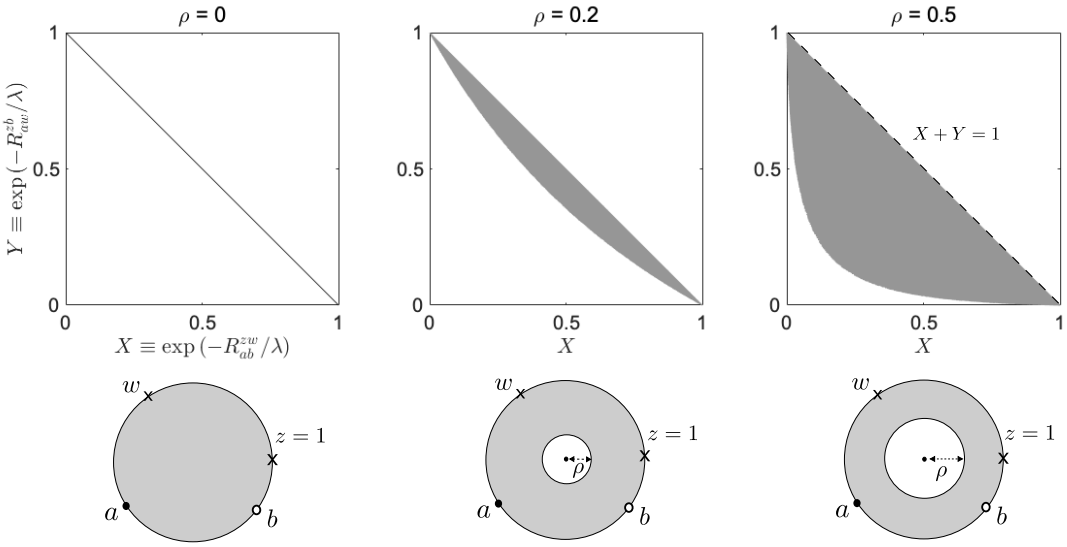

Figure 4.2: Evidence for the two "envelopes". Numerical experiments for pairs (X, Y) where $X \equiv \exp(-R_{ab}^{zw}/\lambda)$ and $Y \equiv \exp(-R_{aw}^{zb}/\lambda)$ following [138]. The point $z = 1$ is fixed, but (a, b, w) are picked at random with the ordering $\arg[z] < \arg[w] < \arg[a] < \arg[b] < 2\pi$. When $\rho = 0$, all pairs (X, Y) are on the line $X + Y = 1$ which is (4.1). However, when $\rho > 0$, all points (X, Y) lie in the gray-shaded region bounded by $X + Y = 1$ and a "lower envelope" which is curved. As shown in the center and right, the size of the gray-shaded area increases with ρ.

one of the new contributions of the present chapter which we now describe.

Figure 4.2 shows the results of the same numerical experiment conducted in [138]. It shows the data from 40,000 pairs (X, Y), where the more convenient designations

$$X \equiv \exp(-R_{ab}^{zw}/\lambda), \qquad Y \equiv \exp(-R_{aw}^{zb}/\lambda) \tag{4.3}$$

are introduced. In Figure 4.2 three different samples are used, corresponding to three different values of ρ. The contact points z, w, a, and b are chosen at random but always such that they retain the ordering $0 = \arg[z] < \arg[w] < \arg[a] < \arg[b] < 2\pi$. The data is found to fall in the gray-shaded regions in Figure 4.2. If there is no hole, which means $\rho = 0$, the pair satisfies $X + Y = 1$ as must be true since that data is known to satisfy the original van der Pauw equation (4.1). However, if $\rho > 0$, this is no longer true and the data (X, Y) "fills in" a crescent-shaped domain shown shaded in Figure 4.2. Szymański *et al.* conjecture that the data (X, Y) always lies in such a domain bounded by the upper envelope $X + Y \leq 1$ and some lower envelope, dependent purely on ρ. Those authors do not, however, give a definite equation for the curve described by this envelope. The same authors also conjecture, again without a rigorous mathematical proof, that the lower envelope might correspond to the pair of (X_θ, Y_θ), where (X_θ, Y_θ) are measurements with

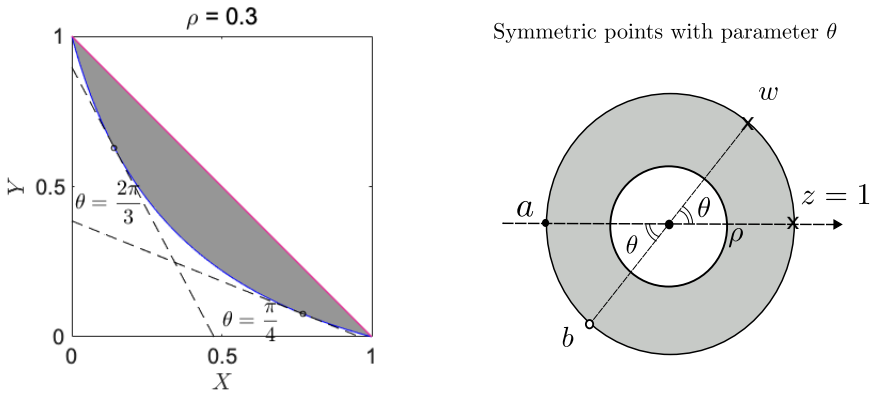

Figure 4.3: The upper envelope (red line) and the lower envelope (blue line). The lower envelope, parametrized by the variable θ, is defined by its set of tangents as in (4.4): any point in the gray region, which is where all measurement pairs lie, is above the tangent line for each point on the lower envelope. The right-most figure gives a geometrical interpretation of θ and shows what we mean by "symmetric resistance measurements": the sector formed by the pair (a, b) subtends the same angle θ at the origin as that formed by the pair (z, w).

the four electrical contacts having the "symmetry" shown on the right of Figure 4.3; for brevity, we will refer to these as "symmetric resistance measurements". The angle θ is defined as $\theta \equiv \arg[w/z] = \arg[b/a]$; for such contact points the sector formed by the pair (a, b) subtends the same angle θ at the origin as that formed by the pair (z, w). Based on these conjectures, Szymański et al. [138] propose a method to determine λ by measuring some pairs of resistances which lie on the lower envelope. If these conjectures hold then the form of the upper and lower envelopes can be expressed mathematically as

$$X + Y \leq 1, \qquad Y - Y_\theta \geq \frac{\partial Y_\theta/\partial\theta}{\partial X_\theta/\partial\theta}(X - X_\theta), \qquad \text{for } \; 0 < \theta < \pi, \tag{4.4}$$

where θ parametrizes the lower envelope which is defined by its set of tangents. Two examples of such tangents (4.4) are shown on the left of Figure 4.3. These inequalities have been proposed in several papers [112, 136–138], but no rigorous proof has yet been obtained.

The next sections aims to understand the envelope structure mathematically. This is done by introducing, for the first time, two important tools into this area of investigation: (i) use of the prime function $\omega(\zeta, c)$ [40] associated with the concentric annulus $\rho < |\zeta| < 1$ that generalizes the simple monomial prime function relevant when the sample if free of holes; (ii) use of the Fay trisecant identity [40, 57, 121] satisfied by this new prime function to gain insights into the two envelopes associated with the two resistance measurements

(4.3).

In section 4.4 the prime function for the annulus is revisited and the electrical potentials for annular samples are expressed by using the prime function. In section 4.4.2, the Fay trisecant identity satisfied by this particular prime function is presented. Section 4.5 shows how these mathematical tools can be used to understand the structure of the envelopes associated with a holey sample. This involves analysis of an integrated form of the Fay trisecant identity. In section 4.7 we propose how to use the new expressions for the lower envelope curve in a generalized van der Pauw setting and carry out some numerical tests to validate the scheme.

4.3 The van der Pauw equation for simply connected domains

We start by considering the voltage potential of a sample with no holes to derive the original van der Pauw equation (4.1). Because the electrical potential is harmonic, it is reasonable to define the complex potential $H_0(\Omega)$ of the complex variable $\Omega = x + \mathrm{i}y$, whose real part is the harmonic voltage potential $V(x, y)$ in the sample:

$$H_0(\Omega) = V(x, y) + \mathrm{i}\chi(x, y), \tag{4.5}$$

where (x, y) denotes Cartesian coordinates in the physical plane. We have introduced $\chi(x, y)$ as the harmonic conjugate of the potential $V(x, y)$. The voltage $V(x, y)$ is harmonic in the sample and its normal derivative vanishes on the sample boundary; equivalently, by the Cauchy-Riemann equations, its harmonic conjugate $\chi(x, y)$ is constant on the boundary. Let σ be the specific resistance of the sample. Its thickness is defined as d, which is measured beforehand. By the Riemann mapping theorem, we can introduce a conformal mapping $\Omega = f(\zeta)$ between the unit disc in a complex parametric ζ-plane and the sample in the physical Ω-plane. By the conformal invariance of the boundary value problem for $V(x, y)$ [1], the complex potential $h_0(\zeta) \equiv H_0(\Omega)$ for the voltage distribution caused by a current source at Ω_a and a compensating sink at Ω_b is then given, as a function of ζ, by

$$h_0(\zeta) = \frac{\sigma J_{ab}}{\pi d} \log\left(\frac{\zeta - a}{\zeta - b}\right) = \lambda J_{ab} \log\left(\frac{\omega(\zeta, a)}{\omega(\zeta, b)}\right), \tag{4.6}$$

where

$$\Omega_a = f(a), \qquad \Omega_b = f(b), \tag{4.7}$$

and where $\lambda \equiv \sigma/\pi d$ is the resistivity. We have used $\omega(\zeta, c)$ above as the prime function of simply connected domain defined by

$$\omega(\zeta, c) = \zeta - c. \tag{4.8}$$

The potential difference V_{zw} is therefore given by

$$V_{zw} \equiv \mathrm{Re}[h_0(z)] - \mathrm{Re}[h_0(w)] = \lambda J_{ab} \log \left| \frac{\omega(z,a)\omega(w,b)}{\omega(z,b)\omega(w,a)} \right| = \lambda J_{ab} \log |p_0(z,w;a,b)| \,. \tag{4.9}$$

It follows that

$$R_{ab}^{zw} = \frac{V_{zw}}{J_{ab}} = \lambda \log p_0(z,w;a,b), \tag{4.10}$$

where the classical cross-ratio is defined by

$$p_0(z,w;a,b) \equiv \frac{\omega(z,a)\omega(w,b)}{\omega(z,b)\omega(w,a)}. \tag{4.11}$$

We have removed the modulus symbols because the cross-ratio is real and positive when all (z, w, a, b) are on the unit circle in the ζ plane, and $0 \leq \arg[z] < \arg[w] < \arg[a] < \arg[b] < 2\pi$.

The other measurement R_{aw}^{zb} is also given by the potential difference between z and b with a current source at a and sink at w. Switching of b and w in (4.10) yields

$$R_{aw}^{zb} = \frac{V_{zb}}{J_{aw}} = \lambda \log p_0(z,b;a,w). \tag{4.12}$$

It is well-known that the cross ratio satisfies the cross-ratio identity:

$$p_0(z,w;b,a) + p_0(z,b;w,a) = 1. \tag{4.13}$$

The identity (4.13) is easily verified by a simple calculation:

$$\begin{aligned} p_0(z,w;b,a) + p_0(z,b;w,a) &= \frac{\omega(z,b)\omega(w,a)}{\omega(z,a)\omega(w,b)} + \frac{\omega(z,w)\omega(b,a)}{\omega(z,a)\omega(b,w)} \\ &= \frac{(z-b)(w-a)}{(z-a)(w-b)} + \frac{(z-w)(b-a)}{(z-a)(b-w)} \\ &= \frac{(z-b)(w-a) - (z-w)(b-a)}{(z-a)(w-b)} = 1. \end{aligned} \tag{4.14}$$

Hence the cross ratio identity (4.13) is equivalent to the original van der Pauw equation (4.1).

In complex analysis the cross-ratio [1,40] is most commonly encountered in a geometrical context as the Möbius mapping that provides a conformal mapping, as a function of the variable z say, between 3 arbitrary complex points (a, w, b) in the complex z plane and the

canonical choice of points $(0, 1, \infty)$.

Concerning the function (4.8), it is so simple in this case that it is rarely given the designation "prime function". However, the monograph [40] makes the case that recognizing it as the simplest instance of a more general notion of a *prime function* is important for generalizing many known results for simply connected planar geometries to multiply connected cases. The van der Pauw problem of interest here is no exception. It will be shown later that the natural way to extend the classical van der Pauw method to multiply connected geometries is to treat the problem using the prime function – more specifically, the multiply connected generalization of (4.8) – and to make use of some important identities satisfied by that function.

4.4 The van der Pauw equation for annular domains

Here we derive a new van der Pauw equation for simplest nontrivial domains, i.e., doubly connected domains. This can be done by considering the voltage potentials of the domain with the use of conformal maps and the Fay's trisecant identity associated with the doubly connected domains. This approach is exactly the same as Section 4.3 except we use the prime function for doubly connected domains.

4.4.1 The voltage potential in annular domains

We start by considering the voltage potential in annular domains. Let D denote a bounded sample with an isolated hole. Let ∂D_0 be the outer boundary of the sample and ∂D_1 the boundary of the hole. Similar to the original van der Pauw method, it is assumed that the sample thickness is d. It is assumed that the hole in the sample carries no net charge. Figure 4.4 shows a schematic diagram of the setup of the van der Pauw method for annular domains.

It is also supposed that 4 point contacts $(\Omega_a, \Omega_b, \Omega_z, \Omega_w)$, of infinitesimal width, are placed on ∂D_0. It is known, by an extension of the Riemann mapping theorem [40], that any such domain is conformally equivalent to a concentric annulus $\rho < |\zeta| < 1$ with circular boundaries C_0 and C_1 and $0 \leq \rho < 1$. The circle C_0 is the unit circle; C_1 is the circle $|\zeta| = \rho$. In other words, there exists an analytic function

$$\Omega = f(\zeta) \tag{4.15}$$

that transplants the annulus $\rho < |\zeta| < 1$ to the domain D with C_0 being transplanted to ∂D_0 and C_1 to ∂D_1.

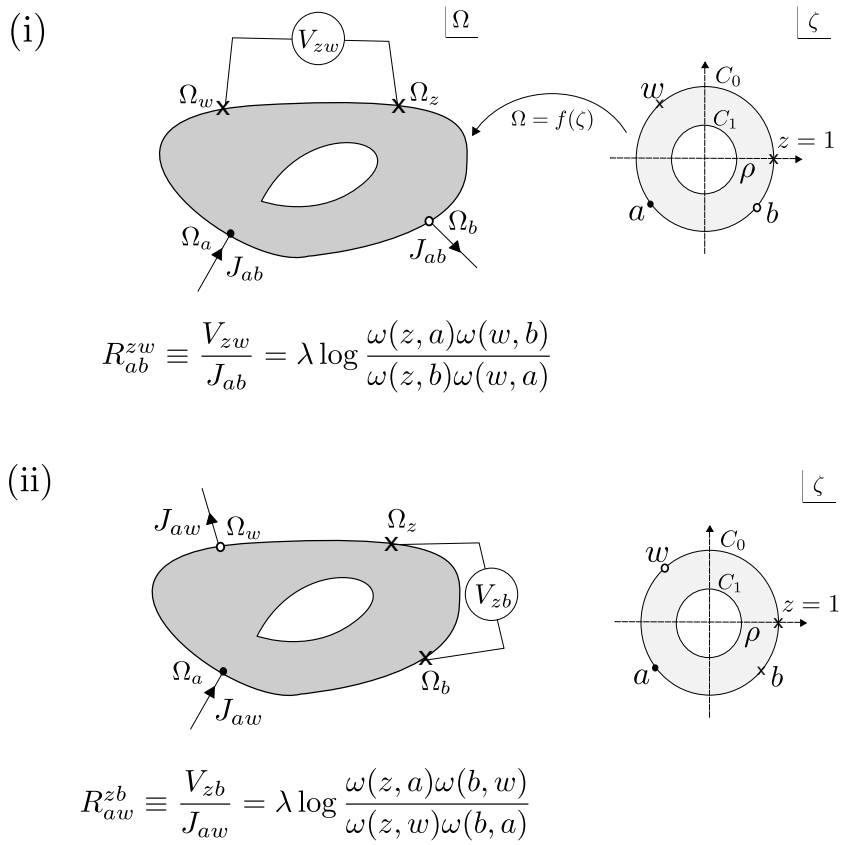

Figure 4.4: The van der Pauw set-up for a sample with an isolated hole. The first measurement is the voltage difference between z and w with a source of current a and a sink of current b. The second measurement is the difference between z and b with a source a and a sink w. Similar to the original van der Pauw method, the measured resistances are denoted by the logarithm of the prime function.

Let the required complex potential, as a function of $\Omega = x + \mathrm{i}y$ be

$$H(\Omega) = V(x, y) + \mathrm{i}\chi(x, y). \tag{4.16}$$

We can still exploit the conformal invariance for the problem of determining the potential $V(x, y)$ in this doubly connected domain. Crowdy [37, 40] has shown that the complex potentials for any source/sink driven harmonic field in a multiply connected domain can be written down explicitly in terms of the prime function associated with that domain. It is important to emphasize that this fact holds for domains of any finite connectivity not just the doubly connected case of interest here.

Following [37, 40] the complex potential $h(\zeta) \equiv H(f(\zeta))$ is given by

$$h(\zeta) = \frac{\sigma J_{ab}}{2\pi d} \log\left(\frac{\bar{a}b}{|ab|}\frac{\omega(\zeta,a)\omega(\zeta,\bar{a}^{-1})}{\omega(\zeta,b)\omega(\zeta,\bar{b}^{-1})}\right) = \lambda J_{ab}\log\left(\frac{a}{b}\frac{P(\zeta/a)}{P(\zeta/b)}\right) + \mathrm{i}c, \quad c \in \mathbb{R}, \tag{4.17}$$

where $P(.)$ is the prime function for the annulus domain with inner radius ρ defined in Chapter 2. Although $P(.)$ also depends on the inner radius ρ we omit ρ here for notational brevity. The first equality of (4.17) is derived in [37, 40] and follows from the general properties of the prime function, and where we have used (2.10) in the second equality. The relation (4.15) gives the relationship between (a, b, z, w) and $(\Omega_a, \Omega_b, \Omega_z, \Omega_w)$ although it is understood that the mapping $f(\zeta)$ is now the new mapping from the concentric annulus to the holey sample. The specific resistivity λ is defined as $\lambda = \sigma/\pi d$. Note that, because two electrical contacts a and b are on C_0, $\bar{a} = a^{-1}$ and $\bar{b} = b^{-1}$.

The voltage difference between z and w is given by

$$V_{zw} \equiv \mathrm{Re}[h(z)] - \mathrm{Re}[h(w)] = \lambda J_{ab}\log\frac{P(z/a)P(w/b)}{P(z/b)P(w/a)}. \tag{4.18}$$

It is important to note that because all contacts are located on the same boundary of the annulus, $\mathrm{Im}[h(z)] - \mathrm{Im}[h(w)] = 0$. This relation is also proven mathematically by direct calculation

$$\begin{aligned}\overline{h(z) - h(w)} &= \log\overline{\left(\frac{P(z/a)P(w/b)}{P(z/b)P(w/a)}\right)} = \log\left(\frac{P(a/z)P(b/w)}{P(b/z)P(a/w)}\right)\\ &= \log\left(\frac{P(z/a)P(w/b)}{P(z/b)P(w/a)}\right) = h(z) - h(w),\end{aligned} \tag{4.19}$$

where we note that $P(\zeta)$ has functional properties (2.12) and (2.13) and the fact that $z, w, a, b \in C_0$ has been used. The measured resistance R_{ab}^{zw} is defined as

$$R_{ab}^{zw} \equiv \frac{V_{zw}}{J_{ab}} = \lambda\log\frac{P(z/a)P(w/b)}{P(z/b)P(w/a)}. \tag{4.20}$$

In the same way, the resistance R_{aw}^{zb} is given by swapping w and b:

$$R_{aw}^{zb} \equiv \frac{V_{zb}}{J_{aw}} = \lambda\log\frac{P(z/a)P(b/w)}{P(z/w)P(b/a)}. \tag{4.21}$$

It is straightforward to check that formulas (4.20) and (4.21) above are equivalent to those given in the previous definition given by Szymański et.al. [137]. More precisely, it can be checked that the function $G(\phi)$ used in [137] is related to $P(\zeta)$ – and hence to the prime

function (2.10) – by the formula

$$\begin{aligned} P(e^{\mathrm{i}\phi}) &= (1-e^{\mathrm{i}\phi})\prod_{n=1}^{\infty}(1-\rho^{2n}e^{\mathrm{i}\phi})(1-\rho^{2n}e^{-\mathrm{i}\phi}) \\ &= -2\mathrm{i}e^{\frac{\mathrm{i}\phi}{2}}\sin\frac{\phi}{2}\prod_{n=1}^{\infty}(1+\rho^{4n}-2\rho^{2n}\cos\phi) \\ &= -2\mathrm{i}e^{\frac{\mathrm{i}\phi}{2}}\sin\frac{\phi}{2}\prod_{n=1}^{\infty}(1+\rho^{4n})\cdot\prod_{n=1}^{\infty}\left(1-\frac{2\cos\phi}{\rho^{2n}+\rho^{-2n}}\right) \\ &= -2\mathrm{i}e^{\frac{\mathrm{i}\phi}{2}}\hat{P}(\mathrm{i})G(\phi), \end{aligned} \tag{4.22}$$

where

$$G(\phi)\equiv\sin\frac{\phi}{2}\prod_{n=1}^{\infty}\left(1-\frac{\cos\phi}{\cosh hn}\right), \qquad h\equiv 2\log\rho. \tag{4.23}$$

Although (4.22) shows that our new expressions (4.20)–(4.21) coincide with those of [137], there is much significance in having recognized that the resistances can be written in terms of this special transcendental function known as the prime function [40] of the preimage concentric annulus. First, the notion of a prime function extends to a planar domain of any finite connectivity [40] which means that we already have a route to generalizing all the ideas in this chapter (presented here for the annulus) to any higher connected domain (i.e. a sample with more than one hole). Crowdy [37] was the first to show how the complex potentials for source/sink driven harmonic fields in multiply connected domains can be written explicitly. His treatment uses irrotational fluid mechanics as the physical context but mathematically the problem is equivalent to the electrical conduction problems of interest here. Second, it is known [40] that prime functions, including those associated with domains of connectivity higher than one, satisfy a so-called Fay trisecant identity. This identity can be viewed as an analogue of the cross-ratio identity (4.13) on a higher genus Riemann surface [57] and is the topic of the next subsection.

4.4.2 The Fay trisecant identity for the annulus

It is useful to introduce the function

$$p(z,w;a,b)\equiv\frac{\omega(z,a)\omega(w,b)}{\omega(z,b)\omega(w,a)}. \tag{4.24}$$

Although this formula is identical to that defining the cross-ratio (4.13) this quantity is no longer a cross-ratio since the definition of the prime function has changed. On use of (2.10)

formula (4.24) can be written in terms of $P(\zeta)$ as

$$p(z,w;a,b) = \frac{P(z/a)P(w/b)}{P(z/b)P(w/a)}. \tag{4.25}$$

From (4.25) and (4.20)-(4.21) we see that

$$\exp(-R_{ab}^{zw}/\lambda) = \frac{P(z/b)P(w/a)}{P(z/a)P(w/b)} = p(z,w;b,a), \tag{4.26}$$

$$\exp(-R_{aw}^{zb}/\lambda) = \frac{P(z/w)P(b/a)}{P(z/a)P(b/w)} = p(z,b;w,a). \tag{4.27}$$

For the cross ratio in annular domains, the Fay trisecant identity is an analogue of the cross ratio identity of simply connected domains [57]. The Fay trisecant identity associated with this prime function is

$$\frac{P(kz/w)P(ka/b)}{P(kza/wb)}p(z,w;b,a) + \frac{P(kz/b)P(ka/w)}{P(kza/wb)}p(z,b;w,a) = P(k), \tag{4.28}$$

where k is an arbitrary complex number. This statement (4.28) of the genus-1 Fay trisecant identity expressed purely in terms of the prime function of the concentric annulus has been taken from Exercise 8.9 of Chapter 8 of the monograph [40] which asks the reader to prove it using the properties of so-called loxodromic functions. Although it is well established [57, 121] from more general arguments, we sketch a proof of this form (4.28) of the genus-one Fay trisecant identity. First we consider the left hand side of (4.28) as a function of z with all other quantities being treated as parameters. Let

$$J(z) \equiv \frac{P(kz/w)P(ka/b)}{P(kza/wb)}p(z,w;b,a) + \frac{P(kz/b)P(ka/w)}{P(kza/wb)}p(z,b;w,a). \tag{4.29}$$

By direct calculation and the use of the properties (2.12) and (2.13) of the function $P(\zeta)$, we have

$$\begin{aligned} J(\rho^2 z) &= \frac{P(\rho^2 kz/w)P(ka/b)}{P(\rho^2 kza/wb)}\frac{P(\rho^2 z/b)P(w/a)}{P(\rho^2 z/a)P(w/b)} + \frac{P(\rho^2 kz/b)P(ka/w)}{P(\rho^2 kza/wb)}\frac{P(\rho^2 z/b)P(w/a)}{P(\rho^2 z/a)P(w/b)} \\ &= \frac{P(kz/w)P(ka/b)}{P(kza/wb)}\frac{P(z/b)P(w/a)}{P(z/a)P(w/b)} + \frac{P(kz/b)P(ka/w)}{P(kza/wb)}\frac{P(z/b)P(w/a)}{P(z/a)P(w/b)} \\ &= J(z). \end{aligned} \tag{4.30}$$

Hence, since it is also meromorphic as a function of z, it is a loxodromic function of z; see Chapter 8 of [40]. A loxodromic function is the name of an automorphic function on the Schottky double of the concentric annulus; it is a meromorphic function of that surface

satisfying the functional identity (4.30). If we write

$$J(z) = \frac{N(z)}{P(kza/wb)P(z/a)P(w/b)} \tag{4.31}$$

so that

$$\begin{aligned} N(z) = {} & P(kz/w)P(ka/b)P(z/b)P(w/a) \\ & - (w/b)P(kz/b)P(ka/w)P(z/w)P(b/a) \end{aligned} \tag{4.32}$$

then, it can be verified, again using the properties (2.12) and (2.13) of $P(\zeta)$, that

$$N(a) = N(wb/ka) = 0. \tag{4.33}$$

Since $J(z)$ is a loxodromic function with removable poles at $z = a$ and $z = wb/ka$ – and, therefore, having no poles on the surface – then it must be independent of z, which means it is a constant when considered as a function of z. We are employing a Liouville-type theorem on this genus-one Schottky double: any meromorphic function on it having no poles must be constant. Such results will be used extensively throughout this chapter.

We can also consider the left hand side of (4.28) as a function for w and write

$$\tilde{J}(w) \equiv \frac{P(kz/w)P(ka/b)}{P(kza/wb)}p(z,w;b,a) + \frac{P(kz/b)P(ka/w)}{P(kza/wb)}p(z,b;w,a). \tag{4.34}$$

This can also be shown to be loxodromic, i.e.,

$$\tilde{J}(\rho^2 w) = \tilde{J}(w) \tag{4.35}$$

and to have removable poles at $w = b$ and $w = kza/b$. It is therefore independent of w.

By similar arguments, considering the left hand side of (4.28) successively as a function of a and b it can be shown to be independent of those variables too. Putting all these facts together, it is concluded that

$$\frac{P(kz/w)P(ka/b)}{P(kza/wb)}p(z,w;b,a) + \frac{P(kz/b)P(ka/w)}{P(kza/wb)}p(z,b;w,a) = C(k), \tag{4.36}$$

where $C(k)$ is a function to be determined. It can be found by matching to the limit of the left hand side of (4.36) in the double limit $w \to z$ and $b \to a$ which yields

$$C(k) = P(k). \tag{4.37}$$

Thus we have established the Fay trisecant identity (4.28).

A key observation is that, on substituting (4.20) and (4.21) into (4.28), we obtain

$$\frac{P(kz/w)P(ka/b)}{P(k)P(kza/wb)}\exp\left(-\frac{R_{ab}^{zw}}{\lambda}\right)+\frac{P(kz/b)P(ka/w)}{P(k)P(kza/wb)}\exp\left(-\frac{R_{aw}^{zb}}{\lambda}\right)=1\ . \tag{4.38}$$

When $\rho \to 0$, so that there is no hole in a sample, it is straightforward to check that

$$\frac{P(kz/w)P(ka/b)}{P(k)P(kza/wb)}=\frac{P(kz/b)P(ka/w)}{P(k)P(kza/wb)}=1 \tag{4.39}$$

by choosing $k = 0$, because, from (2.11), it follows that $P(\zeta) = 1 - \zeta$ when $\rho = 0$. The original van der Pauw equation (4.1) is therefore retrieved from (4.38) in the simply connected (i.e. "no hole") limit.

It is clear that (4.38) opens up new perspectives: that it reduces, as $\rho \to 0$, to the original van der Pauw equation (4.1) is tantalizing. It also makes it a natural candidate, at least from the mathematical point of view, to find natural ways to extend the van der Pauw method to holey samples. In contrast to the original van der Pauw equation, the coefficients of $\exp(-R_{ab}^{zw}/\lambda)$ and $\exp(-R_{aw}^{zb}/\lambda)$ in (4.38) now depend not only on the electrical contact locations z, w, a, b but also on a fifth complex parameter k. It should be emphasized that (4.38) holds for arbitrary choices of a, b, z, w and k even though, for present purposes, we have assumed that a, b, z and w lie on C_0. This degree of freedom in the choice of k will be exploited in the next section to gain insights into the envelope structure evident in Figure 4.2.

4.5 Analysis of the envelopes: the integrated Fay identity

In the introduction of this chapter the existence of two envelopes, an "upper" and a "lower" envelope, were discussed based on the observations of previous authors. These envelopes have the conjectured mathematical definitions given in (4.4). In this section it is shown how the new tools introduced in the previous two sections allow us to prove the conjectured form of these envelopes.

4.5.1 Expressions for two envelopes

First we will rephrase the two inequalities (4.4) in terms of the Fay trisecant identity. For arbitrary z, w, a, and b on C_0 we can introduce the special choice of angular coordinates θ, θ_1 and θ_3 defined by

$$z=1,\qquad w=\exp(\mathrm{i}(\theta_1+\theta)),\qquad a=\exp(\mathrm{i}(\theta_1+\theta_3)),\qquad b=\exp(\mathrm{i}(\theta+\theta_3)). \tag{4.40}$$

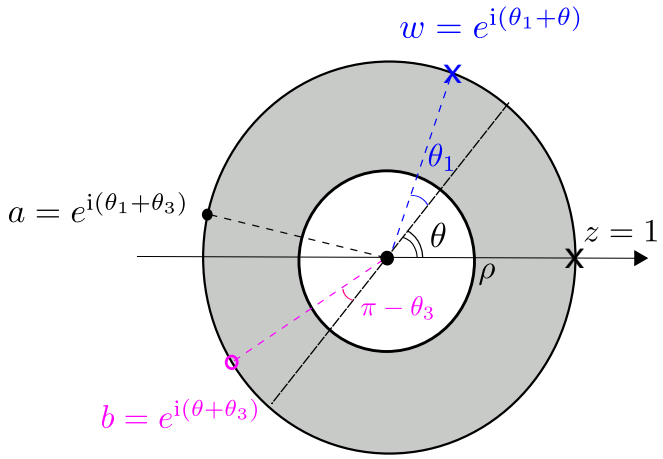

Figure 4.5: Special choice of angular coordinates. It can be seen that the angles θ_1 and θ_3 are displacements from symmetric choice of contact points.

The arbitrary points with the angular coordinates is described in Figure 4.5. Because $0 < \arg[w] < \arg[a] < \arg[b] < 2\pi$, the ranges of $\theta_1,\ \theta,\ \theta_3$ are given by

$$-\theta < \theta_1 < \theta, \qquad \theta < \theta_3 < 2\pi - \theta, \qquad 0 < \theta < \pi. \tag{4.41}$$

It is important to point out that the case of symmetric contact points shown in Figure 4.3 corresponds to $\theta_1 = 0$ and $\theta_3 = \pi$.

The choice (4.40) of angular variables may not seem very intuitive but they have been chosen because they allow us to make progress with the mathematical proofs.

The Fay trisecant identity (4.38) can be written

$$A(\theta_1, \theta, \hat{k}) X_{\theta_1,\theta_3,\theta} + B(\theta_3, \theta, \hat{k}) Y_{\theta_1,\theta_3,\theta} = 1, \tag{4.42}$$

where $X_{\theta_1,\theta_3,\theta} \equiv \exp(-R^{zw}_{ab}/\lambda)$, $Y_{\theta_1,\theta_3,\theta} \equiv \exp(-R^{zb}_{aw}/\lambda)$ and the coefficient functions are

$$A(\theta_1, \theta, \hat{k}) \equiv \frac{P(kz/w)P(ka/b)}{P(k)P(kza/wb)} = \frac{P(ke^{-\mathrm{i}(\theta+\theta_1)})P(ke^{\mathrm{i}(-\theta+\theta_1)})}{P(k)P(ke^{-2\mathrm{i}\theta})} = \frac{P(\hat{k}e^{-\mathrm{i}\theta_1})P(\hat{k}e^{\mathrm{i}\theta_1})}{P(\hat{k}e^{-\mathrm{i}\theta})P(\hat{k}e^{\mathrm{i}\theta})}, \tag{4.43}$$

$$B(\theta_3, \theta, \hat{k}) \equiv \frac{P(kz/b)P(ka/w)}{P(k)P(kza/wb)} = \frac{P(ke^{-\mathrm{i}(\theta+\theta_3)})P(ke^{\mathrm{i}(-\theta+\theta_3)})}{P(k)P(ke^{-2\mathrm{i}\theta})} = \frac{P(\hat{k}e^{-\mathrm{i}\theta_3})P(\hat{k}e^{\mathrm{i}\theta_3})}{P(\hat{k}e^{-\mathrm{i}\theta})P(\hat{k}e^{\mathrm{i}\theta})}, \tag{4.44}$$

and where we have set $k = \hat{k}e^{\mathrm{i}\theta}$ because k is arbitrary. Because of this choice, $A(\theta_1, \theta, \hat{k})$ becomes independent of θ_3 and $B(\theta_3, \theta, \hat{k})$ becomes independent of θ_1.

The next step is to consider contour integrals of $A(\theta_1, \theta, \hat{k})$ and $B(\theta_3, \theta, \hat{k})$ with respect to $\hat{k}$ around the circle $|\hat{k}| = \rho$. From (4.42), we thus obtain an *integrated Fay trisecant identity*:

$$\alpha(\theta_1, \theta) X_{\theta_1,\theta_3,\theta} + \beta(\theta_3, \theta) Y_{\theta_1,\theta_3,\theta} = 1, \tag{4.45}$$

where

$$\alpha(\theta_1, \theta) \equiv \frac{1}{2\pi} \int_0^{2\pi} A(\theta_1, \theta, \rho e^{\mathrm{i}\phi}) d\phi = \frac{1}{2\pi} \int_0^{2\pi} \frac{P(\rho e^{\mathrm{i}(\phi-\theta_1)}) P(\rho e^{\mathrm{i}(\phi+\theta_1)})}{P(\rho e^{\mathrm{i}(\phi-\theta)}) P(\rho e^{\mathrm{i}(\phi+\theta)})} d\phi, \tag{4.46}$$

$$\beta(\theta_3, \theta) \equiv \frac{1}{2\pi} \int_0^{2\pi} B(\theta_3, \theta, \rho e^{\mathrm{i}\phi}) d\phi = \frac{1}{2\pi} \int_0^{2\pi} \frac{P(\rho e^{\mathrm{i}(\phi-\theta_3)}) P(\rho e^{\mathrm{i}(\phi+\theta_3)})}{P(\rho e^{\mathrm{i}(\phi-\theta)}) P(\rho e^{\mathrm{i}(\phi+\theta)})} d\phi. \tag{4.47}$$

The integrated Fay trisecant identity (4.45) is essential for understanding the envelope structure and proving the conjectures made about it in the literature.

On taking a derivative of (4.45) with respect to θ, we find

$$\frac{\partial \alpha(\theta_1, \theta)}{\partial \theta} X_{\theta_1,\theta_3,\theta} + \frac{\partial \beta(\theta_3, \theta)}{\partial \theta} Y_{\theta_1,\theta_3,\theta} + \alpha(\theta_1, \theta) \frac{\partial X_{\theta_1,\theta_3,\theta}}{\partial \theta} + \beta(\theta_3, \theta) \frac{\partial Y_{\theta_1,\theta_3,\theta}}{\partial \theta} = 0. \tag{4.48}$$

The sum of the first two terms is zero because

$$\begin{aligned}
&\frac{\partial \alpha(\theta_1, \theta)}{\partial \theta} X_{\theta_1,\theta_3,\theta} + \frac{\partial \beta(\theta_3, \theta)}{\partial \theta} Y_{\theta_1,\theta_3,\theta} \\
&= \frac{\mathrm{i}}{2\pi} \int_0^{2\pi} [A(\theta_1, \theta, \rho e^{\mathrm{i}\phi}) X_{\theta_1,\theta_3,\theta} + B(\theta_3, \theta, \rho e^{\mathrm{i}\phi}) Y_{\theta_1,\theta_3,\theta}][K(\rho e^{\mathrm{i}(\phi-\theta)}) - K(\rho e^{\mathrm{i}(\phi+\theta)})] d\phi \\
&= \frac{\mathrm{i}}{2\pi} \int_0^{2\pi} [K(\rho e^{\mathrm{i}(\phi-\theta)}) - K(\rho e^{\mathrm{i}(\phi+\theta)})] d\phi = 0,
\end{aligned} \tag{4.49}$$

where we used the Fay identity (4.42) in the second equality. The function $K(.)$ is related to the first derivative of the prime function $P(.)$ introduced in Chapter 2. On use of (4.49) in (4.48), we find

$$\alpha(\theta_1, \theta) \frac{\partial X_{\theta_1,\theta_3,\theta}}{\partial \theta} + \beta(\theta_3, \theta) \frac{\partial Y_{\theta_1,\theta_3,\theta}}{\partial \theta} = 0. \tag{4.50}$$

Suppose now that we fix the two parameters θ_1 and θ_3. Then the points $(X_{\theta_1,\theta_3,\theta}, Y_{\theta_1,\theta_3,\theta})$ lie on some curve dependent only on the single parameter θ with the tangent at $(X_{\theta_1,\theta_3,\theta}, Y_{\theta_1,\theta_3,\theta})$, when viewed as a function of θ, defined as the set of points (X, Y) satisfying

$$Y - Y_{\theta_1,\theta_3,\theta} = \frac{\partial Y_{\theta_1,\theta_3,\theta}/\partial \theta}{\partial X_{\theta_1,\theta_3,\theta}/\partial \theta} (X - X_{\theta_1,\theta_3,\theta}). \tag{4.51}$$

If we now make use of both (4.50) and (4.45) we can see that the tangent line (4.51) is equivalent to

$$\alpha(\theta_1, \theta)X + \beta(\theta_3, \theta)Y = 1. \tag{4.52}$$

This is an important observation and it is helpful to visualize this pictorially. Figure 4.6 shows some examples of these tangent lines. The red line represents the collection of data points $(X_{\theta_1,\theta_3,\theta}, Y_{\theta_1,\theta_3,\theta})$ sketched out when both θ_1 and θ_3 are fixed and the parameter θ is varied; the blue lines in Figure 4.6, given by (4.52), are clearly tangent to those red lines (each blue line corresponds to a particular choice of θ).

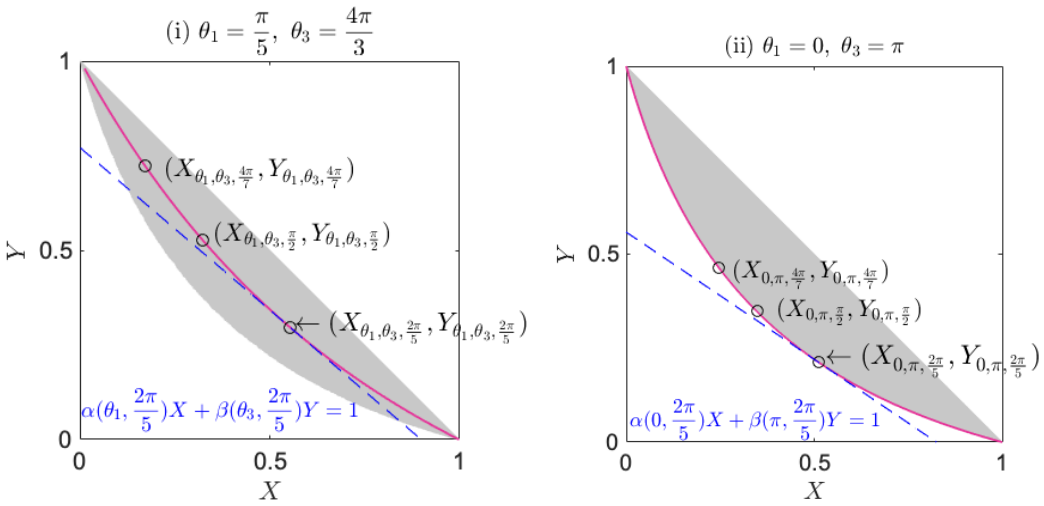

Figure 4.6: The red lines are collections of data points $(X_{\theta_1,\theta_3,\theta}, Y_{\theta_1,\theta_3,\theta})$ with both θ_1 and θ_3 fixed and only parameter θ changed. The blue lines, given by (4.52), are typical tangents to the red lines at $(X_{\theta_1,\theta_3,\frac{2\pi}{5}}, Y_{\theta_1,\theta_3,\frac{2\pi}{5}})$. When the fixed parameters θ_1 and θ_3 take the particular values $\theta_1 = 0$ and $\theta_3 = \pi$ the red line, parameterized by θ, corresponds to the lower envelope.

The important point is that, in view of the observation (4.52), and the observation made earlier that the symmetric choice of (a, b, z, w) shown in Figure 4.3 corresponds to $\theta_1 = 0$ and $\theta_3 = \pi$, the two inequalities in (4.4) are equivalent to

$$X + Y \leq 1, \tag{4.53}$$

$$\alpha_\theta X + \beta_\theta Y \geq 1, \qquad \alpha_\theta \equiv \alpha(0, \theta), \qquad \beta_\theta \equiv \beta(\pi, \theta), \tag{4.54}$$

for all pairs (X, Y) and $0 < \theta < \pi$. The first statement simply states that all pairs (X, Y) for $\rho \geq 0$ lie on or below the line $X + Y = 1$ relevant to the classical van der Pauw

case $\rho = 0$; the second statement states that all pairs (X, Y) for $\rho \geq 0$ lie above a curve, parametrized by θ associated with the symmetric choice of points shown in Figure 4.3, and defined for $\theta_1 = 0$ and $\theta_3 = \pi$.

Now, the strategy is to prove (4.53) and (4.54) for all (X, Y) by considering the maximum values and minimum values of the coefficient functions $\alpha(\theta_1, \theta)$ and $\beta(\theta_3, \theta)$ subject to the condition (4.41). From the integrated Fay identity (4.45) and the principles of the minimum and the maximum, we have that

$$\begin{aligned} \min_{-\theta<\theta_1<\theta}(\alpha(\theta_1,\theta))X_{\theta_1,\theta_3,\theta} + \min_{\theta<\theta_3<2\pi-\theta}(\beta(\theta_3,\theta))Y_{\theta_1,\theta_3,\theta} \\ \leq \alpha(\theta_1,\theta)X_{\theta_1,\theta_3,\theta} + \beta(\theta_3,\theta)Y_{\theta_1,\theta_3,\theta} = 1, \end{aligned} \tag{4.55}$$

$$\begin{aligned} \max_{-\theta<\theta_1<\theta}(\alpha(\theta_1,\theta))X_{\theta_1,\theta_3,\theta} + \max_{\theta<\theta_3<2\pi-\theta}(\beta(\theta_3,\theta))Y_{\theta_1,\theta_3,\theta} \\ \geq \alpha(\theta_1,\theta)X_{\theta_1,\theta_3,\theta} + \beta(\theta_3,\theta)Y_{\theta_1,\theta_3,\theta} = 1. \end{aligned} \tag{4.56}$$

The idea is to show that (4.55) is equivalent to (4.53), and (4.56) is equivalent to (4.54).

Before presenting the details, the strategy just explained above is illustrated in Figure 4.7. By minimising both $\alpha(\theta_1, \theta)$ and $\beta(\theta_3, \theta)$, the upper envelope $X + Y = 1$ is obtained. In contrast, by maximising both $\alpha(\theta_1, \theta)$ and $\beta(\theta_3, \theta)$, a tangent line to the lower envelope is obtained and, consequently, an explicit equation (4.91) for the curve traced out by this lower envelope.

4.5.2 Analysis of the functions

Now we will see how two functions $\alpha(\theta_1, \theta)$ and $\beta(\theta_1, \theta)$ behave. To study the extrema of $\alpha(\theta_1, \theta)$ and $\beta(\theta_1, \theta)$, we define the function

$$g_\theta(\eta) \equiv \frac{1}{2\pi}\int_0^{2\pi} \frac{P(\rho e^{\mathrm{i}(\phi-\eta)})P(\rho e^{\mathrm{i}(\phi+\eta)})}{P(\rho e^{\mathrm{i}(\phi-\theta)})P(\rho e^{\mathrm{i}(\phi+\theta)})}d\phi = \frac{1}{2\pi}\int_0^{2\pi} \mathcal{G}_{\theta,\eta}(\rho e^{\mathrm{i}\phi})d\phi, \tag{4.57}$$

where $0 \leq \eta \leq 2\pi$ and the integrand is defined as

$$\mathcal{G}_{\theta,\eta}(\zeta) \equiv \frac{P(\zeta/\mu)P(\zeta\mu)}{P(\zeta/\nu)P(\zeta\nu)}, \qquad \mu \equiv e^{\mathrm{i}\eta}, \qquad \nu \equiv e^{\mathrm{i}\theta}. \tag{4.58}$$

From the definitions (4.47) it is clear that the two coefficients functions in (4.45) can be written in terms of this single function:

$$\alpha(\theta_1, \theta) = g_\theta(\theta_1), \qquad \beta(\theta_3, \theta) = g_\theta(\theta_3). \tag{4.59}$$

Analysis of this function $g_\theta(\eta)$ provides the key to the proofs of the conjectures.

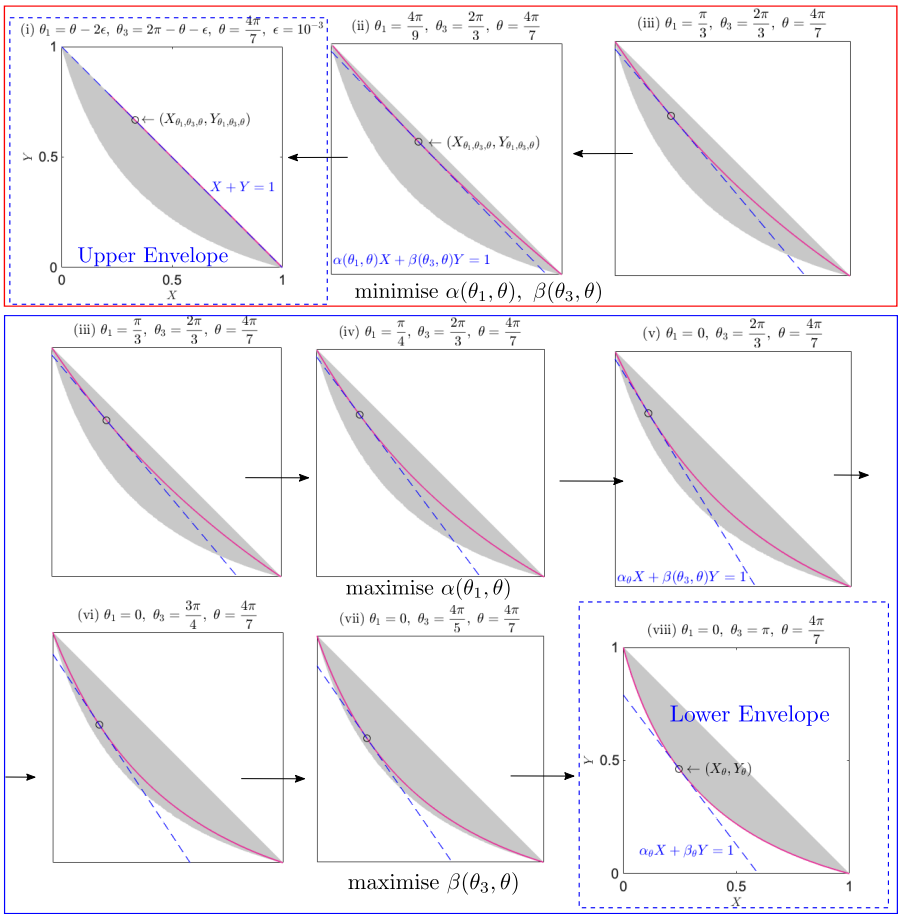

Figure 4.7: Visualizing the relationship between tangent lines and the upper and lower envelopes. The parameter $\theta = \frac{4\pi}{7}$ is fixed in all figures. Red lines show the curves produced by changing only θ, and blue lines are tangents to the envelope at $(X_{\theta_1,\theta_3,\theta}, Y_{\theta_1,\theta_3,\theta})$. When $\alpha(\theta_1, \theta)$ and $\beta(\theta_3, \theta)$ are minimised, the tangent line corresponds to $X + Y = 1$. When $\alpha(\theta_1, \theta)$ and $\beta(\theta_3, \theta)$ are maximised, the line becomes a tangent line to the lower envelope at (X_θ, Y_θ), where $X_\theta \equiv X_{0,\pi,\theta}$ and $Y_\theta \equiv Y_{0,\pi,\theta}$.

It is important to mention that because of the definition of $P(\zeta)$,

$$P(\rho e^{\mathrm{i}\phi}) = \prod_{n=1}^{\infty}(1 + \rho^{4n-2} - 2\rho^{2n-1}\cos\phi) > 0, \tag{4.60}$$

which means $\mathcal{G}_{\theta,\eta}(\rho e^{\mathrm{i}\phi})$ is real and positive. By a log-sum and sum-log inequality, we obtain

$$\begin{aligned}\log g_\theta(\eta) &= \log\left[\frac{1}{2\pi}\int_0^{2\pi}\frac{P(\rho e^{\mathrm{i}(\phi-\eta)})P(\rho e^{\mathrm{i}(\phi+\eta)})}{P(\rho e^{\mathrm{i}(\phi-\theta)})P(\rho e^{\mathrm{i}(\phi+\theta)})}d\phi\right]\\ &\geq \frac{1}{2\pi}\int_0^{2\pi}\log\frac{P(\rho e^{\mathrm{i}(\phi-\eta)})P(\rho e^{\mathrm{i}(\phi+\eta)})}{P(\rho e^{\mathrm{i}(\phi-\theta)})P(\rho e^{\mathrm{i}(\phi+\theta)})}d\phi\\ &= \frac{1}{2\pi}\int_0^{2\pi}[\log(P(\rho e^{\mathrm{i}(\phi-\eta)}))+\log(P(\rho e^{\mathrm{i}(\phi+\eta)}))\\ &\qquad -\log(P(\rho e^{\mathrm{i}(\phi-\theta)})-\log(P(\rho e^{\mathrm{i}(\phi+\theta)}))]d\phi = 0.\end{aligned} \tag{4.61}$$

Thus, we can conclude that $g_\theta(\eta) \geq 1$ for all θ and η.

We propose an alternative expression of $g_\theta(\eta)$ to be:

$$g_\theta(\eta) = \frac{P(\nu/\mu)P(\mu\nu)}{\hat{P}(1)P(\nu^2)}[K(\mu/\nu)-K(\mu\nu)], \tag{4.62}$$

where we recall that $\mu = e^{\mathrm{i}\eta}$ and $\nu = e^{\mathrm{i}\theta}$. This expression is useful for the analysis of $g_\theta(\eta)$.

To explain the derivation of (4.62) we note that the integrand $\mathcal{G}_{\theta,\eta}(\zeta)$ defined in (4.58) has two simple poles at $\zeta = \nu$ and $\zeta = 1/\nu$ and is readily confirmed, on use of (2.12) and (2.13), to be loxodromic. The function $\mathcal{G}_{\theta,\eta}(\zeta)$ can therefore also be written as

$$\mathcal{G}_{\theta,\eta}(\zeta) = \frac{P(\zeta/\mu)P(\zeta\mu)}{P(\zeta/\nu)P(\zeta\nu)} = c_1[K(\zeta/\nu)-K(\zeta\nu)]+c_2, \tag{4.63}$$

where $c_1, c_2 \in \mathbb{C}$. Since $K(\zeta)$ is a logarithmic derivative of $P(\zeta)$ and has functional properties (2.18), the right hand side of (4.63) is also a loxodromic function and has two simple poles at $\zeta = \nu$ and $\zeta = 1/\nu$. The coefficients c_1 and c_2 are determined by considering the limits $\zeta \to \nu$ and $\zeta \to \mu$,

$$c_2 = -c_1[K(\mu/\nu)-K(\mu\nu)], \qquad c_2 = \frac{P(\nu/\mu)P(\mu\nu)}{\hat{P}(1)P(\nu^2)}[K(\mu/\nu)-K(\mu\nu)]. \tag{4.64}$$

A Liouville-type argument then confirms the equivalence of the two expressions for $\mathcal{G}_{\theta,\eta}(\zeta)$ in (4.63). We therefore conclude by using (4.57) and (4.63) that

$$\begin{aligned}g_\theta(\eta) &= \frac{1}{2\pi}\int_0^{2\pi}\mathcal{G}_{\theta,\eta}(\rho e^{\mathrm{i}\phi})d\phi\\ &= \frac{1}{2\pi}\int_0^{2\pi}\Big(c_1[K(\rho e^{\mathrm{i}(\phi-\theta)})-K(\rho e^{\mathrm{i}(\phi+\theta)})]+c_2\Big)\,d\phi = c_2,\end{aligned} \tag{4.65}$$

which is precisely (4.62).

Now, we consider the behavior of the function $g_\theta(\eta)$ by exploiting the derivative of

$g_\theta(\eta)$:

$$\frac{\partial g_\theta}{\partial \eta} = \frac{\partial \mu}{\partial \eta}\frac{\partial g_\theta}{\partial \mu} = \mathrm{i}\frac{P(\nu/\mu)P(\mu\nu)}{\hat{P}(1)P(\nu^2)}(L(\mu/\nu) - L(\mu\nu)) + \mathrm{i}g_\theta[K(\mu\nu) - K(\nu/\mu)]. \tag{4.66}$$

The function $L(\mu/\nu) - L(\mu\nu)$ is a loxodromic function as a function of μ, and has two second-order poles at $\mu = \nu$ and $\mu = 1/\nu$. Similar to the expression of $g_\theta(\eta)$, we propose another expression of $L(\mu/\nu) - L(\mu\nu)$ given by

$$L(\mu/\nu) - L(\mu\nu) = \frac{\hat{P}(1)^2 P(\mu^2)P(\nu^2)}{P(\nu/\mu)P(\mu/\nu)P(\mu\nu)^2}. \tag{4.67}$$

To establish this expression, consider a new function

$$\mathcal{L}(\mu) \equiv L(\mu/\nu) - L(\mu\nu) - \frac{\hat{P}(1)^2 P(\mu^2)P(\nu^2)}{P(\nu/\mu)P(\mu/\nu)P(\mu\nu)^2}. \tag{4.68}$$

The function $\mathcal{L}(\mu)$ is shown to be a loxodromic function by using the functional properties (2.12), (2.13), (2.18), and (2.19) as follows:

$$\begin{aligned}
\mathcal{L}(\rho^2\mu) &= L(\rho^2\mu/\nu) - L(\rho^2\mu\nu) - \frac{\hat{P}(1)^2 P(\rho^4\mu^2)P(\nu^2)}{P(\nu/\rho^2\mu)P(\rho^2\mu/\nu)P(\rho^2\mu\nu)^2} \\
&= L(\mu/\nu) - L(\mu\nu) - \frac{\hat{P}(1)^2 (\rho^2\mu^4)^{-1} P(\mu^2)P(\nu^2)}{(\rho^2\mu/\nu)^{-1}P(\nu/\mu)(\mu/\nu)^{-1}P(\mu/\nu)(\mu\nu)^{-2}P(\mu\nu)^2} \\
&= \mathcal{L}(\mu).
\end{aligned} \tag{4.69}$$

Furthermore, the asymptotic expansions of each term at $\mu = \nu$ and $\mu = 1/\nu$ are

$$\begin{aligned}
L(\mu/\nu) - L(\mu\nu) &\sim -\frac{1}{(1-\mu/\nu)^2} + \frac{1}{1-\mu/\nu} + \mathcal{O}(1) \quad \text{at} \quad \mu = \nu, \\
L(\mu/\nu) - L(\mu\nu) &\sim \frac{1}{(1-\mu\nu)^2} - \frac{1}{1-\mu\nu} + \mathcal{O}(1) \quad \text{at} \quad \mu = 1/\nu, \\
\frac{\hat{P}(1)^2 P(\mu^2)P(\nu^2)}{P(\nu/\mu)P(\mu/\nu)P(\mu\nu)^2} &\sim \frac{1}{(1-\nu/\mu)(1-\mu/\nu)} + \mathcal{O}(1) \\
&= -\frac{1}{(1-\mu/\nu)^2} + \frac{1}{1-\mu/\nu} + \mathcal{O}(1) \quad \text{at} \quad \mu = \nu, \\
\frac{\hat{P}(1)^2 P(\mu^2)P(\nu^2)}{P(\nu/\mu)P(\mu/\nu)P(\mu\nu)^2} &\sim \frac{1}{(1-\mu\nu)^2} - \frac{1}{1-\mu\nu} + \mathcal{O}(1) \quad \text{at} \quad \mu = 1/\nu.
\end{aligned} \tag{4.70}$$

Thus the two poles at ν and $1/\nu$ are removable. We conclude that $\mathcal{L}(\mu)$ is a constant function, i.e., it is independent of μ. In addition, we define another function

$$\tilde{\mathcal{L}}(\nu) \equiv L(\mu/\nu) - L(\mu\nu) - \frac{\hat{P}(1)^2 P(\mu^2)P(\nu^2)}{P(\nu/\mu)P(\mu/\nu)P(\mu\nu)^2}. \tag{4.71}$$

By similar arguments, the function $\tilde{\mathcal{L}}(\nu)$ can be seen to be a loxodromic function of ν with removable poles $\nu = \mu$ and $\nu = 1/\mu$. Thus, $\mathcal{L}(\mu)$ is independent of both μ and ν.

On use of the functional property (2.19) of $L(\zeta)$, it can be verified that $\mathcal{L}(\rho) = 0$, which means $\mathcal{L}(\mu)$ vanishes everywhere leading to expression (4.67).

Expression (4.67) can now be used to analyse the behaviour of $g_\theta(\eta)$. By substituting (4.67) into (4.66),

$$\begin{aligned}\frac{\partial g_\theta}{\partial \eta} &= \mathrm{i}\left[\frac{\hat{P}(1)P(\mu^2)}{P(\mu/\nu)P(\mu\nu)} + g_\theta(\eta)(K(\mu\nu) - K(\nu/\mu))\right] \\ &= \mathrm{i}(K(\mu\nu) - K(\nu/\mu))\left[g_\theta(\eta) - \frac{1}{K(\nu/\mu) - K(\mu\nu)}\frac{\hat{P}(1)P(\mu^2)}{P(\mu/\nu)P(\mu\nu)}\right] \\ &= \mathrm{i}(K(\mu\nu) - K(\nu/\mu))\left[g_\theta(\eta) - \frac{1}{g_\eta(\theta)}\right] .\end{aligned} \tag{4.72}$$

Since, from (4.61), $g_\theta(\eta) \geq 1$ and $g_\eta(\theta) \geq 1$ then

$$g_\theta(\eta) - \frac{1}{g_\eta(\theta)} \geq 0. \tag{4.73}$$

The sign of the derivative (4.72) is therefore determined by the function

$$k_\theta(\eta) \equiv \mathrm{i}(K(\mu\nu) - K(\nu/\mu)). \tag{4.74}$$

The derivative of $k_\theta(\eta)$ with respect to η is

$$\frac{\partial k_\theta}{\partial \eta} = -(L(\mu\nu) + L(\nu/\mu)). \tag{4.75}$$

But it can also be shown that $L(e^{\mathrm{i}\phi})$ for $0 < \phi < 2\pi$ is real and positive – the proof is given in appendix A.1. This means that

$$\frac{\partial k_\theta}{\partial \eta} < 0, \qquad 0 < \eta < 2\pi. \tag{4.76}$$

It is straightforward to check that $k_\theta(0) = k_\theta(\pi) = 0$ and consequently, using continuity arguments,

$$\lim_{\eta\to\theta-0} k_\theta(\eta) = -\infty, \qquad \lim_{\eta\to\theta+0} k_\theta(\eta) = +\infty, \tag{4.77}$$

$$\lim_{\eta\to 2\pi-\theta-0} k_\theta(\eta) = -\infty, \qquad \lim_{\eta\to 2\pi-\theta+0} k_\theta(\eta) = +\infty. \tag{4.78}$$

With this information we can determine the maxima and the minima of $g_\theta(\eta)$. The local

minima occur when $\eta = \theta$ or $\eta = 2\pi - \theta$. By the definition (4.57),

$$g_\theta(\theta) = g_\theta(2\pi - \theta) = 1. \tag{4.79}$$

On the contrary, local maxima occur when $\eta = 0$ and $\eta = \pi$. Recall that this case corresponds to the symmetric choice of points with parameter θ. Recall that $P(\zeta)$, and hence $g_\theta(\eta)$ and $k_\theta(\eta)$ depend on the parameter ρ although this dependence is hidden in our notation.

4.5.3 Proof of two conjectures (4.53)–(4.54)

We will now prove the two conjectures (4.53) and (4.54) using what we have established about the behavior of $g_\theta(\eta)$. From (4.55) and (4.79), we can conclude that

$$X_{\theta_1,\theta_3,\theta} + Y_{\theta_1,\theta_3,\theta} \leq 1 \tag{4.80}$$

for all $(X_{\theta_1,\theta_3,\theta}, Y_{\theta_1,\theta_3,\theta})$. This is equivalent to the conjecture (4.53).

The maxima of $\alpha(\theta_1, \theta)$ and $\beta(\theta_3, \theta)$ occur when $\theta_1 = 0$ and $\theta_3 = \pi$. Hence, from (4.56), we conclude that

$$\alpha_\theta X_{\theta_1,\theta_3,\theta} + \beta_\theta Y_{\theta_1,\theta_3,\theta} \geq 1. \tag{4.81}$$

The inequality (4.81) is not, however, equivalent to the inequality (4.54). What has been proven in (4.81) is that for $0 < \theta < \pi$, the pair $(X_{\theta_1,\theta_3,\theta}, Y_{\theta_1,\theta_3,\theta})$ is above the tangent at $(X_{0,\pi,\theta}, Y_{0,\pi,\theta})$ on the lower envelope. Thus, for the final step, we need to prove that for another $\theta' \neq \theta$, the pair $(X_{\theta_1,\theta_3,\theta}, Y_{\theta_1,\theta_3,\theta})$ lies above the tangent at $(X_{0,\pi,\theta'}, Y_{0,\pi,\theta'})$. The condition is equivalent to

$$\alpha_{\theta'} X_{\theta_1,\theta_3,\theta} + \beta_{\theta'} Y_{\theta_1,\theta_3,\theta} \geq 1. \tag{4.82}$$

Notice that because of the condition of angular coordinates (4.41) the range of θ_1 and θ_3 are related to θ, but θ' should be chosen independently of θ_1 and θ_3 since we need it to parametrize the whole of the lower envelope.

The procedure to prove (4.82) can be divided by two steps.

In the first step (Step 1) we find a specific $\tilde{\theta}$ such that $\alpha_{\theta'} \geq \alpha(\theta_1, \tilde{\theta})$ and $\beta_{\theta'} \geq \beta(\theta_3, \tilde{\theta})$. This step can be viewed as a movement from a point on the lower envelope (the set of 3 blue curves in Figure 4.8) to a point on another curve (the red curve in Figure 4.8) on which the point $(X_{\theta_1,\theta_3,\theta}, Y_{\theta_1,\theta_3,\theta})$ lies.

In the next step (Step 2) we make a use of a log-sum and sum-log inequality to prove

that

$$\alpha(\theta_1, \tilde{\theta}) X_{\theta_1,\theta_3,\theta} + \beta(\theta_3, \tilde{\theta}) Y_{\theta_1,\theta_3,\theta} \geq 1. \tag{4.83}$$

First let us explain Step 1. For an arbitrary value of θ' with $0 < \theta' < \pi$, there are three possible cases for the sets $(\theta', \theta_1, \theta_3)$. The three cases are illustrated in Figure 4.8: they can be understood as corresponding to the lower envelope being split into three parts: the three blue curve segments sitting on the lower envelope in Figure 4.8 as shown in top, middle, and bottom of this Figure. These will be called cases 1, 2a and 2b, respectively. The red solid curve on each Figure 4.8 is drawn by changing θ from $|\theta_1|$ to $\pi - |\pi - \theta_3|$ while θ_1 and θ_3 are fixed. The range of θ comes from the condition of angular coordinates (4.41). The reason for the separation into three cases is that when $\theta' < |\theta_1|$ or $\pi - |\pi - \theta_3| < \theta'$, an auxiliary point $(X_{\theta_1,\theta_3,\theta'}, Y_{\theta_1,\theta_3,\theta'})$ does not lie on the red curve. Based on the argument above, we therefore assign a value $\tilde{\theta}$ to a value of θ' according to the following three conditions:

- Case 1: When $|\theta_1| \leq \theta' \leq \pi - |\pi - \theta_3|$, which means that the point $(X_{\theta'}, Y_{\theta'})$ marked as "+" in the top right of Figure 4.8 lies on the blue solid curve shown there, an auxiliary point $(X_{\theta_1,\theta_3,\theta'}, Y_{\theta_1,\theta_3,\theta'})$ also lies on the red curve marked as "x". From the behavior of $g_{\theta'}(\eta)$, we can see that $\alpha_{\theta'} \geq \alpha(\theta_1, \theta')$ and $\beta_{\theta'} \geq \beta(\theta_3, \theta')$. In this case, we choose $\tilde{\theta} = \theta'$.

- Case 2a: When $\theta' < |\theta_1|$ as shown in the middle of Figure 4.8, an auxiliary point $(X_{\theta_1,\theta_3,\theta'}, Y_{\theta_1,\theta_3,\theta'})$ does not lie on the red curve. In this case, the end point of the red curve is chosen, that is, we make the choice $\tilde{\theta} = |\theta_1|$. From the behavior of $g_\theta(\eta)$, it is apparent that $\alpha_{\theta'} \geq \alpha(\theta_1, |\theta_1|) = 1$. Because of the angular condition (4.41) such that $|\theta_1| < \theta_3 < 2\pi - |\theta_1|$ and because β_θ is a monotonically decreasing function with respect to θ for $0 < \theta < \pi$ (Appendix B), $\beta_{\theta'} > \beta_{|\theta_1|} = \beta(\pi, |\theta_1|) \geq \beta(\theta_3, |\theta_1|)$.

- Case 2b: This is the same as case 2a but refers to the other end of the red curve. When $\pi - |\pi - \theta_3| < \theta'$ as shown in the bottom of Figure 4.8, a point $(X_{\theta_1,\theta_3,\theta'}, Y_{\theta_1,\theta_3,\theta'})$ does not lie on the red curve (cf: Case 2a). In this case, the opposite boundary point of the red curve is chosen, which means that we choose $\tilde{\theta} = \pi - |\pi - \theta_3|$. From the behavior of $g_\theta(\eta)$, it is apparent that $\beta_{\theta'} \geq \beta(\theta_3, \pi - |\pi - \theta_3|) = 1$. Because $\pi - |\pi - \theta_3| < \theta'$, $|\theta_1| < \pi - |\pi - \theta_3|$, and because α_θ is a monotonically increasing function with respect to θ for $0 < \theta < \pi$ (Appendix B), $\alpha_{\theta'} > \alpha_{\pi - |\pi - \theta_3|} \geq \alpha(\theta_1, \pi - |\pi - \theta_3|)$.

In any case, it is possible to find a specific $\tilde{\theta}$ such that $\alpha_{\theta'} \geq \alpha(\theta_1, \tilde{\theta})$ and $\beta_{\theta'} \geq \beta(\theta_3, \tilde{\theta})$.

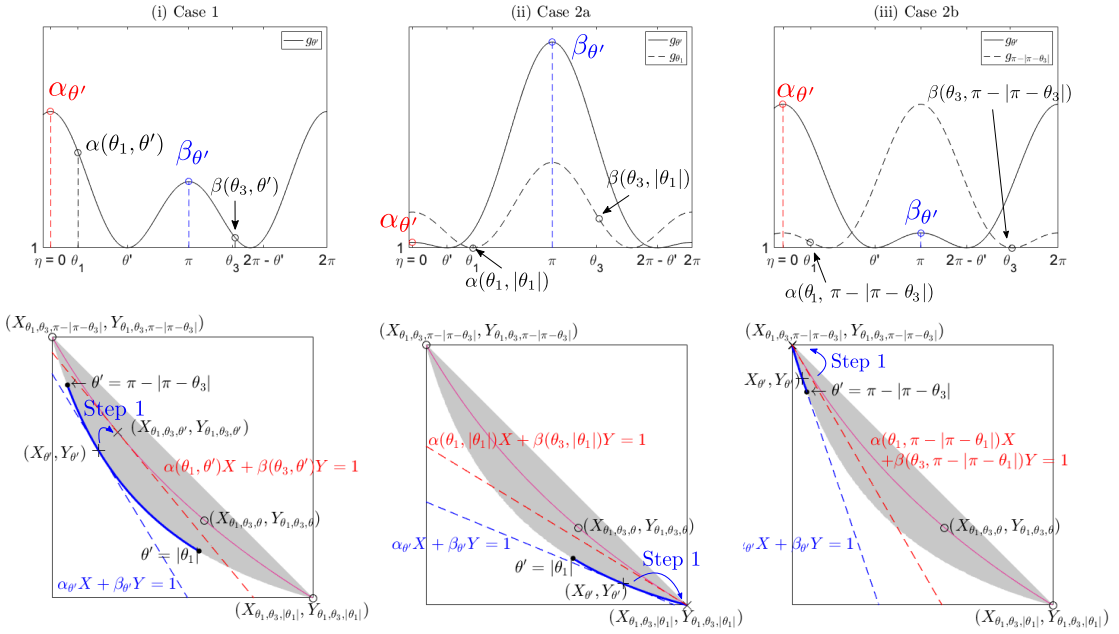

Figure 4.8: Three possible cases for pairs $(\theta', \theta_1, \theta_3)$. (i) Case 1: $\alpha_{\theta'} \geq \alpha(\theta_1, \theta')$ and $\beta_{\theta'} \geq \beta(\theta_3, \theta')$. (ii) Case 2a: Because $|\theta_1| > \theta'$, we choose $\tilde{\theta} = |\theta_1|$. We can see that $\alpha_{\theta'} \geq \alpha(\theta_1, |\theta_1|) = 1$ and $\beta_{\theta'} > \beta(\theta_3, |\theta_1|)$. (iii) Case 2b: Because $|\pi - \theta_3| > \pi - \theta'$, we choose $\tilde{\theta} = \pi - |\pi - \theta_3|$. We can see that $\alpha_{\theta'} \geq \alpha(\theta_1, \pi - |\pi - \theta_3|)$ and $\beta_{\theta'} > \beta(\theta_3, \pi - |\pi - \theta_3|) = 1$.

Thus, we obtain the important result that

$$\alpha_{\theta'} X_{\theta_1,\theta_3,\theta} + \beta_{\theta'} Y_{\theta_1,\theta_3,\theta} \geq \alpha(\theta_1, \tilde{\theta}) X_{\theta_1,\theta_3,\theta} + \beta(\theta_3, \tilde{\theta}) Y_{\theta_1,\theta_3,\theta}. \tag{4.84}$$

This facilitates Step 2 where we use a log-sum and sum-log inequality for the right hand side of (4.84) as follows:

$$\begin{aligned} &\log \left[\alpha(\theta_1, \tilde{\theta}) X_{\theta_1,\theta_3,\theta} + \beta(\theta_3, \tilde{\theta}) Y_{\theta_1,\theta_3,\theta} \right] \\ &= \log \left[\frac{1}{2\pi} \int_0^{2\pi} (A(\theta_1, \tilde{\theta}, \rho e^{\mathrm{i}\phi}) X_{\theta_1,\theta_3,\theta} + B(\theta_3, \tilde{\theta}, \rho e^{\mathrm{i}\phi}) Y_{\theta_1,\theta_3,\theta}) d\phi \right] \\ &\geq \frac{1}{2\pi} \int_0^{2\pi} \log \left[A(\theta_1, \tilde{\theta}, \rho e^{\mathrm{i}\phi}) X_{\theta_1,\theta_3,\theta} + B(\theta_3, \tilde{\theta}, \rho e^{\mathrm{i}\phi}) Y_{\theta_1,\theta_3,\theta} \right] d\phi. \end{aligned} \tag{4.85}$$

However the right hand side can be written

$$\begin{aligned}
&\frac{1}{2\pi}\int_0^{2\pi}\log\left[X_{\theta_1,\theta_3,\theta}+\frac{B(\theta_3,\tilde{\theta},\rho e^{\mathrm{i}\phi})}{A(\theta_1,\tilde{\theta},\rho e^{\mathrm{i}\phi})}Y_{\theta_1,\theta_3,\theta}\right]d\phi+\frac{1}{2\pi}\int_0^{2\pi}\log A(\theta_1,\tilde{\theta},\rho e^{\mathrm{i}\phi})d\phi\\
&=\frac{1}{2\pi}\int_0^{2\pi}\log\left[X_{\theta_1,\theta_3,\theta}+\frac{B(\theta_3,\theta,\rho e^{\mathrm{i}\phi})}{A(\theta_1,\theta,\rho e^{\mathrm{i}\phi})}Y_{\theta_1,\theta_3,\theta}\right]d\phi+\frac{1}{2\pi}\int_0^{2\pi}\log A(\theta_1,\theta,\rho e^{\mathrm{i}\phi})d\phi\\
&=\frac{1}{2\pi}\int_0^{2\pi}\log\Big[A(\theta_1,\theta,\rho e^{\mathrm{i}\phi})X_{\theta_1,\theta_3,\theta}+B(\theta_3,\theta,\rho e^{\mathrm{i}\phi})Y_{\theta_1,\theta_3,\theta}\Big]d\phi=0,
\end{aligned}\tag{4.86}$$

where we used the fact that the integral of $\log A(\theta_1,\theta,\rho e^{\mathrm{i}\phi})$ is

$$\begin{aligned}
&\frac{1}{2\pi}\int_0^{2\pi}\log A(\theta_1,\theta,\rho e^{\mathrm{i}\phi})d\phi=\frac{1}{2\pi}\int_0^{2\pi}\log\left(\frac{P(\rho e^{\mathrm{i}(\phi-\theta_1)})P(\rho e^{\mathrm{i}(\phi+\theta_1)})}{P(\rho e^{\mathrm{i}(\phi-\theta)})P(\rho e^{\mathrm{i}(\phi+\theta)})}\right)d\phi\\
&=\frac{1}{2\pi}\int_0^{2\pi}[\log P(\rho e^{\mathrm{i}(\phi-\theta_1)})+\log P(\rho e^{\mathrm{i}(\phi+\theta_1)})\\
&\qquad\qquad-\log P(\rho e^{\mathrm{i}(\phi-\theta)})-\log P(\rho e^{\mathrm{i}(\phi+\theta)})]d\phi=0
\end{aligned}\tag{4.87}$$

and the fact that

$$\frac{B(\theta_1,\tilde{\theta},\rho e^{\mathrm{i}\phi})}{A(\theta_3,\tilde{\theta},\rho e^{\mathrm{i}\phi})}=\frac{B(\theta_1,\theta,\rho e^{\mathrm{i}\phi})}{A(\theta_3,\theta,\rho e^{\mathrm{i}\phi})}=\frac{P(\rho e^{\mathrm{i}(\phi-\theta_3)})P(\rho e^{\mathrm{i}(\phi+\theta_3)})}{P(\rho e^{\mathrm{i}(\phi-\theta_1)})P(\rho e^{\mathrm{i}(\phi+\theta_1)})}\tag{4.88}$$

is independent of θ and $\tilde{\theta}$. In the last line, we have used the Fay trisecant identity (4.42). Putting all this together it has been shown that

$$\log\Big[\alpha(\theta_1,\tilde{\theta})X_{\theta_1,\theta_3,\theta}+\beta(\theta_3,\tilde{\theta})Y_{\theta_1,\theta_3,\theta}\Big]\geq 0.\tag{4.89}$$

From (4.89) it follows that

$$\alpha_{\theta'}X_{\theta_1,\theta_3,\theta}+\beta_{\theta'}Y_{\theta_1,\theta_3,\theta}\geq 1,\tag{4.90}$$

which means for $0<\theta<\pi$, $\alpha_\theta X+\beta_\theta Y\geq 1$ for all (X,Y). We have proved all the conjectured features of the envelope structure observed by previous authors.

To finish, we summarize what was done in steps 1 and 2 geometrically using Figure 4.8. In step 1 we found a choice of an auxiliary tangent line (the red line) to the pink curve on which $(X_{\theta_1,\theta_3,\theta},Y_{\theta_1,\theta_3,\theta})$ sits (and which corresponds to fixed θ_1 and θ_3) which is above the tangential line on the lower envelope (the blue line) for the three segments of the lower envelope into which it naturally divides for any fixed θ_1 and θ_3 (i.e., cases 1, 2a and 2b). In step 2 the point $(X_{\theta_1,\theta_3,\theta},Y_{\theta_1,\theta_3,\theta})$ is then shown to be above that red tangent line by using the log-sum and sum-log inequalities. We thus prove that $(X_{\theta_1,\theta_3,\theta},Y_{\theta_1,\theta_3,\theta})$ is above any point on the lower envelope.

4.6 Lower envelope formula

In the previous section we have proved that (X, Y) is always on the crescent-shaped domain and lies on the lower envelope when the contacts (a, b, z, w) have the symmetry. We will use these properties to obtain new formulas for the resistivity λ.

Here two explicit formulas for the lower envelope are derived. First, the following explicit formula for the lower envelope is derived:

$$\int_0^{2\pi} \log\left(\exp\left(-\frac{R_X^\theta}{\lambda}\right) + \frac{P(-\rho e^{\mathrm{i}\phi})^2}{P(+\rho e^{\mathrm{i}\phi})^2}\exp\left(-\frac{R_Y^\theta}{\lambda}\right)\right) d\phi = 0, \tag{4.91}$$

where R_X^θ and R_Y^θ form a pair of resistance measurements corresponding to contact points (a, b, z, w) with the symmetry depicted in Figure 4.3 and parametrized by the angle θ shown there; for a fixed ρ and λ, formula (4.91) therefore defines a curve as θ varies between 0 and π and this is precisely the lower envelope. The formula (4.91) for the lower envelope follows from (4.86) on setting $\theta_1 = 0, \theta_3 = \pi$:

$$\begin{aligned}&\frac{1}{2\pi}\int_0^{2\pi} \log\left[X_{0,\pi,\theta} + \frac{B(\pi,\theta,\rho e^{\mathrm{i}\phi})}{A(0,\theta,\rho e^{\mathrm{i}\phi})}Y_{0,\pi,\theta}\right] d\phi \\ &= \frac{1}{2\pi}\int_0^{2\pi} \log\left[A(0,\theta,\rho e^{\mathrm{i}\phi})X_{0,\pi,\theta} + B(\pi,\theta,\rho e^{\mathrm{i}\phi})Y_{0,\pi,\theta}\right] d\phi = 0.\end{aligned} \tag{4.92}$$

Using the definitions in (4.43)–(4.44), and with $X_{0,\pi,\theta} = \exp(-R_X^\theta/\lambda)$, and $Y_{0,\pi,\theta} = \exp(-R_Y^\theta/\lambda)$, we obtain (4.91).

Another formula for the lower envelope is derived by the approximation of small $\rho \ll 1$. An approximation of small $\rho \ll 1$ can be used to provide a more explicit expression of van der Pauw type relating the measured resistances. The values $X_{0,\pi,\theta}$ and $Y_{0,\pi,\theta}$ are written down explicitly as

$$X_{0,\pi,\theta} = \frac{P(-e^{\mathrm{i}\theta})P(-e^{-\mathrm{i}\theta})}{P(-1)P(-1)} \sim \frac{(1+\cos\theta)(1+4\rho^2\cos\theta)}{2(1+4\rho^2)}, \tag{4.93}$$

$$Y_{0,\pi,\theta} = \frac{P(e^{\mathrm{i}\theta})P(e^{-\mathrm{i}\theta})}{P(-1)P(-1)} \sim \frac{(1-\cos\theta)(1-4\rho^2\cos\theta)}{2(1+4\rho^2)}, \tag{4.94}$$

where we used the first order approximation in ρ^2:

$$P(\zeta) = (1-\zeta)(1-\rho^2\zeta)(1-\rho^2\zeta^{-1})\cdots \tag{4.95}$$

$$\sim (1-\zeta)(1-\rho^2(\zeta+\zeta^{-1})) + \mathcal{O}(\rho^4). \tag{4.96}$$

We can calculate

$$(1-4\rho^2)(X_{0,\pi,\theta}+Y_{0,\pi,\theta})^2+32\rho^2X_{0,\pi,\theta}Y_{0,\pi,\theta}=\frac{(1-4\rho^2)(1+4\rho^2\cos^2\theta)^2+8\rho^2\sin^2\theta}{(1+4\rho^2)^2}$$
$$=\frac{1}{1+4\rho^2}+\mathcal{O}(\rho^4)=1-4\rho^2+\mathcal{O}(\rho^4).$$

Note that $X_{0,\pi,\theta}=\exp(-R_X^\theta/\lambda)$ and $Y_{0,\pi,\theta}=\exp(-R_Y^\theta/\lambda)$. By expanding in powers of ρ^2 and eliminating terms of order ρ^4 and higher, an approximation for the lower envelope is obtained as follows:

$$\left(\exp\left(-\frac{R_X^\theta}{\lambda}\right)+\exp\left(-\frac{R_Y^\theta}{\lambda}\right)\right)^2+\frac{32\rho^2}{1-4\rho^2}\exp\left(-\frac{R_X^\theta+R_Y^\theta}{\lambda}\right)=1. \tag{4.97}$$

Equation (4.97) includes two unknown parameters ρ and λ but ρ can be eliminated explicitly by considering the ratio of the first term and the second term in (4.97). We then obtain the approximate formula for λ:

$$\exp\left(\frac{R_X^{\theta_1}-R_Y^{\theta_1}}{\lambda}\right)+\exp\left(\frac{R_Y^{\theta_1}-R_X^{\theta_1}}{\lambda}\right)-\exp\left(\frac{R_X^{\theta_1}+R_Y^{\theta_1}}{\lambda}\right)=$$
$$\exp\left(\frac{R_X^{\theta_2}-R_Y^{\theta_2}}{\lambda}\right)+\exp\left(\frac{R_Y^{\theta_2}-R_X^{\theta_2}}{\lambda}\right)-\exp\left(\frac{R_X^{\theta_2}+R_Y^{\theta_2}}{\lambda}\right). \tag{4.98}$$

The significance of equation (4.98) is that it more closely resembles the classical van der Pauw equation (4.1) since it depends only on λ and the resistance measurements although, in this case, there are 4 such measurements involved not just 2. The important point is that dependence on the parameter ρ has disappeared in (4.98). An approximation for the resistivity λ can be calculated by solving the single equation (4.98) provided data from the two pairs of resistances $(R_X^{\theta_j}, R_Y^{\theta_j})$, $j=1,\ 2$ is available. Formula (4.98) also appears to be new.

Roughly speaking, one would expect this formula to give good results for a sample with relatively small holes located away from the sample boundaries since then one might expect ρ to be small. In any event, (4.98) provides a useful first approximation for any sample with a single hole and will certainly be more accurate than use of (4.1).

Figure 4.9 shows the comparison between the actual lower envelope (4.91) and the asymptotic expansion (4.97) as the conformal modulus ρ varies. These graphs show that the asymptotic expansion yields a very satisfactory approximation for the lower envelope when $\rho<0.3$ and it remains quite accurate for larger ρ.

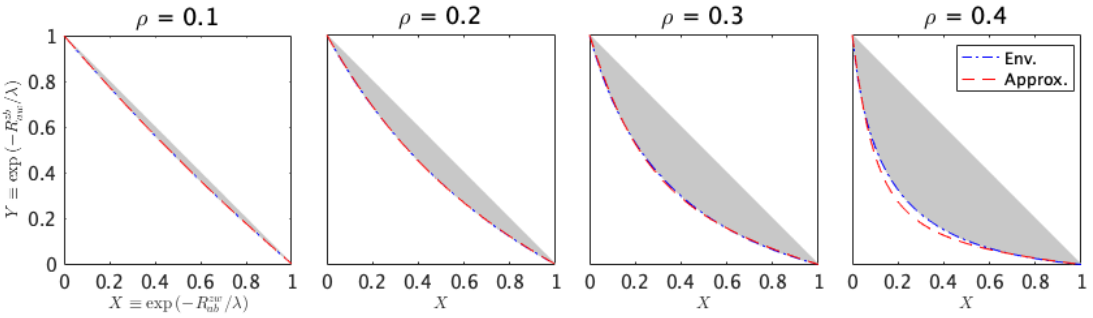

Figure 4.9: The approximation (4.97) of the lower envelope is superposed on data from numerical experiments for different values of ρ. The exact formula (4.91) lies precisely on the lower envelope formed by the data. For small ρ the lower envelope is well approximated by a quadratic in X and Y.

4.7 Determining the resistivity using the lower envelope equation

A method to obtain λ based on the lower envelope has already been proposed in [138]. Because the resistance $(R^{zw}_{ab}, R^{zb}_{aw})$ from the symmetric points shown in Figure 4.3 can be parametrized by the angle θ the corresponding resistances can be denoted by the parameter θ as follows:

$$R^{\theta}_{X} \equiv R^{\hat{z}\hat{w}}_{\hat{a}\hat{b}}, \qquad R^{\theta}_{Y} \equiv R^{\hat{z}\hat{b}}_{\hat{a}\hat{w}}, \tag{4.99}$$

where $\hat{z} = 1 = -\hat{a}$, $\hat{w} = \exp(\mathrm{i}\theta) = -\hat{b}$, $0 < \theta < \pi$. The chapter [138] proposed to measure several resistivities on the lower envelope and conducted a standard fit to obtain λ.

If the given sample has clear reflectional symmetries about two perpendicular axes, it is an easy matter to find resistances within the class (4.99) associated with symmetrically-disposed points in the preimage domain as shown in Figure 4.3. This is because one expects to be able to identify reflectionally symmetric points in the physical domain with reflectionally symmetric preimage points in the annulus.

However, for a generally non-symmetric sample it is not obvious how one might obtain this resistance information for such symmetrically-disposed points in the preimage domain. If one knows the conformal mapping to the given doubly connected sample from a preimage annulus then the contact points corresponding to such symmetric preimage points can be determined in principle. However, one of the advantages of the traditional van der Pauw method is that it exploits the underlying conformal invariance of the problem; this manifests itself in a practical way by formula (4.1) being valid for *any* shapes and, in particular, without the need to determine any conformal mapping functions. Ideally, any practical method for a holey sample should also avoid the need to compute any conformal

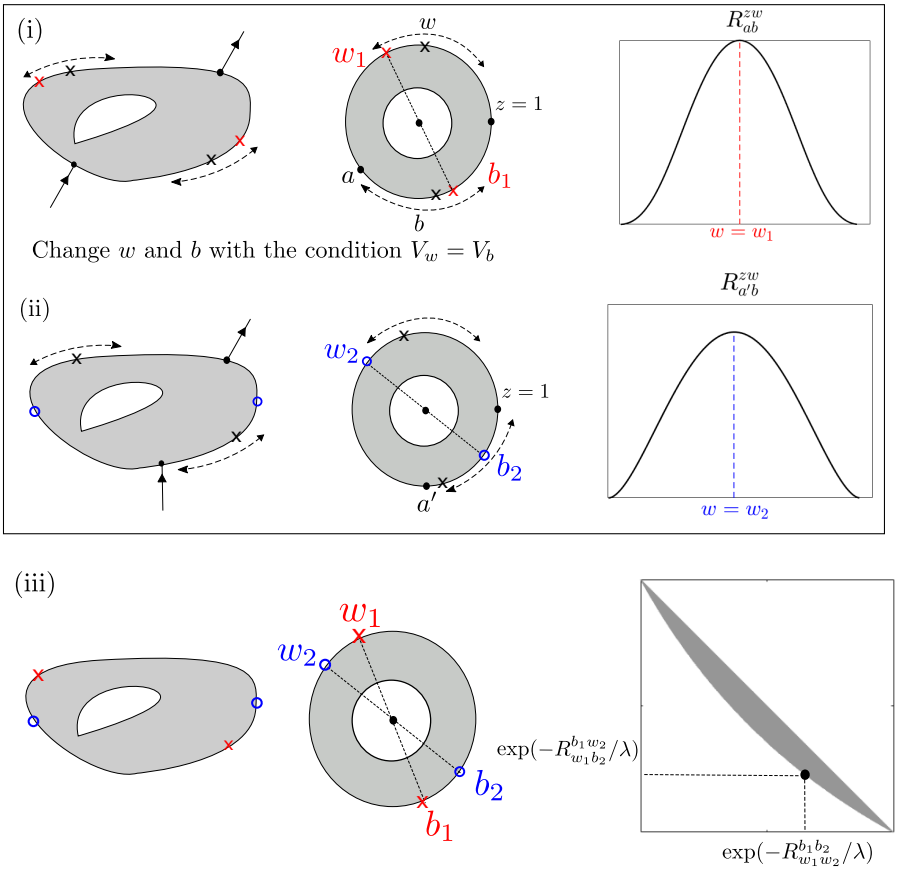

Figure 4.10: (i), (ii) Illustration of the practical procedure proposed in [138] to obtain contact points w_1, b_1, w_2, b_2 with the symmetry shown in Figure 4.3. By searching for the local extrema of R^{zw}_{ab} a symmetrical choice of points shown in (iii) and corresponding to resistances lying on the lower envelope can be found.

mappings.

A practical method has been proposed in [138] based on searching for the extrema of the resistance measurements. That procedure is as follows: firstly, as shown in (i) in Figure 4.10, arbitrary points are chosen on the sample boundary with preimage points z and a with a source placed at z and a sink at a. Then, by changing the two contact points with preimages w and b, with the condition that the potential at w remains the same as the potential at b, the local extremum of the measured resistance R^{zw}_{ab} is found. When the resistance R^{zw}_{ab} is at the local extremum, the claim in [138] is that the line wb become diametrically opposed points in the preimage annulus; this special choice of points are then marked as w_1 and b_1. In a second step, as shown in (ii) in Figure 4.10, the point a is changed to a', and the same procedure as in (i) is repeated in order to obtain a second such diametrically-opposed pair w_2 and b_2. It is then clear from (iii) in Figure 4.10 that the four-point pair (w_1, w_2, b_1, b_2) has the sought-after symmetry shown in Figure 4.3 and

which, therefore, correspond to resistance measurements that lie on the lower envelope.

Szymański et al. [138] verified experimentally that this method works, but appeared not to give any mathematical explanation of *why* it works. We now provide such an explanation.

When there are a source a and sink z as shown in (i) in Figure 4.10, the potential difference between w and b is

$$V_{wb} \equiv V_w - V_b = \lambda J_{az} \log \frac{P(w/a)P(b/z)}{P(w/z)P(b/a)}. \tag{4.100}$$

Suppose we search for a local extremum of R_{ab}^{zw} while changing w and b with the condition that $V_{wb} = 0$. This problem is expressed mathematically using a Lagrange multiplier γ:

$$F(w,b) \equiv \frac{1}{\lambda}(R_{ab}^{zw} + \gamma V_{wb}) = \log \frac{P(z/a)P(w/b)}{P(z/b)P(w/a)} + \hat{\gamma} \log \frac{P(w/a)P(b/z)}{P(w/z)P(b/a)}, \tag{4.101}$$

where $\hat{\gamma} \equiv \gamma / J_{az}$. By considering the derivative with respect to w and b, we obtain two conditions for local extrema:

$$\frac{\partial F}{\partial w} = \frac{1}{w}[K(w/b) - K(w/a) + \hat{\gamma}(K(w/a) - K(w/z))] = 0, \tag{4.102}$$

$$\frac{\partial F}{\partial b} = \frac{1}{b}[K(z/b) - K(w/b) + \hat{\gamma}(K(b/z) - K(b/a))] = 0. \tag{4.103}$$

It can be verified that both conditions are satisfied when $w = -b$ and $a/w = w/z$, which correspond to the symmetric choice of contact points. This explains why the practical procedure just described does indeed pick out points with diametrically-opposed preimages w and b in the annulus.

In view of the above discussion we now proceed under the assumption that two pairs of resistances $(R_X^{\theta_j}, R_Y^{\theta_j})$, $j = 1,\ 2$, for two sets of contact points in the symmetric arrangement shown in Figure 4.3 are available. The method proposed here is to make use of the two explicit formulas (4.91) and (4.98) to determine the resistivity λ.

Some simple numerical experiments validate that the resistivity λ can indeed be robustly found using the new expressions (4.91) and (4.98) for the lower envelope. We set $\lambda = 0.25$ and then used the explicit formulas for the voltage based on (4.17) to generate the "data" giving the resistances corresponding to two four-point pairs in symmetric configurations around C_0; in a real experiment, this data would be found by measurement on the physical sample such as those just described. Those values are used both in (two instances of) formula (4.91) and in the single approximate formula (4.98) and a standard nonlinear solver (interior-point method) is used to solve them for λ. Table 4.1 show the values of λ and ρ. As expected, the methods retrieve the known results to the expected degrees of accuracy.

Table 4.1: Numerical determination of λ and ρ on solving (4.91) and (4.98)

λ	(i)	(ii)	(iii)
Env. method	0.25000	0.25000	0.25000
Approx. method	0.25061	0.25705	0.27608
True value	0.25	0.25	0.25
ρ	(i)	(ii)	(iii)
Env. method	0.100001	0.20000	0.30000
Approx. method	0.097726	0.18445	0.25401
True value	0.1	0.2	0.3

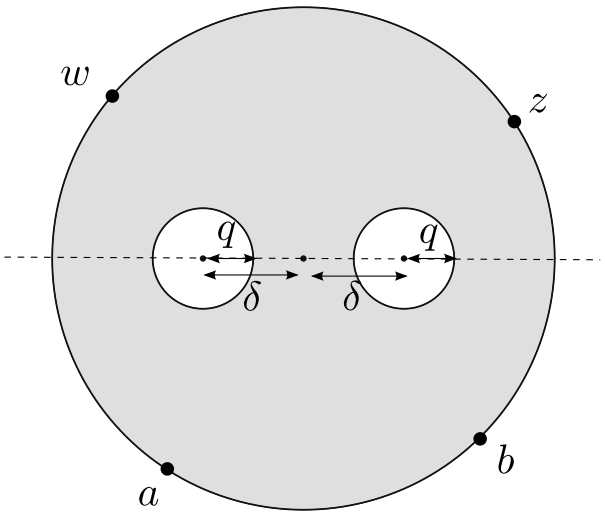

Figure 4.11: The van der Pauw setup for triply connected domains which has symmetries on real and imaginary axes. The contact points (a, b, z, w) lie on the boundary of the unit disc.

4.8 Van der Pauw method for triply connected domains

Here we propose a new van der Pauw formula for multiply connected domains and give some numerical experiments of resistances in triply connected domains. This can be done by considering the complex potential of multiply connected domains with a source and a sink using the prime function.

Let D_ζ be a multiply connected domain consisting of the unit disc with M, $M \geq 1$, be inner circles separated from each other. Let C_0 be the boundary of the unit circle and C_j, $j = 1, \ldots, M$ be the boundaries of circular discs with centres $\{\delta_j \in \mathbb{C} | j = 1, \ldots, M\}$, and radii $\{q_j \in \mathbb{C} | j = 1, \ldots, M\}$. According to [40], the prime function is expressed by

multidimensional theta functions as follows:

$$\omega(z,a)=\frac{\theta(\boldsymbol{v}(z,a);\tau)}{\sqrt{\sum_{j=1}^{M}b_kv_k'(z)}\sqrt{\sum_{j=1}^{M}b_kv_k'(a)}}, \tag{4.104}$$

where the row vector $\boldsymbol{v}(z,a)$ is defined by $\boldsymbol{v}(z,a)\equiv(v_1(z)-v_1(a),\ldots,v_M(z)-v_M(a))\in\mathbb{C}^M$, and b_k, $k=1,\ldots,M$ are complex constants. Note that v_k, $k=1,\ldots,M$ are the functions defined in Chapter 2. The multidimentional theta function is given by

$$\theta(\boldsymbol{v};\tau)\equiv\sum_{\boldsymbol{m}\in\mathbb{Z}^M}\exp\left[\pi\mathrm{i}(\boldsymbol{m}+\boldsymbol{\delta})\tau(\boldsymbol{m}+\boldsymbol{\delta})^\top+2\pi\mathrm{i}(\boldsymbol{v}+\boldsymbol{\epsilon})(\boldsymbol{m}+\boldsymbol{\delta})^\top\right], \tag{4.105}$$

where $\boldsymbol{\delta},\boldsymbol{\epsilon}\in\mathbb{R}^M$ are M-dimensional vectors defined by

$$\boldsymbol{\delta}=\left(\frac{1}{2},\underbrace{0,\ldots,0}_{M-1}\right),\quad \boldsymbol{\epsilon}=\left(\frac{1}{2},\ldots,\frac{1}{2}\right), \tag{4.106}$$

and the matrix components of $\tau\in\mathbb{C}^{M\times M}$ are defined by the functional property:

$$v_k(\theta_j(z))-v_k(z)=\tau_{jk}. \tag{4.107}$$

Because of the property above, the following important property is derived:

$$\boldsymbol{v}(\theta_j(z),a)=\boldsymbol{v}(z,a)+\boldsymbol{e}_j\tau. \tag{4.108}$$

For complex parameters $a,b,z,w\in\mathbb{C}$, Fay's trisecant identity for genus M is written using the multidimensional theta function as follows [57]:

$$\begin{aligned}\theta(\boldsymbol{k}+\boldsymbol{v}(z,w))\theta(\boldsymbol{k}+\boldsymbol{v}(a,b))p(z,w;b,a)+\theta(\boldsymbol{k}+\boldsymbol{v}(z,b))\theta(\boldsymbol{k}+\boldsymbol{v}(a,w))p(z,b;w,a)\\ =\theta(\boldsymbol{k})\theta(\boldsymbol{k}+\boldsymbol{v}(z,w)+\boldsymbol{v}(a,b)),\end{aligned} \tag{4.109}$$

where

$$p(z,w;b,a)\equiv\frac{\omega(z,b)\omega(w,a)}{\omega(z,a)\omega(w,b)},\qquad p(z,b;w,a)\equiv\frac{\omega(z,w)\omega(b,a)}{\omega(z,a)\omega(b,w)}. \tag{4.110}$$

Therefore, the van der Pauw equation for multiply connected domains is given by

$$\frac{\theta(\boldsymbol{k}+\boldsymbol{v}(z,w))\theta(\boldsymbol{k}+\boldsymbol{v}(a,b))}{\theta(\boldsymbol{k})\theta(\boldsymbol{k}+\boldsymbol{v}(z,w)+\boldsymbol{v}(a,b))}\exp\left(-\frac{R_{ab}^{zw}}{\lambda}\right)+\frac{\theta(\boldsymbol{k}+\boldsymbol{v}(z,b))\theta(\boldsymbol{k}+\boldsymbol{v}(a,w))}{\theta(\boldsymbol{k})\theta(\boldsymbol{k}+\boldsymbol{v}(z,w)+\boldsymbol{v}(a,b))}\exp\left(-\frac{R_{aw}^{zb}}{\lambda}\right)=1. \tag{4.111}$$

It is important to note that for doubly connected domains, $\boldsymbol{v}(z, a)$ is a simple logarithmic function, so we have $v(z, w) + v(a, b) = v(za, wb)$. By using this property, the van der Pauw equation for doubly connected domain (4.38) can be derived. However, for the triply connected domains, the relation is no longer satisfied, which means the van der Pauw equation for multiply connected domains is not reduced to the simple form. However, the same technique as the annular domain could be used to analyze the van der Pauw equation (4.111).

4.9 Summary

This chapter has introduced two new mathematical tools to this area of investigation – the prime function of a multiply connected domain and the Fay trisecant identity – and used them to show how the van der Pauw method can be extended to find the resistivity of a sample with a hole. We have shown that an integrated form of the Fay trisecant identity provides valuable information concerning the appearance of "envelopes" observed in the case of holey samples by previous authors. We find an explicit formula for the curves described by the envelopes, as well as a useful approximate formula relating two pairs of resistance measurements to the sample resistivity that is valid when the hole is sufficiently small. It is also described how these new mathematical tools have enabled us to prove certain conjectures recently made in the engineering literature.

We are also able to justify mathematically a practical procedure for obtaining such data for a general non-symmetric sample as proposed by Szymański et al. [138]. Those authors gave evidence that their practical construction does indeed produce such data, but did not give any mathematical justification as to why the method works.

The van der Pauw for triply connected domains or domains of higher genus will open a new perspective in both mathematics and engineering. It should be possible to analyze the van der Pauw equation (4.111) by the same technique as the annulus case.

Chapter 5

Capacity calculation by matched asymptotic expansions

In this chapter we solve another electrical transport problem to obtain the capacity of electrical circuits. New methods for deriving explicit estimates for electrical capacity in circuits with multiple boundaries are presented. This can be done by incorporating the prime function described in Chapter 2 with matched asymptotic expansions [150]. We present new explicit formulas that can be easily evaluated by using the github code [9] for the evaluation of the prime function.

5.1 Introduction

Electrical capacity is a fundamental property of materials or circuits that describes how much charge they can store. Accurate measurement of electrical capacity is essential; for example, the performance of two-dimensional interconnects in MOSFET VLSI circuits depends on their electrical capacity [55, 162]. The gate capacity of a MOS transistor also affects the delay time of a MOS gate [50], which determines the performance of electrical circuits.

Figure 5.1 shows typical circuits that include a ground plane and a metal plate with unit voltage. It is known that the coupling circuit has a fringing effect, which was suggested by Thomson [144]. Accurate evaluation of electrical capacity usually requires two or three dimensional calculations solving Laplace equations with Dirichlet conditions [127]. This type of calculation is sometimes time consuming due to the geometry of the circuits. The circuits usually have several plates and ground planes, which become multiply connected domains.

Electrical capacity has many connections with transport theory arising in engineering fields. A number of other physical applications are discussed in detail by Papamichael [114,

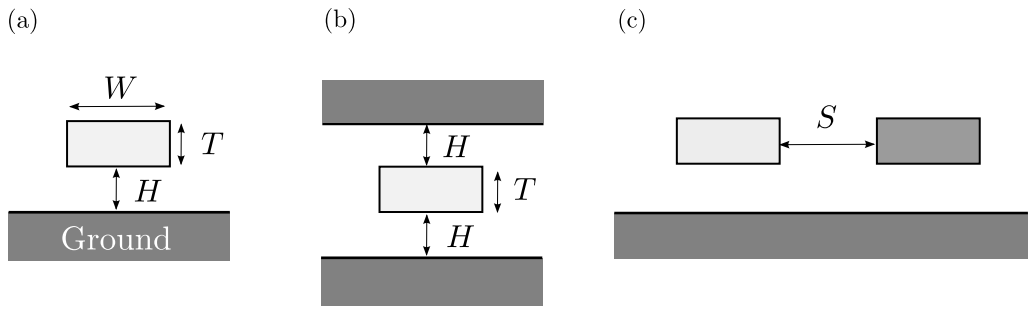

Figure 5.1: Examples of the electrical circuits. The white region is a wire and the black areas are ground.

115]. For example, the effective transport coefficients of materials can be calculated by obtaining the conformal modulus of holey materials [81]. Acker [2] studied the heat loss of a cylindrical pipe in order to obtain the appropriate shape of the outer boundary of the pipe which minimises the heat loss of the whole domain. The effective diffusion coefficients of diffusive material can be calculated by solving the 2D Laplace equation and integrating the flow along the flow domain [19]. These physical quantities have physical meaning in each field, but mathematically they can be related to the calculation of the electrical capacity of the domain.

There has been much research into obtaining explicit formulas for electrical capacity. Chang obtained the analytical formulas for IC metal-line capacity in case (a) and (b) in Figure 5.1 [25] using Schwarz-Christoffel mappings. Palmer used a Schwarz-Christoffel map to calculate the capacity of the parallel plate [113] and the result was verified by [26]. Sakurai and Tamaru [129] derived an empirical formula for calculating the capacity in case (b) in Figure 5.1.

Despite its many applications it is rare to find explicit formulas for electrical capacity. Because the voltage potential satisfies the 2D Laplace's equation with Dirichlet boundary conditions, a common tool for calculating capacity is conformal mappings. For very general polygonal or polycircular domains, including multiply connected cases, the general theory for the construction of such mappings has now been developed by Crowdy [29, 40, 43, 44]. On the other hand, one can use purely numerical approaches based on boundary integral formulations or their kin: for example, Nassar *et al.* used the generalized Neumann kernel to calculate the capacity of a doubly connected domain [105]. Baddoo and Trefethen recently proposed an algorithm to evaluate the capacity using rational function approximations [14]. Indeed, many different numerical schemes for the computation of conformal capacity have now been proposed [20, 63, 86].

The purpose of this chapter is to show how a quite different mathematical idea –

the theory of matched asymptotics [150] – can be used to great advantage in providing *estimates* of the capacity. Perhaps surprisingly, we have not seen this idea applied to the computation of capacity which is all the more remarkable because the estimates it provides are, as will be shown here, very accurate even well beyond the expected range of validity. While the idea may not be familiar in the literature on the computation of capacity, asymptotic analysis is a powerful tool in the applied sciences and its principal tenets are well known [68, 150]. Tuck [146] advocated its use in the calculation of so-called "blockage coefficients" characterizing the net effect of occlusions obstructing ideal flows in channels as well as the "effective size" of holes in a wall, and both concepts have much in common with conformal capacity. And, just as the notion of conformal capacity manifests itself in applications in many different guises, Crowdy [36] has shown how the idea of a blockage coefficient is analogous to the so-called hydrodynamic slip length used in surface engineering to quantify the frictional properties of superhydrophobic surfaces. In many ways, the present article adopts the spirit of Tuck's approach to estimates of blockage coefficients and effective size but now for the estimation of the electrical capacity.

5.2 The definition of electrical capacity and simple examples

In this section, the mathematical definition of the electrical capacity of the circuit in two dimension is presented. Let $\mathcal{G}$ be a domain whose boundary $\partial\mathcal{G}$ is grounded, and let E be a domain E in $\mathcal{G}$, where the unit voltage is induced on the boundary of E, define as ∂E. Note that $\mathcal{G}$ and E can have multiple boundaries, which means that the region $\mathcal{G}\backslash E$ becomes multiply connected domains. The voltage ϕ of the boundary of E is set as the unit voltage. A typical geometry is shown in Figure 5.2.

The 2D voltage potential ϕ then satisfies the following classical Dirichlet problem [3, 63]:

$$\nabla^2\phi(x,y) = 0, \qquad (x,y) \in \mathcal{G}\backslash E, \tag{5.1}$$

with the following boundary conditions

$$\begin{cases} \phi(x,y) = 0, & (x,y) \in \partial\mathcal{G}, \\ \phi(x,y) = 1, & (x,y) \in \partial E. \end{cases} \tag{5.2}$$

The electrical capacity is defined as the total current flowing in the domain $\mathcal{G}\backslash E$ as follows:

$$\mathrm{cap}(\mathcal{G}, E) \equiv \int_{\mathcal{G}\backslash E} |\nabla\phi|^2 dxdy = \int_{\partial E} \frac{\partial\phi}{\partial n} ds, \tag{5.3}$$

where $\partial/\partial n$ denotes the normal derivative outward to the boundary E. In the second

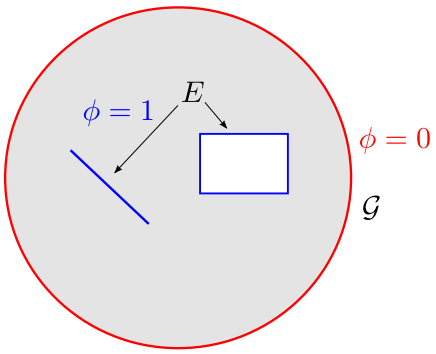

Figure 5.2: A typical domain for capacity calculation.

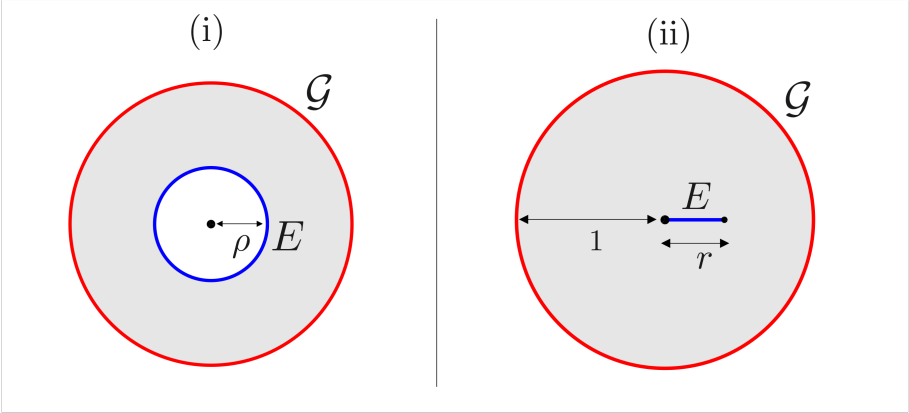

Figure 5.3: (i) Concentric annulus. (ii) A slit in the unit circle.

equality, we have used Gauss's divergence theorem and the fact that $\phi = 1$ on $(x, y) \in \partial E$.

An elementary example is where $\mathcal{G}$ is taken as the unit disc with centre at the origin and E is a concentric disc of radius ρ, $0 < \rho < 1$, as shown in (i) of Figure 5.3. The solution for the Dirichlet problem (5.1) in this geometry is found by introducing the complex potential $W(z)$, $\phi = \mathrm{Re}[W(z)]$, where the analytic function

$$W(z) = \frac{\log z}{\log \rho}, \qquad z \equiv x + \mathrm{i}y, \tag{5.4}$$

is called a complex potential for the problem. The capacity can then be calculated from (5.3) by using the Green's second identity [3, 63] with the result

$$\mathrm{cap}(\mathcal{G}, E) = \int_{\partial E} \frac{\partial \phi}{\partial n} ds = \frac{2\pi}{\log(1/\rho)}. \tag{5.5}$$

Since the capacity is conformally invariant, the calculation of capacity in doubly connected

domains (where ∂E forms an internal boundary component of a doubly connected domain) can be related to the problem of finding the conformal modulus ρ of the conformal mapping to the target annular domain from a canonical concentric annulus, $\rho < |\zeta| < 1$ say, with $|\zeta| = 1$ mapping to $\partial\mathcal{G}$ and $|\zeta| = \rho$ mapping to ∂E.

Another example where the capacity can be found in closed form is where $\mathcal{G}$ is the unit disc and E is the slit $\{(x, y)|x \in [0, r], y = 0, 0 < r < 1\}$, as shown in (ii) of Figure 5.3. This domain, called "Grötzsch ring", has broad application in the theory of conformal mappings, in physics, and in number theory [5]. The expression for the ring can be derived because the explicit conformal map from an annulus $\rho < |\zeta| < 1$ to this domain can be determined in closed form; see, for example, Exercise 5.16 of [40], or pp. 293 of [107].

The conformal map from the concentric annulus to the unit disc exterior to the slit $x \in [-r', r']$ is given by [40]

$$w(\zeta) = -\frac{P(\zeta, \rho) - P(-\zeta, \rho)}{P(\zeta, \rho) + P(-\zeta, \rho)}, \tag{5.6}$$

where the function $P(.,.)$ is the prime function [40] of the annulus introduced in Chapter 2 and

$$r' = w(\rho). \tag{5.7}$$

Because of the properties of $P(\zeta)$ explained in Chapter 2, it is easy to see that, when ζ lies on C_0, i.e., $\overline{\zeta} = \zeta^{-1}$,

$$\overline{w(\zeta)} = -\frac{\overline{P(\zeta, \rho)} - \overline{P(-\zeta, \rho)}}{\overline{P(\zeta, \rho)} + \overline{P(-\zeta, \rho)}} = -\frac{P(\zeta^{-1}, \rho) - P(-\zeta^{-1}, \rho)}{P(\zeta^{-1}, \rho) + P(-\zeta^{-1}, \rho)} \tag{5.8}$$

$$= -\frac{P(\zeta, \rho) + P(-\zeta, \rho)}{P(\zeta, \rho) - P(-\zeta, \rho)} = \frac{1}{w(\zeta)}. \tag{5.9}$$

Changing the slit region $x \in [-r', r']$ to a different slit $x \in [0, r]$, without changing the unit circle, just requires an automorphism of the unit disc:

$$z(w) = \frac{w + r'}{r'w + 1}. \tag{5.10}$$

Combining these two conformal maps gives the formula for the capacity implicitly as follows:

$$\mathrm{cap}(\mathcal{G}, E) = \frac{2\pi}{\log(1/\rho)}, \qquad r = \frac{P(-\rho, \rho)^2 - P(\rho, \rho)^2}{P(-\rho, \rho)^2 + P(\rho, \rho)^2}. \tag{5.11}$$

As shown in Chapter 4, the prime function of the concentric annulus can be represented by

elliptic functions, so that (5.11) can be related to an alternative expression (2.6) featured in [63]. To be more precise, the capacity of the Grötzsch ring is given by the complete elliptic integral of the first kind as follows: (see the equation (3.11) of [5])

$$\mathrm{cap}(\mathcal{G}, E) = \frac{2\pi}{\mu(r)}, \quad \mu(r) \equiv \frac{\pi}{2}\frac{K(\sqrt{1-r^2})}{K(r)}, \quad K(r) \equiv \int_0^{\pi/2} \frac{d\theta}{\sqrt{1-r^2\sin^2\theta}}, \tag{5.12}$$

and hence ρ in (5.11) has an explicit formula such that $\rho = \exp(-\mu(r))$.

These two examples, the annular region and the Grötzsch ring, are special cases because these capacities can be expressed in closed form. In general, however, the capacity in multiply connected domains cannot be obtained explicitly. The unit disc with a small lens-shaped inclusion is a simple example whose capacity is not available in closed form. In the next section we present a new method for obtaining an "estimate" of this capacity. This method gives us an analytical expression for the capacity, which can be easily evaluated using the prime function and is shown to be quite accurate.

5.3 The theory of matched asymptotic expansions for the capacity calculation

In this section, we will show how a quite different mathematical idea – the theory of matched asymptotics [150] – can be used to great advantage in providing *estimates* of capacity. This can be done by providing a simple capacity formula for one of the simplest non-trivial examples, i.e., the unit disc with a small lens-shaped inclusion as shown at the top of Figure 5.4. Based on the proposed method, estimates of the capacity for various geometries can be obtained in closed form.

Here we consider a small lens located at the center of a unit disc shown in Figure 5.4; this same geometry is featured in Figure 1 of [63]. Let the unit disc be denoted by $\mathcal{G}$ and denote the lens by E. The domain $\mathcal{G}\backslash E$ is a doubly connected polycircular-arc domain (defined as a domain with boundaries made up of a union of circular arcs) and the general theory exists – see [40, 43, 44] – to compute the capacity of this domain using conformal mapping from a canonical concentric annulus; that calculation, while relatively straightforward (indeed, it will be carried out later), still requires numerical integration of a differential equation. However, using the matching approach to be described next, an explicit formula estimating the required capacity can be obtained using more elementary, albeit still non-trivial, considerations.

The main assumption is that the lens is small compared to the unit circle and also well separated from it. Then, using an electric circuit analogy for concreteness, an "outer" observer viewing this set-up on the scale of the unit circle sees the small lens, set to unit

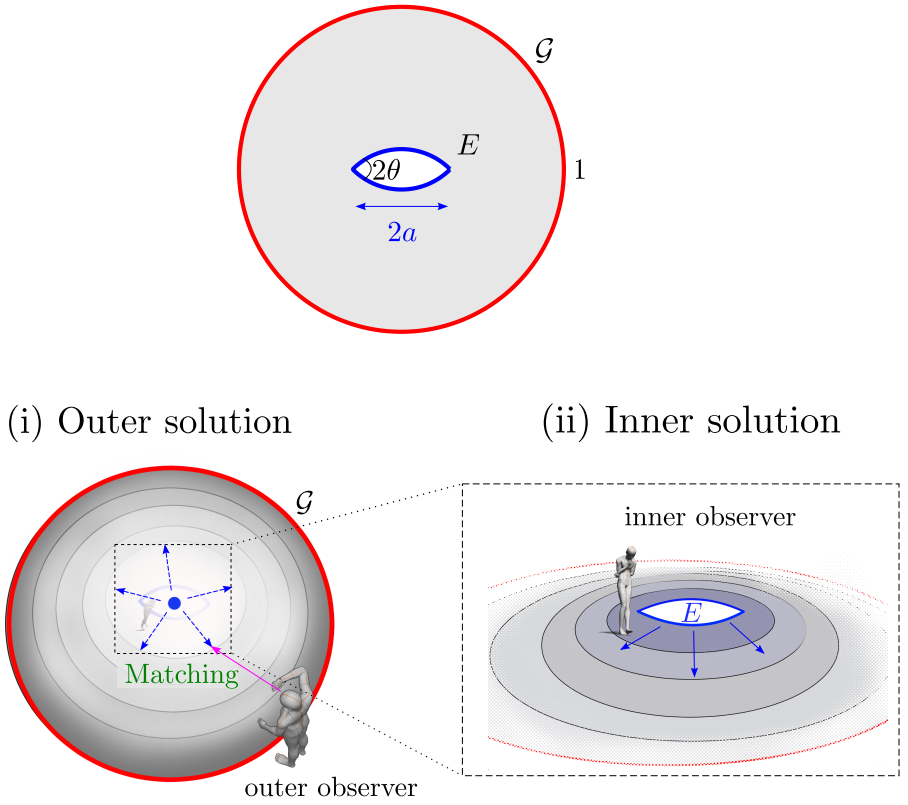

Figure 5.4: The idea of the matching approach. The capacity of a grounded unit disc with a small lens-shaped inclusion held at unit voltage can be estimated to great accuracy by viewing the problem at two different scales: an "outer" problem and an "inner" problem.

voltage, effectively as a point current source at the origin and of (as yet) unknown strength m. Resolution of the detailed geometry of the lens is not possible for this observer, as indicated in Figure 5.4 (i), and the corresponding complex potential for this outer observer is well approximated by

$$W_{\text{outer}}(z) = \frac{m}{2\pi} \log z, \tag{5.13}$$

where the real part of this analytic function is the voltage potential, ϕ say. This potential incorporates the condition that the outer boundary is grounded, $\phi = 0$ on $|z| = 1$. On the other hand, an "inner" observer viewing the same configuration at the smaller scale of the lens does not notice the grounded outer boundary in the far distance; this is indicated in Figure 5.4 (ii). Hence, for the inner observer, the boundary value problem for the voltage potential ϕ requires that $\phi = 1$ on ∂E with the total current out of the lens equal to m. The solution to this inner problem is more difficult to solve, but is readily done by utilizing

the conformal map from the unit disc in a complex ζ-plane to the outside of the lens with opening angle 2θ in the z-plane as determined in [35] as

$$\begin{aligned} z = f(\zeta) &= a\left[\frac{(1-\zeta)^{2(1-\theta/\pi)} + (1+\zeta)^{2(1-\theta/\pi)}}{(1-\zeta)^{2(1-\theta/\pi)} - (1+\zeta)^{2(1-\theta/\pi)}}\right], \\ \zeta = f^{-1}(z) &= \frac{(z/a-1)^{\pi/2(\pi-\theta)} - (z/a+1)^{\pi/2(\pi-\theta)}}{(z/a-1)^{\pi/2(\pi-\theta)} + (z/a+1)^{\pi/2(\pi-\theta)}}, \end{aligned} \tag{5.14}$$

where $2a$ is the width of the lens and, for the matching approach to work, we assume $a \ll 1$. Given that $\phi = 1$ on ∂E, the solution to the inner problem is

$$W_{\text{inner}}(z) = 1 - \frac{m}{2\pi}\log(-\zeta) = 1 - \frac{m}{2\pi}\log(-f^{-1}(z)). \tag{5.15}$$

A constant in this expression has been chosen to ensure that the imaginary part of $W_{\text{inner}}(z)$ is zero to the right of the meniscus. It should be emphasized that the outer solution incorporates information on the grounded nature of the outer boundary, while the inner solution encodes the fact that the inner boundary has been set to unit voltage. The idea now is to *match* the outer and inner solutions at an intermediate length scale at which their validity is assumed to overlap. Practically, this means that the limit of the inner solution as $z \to \infty$ must be made to "match" with the the outer solution as $z \to 0$. As $z \to \infty$,

$$\zeta = f^{-1}(z) \to -\frac{\pi a}{2(\pi-\theta)z} + \mathcal{O}(z^{-2}), \quad z \to \infty, \tag{5.16}$$

so that, in the same limit, the inner potential behaves as

$$W_{\text{inner}}(z) = 1 - \frac{m}{2\pi}\log\left(\frac{\pi a}{2(\pi-\theta)z} + \mathcal{O}(z^{-2})\right) \to \frac{m}{2\pi}\log z + 1 - \frac{m}{2\pi}\log\left(\frac{\pi a}{2(\pi-\theta)}\right) + ... \tag{5.17}$$

Notice first that (5.13) and (5.17) have the same leading order asymptotics. Furthermore, the "matching" of the constant terms in (5.13) and (5.17) determines a leading-order approximation to m via the relation

$$1 - \frac{m}{2\pi}\log\left(\frac{\pi a}{2(\pi-\theta)}\right) = 0. \tag{5.18}$$

The capacity of the domain is then approximated by

$$\text{cap}(\mathcal{G}, E) = \int_{\mathcal{G}\setminus E} |\nabla\phi|^2 dxdy = \int_{\partial E} \frac{\partial\phi}{\partial n} ds = -m \approx \frac{2\pi}{\log\left(\frac{2(\pi-\theta)}{\pi a}\right)}, \tag{5.19}$$

where $\partial/\partial n$ denotes the normal derivative outward to the boundary of E. This simple explicit formula is found to furnish an excellent approximation even when the size of the inner polycircular lens becomes large. Figure 5.7 shows a comparison of the estimates given by this formula and a calculation of the capacity based on construction of a doubly connected polycircular-arc conformal mapping to be described in the next section. The capacity for this example was also calculated using very different numerical methods in [63].

This simple example demonstrates the power of the matching approach in providing useful estimates of the capacity. These is useful, for example, in obtaining initial guesses for iterative procedures to find more precise values based on solution of a conformal mapping accessory parameter problem as described in Chapter 7. The remainder of this paper demonstrates, using a series of illustrative cases, the scope of these ideas.

5.4 Capacity calculation for doubly connected domains

The matching technique just described can also be applied to cases (A), (B), and (C) shown in Figure 5.5. The choice of domain $\mathcal{G}$ in cases (A) and (B) is an infinite channel with height $2H$. We also aim to validate the matching approach by comparing the capacity of the Grötzsch ring with the exact formula (5.11).

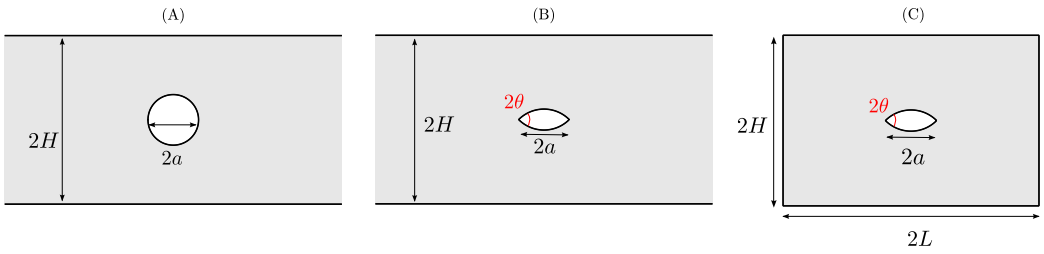

Figure 5.5: Three example geometries: (A) a circular disc in a channel: (B) a lens in a channel; (C) a lens in a rectangle.

Case (A): Circle in a channel

The geometry for a circle in a channel is illustrated in Figure 5.5 (A). First we assume that the parameter a characterizing the size of E is small compared to H so that the total flux out of the inner region can be seen as a total flux from a point source with strength m at the center of lens. The solution to the "outer problem" of a single point source of strength m in a channel with grounded walls can be found using elementary conformal mapping techniques [1]:

$$W_{\text{outer}}(z) = \frac{m}{2\pi} \log \tanh\left(\frac{\pi z}{4H}\right) = \frac{m}{2\pi} \log\left(\frac{\pi}{4H}\right) + \frac{m}{2\pi} \log z + \ldots, \tag{5.20}$$

where the Taylor expansion of the hyperbolic tangent is used to find the behaviour as $z \to 0$. Since E is a circular disc in this case, which is a special case of a lens, then the inner solution is still (5.15) but now with $z = f(\zeta) = -a/\zeta$:

$$W_{\text{inner}}(z) = 1 - \frac{m}{2\pi}\log(-\zeta) = 1 - \frac{m}{2\pi}\log(a/z) = \frac{m}{2\pi}\log z + \left(1 - \frac{m}{2\pi}\log a\right) + \dots \quad (5.21)$$

The matching of constants in the inner and outer solution gives

$$\frac{m}{2\pi}\log\frac{\pi}{4H} = 1 - \frac{m}{2\pi}\log a, \qquad \text{or} \qquad m = \frac{2\pi}{\log\left(\frac{\pi a}{4H}\right)}. \quad (5.22)$$

Hence, the capacity for case (A) is

$$\text{cap}(\mathcal{G}, E) = -m \approx \frac{2\pi}{\log\left(\frac{4H}{\pi a}\right)}. \quad (5.23)$$

Case (B): Lens in a channel

Case (A) is actually a special case of (B). For a general lens with opening angle θ, a combination of the inner solution (5.17) and the outer solution (5.20) gives the matching condition

$$\frac{m}{2\pi}\log\frac{\pi}{4H} = 1 - \frac{m}{2\pi}\log\left(\frac{\pi a}{2(\pi-\theta)}\right) \quad (5.24)$$

from which the capacity for case (B) is calculated as

$$\text{cap}(\mathcal{G}, E) = -m \approx \frac{2\pi}{\log\left(\frac{8H(1-\theta/\pi)}{\pi a}\right)}. \quad (5.25)$$

The result (5.23) for case (A) is retrieved when $\theta = \pi/2$.

Case (C): Lens in a rectangle

For case (C), only the outer solution needs to be modified. The relevant complex potential for the outer solution is that for a point source with strength m situated at the center of a rectangle with height $2H$ and width $2L$. It can be calculated using a simple exponential conformal mapping from the rectangle to a half annular region and the theory of the prime function associated with that annulus as described in [37, 40].

We explain how to derive the potentials of this problem. The potential is a solution which satisfies $\text{Re}[W_{\text{outer}}(z)] = 0$ on the boundary of rectangle with a source m at the center of the rectangle. By using the conformal map $\zeta = e^{-\pi(z+L+\mathrm{i}H)/2H}$, the rectangle

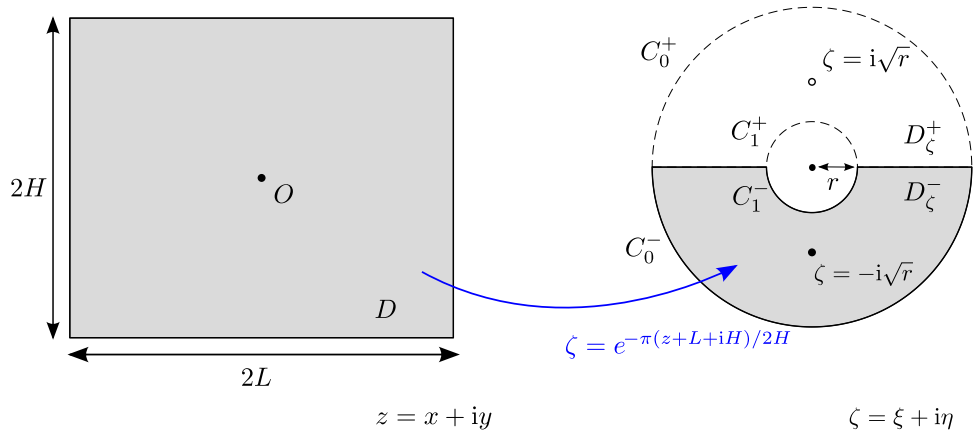

Figure 5.6: Geometry of the exponential maps $\zeta = e^{-\pi(z+L+\mathrm{i}H)/2H}$.

region is transformed into the lower half annular domain D_ζ^- with radius $r = e^{-\pi L/H}$. Figure 5.6 shows the rectangle and lower half annular domain. The location of the point source with strength m is now $\zeta = -\mathrm{i}\sqrt{r}$. The conformal invariance of the potential shows that the function $X(\zeta) \equiv W_{\text{outer}}(z(\zeta))$ has a simple source term with a strength m at $\zeta = -\mathrm{i}\sqrt{r}$ and satisfies

$$\begin{cases} \mathrm{Re}[X(\zeta)] = 0, & \zeta \in C_0^-,\ C_1^- \\ \mathrm{Re}[X(\zeta)] = 0, & r < |\xi| < 1, \quad \eta = 0. \end{cases} \tag{5.26}$$

On the real axis, i.e. $\overline{\zeta} = \zeta$, the second condition of (5.26) means $\overline{X(\zeta)} = \overline{X}(\zeta) = -X(\zeta)$. The use of Schwarz reflection principle shows that the function $X(\zeta)$ satisfies $\overline{X}(\zeta) \equiv \overline{X(\overline{\zeta})} = -X(\zeta)$ on D_ζ. This property indicates that $X(\zeta)$ has a sink at $\zeta = \mathrm{i}\sqrt{r}$. On $\zeta \in C_j^+$, $\overline{\zeta} \in C_j^-$ for $j = 1, 2$, so

$$\mathrm{Re}[X(\zeta)] = \frac{1}{2}(X(\zeta) + \overline{X(\zeta)}) = \frac{1}{2}(-\overline{X(\overline{\zeta})} - X(\overline{\zeta})) = -\mathrm{Re}[X(\overline{\zeta})] = 0, \quad \zeta \in C_j^+,\ j = 1, 2. \tag{5.27}$$

Thus, $X(\zeta)$ has a source at $\zeta = -\mathrm{i}\sqrt{r}$ and a sink at $\zeta = \mathrm{i}\sqrt{r}$ and satisfies

$$\mathrm{Re}[X(\zeta)] = 0, \qquad \zeta \in C_0,\ C_1. \tag{5.28}$$

Now we define

$$X(\zeta) = \frac{m}{2\pi} \log \left[\frac{P(-\mathrm{i}\sqrt{r}\zeta, r) P(-\zeta/(\mathrm{i}\sqrt{r}), r)}{P(\zeta/(\mathrm{i}\sqrt{r}), r) P(\mathrm{i}\sqrt{r}\zeta, r)} \right]. \tag{5.29}$$

Because $P(\zeta, r)$ has a simple zero at $\zeta = 1$, $X(\zeta)$ has a source $\zeta = -\mathrm{i}\sqrt{r}$ and a sink at $\zeta = \mathrm{i}\sqrt{r}$. On $\zeta \in C_0$, i.e., $\overline{\zeta} = \zeta^{-1}$, we have

$$\overline{X(\zeta)} = \frac{m}{2\pi} \log \left[\frac{P(\mathrm{i}\sqrt{r}\zeta^{-1}, r) P(\zeta^{-1}/(\mathrm{i}\sqrt{r}), r)}{P(-\zeta^{-1}/(\mathrm{i}\sqrt{r}), r) P(-\mathrm{i}\sqrt{r}\zeta^{-1}, r)} \right] \tag{5.30}$$

$$= \frac{m}{2\pi} \log \left[\frac{P(\zeta/(\mathrm{i}\sqrt{r}), r) P(\mathrm{i}\sqrt{r}\zeta, r)}{P(-\mathrm{i}\sqrt{r}\zeta, r) P(-\zeta/(\mathrm{i}\sqrt{r}), r)} \right] = -X(\zeta), \tag{5.31}$$

where we used the properties of the prime function (2.12) and (2.13). Hence, $\mathrm{Re}[X(\zeta)] = 0$ on $\zeta \in C_0$. It is also easy to check that $\mathrm{Re}[X(\zeta)] = 0$ on C_1 and $\overline{X}(\zeta) = -X(\zeta)$. Thus, the outer solution for case (iii) is given by

$$W_{\mathrm{outer}}(z) = \frac{m}{2\pi} \log \left[\frac{P(-\mathrm{i}\sqrt{r}\zeta, r) P(-\zeta/(\mathrm{i}\sqrt{r}), r)}{P(\zeta/(\mathrm{i}\sqrt{r}), r) P(\mathrm{i}\sqrt{r}\zeta, r)} \right], \tag{5.32}$$

where

$$\zeta = e^{-\pi(z+L+\mathrm{i}H)/2H}, \quad r \equiv e^{-\pi L/H}. \tag{5.33}$$

As $z \to 0$, which corresponds to $\zeta \to -\mathrm{i}\sqrt{r}$, the outer solution has the local expansion

$$W_{\mathrm{outer}}(z) = \frac{m}{2\pi} \log z + \frac{m}{2\pi} \log \left[\frac{\pi}{2H} \frac{P(-r, r) \hat{P}(1, r)}{P(-1, r) P(r, r)} \right] + \dots \tag{5.34}$$

On matching (5.34) and (5.21) the capacity of this geometry is estimated by the non-trivial explicit formula

$$\mathrm{cap}(\mathcal{G}, E) \approx \frac{2\pi}{\log \left[\dfrac{4H(1-\theta/\pi)}{\pi a} \left(\dfrac{P(r, r) P(-1, r)}{\hat{P}(1, r) P(-r, r)} \right) \right]}. \tag{5.35}$$

Case: Grötzsch ring

It is important to note that the capacity of the Grötzsch ring obtained in (5.11) is also approximated with great accuracy by the proposed matching approach. When the length of the slit in the Grötzsch ring becomes short, an outer observer will see the point source of strength m at the centre of the slit $[0, r]$. Since $\mathrm{Re}[W_{\mathrm{outer}}(z)] = 0$ on the unit circle, we

have

$$W_{\text{outer}}(z) = \frac{m}{2\pi} \log\left(\frac{z - r/2}{(r/2)(z - 2/r)}\right). \tag{5.36}$$

By using the same conformal map (5.14) with $\theta = 0$ and $z \to z - r/2$, the inner solution around the slit is given by

$$W_{\text{inner}}(z) = 1 - \frac{m}{2\pi} \log\frac{r}{4} + \frac{m}{2\pi} \log(z - r/2) + \dots. \tag{5.37}$$

Combining the outer solution (5.36) and the inner solution (5.37) gives the approximation for the capacity of the Grötzsch ring:

$$\text{cap}(\mathcal{G}, E) = -m \approx \frac{2\pi}{\log\left(\dfrac{4 - r^2}{r}\right)}. \tag{5.38}$$

5.5 Numerical evaluations for capacities of doubly connected domains

In this section, we evaluate the estimate of capacity with the results calculated by conformal mappings. Cases (A), (B) and (C) all involve doubly connected polycircular-arc domains [43]. These examples were chosen so that the accuracy of the estimates from the matching approach can be validated by computing the capacity using the conformal map of each doubly connected domain using the general theory described in [43] (see also [40]). Crowdy and Fokas [43] have shown that the conformal map $z = f(\zeta)$ from a concentric annulus in ζ-plane to a doubly connected polycircular region in z-plane satisfies the ordinary differential equation

$$\zeta^2\{f, \zeta\} = T(\zeta), \qquad \{f, \zeta\} \equiv \left(\frac{f''}{f'}\right)' - \frac{1}{2}\left(\frac{f''}{f'}\right)^2, \quad ' \equiv \frac{d}{d\zeta}, \tag{5.39}$$

where $T(\zeta)$ is a so-called loxodromic function [40] that depends on the geometry of the domain; the curly brackets denote a Schwarzian derivative. The function $T(\zeta)$ depends on unknown accessory parameters as well as the modulus ρ and these can be found (e.g. by a simple Newton method) using equations derived by solving the ordinary differential equation (5.39).

For the numerical calculation for doubly connected polycircular-arc domains, we need to solve the third-order differential equation [40, 43] for the conformal map $z = Z(\zeta)$ given

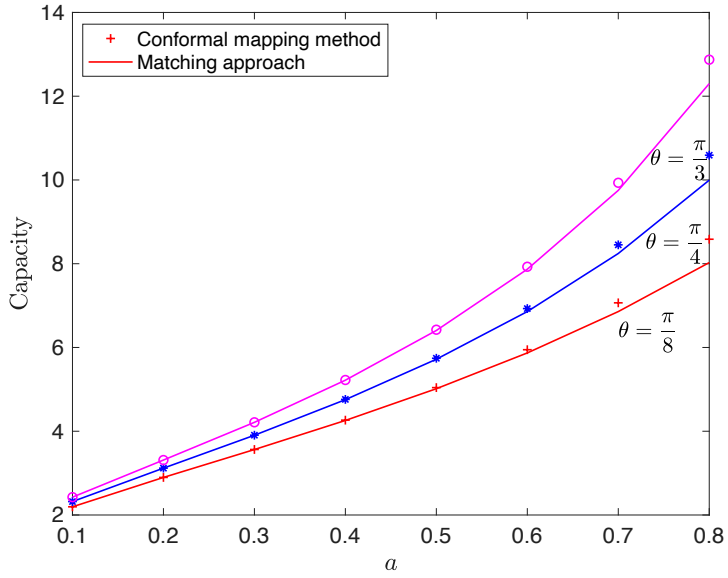

Figure 5.7: Comparison of the capacity of the lens in a circle as calculated using the doubly connected polycircular-arc conformal mapping method and the estimate (5.19) from the matching approach for the example in Figure 5.4. The matching estimates are excellent for small a, as expected, and are good even when a is large.

by

$$\zeta^2\{Z,\zeta\} = T(\zeta), \qquad \{f,\zeta\} \equiv \left(\frac{f''}{f'}\right)' - \frac{1}{2}\left(\frac{f''}{f'}\right)^2, \qquad f' \equiv \frac{df}{d\zeta}, \tag{5.40}$$

where the loxodromic function $T(\zeta)$ and initial conditions on the differential equation depend on each geometry [40]. For the sake of simplicity, we recall two important functions defined in Chapter 2 by

$$K(\zeta,\rho) \equiv \zeta\frac{P'(\zeta,\rho)}{P(\zeta,\rho)}, \qquad L(\zeta,\rho) \equiv \zeta\frac{dK}{d\zeta}(\zeta,\rho). \tag{5.41}$$

We note again that $K(\zeta,\rho)$ has a single pole at $\zeta = 1$, and $L(\zeta,\rho)$ has a double pole at $\zeta = 1$. The turning angle [40, 43] of the meniscus α is related to the opening angle of lens θ as

$$\alpha = 2\left(1 - \frac{\theta}{\pi}\right). \tag{5.42}$$

For completeness, we now list the functional form of the loxodromic function $T(\zeta)$ for each case.

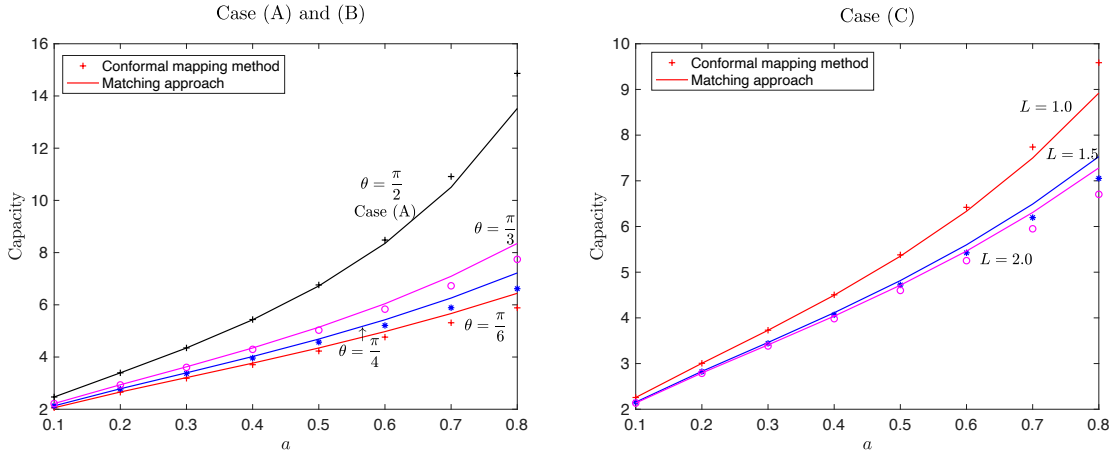

Figure 5.8: Comparison of the capacity as given by the estimates (5.25) and (5.35) from the matching formula and the values given by the solution of the accessory parameter problem for case (A), (B), and (C) in Figure 5.5 with $H = 1$. For case (C), θ is fixed to $\theta = \pi/4$ but L is varied.

1. (Lens in a circle):

Because of the symmetry, the prevertices of the edges of the lens are set to be at $\zeta = \pm\rho$. Then we can write

$$T(\zeta) = \frac{\alpha^2 - 1}{2}[L(\zeta/\rho, \rho) + L(-\zeta/\rho, \rho)] + C, \tag{5.43}$$

where C is a real parameter to be found.

2. Case (A) (Circle in a channel):

We let $\zeta = \pm 1$ be transplanted to $x \to \pm\infty$. Because of the symmetry, we can set

$$T(\zeta) = -\frac{1}{2}[L(\zeta, \rho) + L(-\zeta, \rho)] + C, \tag{5.44}$$

where $C \in \mathbb{R}$ is a parameter to be found.

3. Case (B) (Lens in a channel):

By the combination of the case (i) and case (A), we can derive

$$T(\zeta) = -\frac{1}{2}[L(\zeta, \rho) + L(-\zeta, \rho)] + \frac{\alpha^2 - 1}{2}[L(\zeta/\rho, \rho) + L(-\zeta/\rho, \rho)] + C, \tag{5.45}$$

where $C \in \mathbb{R}$ is a parameter to be found.

4. Case (C) (Lens in a rectangle):

Because of the symmetry, the point β on the unit circle is taken to be transplanted to the top right corner of the rectangle. Then we can derive

$$T(\zeta) = -\frac{3}{8}L_4(\zeta,\rho) + \mathrm{i}\gamma[K(\zeta/\beta,\rho) - K(-\zeta/\overline{\beta},\rho) + K(-\zeta/\beta,\rho) - K(\zeta/\overline{\beta},\rho)] + \frac{\alpha^2-1}{2}[L(\zeta/\rho,\rho) + L(-\zeta/\rho,\rho)] + C, \tag{5.46}$$

where $\gamma,\ C \in \mathbb{R}$ and

$$L_4(\zeta,\rho) \equiv L(\zeta/\beta,\rho) + L(\zeta/\overline{\beta},\rho) + L(-\zeta/\beta,\rho) + L(\zeta/\overline{\beta},\rho). \tag{5.47}$$

First, this method was used to calculate the capacity as graphed in Figure 5.7. The matching gives excellent estimates when the width of lens is less than 0.6.

Next, comparisons of the estimates given by the matching formula with the values given by the solution of the accessory parameter problem for case (A), (B), and (C) are shown in Figure 5.8. For case (C), the half of the opening angle θ is fixed to $\pi/4$. In all cases, the matching procedure gives excellent estimates for the capacity even when a grows comparable with unity.

5. Grötzsch ring

We evaluate our matching approach with the exact values of capacity of Grötzsch ring. We have derived the approximation for the capacity of the Grötzsch ring in the equation (5.38) and it is convenient to note it again:

$$\mathrm{cap}(\mathcal{G},E) = -m \approx \frac{2\pi}{\log\left(\dfrac{4-r^2}{r}\right)}. \tag{5.48}$$

This result agrees with the asymptotics of $\mu(r)$ described in page 8 of [5], where it is shown that $\mu(r)$ behaves $\log(4/r)$ when r tends to zero. The accuracy of the matching (5.38) is displayed in the Table 5.1.

Table 5.1: Comparison of the capacity of the Grötzsch ring between (i) the conformal mapping method, (ii) the explicit equation (5.12), and (iii) the matching approach.

r	Conf. map. method	Elliptic integral (5.12)	Relative error	Matching (5.38)
0.1	1.70443732109	1.70443732092	1.04×10^{-10}	1.70443404447
0.3	2.44777371061	2.44777371083	9.00×10^{-11}	2.44719002877
0.5	3.12680384539	3.12680384564	7.97×10^{-11}	3.11835619040

According to the equation (3.13) of [5], $\mu(r)$ is known to have a famous inequalities:

$$\mu_{\min} = \log\left(\frac{(1+\sqrt{r'})^2}{r}\right) < \mu(r) < \log\left(\frac{2(1+r')}{r}\right) = \mu_{\max}, \tag{5.49}$$

where $r' \equiv \sqrt{1-r^2}$. Figure 5.9 shows the comparison of the capacity of the Grötzsch ring given by the matching approach (5.38) and (5.49). It is not surprising that $\mu_{\min}$ and $\mu_{\max}$ are more accurate than the matching approach because $\mu_{\min}$ and $\mu_{\max}$ include expansions of higher orders than the matching approach. To be more precise, Taylor expansions of $\mu_{\min}$ and $\mu_{\max}$ around $r = 0$ give us

$$\mu_{\min} = \log\left(\frac{(1+\sqrt{r'})^2}{r}\right) = \log\left(\frac{1+\sqrt{1-r^2}+2(1-r^2)^{1/4}}{r}\right) \tag{5.50}$$

$$= \log\left(\frac{4-r^2-5r^4/16}{r} + \cdots\right), \tag{5.51}$$

and

$$\mu_{\max} = \log\left(\frac{2(1+\sqrt{r'})}{r}\right) = \log\left(\frac{4-r^2-r^4/4}{r} + \cdots\right). \tag{5.52}$$

These expansions suggest that the matching approach gives us the first two terms of the asymptotics in this case.

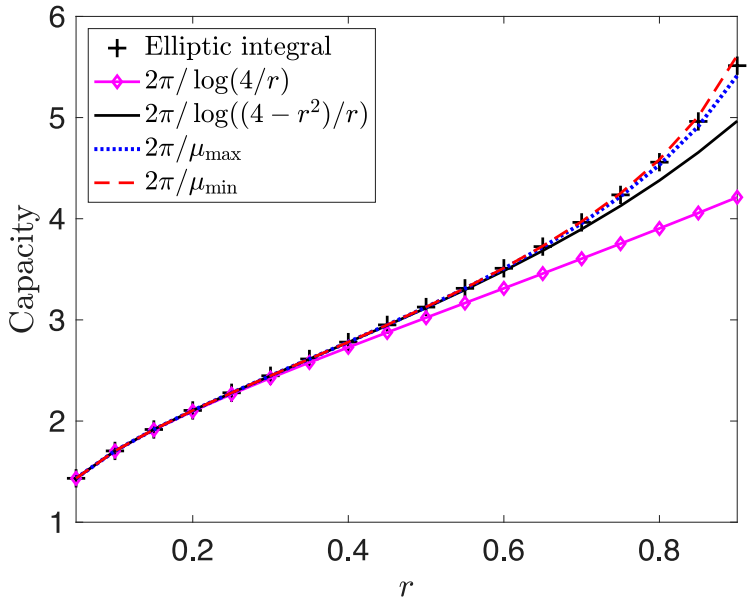

Figure 5.9: Comparison of the capacity of the Grötzsch ring given by (5.38) and the upper and lower bounds given in (5.49).

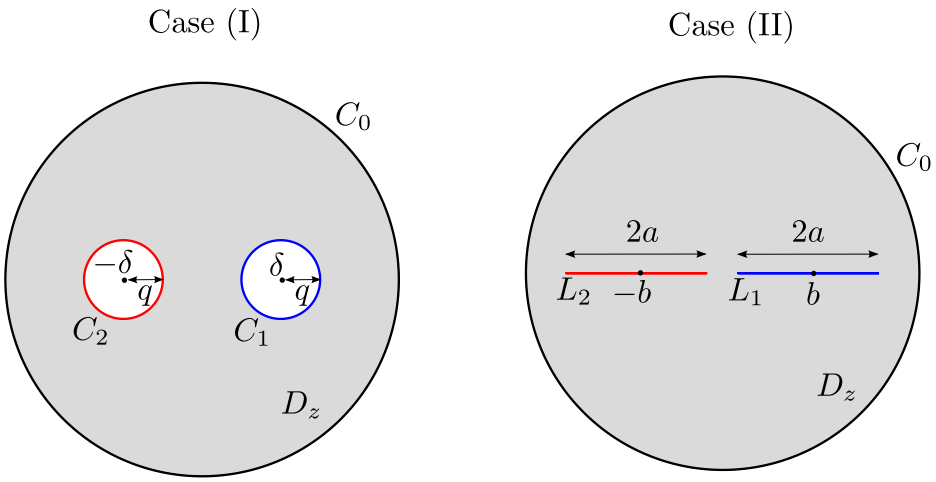

Figure 5.10: Two triply connected domains: cases (I) and (II).

5.6 Capacity calculation for triply connected domains

The matching approach can be easily extended to multiply connected domains such as the two triply connected examples, cases (I) and (II), shown in Figure 5.10. In both examples, $\mathcal{G}$ is again the unit disc.

Case (I): Two circles in the unit circle

First consider case (I) involving the triply connected domain $\mathcal{G}\backslash E$, $E \equiv \{E_1, E_2\}$, denoted by D_z, comprising the unit disc with two equal circular discs E_1 and E_2 excised. To align with the notation of [40] we will denote $\partial\mathcal{G}$ by C_0 and ∂E_j by C_j for $j = 1, 2$. The centers of each disc are at δ, $-\delta$, where $\delta \in \mathbb{R}$, and both have radius $q \in \mathbb{R}$, where q and δ satisfies $0 < q < \delta < 1$, $q + \delta < 1$. In order to find the capacity of the domain, consider the potential ϕ in D_z which satisfies

$$\nabla^2\phi(x, y) = 0, \qquad (x, y) \in D_z, \tag{5.53}$$

with the boundary conditions

$$\phi(x, y) = 1, \qquad (x, y) \in C_1,\ C_2, \tag{5.54}$$

$$\phi(x, y) = 0, \qquad (x, y) \in C_0. \tag{5.55}$$

As in Section 2, the complex potential $W(z)$, $\phi = \mathrm{Re}[W(z)]$, will be sought.

In order to construct the outer solution, suppose that the radii $q \ll 1$ and that the two circles C_1 and C_2 are sufficiently separated from each other, i.e., $q \ll \delta$, and neither are too close to C_0. Hence an outer observer viewing at the scale of the unit circle sees the

point sources with strength m_1 and m_2 at the centers of inner circles. Since $\mathrm{Re}[W(z)] = 0$ on C_0, the outer solution is given by

$$W_{\text{outer}}(z) = \frac{m_1}{2\pi} \log\left(\frac{z-\delta}{\delta(z-1/\delta)}\right) + \frac{m_2}{2\pi} \log\left(\frac{z+\delta}{\delta(z+1/\delta)}\right). \tag{5.56}$$

As before, the strengths of two sources m_1 and m_2 are unknown.

There are now two "inner solutions". The inner solution, valid near C_1, defined as $W^{(1)}_{\text{inner}}$, satisfies $\phi = 1$ on ∂E is

$$W^{(1)}_{\text{inner}}(z) = 1 - \frac{m_1}{2\pi} \log\left(\frac{q}{z-\delta}\right), \tag{5.57}$$

where m_1 is the flux associated with this inclusion. This inner observer sees neither the outer boundary, nor the other circular boundary C_2. Similarly, the inner solution around C_2 is

$$W^{(2)}_{\text{inner}}(z) = 1 - \frac{m_2}{2\pi} \log\left(\frac{q}{z+\delta}\right), \tag{5.58}$$

where m_2 is the flux associated with this inclusion. The observer associated with this inner solution sees neither the outer boundary, nor the other circular boundary C_1.

The outer solution and the two inner solutions must be matched. As $z \to \delta$, or as z approaches C_1, the outer solution (5.56) has the local expansion

$$W_{\text{outer}}(z) = \frac{m_1}{2\pi} \log\left(\frac{1}{\delta(1/\delta-\delta)}\right) + \frac{m_2}{2\pi} \log\left(\frac{2\delta}{\delta(\delta+1/\delta)}\right) + \frac{m_1}{2\pi} \log(z-\delta) + \ldots, \tag{5.59}$$

which should match to $W^{(1)}_{\text{inner}}(z)$. Similar arguments can be made as z approaches C_2. On matching, a linear system for m_1 and m_2 emerges:

$$\begin{cases} 1 - \dfrac{m_1}{2\pi} \log q = \dfrac{m_1}{2\pi} \log\left(\dfrac{1}{\delta(1/\delta-\delta)}\right) + \dfrac{m_2}{2\pi} \log\left(\dfrac{2\delta}{\delta(\delta+1/\delta)}\right), \\ 1 - \dfrac{m_2}{2\pi} \log q = \dfrac{m_1}{2\pi} \log\left(\dfrac{2\delta}{\delta(\delta+1/\delta)}\right) + \dfrac{m_2}{2\pi} \log\left(\dfrac{1}{\delta(1/\delta-\delta)}\right). \end{cases} \tag{5.60}$$

By symmetry we expect $m_2 = m_1$ and consequently,

$$m_1 = m_2 = \frac{2\pi}{\log\left(\dfrac{2q}{\delta(1/\delta^2-\delta^2)}\right)}. \tag{5.61}$$

The capacity for the domain $D_z = \mathcal{G}\backslash E$, $E \equiv \{E_1, E_2\}$ then follows from Green's second

identity as

$$\text{cap}(\mathcal{G}, E) = \int_{D_z} |\nabla\phi|^2 dxdy = \int_{\partial D_z} \frac{\partial\phi}{\partial n} ds = -m_1 - m_2 \approx -\frac{4\pi}{\log\left(\dfrac{2q}{\delta(1/\delta^2 - \delta^2)}\right)}. \quad (5.62)$$

Case (II): Generalized Grötzsch ring

For case (II), there are now two slits with length $2a$ centred at $(b, 0)$ and $(-b, 0)$ in the unit disc $\mathcal{G}$. We call the geometry a generalized Grötzsch ring. These slits are labelled as L_1 and L_2. Suppose that $a \ll 1$ and $a \ll b$. By using the same conformal map (5.14) with $\theta = 0$, the inner solution around L_1 is given by

$$W^{(1)}_{\text{inner}}(z) = 1 - \frac{m_1}{2\pi}\log\frac{a}{2} + \frac{m_1}{2\pi}\log(z - b) + \dots. \quad (5.63)$$

Since the outer boundary is the unit circle, the same expression (5.59) for the outer solution can be used. On matching in this case the linear system for m_1 and m_2 is

$$\begin{cases} 1 - \dfrac{m_1}{2\pi}\log\dfrac{a}{2} = \dfrac{m_1}{2\pi}\log\left(\dfrac{1}{b(1/b - b)}\right) + \dfrac{m_2}{2\pi}\log\left(\dfrac{2b}{b(b + 1/b)}\right), \\ 1 - \dfrac{m_2}{2\pi}\log\dfrac{a}{2} = \dfrac{m_1}{2\pi}\log\left(\dfrac{2b}{b(b + 1/b)}\right) + \dfrac{m_2}{2\pi}\log\left(\dfrac{1}{b(1/b - b)}\right). \end{cases} \quad (5.64)$$

By symmetry we expect $m_1 = m_2$ and after solving the linear system (5.64), the capacity is estimated by

$$\text{cap}(G, E) = -m_1 - m_2 \approx -\frac{4\pi}{\log\left(\dfrac{a}{b(1/b^2 - b^2)}\right)}. \quad (5.65)$$

5.7 Numerical evaluations for capacity of triply connected domains

To test the accuracy of these estimates, the values of the capacity are computed using an alternative scheme. Following a general formulation described in [40], the potential problem (5.53) can be solved using linear combinations of two multi-valued analytic functions $v_1(z)$ and $v_2(z)$ relevant to the general function theory associated with multiply connected domains as described in [40]. Since the functions $v_1(z)$ and $v_2(z)$ can be readily evaluated by using freely available codes [9] we merely make use of these resources here.

For Case (I), the exact solution of the potential problem is given by

$$W(z) = \mathrm{i}(\alpha_1 v_1(z) + \alpha_2 v_2(z)), \quad (5.66)$$

where the parameters α_1 and α_2 are determined by the boundary conditions (5.54). The following capacity is then given by the same technique as (5.62)

$$\mathrm{cap}(G, E) = -\alpha_1 - \alpha_2. \tag{5.67}$$

For Case (II), the potential is also given by formula (5.66), but now the preimage circular domain, D_ζ say, for which the two functions v_1 and v_2 are defined is different. The geometry of the circular domain D_ζ resembles that of D_z in Case (I), but the two preimage circles C_1 and C_2 have different centers, at $(\tilde{\delta}, 0)$ and $(-\tilde{\delta}, 0)$ say, and both have a different radius, $\tilde{q}$ say [40]. To find $\tilde{\delta}$ and $\tilde{q}$ it happens that the conformal mapping from the triply connected circular domain D_ζ to the domain D_z of Case (II) can be found using the following sequence of conformal maps [44]:

$$z = Z(\chi(\zeta)), \quad \chi = -\frac{\omega(\zeta, +1)}{\omega(\zeta, -1)}, \qquad Z(\chi) = \frac{1-\chi}{1+\chi}, \tag{5.68}$$

where $\omega(.,.)$ is the prime function associated with D_ζ [40]. The parameters $\tilde{\delta}$ and $\tilde{q}$ are determined by conditions

$$z(\tilde{\delta} - \tilde{q}) = b - a, \qquad z(\tilde{\delta} + \tilde{q}) = b + a. \tag{5.69}$$

The prime function $\omega(.,.)$ can be readily evaluated by using the same freely available codes [9] and the two equations (5.69) readily solved using standard methods.

Figure 5.11 shows the comparison of the capacity calculated by the matching approach and those calculated using the method just described. As expected, the matching approach gives excellent approximations when the size of the inclusions are small.

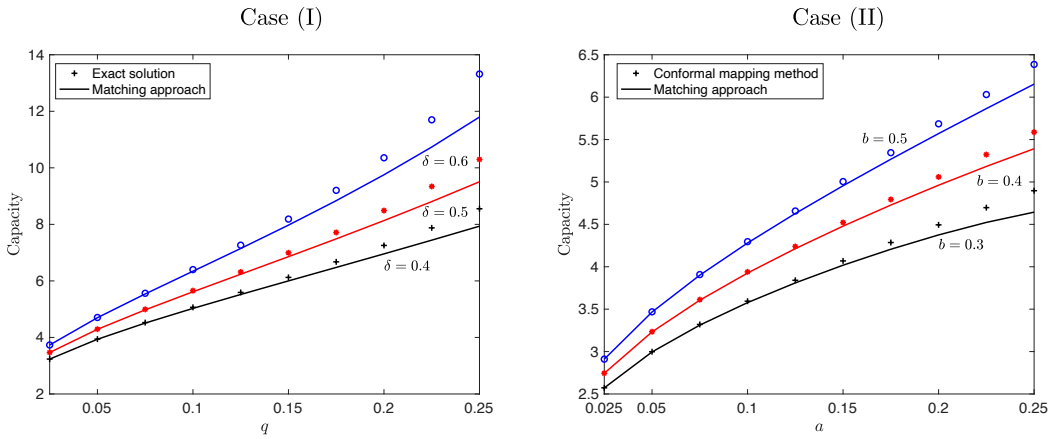

Figure 5.11: Comparison of the capacity as calculated by the conformal mapping approach and the matching approach for cases (I) and (II) in Figure 5.10. The matching approach approximates the capacities when the size of holes are small.

5.8 The capacity calculation for single interdigitated electrodes (Case 1.)

In this section, we focus on physical examples of interdigitated electrodes. This geometry contains a single electrode and a single ground line, and has been considered by several authors when calculating the fringing effects of the circuits. The geometry is shown in the right-hand figure in Figure 5.12.

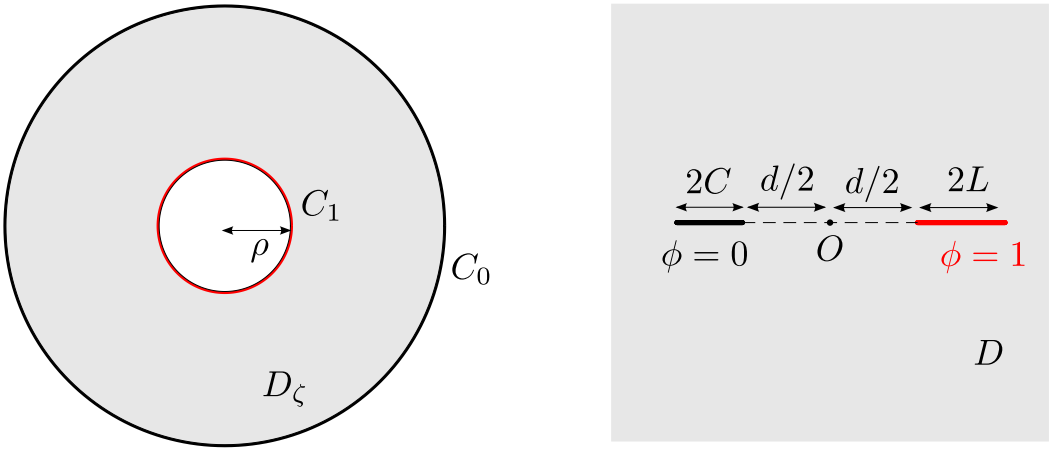

Figure 5.12: Example of the interdigitated electrodes. We can evaluate the capacity of this circuit using the conformal map from the annulus.

The problem now is to solve the potential ϕ which satisfies

$$\phi = 1, \quad \text{for } x \in [d/2, d/2 + 2L], \quad y = 0, \tag{5.70}$$

$$\phi = 0, \quad \text{for } x \in [-d/2 - 2C, -d/2], \quad y = 0. \tag{5.71}$$

We calculate the estimate of the capacity using the matching approach. First it is assumed that these two slits are well separated and $L/d, C/d \ll 1$. The inner solution around $z = L + d/2$ is given by

$$W_{\text{inner}}(z) = 1 - \frac{m}{2\pi} \log\left(\frac{L/2}{(z - L - d/2)}\right), \tag{5.72}$$

where m is a flux out of the electrode. The outer solution is a solution of the potential problem which satisfies

$$\phi = 0, \quad \text{for } x \in [-d/2 - 2C, -d/2], \tag{5.73}$$

with the source m at $z = d/2 + L$. The outer solution can be derived by using a famous Joukowski map as follows:

$$W_{\text{outer}}(z) = \frac{m}{2\pi} \log\left(\frac{\xi - \xi_0}{\xi_0(\xi - 1/\xi_0)}\right), \quad \xi = \Theta(z) = \frac{z + d/2 + C}{C} - \sqrt{\frac{(z + d/2 + C)^2}{C^2} - 1}, \tag{5.74}$$

and $\xi_0 = \Theta(d/2 + L)$. By the matching approach, the capacity of the single interdigitated electrodes is given by

$$m \approx \frac{2\pi}{\log\left(\dfrac{LC}{4[(C + d + L)^2 - C^2]}\right)} \tag{5.75}$$

so the capacity is given by

$$\text{cap}(\mathcal{G}, E) = -m = -\frac{2\pi}{\log\left(\dfrac{LC}{4[(C + d + L)^2 - C^2]}\right)}. \tag{5.76}$$

The exact value of the capacity of this geometry is given by the radial slit map presented in Chapter 2. We consider the radial-slit map

$$\eta(\zeta) = \frac{d}{\hat{\eta}(\rho\mathrm{i}) - \hat{\eta}(\mathrm{i})}\hat{\eta}(\zeta), \quad \hat{\eta}(\zeta) \equiv \frac{P(\zeta/a_\eta, \rho)P(\overline{a_\eta}\zeta, \rho)}{P(-\zeta/a_\eta, \rho)P(-\overline{a_\eta}\zeta, \rho)}, \tag{5.77}$$

where a_η is a purely imaginary number. The parameters ρ and a_η can be solved by the

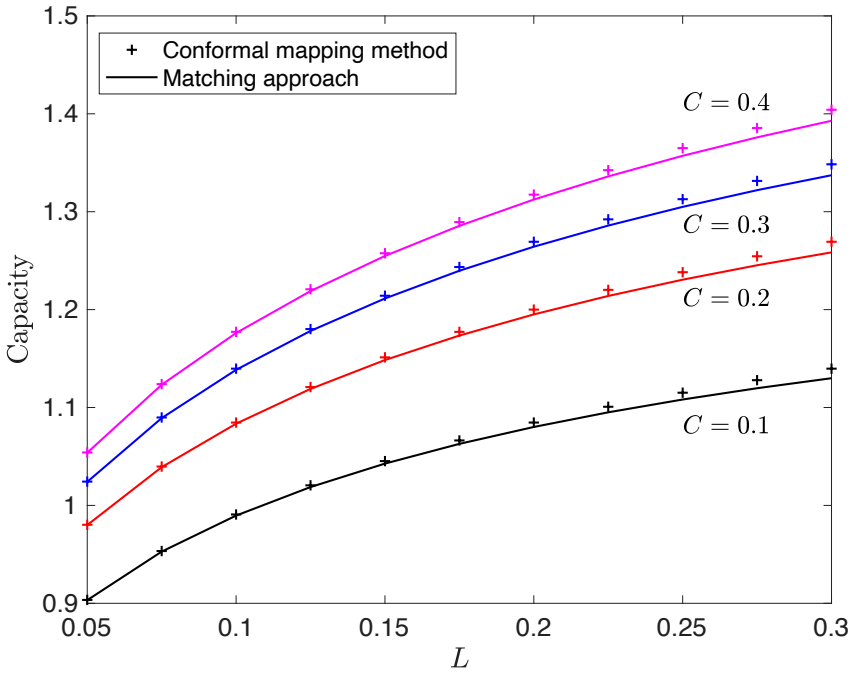

Figure 5.13: Capacity of a single interdigitated electrode. The distance between two electrode is fixed to $d = 1$ for all numerical experiments.

following conditions:

$$\begin{cases} \eta(-\rho\mathrm{i}) - \eta(\rho\mathrm{i}) = 2L, \\ \eta(\mathrm{i}) - \eta(-\mathrm{i}) = 2C. \end{cases} \tag{5.78}$$

These nonlinear equations can be readily solved by the standard method such as the Newton's method. After solving for ρ the capacity of the domain can be calculated by the equation (5.5).

Figure 5.13 shows the numerical comparison of the capacity calculated by the matching approach (5.76) and the conformal mapping approach. Similar to Section 5, the matching procedure gives excellent estimates for the capacity even when the slit lengths L and C grow comparable with the distance d.

5.9 The capacity calculation for periodic interdigitated electrodes (Case 2.)

In this section, we focus on the capacity calculation for periodic interdigitated electrodes. The problem now is to find the potential ϕ generated by the periodic interdigitated electrodes shown in Figure 5.14. The arrangement is $2T$-periodic in the x direction and, in each period window, there are two electrodes: one of length $2L$ held at unit voltage, another of length $2C$ that is grounded. The distance between them is d, so that $T = L + d + C$. The height of the dielectric material containing the electrodes is $2H$. Setting the origin as shown in Figure 5.15 the potential $\phi(x, y)$ in the period window D satisfies

$$\nabla^2\phi(x, y) = 0, \qquad (x, y) \in D, \tag{5.79}$$

with the boundary conditions

$$\phi = 1, \qquad \text{for } x \in [-L, L],\ y = 0, \tag{5.80}$$

$$\phi = 0, \qquad \text{for } x \in [-T, -T + C],\ [T - C, T]\ , y = 0, \tag{5.81}$$

$$\frac{\partial\phi}{\partial y} = 0, \qquad \text{for } y = \pm H. \tag{5.82}$$

In order to use the matching approach for this problem, it is necessary to solve the potential ϕ with source $m/2$ at $z = 0$ that satisfies following boundary conditions

$$\phi = 0, \quad \text{for } x \in [L + d, L + d + 2C], \tag{5.83}$$

and the Neumann derivative vanishes around the rectangle $D_{\text{rect}} = \{(x, y) \in [0, 2(d + L + C)] \times [-H, H]\}$. This can be done by using the conformal mapping of doubly connected domains. However, the explicit solution for the map is difficult to obtain because of the accessory parameter problems [40], which will be explained in detail in Chapter 7. Instead of using the matching approach, we propose to use the other two schemes for calculating the capacity.

5.9.1 The solution given by generalized Schwarz integral formulas

Here we solve the mixed boundary value problem (5.82) by the generalized Schwarz integral proposed in Chapter 3. Since ϕ is harmonic in D, we seek its analytic extension $h(z) \equiv \chi + \mathrm{i}\phi$ where χ is its harmonic conjugate. Owing to a symmetry across the real axis, $\partial\phi/\partial y = 0$ on $L \le |x| \le L + d$, $y = 0$ allowing, by the Cauchy-Riemann equations, the deduction that $\chi = 0$ there, without loss of generality. The Cauchy-Riemann equations

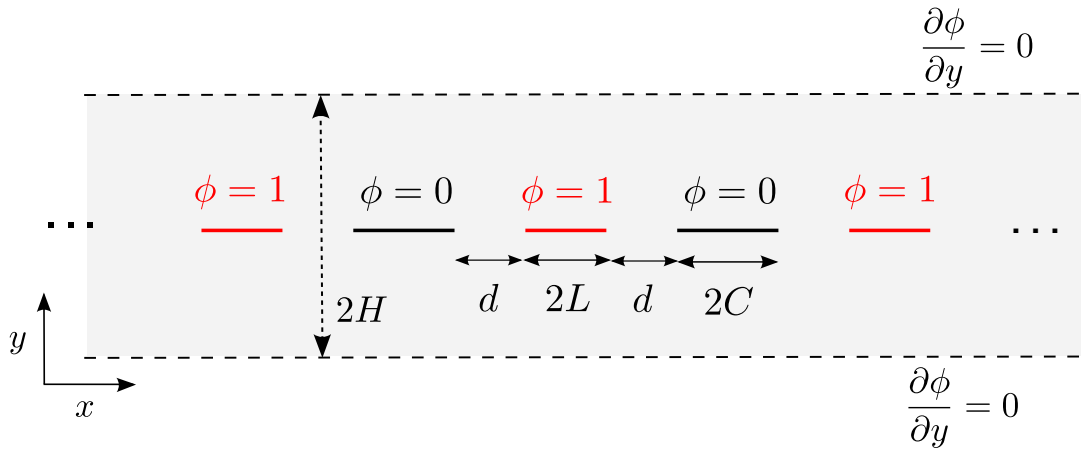

Figure 5.14: The boundary value problem for the potential $\phi(x, y)$ around a periodic array of interdigitated electrode.

and (5.82) also imply that on $y = \pm H$,

$$\frac{\partial \chi}{\partial x} = 0, \qquad \text{or} \qquad \chi = c_{\pm} \qquad \text{for } -T \le x \le T,\ y = \pm H. \tag{5.84}$$

While the domain D is simply connected, an explicit conformal mapping to D from a quadruply connected circular domain D_ζ as shown in Figure 5.15 is known to be

$$\mathcal{Z}(\zeta) = \frac{T}{\pi \mathrm{i}} \log \frac{\omega(\zeta, \theta_2(\infty))}{\omega(\zeta, \theta_3(\infty))}, \tag{5.85}$$

where $\omega(.,.)$ is the prime function associated with D_ζ, and

$$\theta_1(\zeta) = \rho^2 \zeta, \qquad \theta_2(\zeta) = \delta + \frac{q^2 \zeta}{1 - \bar{\delta}\zeta}, \qquad \theta_3(\zeta) = -\delta + \frac{q^2 \zeta}{1 + \bar{\delta}\zeta}, \tag{5.86}$$

where ρ, q, q, and 0, δ, $-\delta$ (δ is pure imaginary) are, respectively, the radii and centres of the interior circular boundaries of D_ζ denoted by C_1, C_2, and C_3. The unit circle, the outer boundary of D_ζ, is denoted by C_0. The function $\mathcal{Z}(\zeta)$ transplants C_0 to the grounded electrode, C_1 to the unit-potential electrode, C_2 to the upper boundary, and C_3 to the lower boundary, respectively.

Having introduced the mapping (5.85), the idea is to seek to find the composed function $H(\zeta) \equiv h(\mathcal{Z}(\zeta))$. Because $\chi = 0$ on $L \le |x| \le L + d$, $\mathrm{Re}[H(\zeta)] = 0$ on the real axis of D_ζ; this allows us to deduce, by a Schwarz reflection argument, that $c_+ = -c_- \equiv B \in \mathbb{R}$ where

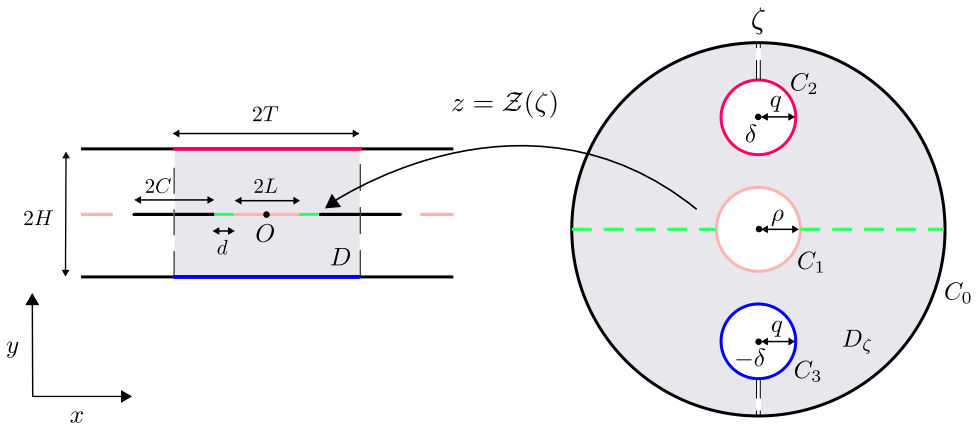

Figure 5.15: Conformal mapping from the quadruply connected domain D_ζ to a single period window D of the physical domain in a complex $z = x + iy$ plane.

B must be determined. The boundary value problem becomes

$$\begin{aligned} &\mathrm{Im}[H(\zeta)] = 0, \qquad \zeta \in C_0, \\ &\mathrm{Im}[H(\zeta)] = 1, \qquad \zeta \in C_1, \\ &\mathrm{Re}[H(\zeta)] = B, \qquad \zeta \in C_2, \\ &\mathrm{Re}[H(\zeta)] = -B, \qquad \zeta \in C_3. \end{aligned} \tag{5.87}$$

It is clear that the usual Schwarz integral formula (2.35) for this quadruply connected domain [32, 40] cannot be used directly because the real part of $H(\zeta)$ is not known on all parts of the boundary. But the problem falls within the class (3.1) and is therefore amenable to the generalized Schwarz integral formulation described in Chapter 3.

Although $\phi = \mathrm{Im}[H(\zeta)]$ must be single-valued in D_ζ, $\mathrm{Re}[H(\zeta)]$ is multi-valued because the electrified electrodes in each period window necessitate a logarithmic branch cut of $H(\zeta)$ between C_0 and C_1. It is convenient to write

$$H(\zeta) = \hat{H}(\zeta) + \alpha v_1(\zeta), \tag{5.88}$$

where $v_1(\zeta)$ is one of the multi-valued function introduced in Chapter 2. It is important to note again that $\mathrm{Re}[v_1(\zeta)]$ is multi-valued around C_0 and C_1, but single-valued around C_2 and C_3. The parameter α will be determined in the next subsection.

As indicated in Chapter 3, to find the single-valued function $\hat{H}(\zeta)$ we consider the modified function $X(\zeta) \equiv \eta(\zeta)\hat{H}(\zeta)$ where $\eta(\zeta)$ is a radial slit mapping given in (3.5). The

two parameters a, b in this slit mapping must be chosen to satisfy

$$\eta(\zeta) = \begin{cases} \text{purely imaginary on } C_0,\ C_1, \\ \text{purely real on } C_2,\ C_3. \end{cases} \tag{5.89}$$

On $\zeta \in C_0$, or C_1,

$$\mathrm{Re}\,[X(\zeta)] = -\frac{\eta(\zeta)}{\mathrm{i}} \cdot \mathrm{Im}[\hat{H}(\zeta)] = \mathrm{i}\eta(\zeta) \cdot \mathrm{Im}[\hat{H}(\zeta)]. \tag{5.90}$$

Similarly, on $\zeta \in C_2, C_3$,

$$\mathrm{Re}\,[X(\zeta)] = \eta(\zeta)\mathrm{Re}[\hat{H}(\zeta)]. \tag{5.91}$$

On subtracting off a simple pole of unknown residue β at $\zeta = b$, the boundary value problem to be solved is therefore

$$\mathrm{Re}\left[X(\zeta) - \frac{\beta}{\zeta - b}\right] = \begin{cases} -\mathrm{i}\alpha\eta(\zeta)\mathrm{Im}[v_1(\zeta)] - \mathrm{Re}\left[\dfrac{\beta}{\zeta - b}\right] \equiv s_0(\zeta) & \zeta \in C_0, \\ \mathrm{i}\eta(\zeta)(1 - \alpha\mathrm{Im}[v_1(\zeta)]) - \mathrm{Re}\left[\dfrac{\beta}{\zeta - b}\right] \equiv s_1(\zeta) & \zeta \in C_1, \\ \eta(\zeta)(B - \alpha\mathrm{Re}[v_1(\zeta)]) - \mathrm{Re}\left[\dfrac{\beta}{\zeta - b}\right] \equiv s_2(\zeta) & \zeta \in C_2, \\ -\eta(\zeta)(B + \alpha\mathrm{Re}[v_1(\zeta)]) - \mathrm{Re}\left[\dfrac{\beta}{\zeta - b}\right] \equiv s_3(\zeta) & \zeta \in C_3. \end{cases} \tag{5.92}$$

A representation for $X(\zeta)$ now follows by the Schwarz integral formula (2.35) of [32, 40]:

$$X(\zeta) = \eta(\zeta)\hat{H}(\zeta) = I(\zeta) + \frac{\beta}{\zeta - b} + \mathrm{i}c_0. \tag{5.93}$$

Thus,

$$\phi(z) = \mathrm{Im}\left[\hat{H}(\zeta) + \alpha v_1(\zeta)\right], \tag{5.94}$$

where

$$\hat{H}(\zeta) = \frac{1}{\eta(\zeta)}\left[I(\zeta) + \frac{\beta}{\zeta - b} + \mathrm{i}c_0\right]. \tag{5.95}$$

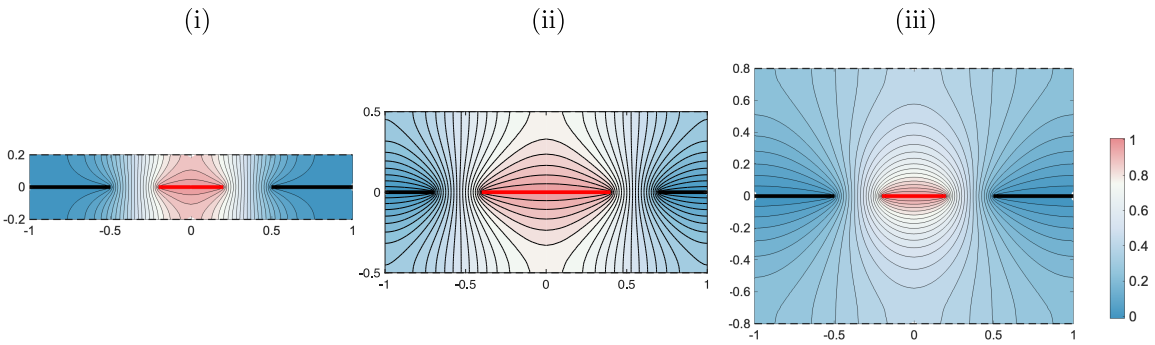

Figure 5.16: Equipotentials of $\phi(x, y)$ for $T = 1$ and $d = 0.3$: (i) $L = 0.2$, $H = 0.2$, (ii) $L = 0.4$, $H = 0.5$, (iii) $L = 0.2$, $H = 0.8$.

The problem now is to find parameters $\alpha, c_0, B \in \mathbb{R}$, and $\beta \in \mathbb{C}$, which is a total of 5 real parameters. Because $\hat{H}(\zeta)$ must be single-valued on D_ζ, the boundary values $\{s_j(\zeta)|j = 0, 1, 2, 3\}$ must satisfy the following solvability conditions [32, 40]:

$$-\int_{C_0} s_0(\zeta)dv_k(\zeta) + \sum_{j=1}^{3}\int_{C_j} s_j(\zeta)dv_k(\zeta) = 0, \qquad k = 1, 2, 3. \tag{5.96}$$

This yields three linear equations. Also, because $\eta(a) = 0$, then we require

$$I(a) + \frac{\beta}{a - b} + \mathrm{i}c_0 = 0. \tag{5.97}$$

The real part and the imaginary part of this equation yield two additional conditions. These are the 5 real linear equations for the 5 unknown real parameters.

Figure 5.16 shows typical equipotentials in a period window for three different geometries with $T = 1$ and $d = 0.3$.

With the solution given by the generalized Schwarz integral formula it is straightforward to calculate the electrical capacity of the circuits in the period window. Let $\mathcal{G}$ be the period window D and $\mathcal{E}$ be the ground line with length $2C$. Because $\hat{H}(\zeta)$ is analytic and single-valued on D_ζ,

$$\mathrm{cap}(\mathcal{G}, E) = \alpha, \tag{5.98}$$

where the positive sign comes from the definition that $\phi = \mathrm{Im}[H(\zeta)]$ in this case.

5.9.2 The Schwarz-Christoffel mapping approach

The boundary value problem can be solved using an alternative technique given in [33], because the boundary data are of different types but all constant.

We define $h(z) = \chi + \mathrm{i}\phi$. Now we use the fact that, because $z = \mathcal{Z}(\zeta)$ is a horizontal map, $dz = dx$ on $\zeta \in C_j$, $j = 0, 1, 2, 3$. This means

$$\frac{dh}{dz} = \frac{d\chi}{dx} + \mathrm{i}\frac{d\phi}{dx} = \frac{d\chi}{dx}, \qquad \zeta \in C_0, C_1, \tag{5.99}$$

where we used the fact that ϕ is constant on C_0, C_1. Also,

$$\frac{dh}{dz} = \frac{d\chi}{dx} + \mathrm{i}\frac{d\phi}{dx} = \mathrm{i}\frac{d\phi}{dx}, \qquad \zeta \in C_2, C_3, \tag{5.100}$$

where we used that χ is constant on C_2, C_3. Thus,

$$\frac{dh}{dz} = \begin{cases} \text{purely real on } C_0,\ C_1 \\ \text{purely imaginary on } C_2,\ C_3 \end{cases} \tag{5.101}$$

We now introduce two key building block functions for the solution defined by

$$R_1(\zeta; \zeta_1, \zeta_2) = \frac{\omega(\zeta, \zeta_1)}{\omega(\zeta, \zeta_2)} \tag{5.102}$$

and

$$R_2(\zeta; \zeta_1, \zeta_2) = \frac{\omega(\zeta, \zeta_1)\omega(\zeta, \zeta_1^{-1})}{\omega(\zeta, \zeta_2)\omega(\zeta, \zeta_2^{-1})}. \tag{5.103}$$

The function $R_1(\zeta; \zeta_1, \zeta_2)$ has a constant argument on each circle C_j, $j = 0, 1, 2, 3$ when ζ_1, ζ_2 are on the same circle. The function $R_2(\zeta; \zeta_1, \zeta_2)$ has a constant argument when ζ_1 and ζ_2 are any two ordinary points of the Schottky group. Because of the symmetry of the geometry, the function satisfies

$$\frac{dh}{dz}(T, H) = \frac{dh}{dz}(0, H) = \frac{dh}{dz}(T, -H) = \frac{dh}{dz}(0, -H) = 0, \tag{5.104}$$

which means $dh/dz = 0$ for $\zeta = a_j$, $j = 1, 2, 3, 4$, where

$$a_1 = q\mathrm{i} + \delta, \quad a_2 = -q\mathrm{i} + \delta, \quad a_3 = q\mathrm{i} - \delta, \quad a_4 = -q\mathrm{i} - \delta. \tag{5.105}$$

In addition, because of the horizontal map $\mathcal{Z}(\zeta)$, $d\mathcal{Z}/d\zeta = 0$ when $\zeta = b_j$, $j = 1, 2, 3, 4$,

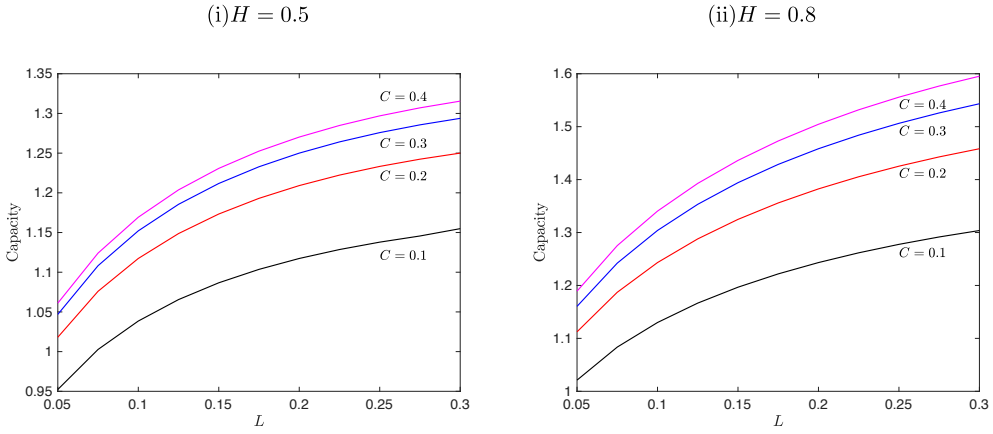

Figure 5.17: Capacity of the periodic interdigitated electrodes calculated by the Schwarz-Christoffel mapping approach. (i) $H = 0.5$, (ii) $H = 0.8$.

where

$$b_1 = \rho, \quad b_2 = -\rho, \quad b_3 = 1, \quad b_4 = -1. \tag{5.106}$$

However, dh/dz must not vanish at these points. This means dh/dz has poles at $\zeta = b_j$, $j = 1, 2, 3, 4$. With the arguments above, we can deduce

$$\frac{dh}{dz} = \hat{\mathcal{C}} \cdot \frac{\omega(\zeta, a_1)\omega(\zeta, a_2)\omega(\zeta, a_3)\omega(\zeta, a_4)}{\omega(\zeta, b_1)\omega(\zeta, b_2)\omega(\zeta, b_3)\omega(\zeta, b_4)} \frac{\omega(\zeta, \gamma_1)}{\omega(\zeta, 1/\overline{\gamma_1})} \frac{\omega(\zeta, 1/\overline{\gamma_2})}{\omega(\zeta, \gamma_2)} \frac{\omega(\zeta, 1/\overline{\gamma_3})}{\omega(\zeta, \gamma_3)}, \tag{5.107}$$

where $\gamma_j \in C_j$, $j = 1, 2, 3$, and $\hat{\mathcal{C}} \in \mathbb{R}$. Because the function $v_j(\zeta)$ has the following property

$$\frac{\omega(\zeta, \gamma_j)}{\omega(\zeta, 1/\overline{\gamma_j})} = \text{const} \cdot e^{2\pi \mathrm{i} v_j(\zeta)}, \quad \gamma_j \in C_j, \tag{5.108}$$

we arrive at the final formula for dh/dz:

$$\frac{dh}{dz} = \mathrm{i}\mathcal{C} \cdot \frac{\omega(\zeta, a_1)\omega(\zeta, a_2)\omega(\zeta, a_3)\omega(\zeta, a_4)}{\omega(\zeta, b_1)\omega(\zeta, b_2)\omega(\zeta, b_3)\omega(\zeta, b_4)} e^{2\pi \mathrm{i}(v_1(\zeta) - v_2(\zeta) - v_3(\zeta))}. \tag{5.109}$$

The parameter $\mathcal{C} \in \mathbb{R}$ can be determined by the condition:

$$\mathrm{Im}[h(L)] = \mathrm{Im}\left[\int_1^{\rho} \frac{dh}{dz}\frac{dz}{d\zeta} d\zeta\right] = 1. \tag{5.110}$$

The capacity is calculated by the definition and the Cauchy-Riemann equation as

follows:

$$\text{cap}(\mathcal{G}, E) = \int_{\partial E} \frac{\partial \phi}{\partial n} ds = -2 \int_{-b}^{b} \frac{\partial \chi}{\partial x}(x, 0) = 2(\chi(-b) - \chi(b)). \tag{5.111}$$

Figure 5.17 shows the capacity of the periodic interdigitated electrodes with different C and H. It has been verified that the two very different methods produce the same numerical results, confirming the viability of the generalized Schwarz integral method.

5.10 Conclusion

By presenting a series of examples, and comparing with numerical calculations, this chapter has demonstrated a practical procedure based on asymptotic matching of suitable "outer" and "inner" solutions to provide estimates of the capacity associated with multiply connected domains. The estimates show excellent agreement when there is a good separation of scales between the inner and outer regions, a feature on which the matching idea relies [68,146,150]. From the selection of examples explored here, it should be clear that the idea is very general and the approach can be applied to a wide variety of geometries.

On a technical note, it is worth remarking that it is usual when using matched asymptotics to introduce a rescaled variable to distinguish the inner region from the outer region and this can be important when doing matching at higher orders in any asymptotic expansions. Here, however, this rescaling has not been introduced explicitly since the estimates for capacity derived here involve only the leading order asymptotics in each region. In principle, more accurate estimates can be obtained by higher order matching, and then the introduction of suitably scaled inner and outer variables is advised.

We have also used the generalized Schwarz integral formulas to calculate the capacity of the periodic interdigitated electrodes. In this example the matching approach is not easily applied because of the famous accessory parameter problems, which will be explained in Chapter 7.

Chapter 6

Longitudinal flow in superhydrophobic channels with partially invaded grooves

In Chapters 4 and 5, we focused on the measurement of effective parameters in electrical engineering, i.e., electrical resistivity of materials and the capacity of electrical circuits. It was shown that the theory of the prime function gives us new mathematical tools for calculating these parameters.

In this chapter, another important transport problem arising in fluid dynamics is studied. We calculate longitudinal channel flows involving superhydrophobic surfaces and propose an explicit formula for the slip length of the channel flow. With the use of the prime function, analytical expressions are derived for the longitudinal flow in a superhydrophobic microchannel, where flat menisci in the Cassie state have partially invaded the grooves between no-slip blades. Using these solutions, the effective slip lengths are calculated and compared with recent analytical results for unbounded shear flow over the same class of surfaces proposed by Crowdy [41]. Expressions are also derived for the first-order corrections to these effective slip lengths when the menisci are weakly curved. A mathematical connection to superhydrophobic channel flows where flat menisci are still pinned to the tops of the pillars is also made, resulting in novel analytical expressions for those solutions too.

6.1 Introduction

Superhydrophobic surfaces, or SHS, can dramatically reduce flow resistance in the manipulation of small volumes of fluid in microchannel devices [83, 126]. At small scales surface tension allows interfaces or menisci to span the gaps between microstructural

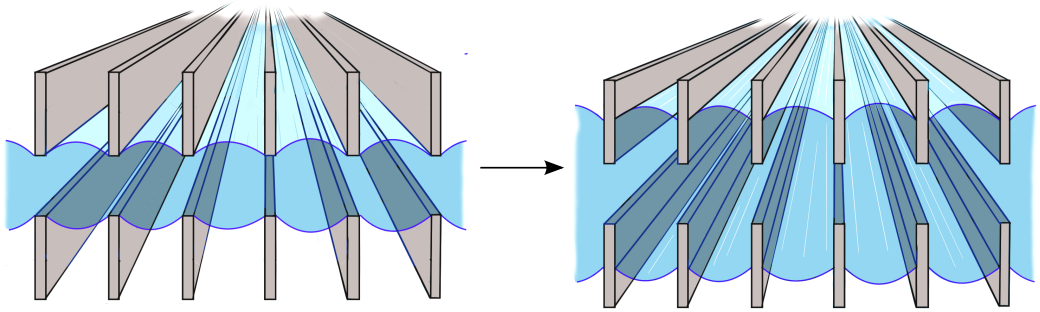

Figure 6.1: A bounded channel flow between two superhydrophobic surfaces making up the top and bottom of the channel with the menisci. Due to pressure fluctuation or mass transfer, the menisci move into the groove, resulting in the transition from the Cassie state to the Wenzel state.

protrusions that prevent fluid from fully penetrating interstitial regions. This leads to trapped gas pockets and enhanced slip over the spanning menisci. This so-called Cassie state can prove difficult to maintain and requires careful pressure control in many situations to prevent reversion to a fully wetted, or Wenzel, state. The use of textured groove sidewalls with reentrant and doubly reentrant pillar designs has been proposed in recent work [4, 66, 84, 147] as a means to improve the robustness of the Cassie state. In many of these configurations the menisci have depinned from the tops of the pillars and have partially invaded the grooves between pillars.

The quantification of the slip properties of superhydrophobic surfaces has been an area of much recent activity. Philip [119] provides explicit solutions to several mixed boundary value problems relevant to the mixture of no-slip and no-shear surfaces, which provide a good model of flow over superhydrophobic surfaces. Philip's solutions are relevant when flat interfaces are flush with interspersed flat no-slip surfaces, a feature shared with later studies [82]. Sbragaglia and Prosperetti [131] examined how weak meniscus curvature affects slip by solving the relevant mixed boundary value problems. Their study was reappraised and extended by Crowdy [39] who showed that their slip length corrections can be found instead using integral identities, or "reciprocal theorems", together with Philip's exact solutions for flat menisci. In practice, this meniscus curvature is caused by pressure differences between the trapped gas and the working fluid.

As discussed above, another circumstance that can often occur is the depinning of the menisci from the top of the grating [66, 67]. The depinning of the menisci is illustrated in Figure 6.1. This could be due to pressure fluctuations or mass transfer out of the cavities,

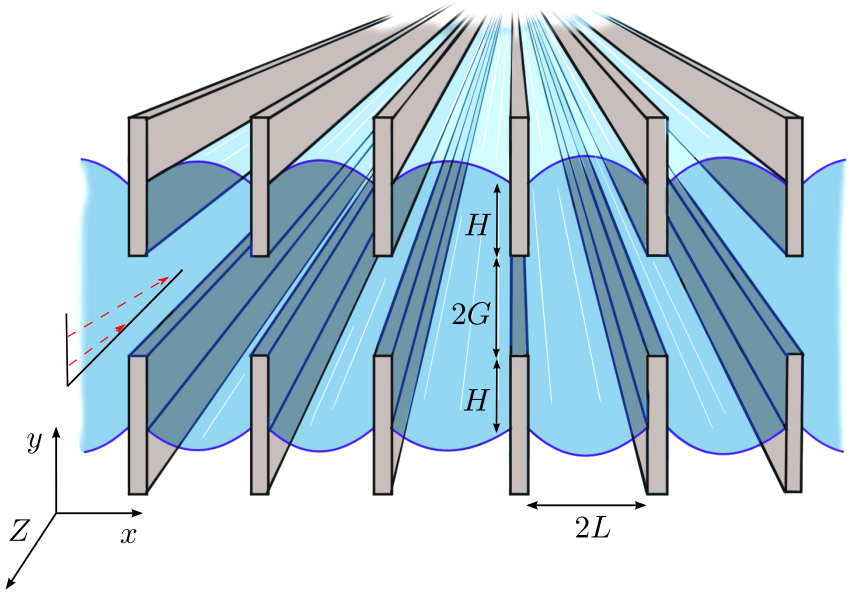

Figure 6.2: The geometry of a bounded channel flow between two superhydrophobic surfaces making up the top and bottom of the channel where the menisci have invaded grooves.

among other reasons (see [89,95] for more details). This causes the menisci to descend into the grooves and partially wet the cavities, a scenario that has received much less attention in the theoretical literature. Lee *et al* [83] have pointed out that meniscus depinning and cavity invasion are significantly more deleterious to slip than mere curving of the menisci without depinning [21]. Several authors have carried out numerical studies to quantify slip for partially filled cavities [61,110,143]. Crowdy [36,41] has derived several analytical results that quantify the effective slip for semi-infinite shear over grooved surfaces when the menisci have partially invaded the cavities.

The purpose of this chapter is to extend the recent work of [41], which involves semi-infinite shear over a single superhydrophobic surface, to the case of a bounded channel flow between two superhydrophobic surfaces making up the "top" and "bottom" of the channel, where fluid flows longitudinally parallel to the grooves. Figure 6.2 shows a schematic.

6.2 Summary of previous work

Here we summarise several papers on longitudinal flows over superhydrophobic surfaces. All analytical results presented here are based on the assumptions that the menisci are flat and that the fully-developed longitudinal flow $\underline{u} = (0, 0, w(x, y))$ satisfies the following

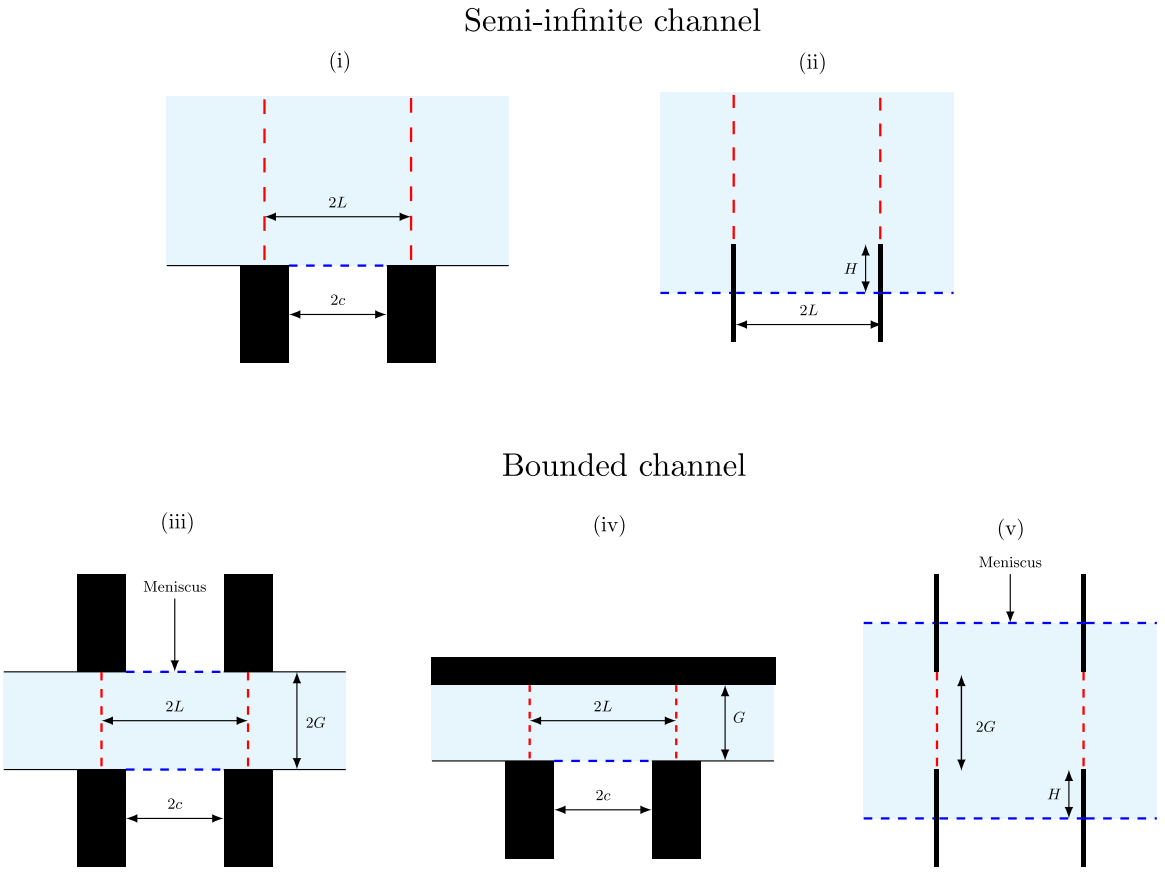

Figure 6.3: Summary of previous work. (i) A semi-infinite channel flow over periodic superhydrophobic surfaces. (ii) A semi-infinite channel flow over periodic superhydrophobic surfaces with partially invaded grooves. (iii), (iv) A bounded channel flow with periodic superhydrophobic surfaces. (v) A bounded channel flow over periodic superhydrophobic surfaces with partially invaded grooves. Philip found the solution for (i) and (iv) [119]. Marshall found the solution for (iii) [93]. Crowdy found the solution for (ii) [41].

boundary conditions:

$$w(x,y) = 0, \qquad (x,y) \in \text{walls}, \tag{6.1}$$

$$\frac{\partial w}{\partial y}(x,y) = 0, \qquad (x,y) \in \text{menisci}. \tag{6.2}$$

6.2.1 Semi-infinite flow

For semi-infinite channel flow in $y > 0$, the flow $w(x, y)$ satisfies

$$\nabla^2 w(x, y) = 0, \qquad \nabla^2 = \frac{\partial^2}{\partial x^2} + \frac{\partial^2}{\partial y^2}, \tag{6.3}$$

with the condition of simple shear with unit shear rate in the far field,

$$\frac{\partial w}{\partial y} = -1, \quad \text{as} \quad y \to \infty. \tag{6.4}$$

Case (i).

Philip found the solution for a semi-infinite flow over periodic superhydrophobic surfaces [119]. The conformal map from the upper half plane to the physical domain gives an explicit solution as follows:

$$w(x, y) = -\frac{2L}{\pi} \mathrm{Im}\left[\cos^{-1}\left(\frac{\cos(\pi z/2L)}{\cos(\pi c/2L)}\right)\right], \tag{6.5}$$

and the well-known slip length expression defined in (1.22) is obtained by

$$\lambda_{\text{Philip}} = \frac{2L}{\pi} \log \sec\left(\frac{\pi c}{2L}\right). \tag{6.6}$$

Case (ii).

For the flow over a superhydrophobic surface with partially invaded grooves, Crowdy has solved the mixed boundary value problem and obtained the solution

$$w(x, y) = -\frac{2L}{\pi} \mathrm{Im}\left[\sin^{-1}\left(\frac{\sin(\pi z/2L)}{\sinh(\pi H/2L)}\right)\right], \tag{6.7}$$

and the slip length is found to be

$$\lambda = \frac{2L}{\pi} \log\left(1 + \coth\left(\frac{\pi H}{2L}\right)\right), \tag{6.8}$$

where the slip length is measured at the level of menisci in this case.

6.2.2 Bounded channel flow

For a bounded channel domain, Philip was the first to calculate longitudinal channel flow with a periodic superhydrophobic surface and a wall one side and a wall on the other [119]. The flow considered here is driven by a constant pressure-driven $\mathcal{S}$. The flow satisfies the

following equation in a bounded channel:

$$\nabla^2 w(x,y) = \mathcal{S}, \tag{6.9}$$

where the origin of the xy-plane is taken at the center of the lower meniscus.

Case (iii).

Marshall found an explicit solution for channel flow by using a conformal map of a doubly connected domain [93]. The flow in this channel is given by

$$w(x,y) = -\frac{\mathcal{S}y}{2}(2G - y) + \mathcal{S}\hat{w}_{(\mathrm{iii})}(x,y), \tag{6.10}$$

where an explicit representation for $\hat{w}_{(\mathrm{iii})}(x,y)$ is derived in the equation (37) in [93]. With this function $w_{(\mathrm{iii})}(x,y)$, the slip length can be calculated as

$$\lambda = -\frac{1}{LG}\int_0^c \hat{w}_{(\mathrm{iii})}(x,0)dx. \tag{6.11}$$

Case (iv).

By using a conformal map from the period window to the upper half plane, Philip found an explicit formula for the flow:

$$w_{(\mathrm{iv})}(x,y) = -\frac{\mathcal{S}y}{2}(G - y) + \mathcal{S}\hat{w}_{(\mathrm{iv})}(x,y), \tag{6.12}$$

where

$$\hat{w}_{(\mathrm{iv})}(x,y) = -\frac{G}{2}\mathrm{Im}\left[\frac{G}{K_q}\mathrm{cn}^{-1}\left(\frac{\mathrm{cn}(zK_p/L,k_1)}{\mathrm{cn}(cK_p/L,k_1)}\right) - z\right], \tag{6.13}$$

where cn is the Jacobi cnoidal function given by

$$\mathrm{cn}(u,k) = \sqrt{1-\mathrm{sn}^2(u,k)}, \quad u = \mathrm{sn}^{-1}(x,k) = \int_0^x \frac{1}{\sqrt{(1-t^2)(1-k^2t^2)}}dt, \tag{6.14}$$

and where the parameters K_p, K_q, and k_1 are chosen so that

$$K_p = K(k_1), \quad K_q = K(\sqrt{1-k_1^2}), \quad \frac{K_q}{K_p} = \frac{G}{L}, \tag{6.15}$$

and where $K(k)$ is an elliptic function of the first kind defined by

$$K(k) = \int_0^1 \frac{1}{\sqrt{(1-t^2)(1-k^2t^2)}} dt. \tag{6.16}$$

The slip length of the channel is given by equating the total flux and the flux with a Navier-slip condition with Navier-slip parameter

$$\lambda = -\frac{G\int_{-c}^{c} \hat{w}_{(\mathrm{iv})}(x,0)dx}{G^2 L + \int_{-c}^{c} \hat{w}_{(\mathrm{iv})}(x,0)dx}. \tag{6.17}$$

It is important to mention that Crowdy also found alternative analytical formulas for the channel flow by using the approach based on the prime function of the annulus [42].

Case (v).

As mentioned earlier, the solution for bounded channel flow with partially invaded groove has not been obtained yet. We first address this problem and then show that the mathematical framework can also be used to calculate the other two bounded channel flows. This can be done by the conformal mapping approach and an implementation of the Schwarz integral formula introduced in Chapters 2 and 3.

6.3 Channel flow with partially invaded menisci

We introduce the basic idea by explaining the calculation of the flow over a superhydrophobic surface with partially invaded grooves. The challenge is to calculate longitudinal flow $(0, 0, w_F(x, y))$ in a typical period window of the superhydrophobic channel shown in (v) of Fig. 6.3. The origin in the cross-sectional (x, y) plane is taken at the intersection of the centerlines shown in Fig. 6.4. The period of the geometry in the x-direction is $2L$, and the distance of displacement of the flat meniscus below to tips of the sidewalls is H. The height of the channel, or distance between the sidewall gratings, is $2G$ as shown in Figs. 6.4 and 6.11. We define Ω as the whole period window bounded by partially invaded grooves as shown in Figs. 6.4 and 6.5.

Following the approach taken in [39, 41, 93], we assume that the fluid satisfies a no-slip condition on the walls and a no-shear condition on each meniscus. At first, it is assumed that the menisci are flat. Steady flow in the Z-direction along the channel is driven by a constant pressure gradient $-\mathcal{S}$.

Let D denote the half-period window of the channel shown in Fig. 6.4, i.e., $D \equiv \{(x, y)|x \in [0, L], y \in [-H - G, H + G]\}$. Then $w_F(x, y)$ satisfies the following boundary

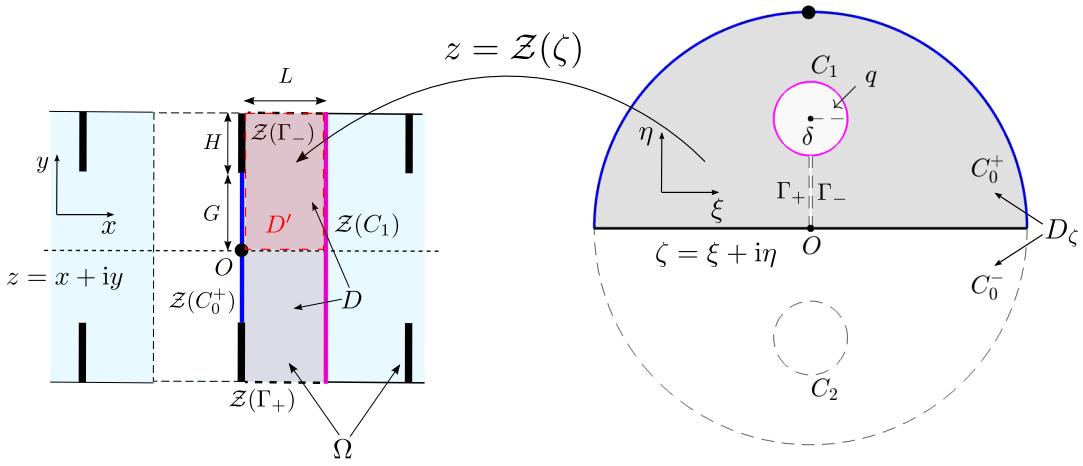

Figure 6.4: Conformal map from the upper half unit disc with a circular hole to a half-period of the channel flow.

value problem:

$$\nabla^2 w_F = \mathcal{S}, \qquad (x, y) \in D, \tag{6.18}$$

$$\frac{\partial w_F}{\partial y} = 0, \qquad 0 < x \leq L, \ y = \pm(H + G), \tag{6.19}$$

$$\frac{\partial w_F}{\partial x} = 0, \qquad x = 0, \ 0 \leq |y| < G, \tag{6.20}$$

$$\frac{\partial w_F}{\partial x} = 0, \qquad x = L, \ 0 \leq |y| \leq H + G, \tag{6.21}$$

$$w_F = 0, \qquad x = 0, \ G \leq |y| \leq H + G. \tag{6.22}$$

The boundary conditions (6.20) and (6.21) follow from a reflectional symmetry of the geometry.

It is convenient to define a new variable $\hat{w}(x, y)$ via

$$w_F = w_P + \mathcal{S}\hat{w}, \qquad w_P(x, y) \equiv -\mathcal{S}x\left(L - \frac{x}{2}\right). \tag{6.23}$$

The corresponding boundary value problem for $\hat{w}$ is then

$$\nabla^2 \hat{w} = 0, \qquad (x, y) \in D, \tag{6.24}$$

$$\frac{\partial \hat{w}}{\partial y} = 0, \qquad 0 < x \leq L,\ y = \pm(H + G), \tag{6.25}$$

$$\frac{\partial \hat{w}}{\partial x} = L, \qquad x = 0,\ 0 \leq |y| < G, \tag{6.26}$$

$$\frac{\partial \hat{w}}{\partial x} = 0, \qquad x = L,\ 0 \leq |y| \leq H + G, \tag{6.27}$$

$$\hat{w} = 0, \qquad x = 0,\ G \leq |y| \leq H + G. \tag{6.28}$$

Since $\hat{w}(x, y)$ is a harmonic function in D we aim to determine its analytic extension $h(z) \equiv \chi + \mathrm{i}\hat{w}$, where χ is the harmonic conjugate of $\hat{w}$.

Use of the Cauchy–Riemann equations and (6.26) implies that

$$\frac{\partial \chi}{\partial y} = -L, \qquad \text{or} \qquad \chi = -Ly + c_1, \qquad x = 0,\ 0 \leq |y| \leq G. \tag{6.29}$$

Similar arguments can be used to show that since $\partial\hat{w}/\partial x = 0$ on $x = L,\ 0 \leq |y| \leq H + G$ and since $\partial\hat{w}/\partial y = 0$ on $0 \leq x \leq L,\ y = \pm(H + G)$, then

$$\chi = c_2, \qquad x = L,\ 0 \leq |y| \leq H + G, \tag{6.30}$$

and

$$\chi = c_\pm, \qquad 0 \leq x < L,\ y = \pm(H + G), \tag{6.31}$$

where $c_2, c_\pm \in \mathbb{R}$. Since χ is defined up to a constant, we set $c_2 = 0$ without loss of generality. The continuity of χ around the boundary of D then requires that $c_\pm = c_2 = 0$. An integral relation also reveals that $c_1 = 0$. To see this, consider the upper-left quadrant of Ω, denoted by $D' := \{(x, y) : x \in [0, L], y \in [0, H + G]\}$. Due to the symmetry of the flow about $y = 0$, $\partial\hat{w}/\partial y = 0$ on the lower boundary of D', i.e., $\{(x, y) : x \in [0, L], y = 0\}$. Thus

$$0 = \int_{D'} \nabla^2 \hat{w}\, dA = \oint_{\partial D'} \frac{\partial \hat{w}}{\partial n}\, ds = \int_G^{H+G} \frac{\partial \hat{w}}{\partial x}\, dy + LG. \tag{6.32}$$

Use of the Cauchy-Riemann equations gives

$$\begin{aligned} 0 = -\int_G^{H+G} \frac{\partial \chi}{\partial y}\, dy + LG &= \chi(G) - \chi(H + G) + LG \\ &= (-LG + c_1) - c_2 + LG = c_1, \end{aligned} \tag{6.33}$$

where we have used the fact that $c_2 = 0$. It follows from (6.29) that

$$\chi = -Ly, \qquad x = 0,\ 0 \le y \le G. \tag{6.34}$$

6.4 Conformal mapping and the prime function

Now we solve the mixed boundary value problem by considering a suitable horizontal slit map, introduced in Chapter 2, from the triply connected domain to the period window. Let D_ζ be the circular domain in a parametric complex ζ plane interior to the unit circle, denoted by C_0, but exterior to two circles C_1 and C_2 each of radius q and having centres at $\pm\delta$ where δ is purely imaginary as shown in Fig. 6.4. It will be convenient later to denote by C_0^+ the semicircular portion of C_0 that is in the upper-half ζ plane, and by C_0^- the semicircle in the lower-half ζ plane.

Now introduce the holomorphic conformal mapping function

$$\mathcal{Z}(\zeta) = -\frac{H+G}{\pi} \log\left(\frac{\omega(\zeta, \theta_1(\infty))}{\omega(\zeta, \theta_2(\infty))}\right), \tag{6.35}$$

where

$$\theta_1(\zeta) \equiv \delta + \frac{q^2\zeta}{1 - \overline{\delta}\zeta}, \qquad \theta_2(\zeta) \equiv -\delta + \frac{q^2\zeta}{1 + \overline{\delta}\zeta} = \overline{\theta_1}(\zeta), \tag{6.36}$$

and where overbars denote the Schwarz conjugate of an analytic function, defined by $\overline{\theta_1}(\zeta) \equiv \overline{\theta_1(\overline{\zeta})}$. The function $\omega(\cdot,\cdot)$ is the prime function [40] of the triply connected domain D_ζ. The function (6.35) provides the one-to-one conformal map, $z = \mathcal{Z}(\zeta)$, from the upper half of D_ζ to D. Figure. 6.4 shows the correspondence between D and D_ζ schematically. The semicircle C_0^+ in the ζ-plane is mapped to the line $|y| \le G$ on the imaginary axis in the z-plane, and the inner circle C_1 is mapped to middle line $x = L,\ |y| \le H + G$ of the periodic channel.

Because D_ζ is reflectionally symmetric about the real axis, its associated prime function has the special property

$$\overline{\omega}(z, \zeta) = \omega(z, \zeta), \tag{6.37}$$

where we use the notation $\overline{\omega}(z,\zeta) \equiv \overline{\omega(\overline{z}, \overline{\zeta})}$. A consequence of this, together with (6.36), is that

$$\overline{\mathcal{Z}}(\zeta) = -\mathcal{Z}(\zeta). \tag{6.38}$$

Armed with this conformal mapping it will now be shown that the composed analytic function

$$\mathcal{H}(\zeta) \equiv h(\mathcal{Z}(\zeta)), \qquad \zeta \equiv \xi + \mathrm{i}\eta \tag{6.39}$$

is the solution to a classical problem in complex analysis known as a Schwarz problem in the triply connected circular domain D_ζ introduced in Chapter 2 [32, 40].

Owing to the fact that we expect $h(z)$ to have the same values on $y = \pm(H+G)$ for any $0 \leq x \leq L$, we seek a function $\mathcal{H}(\zeta)$ that is continuous across $\Gamma_\pm$ and, consequently, analytic in the upper half of D_ζ. On $\overline{\zeta} = \zeta$, we know from (6.28) that

$$\hat{w}(x,y) = \mathrm{Im}[\mathcal{H}(\zeta)] = 0, \tag{6.40}$$

implying that the Schwarz conjugate function of $\mathcal{H}(\zeta)$ defined by $\overline{\mathcal{H}}(\zeta) \equiv \overline{\mathcal{H}(\overline{\zeta})}$ coincides with $\mathcal{H}(\zeta)$, that is,

$$\overline{\mathcal{H}}(\zeta) = \mathcal{H}(\zeta). \tag{6.41}$$

By the Schwarz reflection principle [1], since $\mathcal{H}(\zeta)$ is known to be analytic in the upper half of D_ζ we infer that $\mathcal{H}(\zeta)$ is analytic in the lower half too, that is, in the whole of D_ζ.

If $\zeta \in C_0^+$ it follows from (6.34) that

$$\mathrm{Re}[\mathcal{H}(\zeta)] = -L\mathrm{Im}[\mathcal{Z}(\zeta)], \qquad \zeta \in C_0^+. \tag{6.42}$$

Suppose now that $\zeta \in C_0^-$, then clearly $\overline{\zeta} \in C_0^+$. Furthermore,

$$\mathrm{Re}[\mathcal{H}(\zeta)] = \mathrm{Re}[\overline{\mathcal{H}(\zeta)}] = \mathrm{Re}[\mathcal{H}(\overline{\zeta})] = -L\mathrm{Im}[\mathcal{Z}(\overline{\zeta})] = L\mathrm{Im}[\overline{\mathcal{Z}(\overline{\zeta})}] = -L\mathrm{Im}[\mathcal{Z}(\zeta)], \tag{6.43}$$

where the first and fourth equalities follow from trivial properties of complex quantities, the second and last equalities follow from (6.41) and (6.38) respectively, and the third equality follows from (6.34) since $\overline{\zeta} \in C_0^+$. A similar argument can be used to show that because $\mathrm{Re}[\mathcal{H}(\zeta)]$ vanishes on C_1 due to (6.30), then it also vanishes on C_2.

We therefore arrive at a boundary value problem for the function $\mathcal{H}(\zeta)$, analytic in D_ζ, with boundary values satisfying

$$\mathrm{Re}[\mathcal{H}(\zeta)] = \begin{cases} -L\mathrm{Im}[\mathcal{Z}(\zeta)], & \zeta \in C_0, \\ 0, & \zeta \in C_1,\ C_2. \end{cases} \tag{6.44}$$

This is a standard Schwarz problem in D_ζ: the problem of finding an analytic function in D_ζ given its real part everywhere on the domain boundary. From the results described in Chapter 2, the solution for $\mathcal{H}(\zeta)$ is given by

$$\mathcal{H}(\zeta) \;=\; \frac{L}{\pi}\oint_{C_0} \mathcal{Z}(\zeta')\, d\log\omega(\zeta',\zeta) - A_1 \mathrm{i}v_1 - A_2\mathrm{i}v_2 + \mathrm{i}c_0. \tag{6.45}$$

Note that $\mathcal{H}(\zeta)$ is not only analytic in D_ζ but also single-valued. For the particular

problem in (6.44) it can be shown using properties of the prime function (and confirmed numerically) that, for this problem, $A_1 = A_2 = c_0 = 0$. This means, in particular, that $\mathcal{H}(\zeta)$ is single-valued in D_ζ, a feature that is consistent with earlier arguments (indeed, alternatively we could have stated that the boundary value problem for the single-valued analytic function $\mathcal{H}(\zeta)$ is a *modified Schwarz problem* in D_ζ, and then confirmed that the boundary data satisfies compatibility conditions necessary for such a single-valued function to exist [32, 40]). Consequently, (6.44) can be simplified to the compact expression

$$\mathcal{H}(\zeta) = \frac{L}{\pi} \oint_{C_0} \mathcal{Z}(\zeta')\, d\log\omega(\zeta', \zeta), \tag{6.46}$$

where we have used the fact that $\overline{\zeta'} = 1/\zeta'$ on C_0 and the prime function property $\overline{\omega}(\zeta'^{-1}, \zeta^{-1}) = -\omega(\zeta', \zeta)/\zeta\zeta'$ (see Section 4.7 of [40]). The final expression for $\hat{w}(x, y)$ is

$$\hat{w}(x, y) = \mathrm{Im}\left[\mathcal{H}(\zeta)\right] = -\frac{L(H+G)}{\pi^2}\mathrm{Im}\left[\oint_{C_0} \log\frac{\omega(\zeta', \theta_1(\infty))}{\omega(\zeta', \theta_2(\infty))}\, d\log\omega(\zeta', \zeta)\right]. \tag{6.47}$$

Combining (6.23) and (6.47), we arrive at the explicit integral formula:

$$w(x, y) = -\mathcal{S}x\left(L - \frac{x}{2}\right) - \frac{\mathcal{S}L(H+G)}{\pi^2}\mathrm{Im}\left[\oint_{C_0} \log\frac{\omega(\zeta', \theta_1(\infty))}{\omega(\zeta', \theta_2(\infty))}\, d\log\omega(\zeta', \zeta)\right]. \tag{6.48}$$

6.5 Calculation of the slip lengths

The effective slip length associated with the flow can now readily be determined. We follow the approach expounded in [39] where reciprocity arguments are proposed to determine the volume flux associated with flows over superhydrophobic surfaces of this kind. The total flux in the period window is calculated as

$$Q_F \equiv \int_\Omega w_F\, dA = \int_\Omega (w_P + \mathcal{S}\hat{w})\, dA = -\frac{4}{3}\mathcal{S}(H+G)L^3 + \mathcal{S}\int_\Omega \hat{w}\, dA, \tag{6.49}$$

where the first term has been retrieved by elementary surface integration, and the second term will be evaluated using Green's second identity. We first note that

$$\int_\Omega \left(w_P\nabla^2\hat{w} - \hat{w}\nabla^2 w_P\right) dA = \oint_{\partial\Omega}\left(w_P\frac{\partial\hat{w}}{\partial n} - \hat{w}\frac{\partial w_P}{\partial n}\right) ds. \tag{6.50}$$

Using the symmetry in $y = 0$ of w_F and w_P, this equation reduces to

$$-\mathcal{S}\int_\Omega \hat{w}\, dA = 4\mathcal{S}\int_0^G \hat{w}(0, y)\frac{dw_P}{dx}(0, y)\, dy = -4\mathcal{S}L\int_0^G \hat{w}(0, y)\, dy, \tag{6.51}$$

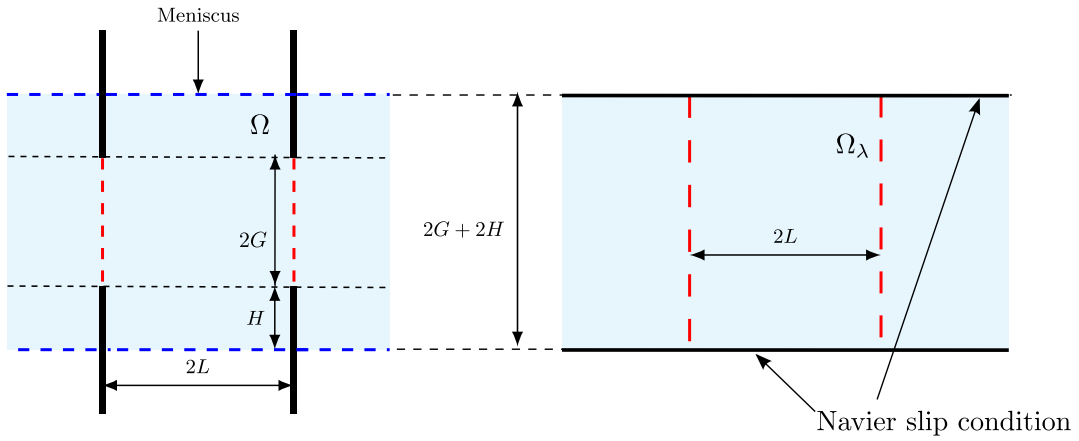

Figure 6.5: The definition of the effective slip length for a channel flow. The flow is compared to a Navier-slip flow with walls taken at the level of the invaded menisci.

and thus, we have

$$Q_F = -\frac{4}{3}\mathcal{S}(H+G)L^3 + 4\mathcal{S}L\int_0^G \hat{w}(0,y)\,dy. \tag{6.52}$$

Next, we compare this flux with that of the Navier slip problem. This is the standard procedure for calculating slip lengths in channels used in [77, 93]. The comparison flow that we have chosen imposes a Navier slip condition on a flat boundary taken at the level of the menisci as shown in Fig. 6.5. We set the origin as the center of a period window. The flow field $w_\lambda(x,y)$ in the period window Ω_λ satisfies

$$\nabla^2 w_\lambda = \mathcal{S}, \qquad (x,y) \in \Omega_\lambda, \tag{6.53}$$

$$w_\lambda = \lambda\frac{\partial w_\lambda}{\partial n}, \qquad 0 \le |x| \le L,\ y = \pm(H+G), \tag{6.54}$$

where n denotes the normal pointing into the liquid in this case. Here λ is the slip length in question. This problem is solved by

$$w_\lambda(x,y) = w_{P,\lambda}(x,y) - \lambda\mathcal{S}(H+G), \qquad w_{P,\lambda}(x,y) \equiv -\frac{\mathcal{S}}{2}[(H+G)^2 - y^2] \tag{6.55}$$

which gives the flux

$$Q_\lambda \equiv \int_{\Omega_\lambda} w_\lambda\,dA = -\frac{4}{3}\mathcal{S}(H+G)^3L - 4\lambda\mathcal{S}(H+G)^2L. \tag{6.56}$$

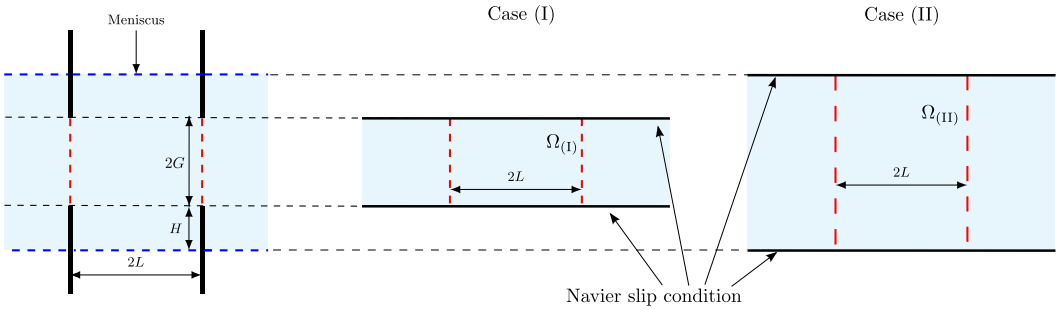

Figure 6.6: Two definitions of the effective slip length for a channel flow. In case (I) the flow is compared to a Navier-slip flow with walls taken level with the tops of the pillars; in case (II) it is compared to a Navier-slip flow with walls taken at the level of the invaded menisci.

Comparing (6.56) and (6.52) then yields

$$\lambda = \frac{L^2}{3(H+G)} - \frac{H+G}{3} - \frac{1}{(H+G)^2}\int_0^G \hat{w}(0,y)\,dy. \tag{6.57}$$

6.6 Two definitions of the effective slip length

It is worth pointing out that there is arbitrariness in the choice of defining the slip length as already observed in Crowdy [41]. For example, consider two definitions of the effective slip length for a channel flow denoted by $\lambda_{(I)}$ and $\lambda_{(II)}$ shown in Fig. 6.6. In (I) the baseline is placed at the top of the grooves, while in (II) the baseline is at the same level as the meniscus. Case (II) is equivalent to the right panel of Fig. 6.5, i.e. $\lambda_{(II)} = \lambda$. For case (I) we can use the same technique as Section 6.5 and obtain a formula for the slip length:

$$\lambda_{(I)} = \frac{(H+G)L^2}{3G^2} - \frac{G}{3} - \frac{1}{G^2}\int_0^G \hat{w}(0,y)\,dy. \tag{6.58}$$

There is a mathematical relation between $\lambda_{(I)}$ and $\lambda_{(II)}$. Multiplying $\lambda_{(I)}$ by G^2 and $\lambda_{(II)}$ by $(H+G)^2$, we find

$$\lambda_{(I)} = \left(1+\frac{H}{G}\right)^2 \lambda_{(II)} + H\left(1+\frac{H}{G}\right) + \frac{H^3}{3G^2}. \tag{6.59}$$

This expression can be seen as a generalization of equation (3.8) derived by Crowdy [41], who calculated the slip length for shear flow over a single surface with partially invaded

grooves. Note that for $G/L \to \infty$, we obtain the asymptotic formula

$$\lambda_{(\mathrm{I})} = \lambda_{(\mathrm{II})} + H, \tag{6.60}$$

which is exactly the relation derived in [41]. For the limiting case of a channel of infinite height, i.e. $G/L \to \infty$, $\lambda_{(\mathrm{I})}$ becomes the analytical result derived by Crowdy [41]:

$$\lambda_{(\mathrm{I}),\infty} = \frac{2L}{\pi} \log\left(1 + \coth\left(\frac{\pi H}{2L}\right)\right). \tag{6.61}$$

6.7 Characterization of the solutions

To study the flow, plot the velocity contours and calculate effective slip lengths, it is necessary to be able to evaluate the prime function $\omega(.,.)$. The prime function for triply connected domains can be evaluated by the the method explained in Chapter 2.

The parameters δ and q are determined uniquely, for a given channel geometry, by solving the two equations

$$\mathcal{Z}(1) = \mathrm{i}G, \qquad \mathcal{Z}(\delta + q\mathrm{i}) = L, \tag{6.62}$$

subject to the constraints $|\delta| + q < 1$, $|\delta| > 0$, and $q > 0$. Equations (6.62) are readily solved using any nonlinear solver such as Newton's method.

The half-period L has been used to non-dimensionalize lengths so that H/L and G/L are the relevant non-dimensional geometrical parameters. Figs. 6.7 and 6.8 show typical velocity contour plots of $w_F(x, y)$. In Fig. 6.7, H/L is varied while fixing $G/L = 0.8$; in Fig. 6.8, the invasion depth G/L is varied while fixing $H/L = 0.8$.

The effective slip length λ discussed in Section 6.5 has also been calculated. The left panel of Fig. 6.9 shows how the normalized slip length $\lambda/2L$ behaves for different values of G/L when the invasion depth H/L is varied. For the limiting case of a channel of infinite height, i.e. $G/L \to \infty$, the problem becomes equivalent to that studied by Crowdy [41], who derived the analytical result

$$\lambda_\infty = \frac{2L}{\pi} \log \operatorname{cosech}\left(\frac{\pi H}{2L}\right). \tag{6.63}$$

The cross-dot line in Fig. 6.9 shows the slip length as given by this formula, which agrees well with the results of the new formulation when $G/L = 8.5$.

There is a value of H/L which yields a "zero slip length". A similar observation was

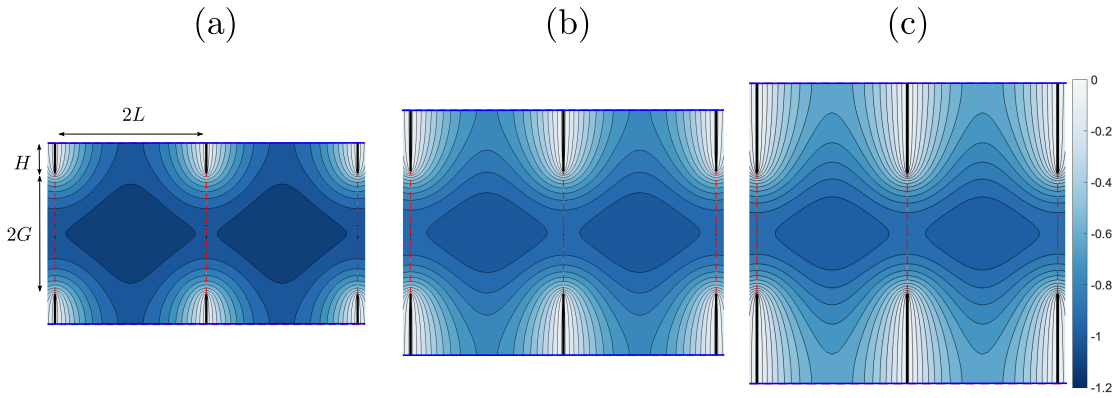

Figure 6.7: Contours of the velocity field $w_F(x, y)$. L and G are fixed to 1 and 0.8 in all figures respectively. (a) $H = 0.4$, (b) $H = 0.8$, (c) $H = 1.2$. The pressure gradient $\mathcal{S}$ is set to be 1.

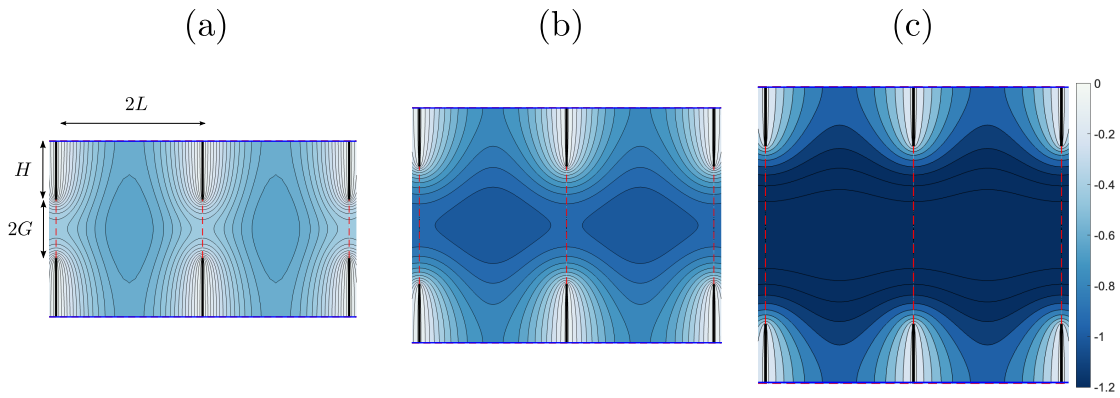

Figure 6.8: Contours of the velocity field $w_F(x, y)$. L and H are fixed to 1 and 0.8 respectively in all figures. (a) $G = 0.4$, (b) $G = 0.8$, (c) $G = 1.2$.

made by Crowdy [41] for the case of semi-infinite flow over a single surface. The reason for the vanishing slip length at this "critical invasion depth" is clear: since the slip length is measured relative to an effective slip flow in a channel taken at the level of the invaded menisci, the more the no-slip blades protrude into the flow, the more they will provide increased resistance. Thus, at a sufficiently large groove invasion depth, or equivalently, when the blades have protruded sufficiently far into the flow, any slip advantage afforded by the no-shear nature of the menisci will eventually be cancelled out by the resistance offered by the protruding no-slip blades. The (non-dimensional) critical invasion depth,

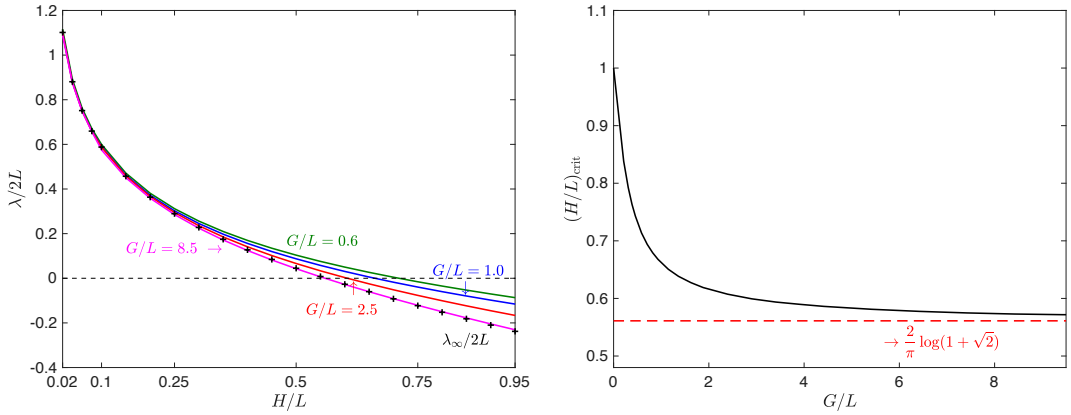

Figure 6.9: (Left) Normalized slip lengths $\lambda/2L$ for four different ratios of channel height G and period length L. The cross dot corresponds to the slip lengths where G tends to infinity, which is calculated explicitly by [41]. (Right) Critical invasion depth $(H/L)_{\mathrm{crit}}$ for increasing G/L.

$(H/L)_{\mathrm{crit}}$ say, is determined as a function of G/L by the criterion

$$\lambda = \lambda((H/L)_{\mathrm{crit}}, G/L) = 0. \tag{6.64}$$

The right panel of Fig. 6.9 shows the behavior of this critical invasion depth. As $G/L \to \infty$, it tends to $(2/\pi)\log(1+\sqrt{2})$, the value found by Crowdy [41]. Interestingly, as G/L tends to 0 (by definition, we must have $G > 0$) the critical invasion depth tends to unity. When G/L tends to 0, the blades touch and form continuous no-slip walls. The menisci are shear-free so the flow resembles a channel flow in a *vertical* channel. Therefore, the comparison problem in a *horizontal* channel has the same mass flux when $\lambda = 0$ and $H = L$ since these two flows are just rotations of each other by 90°. By taking the limit $G/L \to 0$ in equation (6.57) the slip length for this flow is obtained:

$$\lambda = \frac{L^2 - H^2}{3H}, \tag{6.65}$$

which means $\lambda = 0$ when $H/L = 1$.

6.8 Slip correction for weakly curved menisci

If the menisci are weakly curved we expect the slip length to be modified according to a regular perturbation expansion

$$\lambda_\theta = \lambda + \lambda_1\theta + \mathcal{O}(\theta^2), \tag{6.66}$$

where, in order to make contact with other studies [131], the coefficient of the first-order slip correction λ_1 is decomposed as $\lambda_1 = \lambda_{11} + \lambda_{12}$.

We follow the approach of Crowdy [39] who first proposed combining perturbation analysis with the use of integral "reciprocal identities" to find the leading order corrections to the flat-state slip length. Marshall [93] followed the approach of [39] in his analysis of the superhydrophobic channel problem (with non-invaded grooves) shown in Fig. 6.11(a).

Each meniscus is assumed to be a circular arc with a protrusion angle denoted by θ. In our case, the meniscus curves slightly downwards, hence θ is assumed to be small and negative. We write the solution for the flow field $w_\theta(x, y)$ as a series expansion in $\theta \ll 1$:

$$w_\theta(x, y) = w_F(x, y) + \theta w_1(x, y) + \mathcal{O}(\theta^2). \tag{6.67}$$

Since the curved meniscus is a circular arc with protrusion angle θ, the meniscus can be approximated by the quadratic curve $y = \theta Y(x) + \mathcal{O}(\theta^2)$, where $Y(x) = (L^2 - x^2)/2L$ [39]. The normal derivative of w_θ on the curved meniscus is

$$\begin{aligned}\frac{\partial w_\theta}{\partial n}(x, -H - G) = &-\theta \frac{\partial w_1}{\partial y}(x, -H - G) \\ &+ \theta \left(\frac{d}{dx}\left(Y(x) \frac{dw_F}{dx} \right) - \mathcal{S} Y(x) \right) + \mathcal{O}(\theta^2).\end{aligned} \tag{6.68}$$

Green's second identity states that

$$\int_{\Omega_\theta} (w_F \nabla^2 w_\theta - w_\theta \nabla^2 w_F) dS = \int_{\partial\Omega_\theta} \left(w_F \frac{\partial w_\theta}{\partial n} - w_\theta \frac{\partial w_F}{\partial n} \right) ds, \tag{6.69}$$

and thus the volume flux in Ω_θ, denoted by Q_θ, is given by

$$Q_\theta = Q_F + \theta(Q_{11} + Q_{12}) + \mathcal{O}(\theta^2), \tag{6.70}$$

where

$$Q_{11} = -4 \int_0^L \left(w_F(x, -H - G) Y(x) + \frac{Y(x)}{\mathcal{S}} \left(\frac{dw_F}{dx}(x, -H - G) \right)^2 \right) dx, \tag{6.71}$$

$$Q_{12} = -4 \int_0^L w_F(x, -H - G) Y(x) dx. \tag{6.72}$$

By equating Q_θ and Q_λ, we obtain

$$\lambda_\theta = \lambda + \theta \lambda_1 + \mathcal{O}(\theta^2), \tag{6.73}$$

where $\lambda_1 = \lambda_{11} + \lambda_{12}$, and

$$\lambda_{11} = \frac{1}{\mathcal{S}L(H+G)^2}\int_0^L \left(w_F(x,-H-G)Y(x) + \frac{Y(x)}{\mathcal{S}}\left(\frac{dw_F}{dx}(x,-H-G)\right)^2 \right) dx, \tag{6.74}$$

$$\lambda_{12} = \frac{1}{\mathcal{S}L(H+G)^2}\int_0^L w_F(x,-H-G)Y(x)\,dx. \tag{6.75}$$

Fig. 6.10 shows graphs of λ_1. For large G/L, the slip length agrees well with analogous explicit integral formulas for the first-order correction to the slip length given recently in [41] for semi-infinite shear over a single surface. An interesting feature is that, for large G/L, λ_1 is monotonically decreasing, but this behavior is different for smaller values of G/L. At some critical value of G/L (close to unity) the slip length correction becomes negative as H/L increases. This observation means that increasing the curvature of the meniscus does not enhance slip when G/L is small, i.e., for shallow channels.

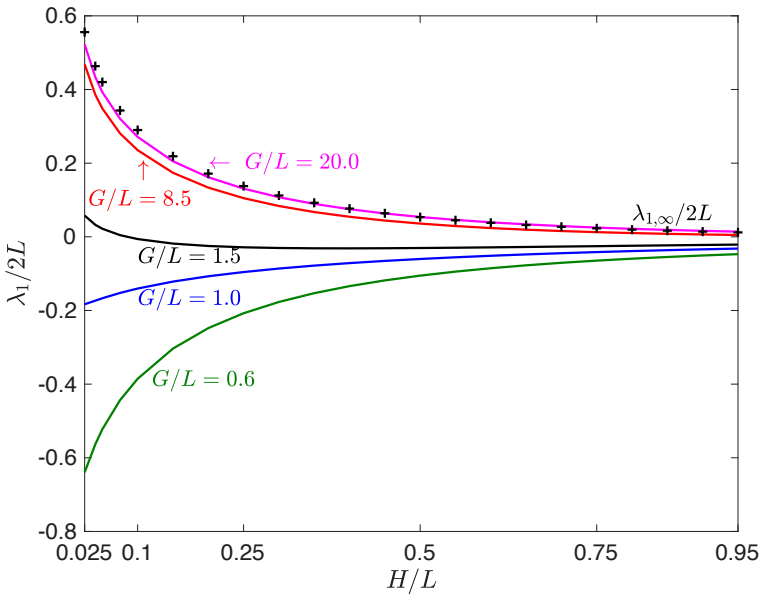

Figure 6.10: The behavior of λ_1. $\lambda_1/2L$ agrees well with the infinite-height case when $G/L = 20.0$.

6.9 Connection with another SHS problem

To motivate his study of semi-infinite shear flow over a single surface of blades where the menisci have partially invaded the grooves, Crowdy [41] includes a figure similar to that shown in Fig 6.11 which shows three different superhydrophobic surface (SHS) channel

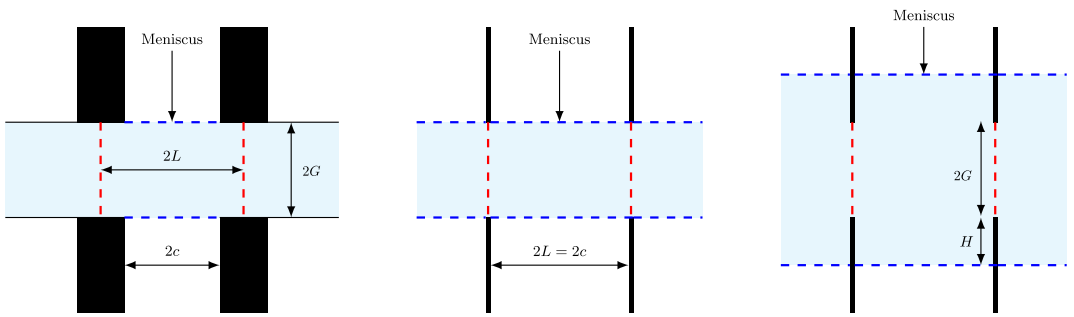

(a) The superhydrophobic channel

(b) Taking $c \to L$, yielding infinitely thin grooves

(c) Partially invaded grooves, $H > 0$

Figure 6.11: Superhydrophobic channel flows. (a) Symmetric channel flow between two superhydrophobic surfaces with menisci spanning the grooves between thick walls. (b) The critical case when the walls become infinitely thin, i.e. $c \to L$; the solution here is known to be singular [41]. (c) The problem solved in this paper: symmetric channel flow where the menisci have partially invaded the grooves between infinitely-thin blades.

flows. Fig 6.11(a) shows the most commonly considered case: longitudinal channel flow over a $2L$-periodic symmetric channel where menisci are flat, of length $2c$, and flush with the tops of the no-slip pillars. The pillars therefore have width $2(L - c)$. As $c \to L$ the pillars become infinitely thin ("blades") as shown in Fig 6.11(b). This flow scenario is singular because there is no solid surface left to retard the flow against the imposed pressure gradient. This manifests itself in the effective slip length associated with the flow in Fig 6.11(a) becoming infinite as $c \to L$. A "continuation" of this singular state, discussed by Crowdy [41], is shown in Fig 6.11(c) and shows the menisci descending by distance H into the grooves between infinitely thin walls. The analytical formulas (6.61) and (6.63) refer to slip lengths associated with the flow shown in Fig 6.11(c) in the limit $G/L \to \infty$ (which can be viewed as the problem of semi-infinite shear over a single SHS).

As explained in [41], both a semi-infinite and a bounded channel flows over a SHS with invaded grooves do not have any singularities in the period window.

6.9.1 Solution to the flow in case (iii)

Remarkably, it turns out that there is a *mathematical* connection between (the physically distinct) Superhydrophobic surface flows shown in Fig 6.11(a) and Fig 6.11(c). This is significant because it renders the new analytical solution (6.48) doubly useful. The observation is that if we take the upper half window in problem (a) and rotate it by 90^o, then we obtain the period window relevant to problem (c) and, moreover, the boundary conditions associated with the two problems (a) and (c) can be seen to be of the same type on each boundary portion (i.e., either no-slip or the normal derivative vanishing). Indeed, it can be shown that the flow field in problem (a) can be deduced from the solution of

problem (c) by using the following transformations:

$$x \mapsto y,\ y \mapsto x,\ L \mapsto G,\ H+G \mapsto L,\ G \mapsto c. \tag{6.76}$$

This mathematical transformation means that we have essentially solved two physically distinct problems at once. Thus, the solution for the flow in the channel (a) is given by

$$w_{(\mathrm{iii})} = w_{(\mathrm{a})} = -\frac{\mathcal{S}y}{2}\,(2G-y) + \mathcal{S}\hat{w}_{(\mathrm{iii})}, \tag{6.77}$$

where

$$\hat{w}_{(\mathrm{iii})} = -\frac{LG}{\pi^2}\mathrm{Im}\left[\oint_{C_0} \log\frac{\omega(\zeta',\theta_1(\infty))}{\omega(\zeta',\theta_2(\infty))}\,d\log\omega(\zeta',\zeta)\right]. \tag{6.78}$$

Here the conformal map $\mathcal{Z}(\zeta)$ is the transformation from triply connected domain D_ζ to the lower half of the period window, which is given by

$$z = \mathcal{Z}(\zeta) = \frac{L}{\pi \mathrm{i}}\log\left(\frac{\omega(\zeta,\theta_1(\infty))}{\omega(\zeta,\theta_2(\infty))}\right), \tag{6.79}$$

and the parameters of the triply connected domain now is determined by solving

$$\mathcal{Z}(1) = -c, \qquad \mathcal{Z}(\delta+\mathrm{i}q) = \mathrm{i}G. \tag{6.80}$$

Fig. 6.12 shows the transformations (6.76) graphically. We can see that both flows in the period window satisfy the same type of boundary conditions.

This observation also means that we have produced a new representation of the solution to problem (a) found by Marshall [93] who used a very different approach. Marshall also adopted use of the prime function technology but he performed the analysis in a doubly connected annulus rather than the triply connected domain D_ζ used here. Conversely, the observation means that, in principle, the partially-invaded meniscus problem (c) could have been solved by adapting Marshall's solution of problem (a). Notwithstanding this observation, we believe that the conciseness of the new formula (6.48) has its own attractions and is interesting in its own right. Furthermore, use of the triply connected preimage domain of this paper has "uniformized" a square-root singularity that appears in the analysis when a doubly connected annulus is used instead. The approach proposed by Marshall involves the incomplete elliptic integral of the first kind, which has square-root singularities at the edges of the menisci. Such integrable singularities are eliminated safely in our approach. Elimination of square root singularities can be desirable for numerical purposes since it obviates the need to deal with branch points and branch cuts associated with those singularities.

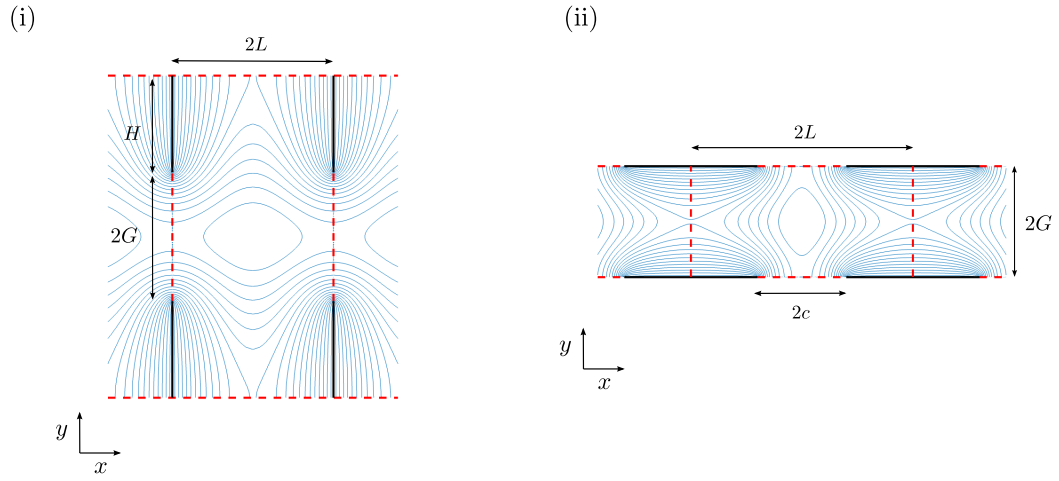

Figure 6.12: (i) Superhydrophobic channel flow in problem (c). (ii) Superhydrophobic channel flow in problem (a). The boundary condition on the black portion is no-slip, while on the red portion it is no-shear. By the transformation (6.76), both flows in the period window can be made to match.

To corroborate this observation, Fig. 6.13 shows the slip length for problem (a), and the coefficient of the first-order correction for small meniscus curvature, as calculated by adapting our approach and making use of the transformation (6.76). The circle-dot lines correspond to the results obtained using Marshall's alternative approach [93]; the cross-dot lines are the slip lengths for the flow in a periodic infinite channel, initially found in [119]:

$$\lambda_{(\mathrm{a}),\infty} = \frac{2L}{\pi} \log \sec\left(\frac{\pi c}{2L}\right). \tag{6.81}$$

Following [93], the slip length in problem (a) is

$$\lambda_{(\mathrm{iii})} = -\frac{1}{LG}\int_0^c \hat{w}_{(\mathrm{iii})}(x,0)\,dx = -\frac{1}{LG}\int_0^G \hat{w}(0,y)\,dy, \tag{6.82}$$

where the transformation (6.76) is used in the second equality. Comparing equation (6.82) with (6.57) shows that λ has an additional term and a different coefficient in front of the integral term, which results in the slip lengths having entirely different behavior as seen in Fig. 6.13. This is of course not surprising because, while the two flows might be related mathematically, they are nevertheless completely different flows.

It is interesting that, compared to problem (a), the channel height G in problem (c) needs to be much larger in order for the channel-flow slip length λ to be well approximated by the semi-infinite flow result λ_∞.

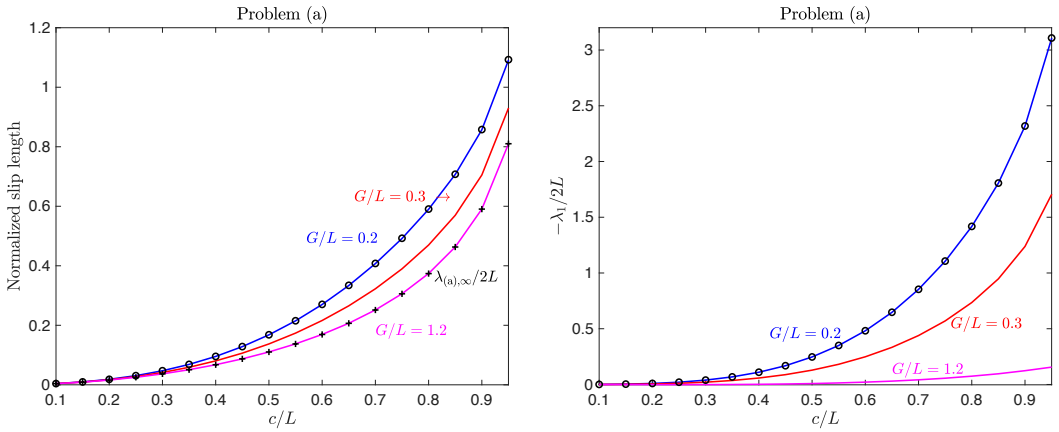

Figure 6.13: Slip length and normalized coefficient of the first-order correction for weak meniscus curvature for problem (a). Solid lines show the quantities calculated using the new approach of this paper; results using Marshall's approach [93] are shown as circle dots. The cross dots correspond to the slip length from formula (6.81).

6.9.2 Solution for the flow in case (iv)

We can obtain the solution for the flow in case (iv) by using the same conformal map $\mathcal{Z}(\zeta)$ defined in (6.79). Here we consider the conformal map $\mathcal{Z}(\zeta)$ to the period window as shown in (iv) in Figure 6.3. First we split the flow $w_{(\mathrm{iv})}$ into a non-harmonic and a harmonic part as follows:

$$w_{(\mathrm{iv})}(x,y) = -\frac{\mathcal{S}y}{2}(H-y) + \hat{w}_{(\mathrm{iv})}, \tag{6.83}$$

where $\hat{w}_{(\mathrm{iv})}$ is a harmonic function in the period window, which satisfies the following boundary conditions:

$$\frac{\partial \hat{w}_{(\mathrm{iv})}}{\partial y} = \frac{H}{2} \quad \text{on } y = 0,\ |x| < c, \tag{6.84}$$

$$\hat{w}_{(\mathrm{iv})} = 0 \quad \text{on } y = 0,\ c < |x| < L, \tag{6.85}$$

$$\hat{w}_{(\mathrm{iv})} = 0 \quad \text{on } y = H,\ |x| < L, \tag{6.86}$$

$$\frac{\partial \hat{w}_{(\mathrm{iv})}}{\partial x} = 0 \quad \text{on } 0 < y < H,\ x = \pm L. \tag{6.87}$$

Here we define $h(z) \equiv \chi + \mathrm{i}\hat{w}_{(\mathrm{iv})}$ and consider $\mathcal{H}_{(\mathrm{iv})}(\zeta) \equiv h(\mathcal{Z}(\zeta))$, where we use the same conformal map defined in (6.79). By using the Cauchy-Riemann equation, we have

$$\frac{\partial \hat{w}_{(\mathrm{iv})}}{\partial y} = \frac{\partial \chi}{\partial x} = \frac{H}{2} \quad \text{on } y = 0,\ |x| < c, \tag{6.88}$$

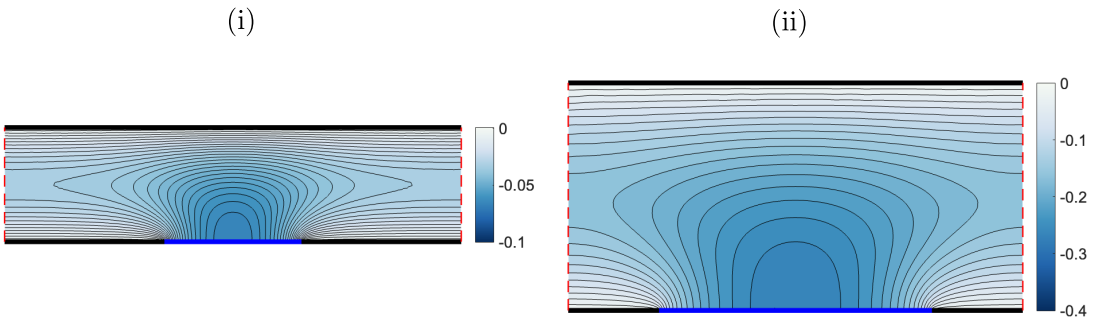

Figure 6.14: Superhydrophobic channel flows in the case (iv) in Figure 6.3. We fixed $L = 1$ for all figures. (i) $c = 0.3$, $H = 0.5$ (ii) $c = 0.6$, $H = 1.0$.

which means $\mathrm{Re}[h(z)] = \frac{H}{2}\mathrm{Re}[z]$, where we set $\mathrm{Re}[h(0)] = 0$ without loss of generality. Therefore, we have the following boundary value problem for $\mathcal{H}_{(\mathrm{iv})}(\zeta)$:

$$\mathrm{Re}[\mathcal{H}_{(\mathrm{iv})}(\zeta)] = \frac{H}{2}\mathrm{Re}[\mathcal{Z}(\zeta)], \qquad \zeta \in C_0, \tag{6.89}$$

$$\mathrm{Im}[\mathcal{H}_{(\mathrm{iv})}(\zeta)] = 0, \qquad \zeta \in C_1, \tag{6.90}$$

$$\mathrm{Im}[\mathcal{H}_{(\mathrm{iv})}(\zeta)] = 0, \qquad \zeta \in C_2. \tag{6.91}$$

The imaginary part of $\mathcal{H}_{(\mathrm{iv})}(\zeta)$ is single-valued by the definition of $h(z)$ but the real part can be multi-valued. The solution can be obtained using the technique explained in Chapter 3. We split the solution into a single-valued function and a multi-valued function as follows:

$$\hat{\mathcal{H}}_{(\mathrm{iv})}(\zeta) \equiv \mathcal{H}_{(\mathrm{iv})}(\zeta) - C\mathcal{Z}(\zeta). \tag{6.92}$$

Note that $\mathrm{Re}[Z(\zeta)]$ has a branch-cut between C_1 and C_2. Then, the boundary value problem for $\hat{\mathcal{H}}_{(\mathrm{iv})}$ becomes

$$\mathrm{Re}[\hat{\mathcal{H}}_{(\mathrm{iv})}(\zeta)] = \left(\frac{H}{2} - C\right)\mathrm{Re}[\mathcal{Z}(\zeta)], \qquad \zeta \in C_0, \tag{6.93}$$

$$\mathrm{Im}[\hat{\mathcal{H}}_{(\mathrm{iv})}(\zeta)] = -C\mathrm{Im}[\mathcal{Z}(\zeta)], \qquad \zeta \in C_1, \tag{6.94}$$

$$\mathrm{Im}[\hat{\mathcal{H}}_{(\mathrm{iv})}(\zeta)] = -C\mathrm{Im}[\mathcal{Z}(\zeta)], \qquad \zeta \in C_2. \tag{6.95}$$

The parameter C is determined by the single-valuedness condition. The final formula is given by

$$\mathcal{H}_{(\mathrm{iv})}(\zeta) = \frac{1}{\eta(\zeta)}\left(I(\zeta) + \frac{A}{\zeta - b} + \mathrm{i}c_0\right) + C\mathcal{Z}(\zeta). \tag{6.96}$$

Figure 6.14 shows typical channel flows with this problem. The numerical values are checked against Philip's solution. It is important to note that Crowdy also found another representation for the flow (iii) in Figure 6.3 using the prime function of the concentric annulus [42].

6.10 Conclusion

This chapter has shown how to use the prime function associated with a triply connected circular domain [40] to find compact representations of longitudinal channel flows over superhydrophobic surfaces where the menisci have depinned from the pillar tops and partially invaded the grooves. The solutions are explicit once two parameters, δ and q, have been found by solving two nonlinear equations given the geometry of the surface. The slip properties of the surfaces have been quantified based on the use of these new formulas. It has also been indicated how previously derived solutions due to Marshall [93] for a different flow in a superhydrophobic channel can be derived by a simple transformation of our formula.

We believe the compact form of the flow solution (6.48) is important since many applications of superhydrophobic surfaces involve additional physical effects, such as heat [77] and mass transfer, or thermocapillary or other surfactant effects [78, 161], making it useful to have available concise representations of the basic flow. Finally, for the convenience of readers wishing to make use of the solutions described herein, the author has prepared downloadable `MATLAB` codes based on the theoretical work in this chapter [10].

Chapter 7

Accessory parameter determinations for canonical domains by matched asymptotic expansions

In this chapter, a method for calculating accessory parameters associated with conformal mappings is proposed. Conformal mappings are powerful tools for solving various problems in the physical transport theory. However, conformal maps always have unknown parameters associated with the geometry, which are sometimes hard to obtain. The radius of the inner circle for doubly connected domain is an example. We show how the matched asymptotics introduced in Chapter 5 can be used to derive explicit estimates for these accessory parameters. This can be done by equating the conformal capacity of the preimage with that of the target domains. The formulas derived here are explicit and they provide excellent approximations to the accessory parameters. The conformal capacity is equivalent to the "electrical capacity" introduced in Chapter 5, but here we use a terminology "conformal capacity".

7.1 Introduction

The study of conformal invariants is of particular importance in the field of complex analysis [3]. The conformal capacity is one of the most essential such invariants and has been studied for many years [120,123]. Mathematically, the conformal capacity of a domain

$\mathcal{G}$ containing a subset E is defined by the extremal value of the integral [52, 104]

$$\text{cap}(\mathcal{G}, E) = \inf_{\phi} \int_{\mathcal{G}} |\nabla \phi|^2 dxdy, \tag{7.1}$$

where $\phi(x, y)$ is a harmonic function with $\phi(x, y) \geq 1$ for all $(x, y) \in E$ and $\phi(x, y) \to 0$ as $(x, y) \to \partial\mathcal{G}$. It is known that the extremal function ϕ satisfies the following classical Dirichlet problem [3, 63]:

$$\nabla^2 \phi(x, y) = 0, \qquad (x, y) \in \mathcal{G} \backslash E, \tag{7.2}$$

with the following boundary conditions

$$\begin{cases} \phi(x, y) = 0, & (x, y) \in \partial\mathcal{G}, \\ \phi(x, y) = 1, & (x, y) \in \partial E. \end{cases} \tag{7.3}$$

An elementary example is where $\mathcal{G}$ is taken as the unit disc with centre at the origin and E is a concentric disc of radius ρ, $0 < \rho < 1$. The solution for the Dirichlet problem (7.2) in this geometry is given by $\phi = \text{Re}[W(z)]$, where the analytic function

$$W(z) = \frac{\log z}{\log \rho}, \qquad z \equiv x + \text{i}y, \tag{7.4}$$

is often called a complex potential for the problem. The conformal capacity can then be calculated from equation (7.1) by using the Green's second identity [3, 63] with the result

$$\text{cap}(\mathcal{G}, E) = \frac{2\pi}{\log(1/\rho)}. \tag{7.5}$$

Since the capacity is conformally invariant, the calculation of capacity in doubly connected domains (where ∂E forms an internal boundary component of a doubly connected domain) can be related to the problem of finding the conformal modulus ρ of the conformal mapping to the target annular domain from a canonical concentric annulus, $\rho < |\zeta| < 1$ say, with $|\zeta| = 1$ mapping to $\partial\mathcal{G}$ and $|\zeta| = \rho$ mapping to ∂E.

The main technique here is to equate the conformal capacity of the target domains with the preimage. As shown in Chapter 5, simple formulas are given for the conformal capacities of both geometries, which makes it possible to relate the capacities of the preimage to that of the target domains.

7.2 Estimating accessory parameters for the doubly connected domains

This section explains two methods for estimating the accessory parameters of doubly connected domains. First the matching approach is proposed to obtain the estimate of the radii and centres of the predomain, by equating the capacities of the predomain to that of the target domain.

7.2.1 Matching approach

This section focuses on the Riemann modulus ρ associated with target domains. As explained in the introduction of this chapter, the conformal capacity of a concentric annulus with the inner radius ρ has the capacity given by (7.5). Here the same three example geometries shown in Figure 5.5 in Chapter 5 are studied again. The matching formula has shown that the conformal capacity for case (A) is

$$\mathrm{cap}(\mathcal{G}, E) = \frac{2\pi}{\log\left(\frac{\pi a}{4H}\right)}. \tag{7.6}$$

Hence, the modulus ρ is approximated by the following simple equation given by

$$\rho_{(\mathrm{A})} = \frac{\pi a}{4H}. \tag{7.7}$$

Similarly, the expressions for the capacity for cases (B) and (C) give simple formulas

$$\rho_{(\mathrm{B})} = \frac{\pi a}{8H(1-\theta/\pi)}, \tag{7.8}$$

and

$$\rho_{(\mathrm{C})} = \frac{\pi a}{4H(1-\theta/\pi)}\left(\frac{\hat{P}(1,r)P(-r,r)}{P(r,r)P(-1,r)}\right), \quad r = e^{-\pi L/H}. \tag{7.9}$$

These simple formulas give remarkably good estimates for unknown modulus of the annulus. Figure 7.1 shows the numerical comparison of the matching approach and the Newton's method. It is verified that the matching approach gives good estimates even for large sizes of inner regions.

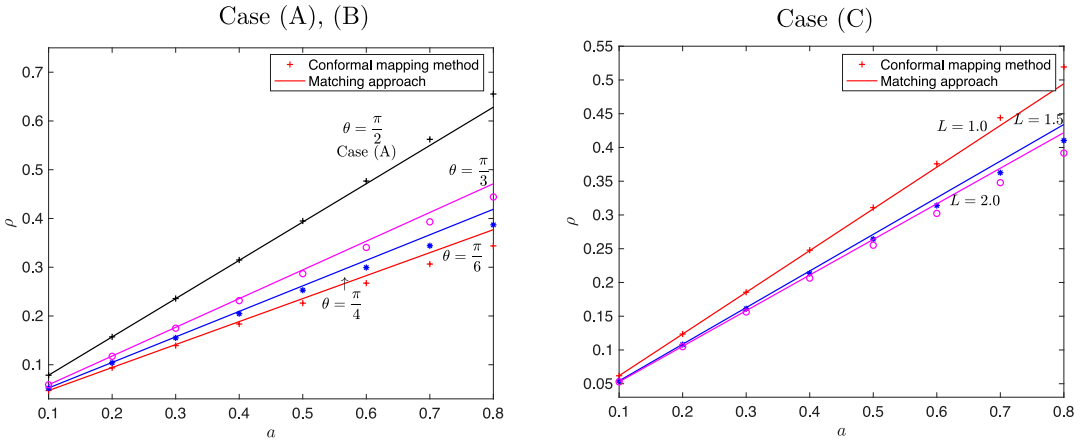

Figure 7.1: Numerical comparison of the value ρ calculated by the matching approach and the conformal mapping method in the case (A), (B), and (C) in Figure 5.5.

7.2.2 Connection to the isomonodromy approach

Another very different method has recently been proposed for the estimation of accessory parameters based on the so-called isomonodromic tau function [7, 8, 24]. In [8, 24], the isomonodromy method was used to find an undetermined pervertex of polycircular arcs with four vertices by finding the zero of the tau function [8, 24].

Here the isomonodromy approach is explained briefly based on [8]. The conformal map $w = f(z)$ from the upper half plane in z-plane to a simply connected polycircular domain with N-vertex is given by [3]

$$\{f, w\} \equiv \left(\frac{f''}{f'}\right)' - \frac{1}{2}\left(\frac{f''}{f'}\right)^2 = \sum_{n=1}^{N}\left[\frac{1-\theta_n^2}{2(w-w_n)^2} + \frac{\beta_n}{w-w_n}\right], \quad ' \equiv \frac{d}{dw}, \tag{7.10}$$

where $\pi\theta_n$ are the interior angles at $z_n = f(w_n)$ in the target domain. It is known that the solution of the Schwarz derivative can be linearlized by considering $f(w) \equiv \tilde{y}_1(w)/\tilde{y}_2(w)$, where $\tilde{y}_1(w)$ and $\tilde{y}_2(w)$ are linearly independent solutions for the following second order differential equation:

$$\tilde{y}'' + \frac{1}{2}\sum_{n=1}^{N}\left[\frac{1-\theta_n^2}{2(w-w_n)^2} + \frac{\beta_n}{w-w_n}\right]\tilde{y} = 0. \tag{7.11}$$

The regularity condition at $w \to \infty$ gives three conditions for these parameters:

$$\sum_{n=1}^{N}\beta_n = \sum_{n=1}^{N}(2w_n\beta_n + (1-\theta_n^2)) = \sum_{n=1}^{N}(w_n^2\beta_n + w_n(1-\theta_n^2)) = 0. \tag{7.12}$$

The differential equation (7.11) is called a 2D Fuchsian equation. When $N > 3$, the

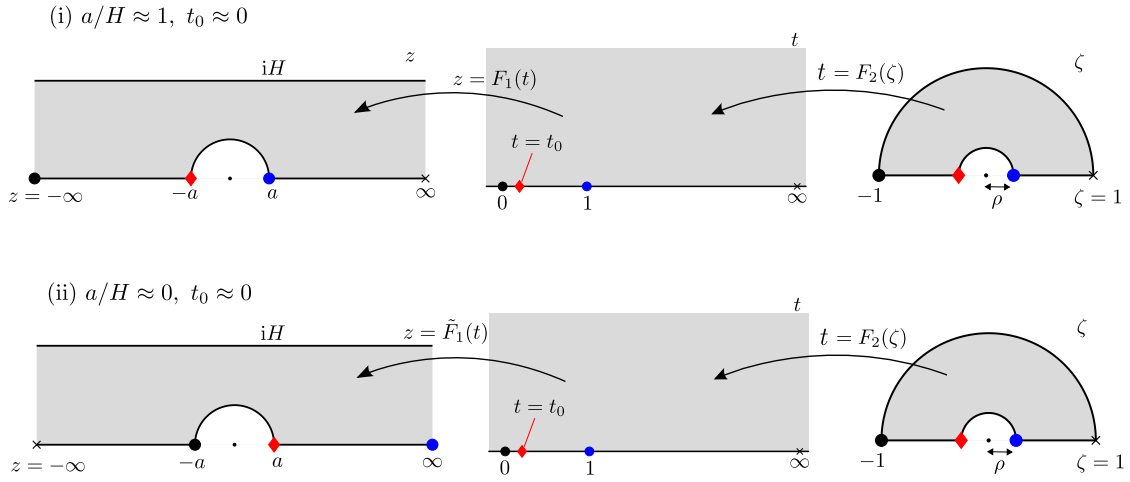

Figure 7.2: The conformal map from the upper half annulus to the half channel outside a semi-circle.

equation always has unknown accessory parameters associated to the target domain. The relationship between the accessory parameters of the conformal mapping and a special function called tau function introduced by Jimbo, Miwa, and Ueno [71] has been revealed by [7,24]. According to [7,24], the explicit expressions for accessory parameters are derived by calculating the zero of tau function associated with the monodromy data of the target domain.

Indeed, with regard to case (A) in Figure 5.5, i.e., the unit circle in a channel, it is possible to make a direct comparison between them. Considering the upper half of the unit circle in a channel region, where the geometry becomes simply connected, the approximation for ρ can be derived by the following procedure. First, as shown in the upper figure of Figure 7.2, the conformal mapping from the upper half plane to the upper half of the unit circle in a channel region is considered. The target domain has four vertices, which means we have one unknown coordinate t_0 in complex t-plane. This accessory parameter $t = t_0$ is given by [7]

$$t_0^{1-\sigma} = \frac{1+\sin\pi\sigma}{1-\sin\pi\sigma}\frac{\Gamma^4(1/4+\sigma/2)\Gamma^2(1-\sigma)}{\Gamma^4(5/4-\sigma/2)\Gamma^2(\sigma-1)}, \qquad H/a = -\cos(\pi\sigma). \tag{7.13}$$

Because this expression comes from the lower orders of the expansion of the tau function around $t = 0$, this expression is accurate when t_0 is small, which corresponds to the case where a/H is large. Now we associate t_0 with the inner radius ρ. A conformal map from

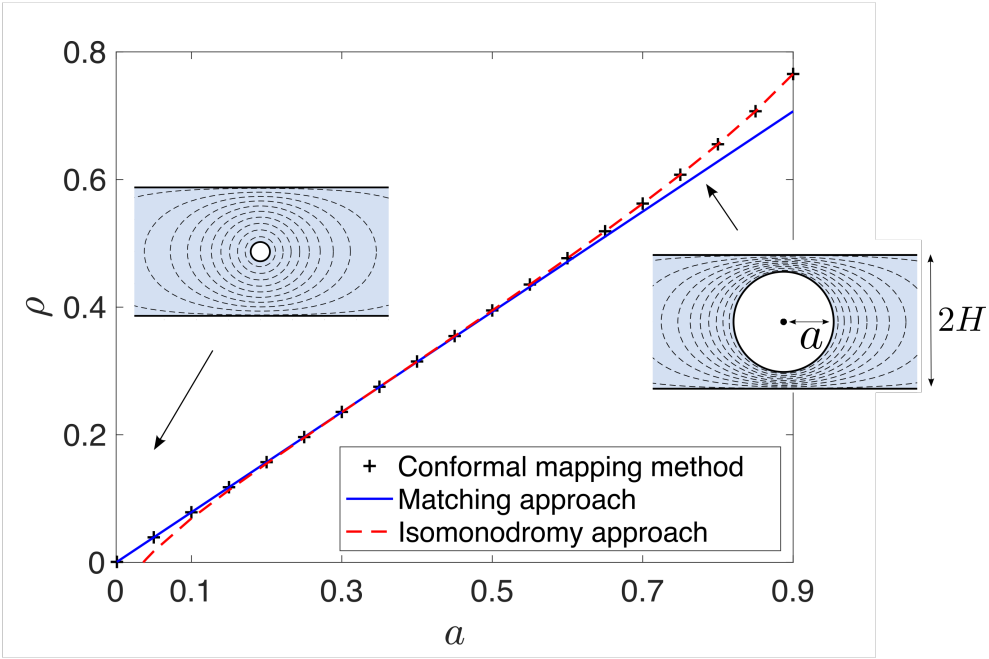

Figure 7.3: Graphs of ρ for a circle in a channel region as calculated by the conformal mapping method, the matching approach, and the isomonodromy approach [8].

the upper annulus region in ζ-plane to the upper half plane in t-plane is defined as

$$t = F_2(\zeta) = \frac{P(\rho,\rho)^2}{P(-\rho,\rho)^2} \cdot \frac{P(-\zeta,\rho)^2}{P(\zeta,\rho)^2}. \tag{7.14}$$

This function $F_2(\zeta)$ maps $\zeta = 1$ to the infinity, $\zeta = -1$ to the origin, $\zeta = \rho$ to $t = 1$, and $\zeta = -\rho$ to $t = t_0$, respectively. The correspondence of the function gives us

$$t_0 = F_2(-\rho) = \frac{P(\rho,\rho)^4}{P(-\rho,\rho)^4} = \prod_{n=1}^{\infty} \left(\frac{1-\rho^{2n-1}}{1+\rho^{2n-1}} \right)^8. \tag{7.15}$$

Figure 7.3 shows a comparison between the estimates from the matching approach (7.7) and from the isomonodromy approach (7.15). Matching is more accurate when the width a is small, while the isomonodromy approach is more accurate when the width a is large. This is natural because the matching approach assumes that the internal circle is small compared to the height of the channel. The isomonodromy approach, however, assumes that the prevertex $t = t_0$ is nearly 0 in order to approximate the tau function, which corresponds to ρ getting large. When combined, these two approximations – each emerging from very different considerations – give excellent estimates across the range of parameters and investigating the relationship between the tau function and the matching approach advocated here is an interesting challenge for the future.

7.3 Estimating accessory parameters for the superhydrophobic surface

As shown in the previous section, the matching approach can provide estimates of a conformal modulus in a conformal mapping problem in doubly connected domains. This section shows that the matching procedure can be extended to provide more general estimates of other accessory parameters as well.

The geometry to be considered happens to be one relevant to a topical problem involving channel flows with superhydrophobic surfaces [102], which is the same region considered in Chapter 6. The period of the channel in the x-direction is $2L$, the distance of displacement of the flat meniscus below to tips of the sidewalls is H, and the distance between the side wall gratings is $2G$ as shown in Figure 7.4. The preimage circular domain D_ζ is taken to be the circular domain in a parametric complex $\zeta = \xi + \mathrm{i}\eta$-plane interior to the unit circle, denoted by C_0, but exterior to two circles C_1 and C_2 each of radius q and having centers at $\pm\delta$, where δ is purely imaginary. The conformal map from D_ζ to the groove region D is known [102] to be given by

$$z = \mathcal{Z}(\zeta) = -\frac{H+G}{\pi}\log\left(\frac{\omega(\zeta,\theta_1(\infty))}{\omega(\zeta,\theta_2(\infty))}\right), \qquad z = x + \mathrm{i}y, \tag{7.16}$$

where

$$\theta_1(\zeta) \equiv \delta + \frac{q^2}{1-\bar{\delta}\zeta}, \qquad \theta_2(\zeta) \equiv -\delta + \frac{q^2}{1+\bar{\delta}\zeta}, \tag{7.17}$$

and where $\omega(.,.)$ is the prime function associated with D_ζ [40]. We note that the circle C_0 in the ζ-plane is mapped to the line $|y| \leq G$ on the imaginary axis in the z-plane, and the inner circles C_1 and C_2 are mapped to the line $x = \pm L$, $|y| \leq H+G$ of the periodic channel. The parameters δ and q depend on the lengths H, G, and L and can easily be solved for given the functional form (7.16) of the conformal mapping. Once again, the prime function $\omega(.,.)$ is readily evaluated using freely available codes [9]. While this procedure is straightforward, it is of interest to examine whether approximate estimates for δ and q are forthcoming from a matching approach akin to that developed in this chapter.

7.3.1 Capacity of predomain

Consider a potential problem for a harmonic $\phi(\xi,\eta)$ on D_ζ where $\phi = \alpha$ on C_1, $\phi = \beta$ on C_2, and $\phi = 0$ on C_0, $\alpha, \beta \in \mathbb{R}$. The analytic extension of ϕ is defined as $W(\zeta) = \phi + \mathrm{i}\chi$ as usual. Suppose that the flux m_α is associated with C_1 and m_β is associated with C_2. For

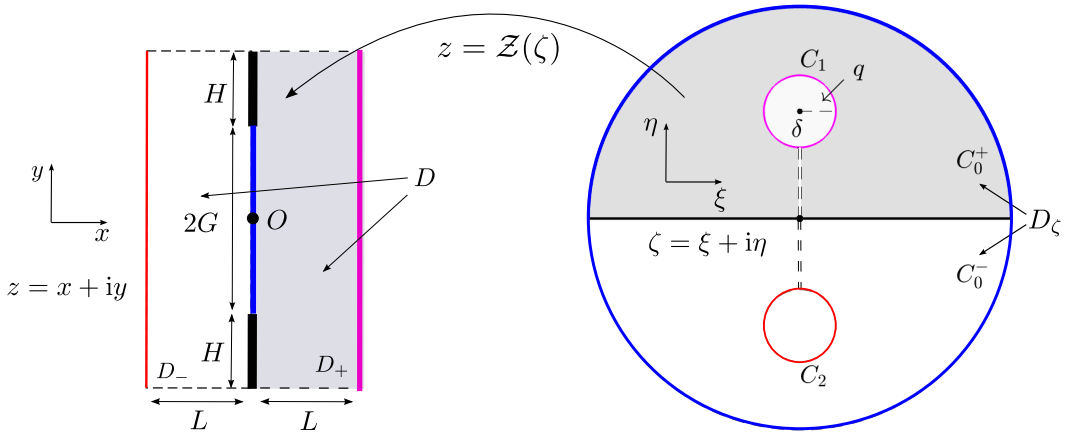

Figure 7.4: The geometry of the superhydrophobic surface (Left) and the triply connected domain (Right).

the two "inner solutions" near to each circle it is easy to argue that

$$W^{(1)}_{\text{inner}}(\zeta) = \frac{m_\alpha}{2\pi}\log\frac{\zeta-\delta}{q} + \alpha, \quad W^{(2)}_{\text{inner}}(\zeta) = \frac{m_\beta}{2\pi}\log\frac{\zeta+\delta}{q} + \beta, \tag{7.18}$$

where the notation should be obvious. Because the sources with strength m_α and m_β lie at $\zeta = \delta$ and $\zeta = -\delta$ respectively, the outer solution is

$$W_{\text{outer}}(\zeta) = \frac{m_\alpha}{2\pi}\log\frac{\zeta-\delta}{|\delta|(\zeta-1/\bar{\delta})} + \frac{m_\beta}{2\pi}\log\frac{\zeta+\delta}{|\delta|(\zeta+1/\bar{\delta})}. \tag{7.19}$$

The matching of constant terms arising from local expansions of (7.18) and (7.19) in the usual way leads to a linear system of equations for m_α and m_β:

$$\begin{cases} \alpha + \dfrac{m_\alpha}{2\pi}\log\dfrac{1}{q} = \dfrac{m_\alpha}{2\pi}\log\left|\dfrac{1}{|\delta|(\delta-1/\bar{\delta})}\right| + \dfrac{m_\beta}{2\pi}\log\left|\dfrac{2\delta}{|\delta|(\delta+1/\bar{\delta})}\right|, \\ \beta + \dfrac{m_\beta}{2\pi}\log\dfrac{1}{q} = \dfrac{m_\alpha}{2\pi}\log\left|\dfrac{2\delta}{|\delta|(\delta+1/\bar{\delta})}\right| + \dfrac{m_\beta}{2\pi}\log\left|\dfrac{1}{|\delta|(-\delta+1/\bar{\delta})}\right|. \end{cases} \tag{7.20}$$

The parameters m_α and m_β therefore satisfy the following linear system:

$$\begin{pmatrix} A & B \\ B & A \end{pmatrix}\begin{pmatrix} m_\alpha \\ m_\beta \end{pmatrix} = \begin{pmatrix} \alpha \\ \beta \end{pmatrix}, \quad A \equiv \frac{1}{2\pi}\log\left|\frac{q}{|\delta|(\delta-1/\bar{\delta})}\right|, \quad B \equiv \frac{1}{2\pi}\log\left|\frac{2\delta}{|\delta|(\delta+1/\bar{\delta})}\right|. \tag{7.21}$$

We can now compute the quantity

$$\text{cap} = \int_{D_\zeta} |\nabla\phi|^2 d\xi d\eta = \int_{\partial D_\zeta} \phi \frac{\partial \phi}{\partial n} ds = -(\alpha m_\alpha + \beta m_\beta) = -\frac{A\alpha^2 - 2\alpha\beta B + A\beta^2}{A^2 - B^2}. \quad (7.22)$$

7.3.2 Capacity of the target domain

This same quantity can be calculated using estimates based on matching in the target region itself. We assume that the distance between the side wall gratings G is small compared to the height of the groove H. Because of the conformal invariance of the boundary value problem, the potential $\Phi(z) \equiv \phi(\zeta(z))$ satisfies

$$\begin{cases} \Phi = 0, & x = 0, \quad -G \le y \le G, \\ \Phi = \alpha, & x = L, \quad -H - G \le y \le H + G, \\ \Phi = \beta, & x = -L, \quad -H - G \le y \le H + G, \\ \dfrac{\partial \Phi}{\partial y} = 0, & -L \le x \le L, \quad y = \pm(H + G), \end{cases} \quad (7.23)$$

where the last flux condition comes from the symmetry of D_ζ about the η-axis. To solve this, consider

$$\Phi = \frac{(\alpha - \beta)x}{2L} + \frac{\alpha + \beta}{2} + \hat{\Phi}, \quad (7.24)$$

where $\hat{\Phi}$ satisfies

$$\begin{cases} \hat{\Phi} = -\dfrac{\alpha + \beta}{2}, & x = 0, \quad -G \le y \le G, \\ \hat{\Phi} = 0, & x = \pm L, \quad -H - G \le y \le H + G, \\ \dfrac{\partial \hat{\Phi}}{\partial y} = 0, & -L \le x \le L, \quad y = \pm(H + G). \end{cases} \quad (7.25)$$

The flux m of $\hat{\Phi}$ associated with the blue portion in Figure 7.4 can now be estimated using the matching approach in the manner developed in this paper. Let the analytic extension of $\hat{\Phi}$ be $\hat{W}(z)$ so that $\hat{\Phi} = \text{Re}[\hat{W}(z)]$. The inner solution for $\hat{W}(z)$ is given by

$$\hat{W}_{\text{inner}}(z) = -\frac{\alpha + \beta}{2} - \frac{m}{2\pi} \log \frac{G}{2} + \frac{m}{2\pi} \log z + \dots. \quad (7.26)$$

Modelling this flux as associated with a point source of strength m at $z = 0$ in the rectangle region, we are going to find the outer solution $\hat{W}_{\text{outer}}(\zeta)$. The potential we need to seek is a solution which satisfies $\hat{\Phi} \equiv \text{Re}[\hat{W}_{\text{outer}}(z)] = 0$ on the left and right sides of a rectangle and $\dfrac{\partial \hat{\Phi}}{\partial y} = 0$ on the top and bottom sides of a rectangle with a source m at the center of

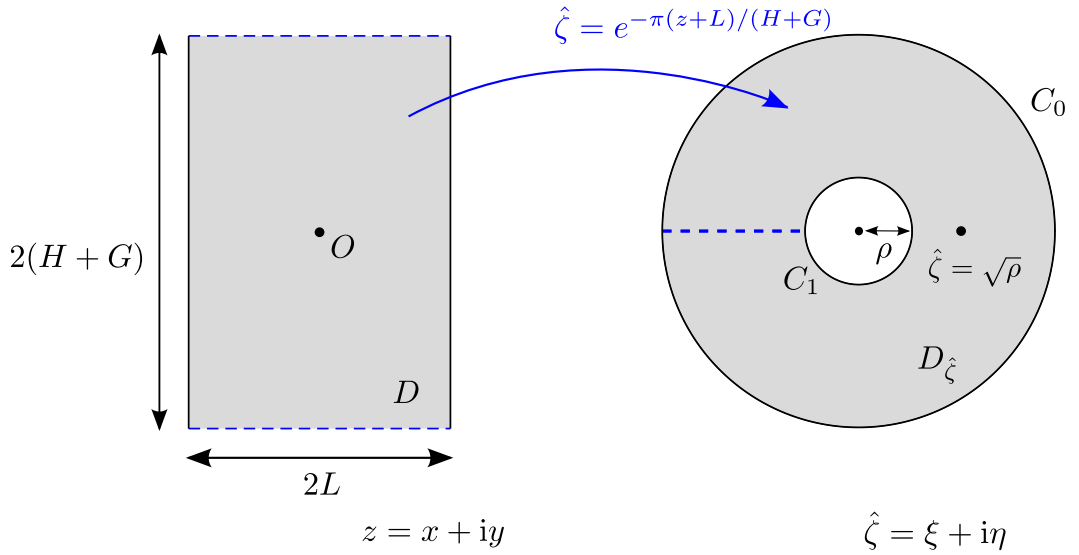

Figure 7.5: Geometry of the exponential maps $\zeta = e^{-\pi(z+L+\mathrm{i}H)/2H}$ (left) and $\hat{\zeta} = e^{-\pi(z+L)/(H+G)}$ (right).

the rectangle. By the Cauchy Riemann equations, the boundary condition on the top and bottom sides becomes that $\mathrm{Im}[\hat{W}_{\mathrm{outer}}(z)]$ is constant on the left and right sides. By using the conformal map $\hat{\zeta} = e^{-\pi(z+L)/(H+G)}$, the rectangle region in the z-plane is transformed into the whole annular domain in the $\hat{\zeta} = \xi + \mathrm{i}\eta$-plane. The figure on the right in Figure 7.5 shows the rectangle and annular domain. The radius of the inner circle is $\rho = e^{-2\pi L/(H+G)}$. The left and right sides of the rectangle are mapped to the boundary of the annulus, and the top and bottom sides of the rectangle are mapped to the same portion $\xi \in [-1, -\rho]$. The location of the point source is now $\hat{\zeta} = \sqrt{\rho}$. The function $Y(\hat{\zeta}) \equiv \hat{W}_{\mathrm{outer}}(z(\hat{\zeta}))$ has a simple source term with a strength m at $\hat{\zeta} = \sqrt{r}$ and satisfies

$$\begin{cases} \mathrm{Re}[Y(\zeta)] = 0, & \zeta \in C_0,\ C_1, \\ \mathrm{Im}[Y(\zeta)] = c_1, & -1 < \xi < -\rho,\ \eta = 0, \\ \mathrm{Im}[Y(\zeta)] = c_2, & \rho < \xi < 1,\ \eta = 0, \end{cases} \tag{7.27}$$

where $c_1, c_2 \in \mathbb{R}$. Note that the last condition of (7.27) comes from the fact that the center line of the rectangle $\{(x, y) | -L < x < L,\ y = 0\}$ is mapped to $\{(\xi, \eta) | \rho < \xi < 1,\ \eta = 0\}$, and by symmetry

$$\frac{\partial \hat{\Phi}}{\partial y} = 0, \quad -L < x < L,\ y = 0. \tag{7.28}$$

Then, the Cauchy Riemann equation means that $\mathrm{Im}[Y(\zeta)]$ is constant on $\rho < \xi < 1,\ \eta = 0$.

Now we define

$$Y(\hat{\zeta}) = \frac{m}{2\pi} \log \left(\frac{P(\hat{\zeta}/\sqrt{\rho}, \rho)\sqrt{\rho}}{P(\hat{\zeta}\sqrt{\rho}, \rho)} \right) - \frac{m}{4\pi} \log \hat{\zeta}. \tag{7.29}$$

The function $Y(\hat{\zeta})$ has a source at $\hat{\zeta} = \sqrt{\rho}$. On $\hat{\zeta} \in C_0$ i.e., $\overline{\hat{\zeta}} = \hat{\zeta}^{-1}$, we have

$$\overline{Y(\hat{\zeta})} = \frac{m}{2\pi} \log \left(\frac{P(\hat{\zeta}^{-1}/\sqrt{\rho}, \rho)\sqrt{\rho}}{P(\hat{\zeta}^{-1}\sqrt{\rho}, \rho)} \right) - \frac{m}{4\pi} \log \hat{\zeta}^{-1} \tag{7.30}$$

$$= \frac{m}{2\pi} \log \left(\frac{P(\hat{\zeta}\sqrt{\rho}, \rho)}{P(\hat{\zeta}/\sqrt{\rho}, \rho)\sqrt{\rho}} \right) + \frac{m}{4\pi} \log \hat{\zeta} = -Y(\hat{\zeta}) \tag{7.31}$$

where we used the properties (2.12) and (2.13). Hence $\mathrm{Re}[Y(\hat{\zeta})] = 0$ on $\hat{\zeta} \in C_0$. It is also easy to show that $\mathrm{Re}[Y(\hat{\zeta})] = 0$ on $\hat{\zeta} \in C_1$. Thus the expression for the outer solution is given as follows:

$$\hat{W}_{\mathrm{outer}}(\hat{\zeta}) = \frac{m}{2\pi} \log \left(\frac{P(\hat{\zeta}/\sqrt{\rho}, \rho)\sqrt{\rho}}{P(\hat{\zeta}\sqrt{\rho}, \rho)} \right) - \frac{m}{4\pi} \log \hat{\zeta}, \tag{7.32}$$

where

$$\hat{\zeta} = e^{-\pi(z+L)/(H+G)}, \qquad \rho = e^{-2\pi L/(H+G)}. \tag{7.33}$$

A local expansion around $\zeta = \sqrt{\rho}$ gives

$$\hat{W}_{\mathrm{outer}}(z) = \frac{m}{2\pi} \log z + \frac{m}{2\pi} \log \left[\frac{\hat{P}(1, \rho)}{P(\rho, \rho)} \cdot \frac{\pi\sqrt{\rho}}{(H+G)} \right] - \frac{m}{4\pi} \log \sqrt{\rho} + \ldots. \tag{7.34}$$

Matching (7.26) and (7.34) implies the following expression for m:

$$m = -\frac{\alpha + \beta}{2} \cdot \frac{2\pi}{\log \left(\dfrac{\pi G \hat{P}(1, \rho)}{2(H+G)P(\rho, \rho)} \cdot \rho^{1/4} \right)}. \tag{7.35}$$

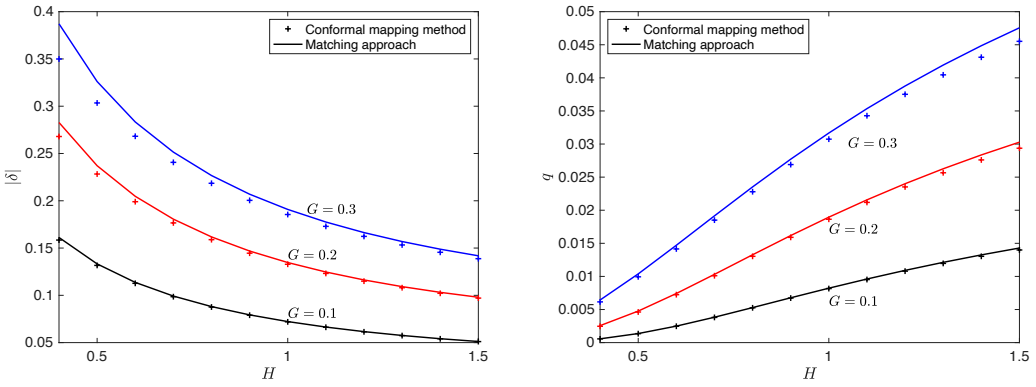

Figure 7.6: The accessory parameter estimations by the matching approach. (Left) Comparison of $|\delta|$. (Right) Comparison of q.

Now, we can calculate the same quantity cap in the target domain as follows:

$$\begin{aligned}\text{cap} &= \int_D |\nabla\phi|^2 dxdy = \frac{H+G}{L}(\alpha-\beta)^2 + \int_{\partial D} \hat{\Phi}\frac{\partial\hat{\Phi}}{\partial n}d\tilde{s} \\ &= \frac{H+G}{L}(\alpha-\beta)^2 + \frac{\alpha+\beta}{2}m \\ &= \frac{H+G}{L}(\alpha-\beta)^2 - \frac{2\pi}{\log\left(\dfrac{\pi G\hat{P}(1,\rho)}{2(H+G)P(\rho,\rho)}\cdot\rho^{1/4}\right)}\frac{(\alpha+\beta)^2}{4}.\end{aligned} \tag{7.36}$$

We now have two expressions for the same quantity: (7.22) and (7.36). On comparing the coefficients in front of α^2 and $\alpha\beta$, we arrive at a system of nonlinear equations for δ and q:

$$\begin{cases} -\dfrac{A}{A^2-B^2} = \dfrac{H+G}{L} - \dfrac{\pi}{2\log\left(\dfrac{\pi G\hat{P}(1,\rho)}{2(H+G)P(\rho,\rho)}\cdot\rho^{1/4}\right)}, \\ \dfrac{B}{A^2-B^2} = -\dfrac{(H+G)}{L} - \dfrac{\pi}{2\log\left(\dfrac{\pi G\hat{P}(1,\rho)}{2(H+G)P(\rho,\rho)}\cdot\rho^{1/4}\right)}. \end{cases} \tag{7.37}$$

Indeed, after some algebra, these can be solved to give

$$\begin{cases} \delta = \mathrm{i}\left(\dfrac{1}{C} - \sqrt{\dfrac{1}{C^2} - 1}\right), \quad C \equiv \dfrac{\pi G}{2(H+G)} \cdot \dfrac{\hat{P}(1,\rho)}{P(\rho,\rho)}, \quad \rho \equiv e^{-2\pi L/(H+G)}. \\ q = 2\sqrt{\rho}\left(C - \dfrac{1}{C} + \sqrt{\dfrac{1}{C^2} - 1}\right). \end{cases} \tag{7.38}$$

Figure 7.6 shows how well these formulas predict the values of δ and q. Similar to the previous results, the matching approach can estimate these parameters even when G becomes large relative to H.

7.4 Estimating accessory parameters for the two slits in a channel

Here new formulas are derived for the accessory parameters associated with a conformal mapping to the channel region which has two slits. First it is important to count the number of parameters in the triply connected circular domain. For doubly connected domains, it is enough to consider the annular domain with radius ρ, which black only one parameter in the predomain (see Chapter 2). For triply connected domains, it is assumed that one inner circle lies at the centre and the other inner circle lies at $z = \tilde{\delta}$, $\tilde{\delta} \in \mathbb{R}$. The radii of these two circles are also parameters associated with the predomain, so there are 3 parameters in total.

Now we set the original domain as triply connected domain with the unit circle for the outer boundary with two inner circles. The centre of these circles are set to $\zeta = \delta$ and $\zeta = -\delta$ respectively, but the radii are q_1, q_2. The geometry is shown in Figure 7.7.

First consider a potential problem for a harmonic ϕ on D_ζ where $\phi = \alpha$ on C_1, $\phi = \beta$ on C_2, and $\phi = 0$ on C_0. Similar to the previous section, suppose that the flux m_α is associated with C_1 and m_β is associated with C_2. The matching of constant terms with inner and outer solutions gives the linear system of equations for m_α and m_β:

$$\begin{cases} \alpha + \dfrac{m_\alpha}{2\pi}\log\dfrac{1}{q_1} = \dfrac{m_\alpha}{2\pi}\log\left|\dfrac{1}{|\delta|(\delta - 1/\bar{\delta})}\right| + \dfrac{m_\beta}{2\pi}\log\left|\dfrac{2\delta}{|\delta|(\delta + 1/\bar{\delta})}\right|, \\ \beta + \dfrac{m_\beta}{2\pi}\log\dfrac{1}{q_2} = \dfrac{m_\alpha}{2\pi}\log\left|\dfrac{2\delta}{|\delta|(\delta + 1/\bar{\delta})}\right| + \dfrac{m_\beta}{2\pi}\log\left|\dfrac{1}{|\delta|(-\delta + 1/\bar{\delta})}\right|. \end{cases} \tag{7.39}$$

Thus we have a linear system for m_α and m_β:

$$\begin{pmatrix} A & B \\ B & C \end{pmatrix}\begin{pmatrix} m_\alpha \\ m_\beta \end{pmatrix} = \begin{pmatrix} \alpha \\ \beta \end{pmatrix}, \tag{7.40}$$

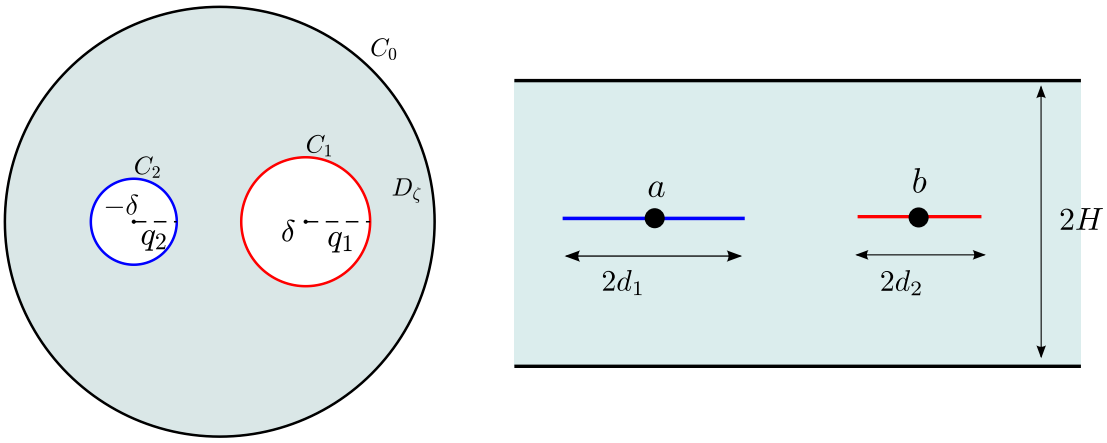

Figure 7.7: (Left) The triply connected domain. (Right) Two slits in a channel.

where

$$A \equiv \frac{1}{2\pi}\log\left(\frac{q_1}{\delta(\delta-1/\delta)}\right), \quad B \equiv \frac{1}{2\pi}\log\left(\frac{2\delta}{\delta(\delta+1/\delta)}\right), \quad C \equiv \frac{1}{2\pi}\log\left(\frac{q_2}{\delta(\delta-1/\delta)}\right), \tag{7.41}$$

where we have used $\delta \in \mathbb{R}$. We can now compute the quantity

$$\text{cap} = \int_{D_\zeta} |\nabla\phi|^2 d\xi d\eta = \int_{\partial D_\zeta} \phi \frac{\partial \phi}{\partial n} ds = -(\alpha m_\alpha + \beta m_\beta) = -\frac{C\alpha^2 - 2\alpha\beta B + A\beta^2}{AC - B^2}. \tag{7.42}$$

The capacity (7.42) is associated to the capacity of a channel with height $2H$, which contains two slits with lengths $2d_1$ and $2d_2$, $d_1, d_2 > 0$, at the center line of the channel. The coordinates of the centres of two slits are set to be a and b, $a, b \in \mathbb{R}$, respectively. We consider a potential problem for a harmonic function where $\phi = \alpha$ on the right slit, $\phi = \beta$ on the left slit, and $\phi = 0$ on the boundary of the channel. First from the view point of the outer observer, there is a point source at the centre of each slit and the strengths of two sources defined by m_α and m_β, are unknown. The two inner solutions are then given by

$$W^{(1)}_{\text{inner}}(z) = \alpha - \frac{m_\alpha}{2\pi}\log\left(\frac{d_1}{2(z-a)}\right), \tag{7.43}$$

$$W^{(2)}_{\text{inner}}(z) = \beta - \frac{m_\beta}{2\pi}\log\left(\frac{d_2}{2(z-b)}\right). \tag{7.44}$$

The outer solution is given by the summation of the two point sources at the center line of

the channel:

$$W_{\text{outer}}(z) = \frac{m_\alpha}{2\pi} \log\tanh\left(\frac{\pi(z-a)}{4H}\right) + \frac{m_\beta}{2\pi} \log\tanh\left(\frac{\pi(z-b)}{4H}\right). \tag{7.45}$$

By using the matched asymptotic expansions of two inner solutions (7.43) and (7.44), and one outer solution (7.45), we have a linear system for m_α and m_β as follows:

$$\begin{pmatrix} \hat{A} & \hat{B} \\ \hat{B} & \hat{C} \end{pmatrix} \begin{pmatrix} m_\alpha \\ m_\beta \end{pmatrix} = \begin{pmatrix} \alpha \\ \beta \end{pmatrix}, \tag{7.46}$$

where

$$\hat{A} = \frac{1}{2\pi} \log\frac{\pi d_1}{8H}, \quad \hat{B} = \frac{1}{2\pi} \log\tanh\frac{\pi(b-a)}{4H}, \quad \hat{C} = \frac{1}{2\pi} \log\frac{\pi d_2}{8H}. \tag{7.47}$$

Using the same technique as (7.42), the capacity of this geometry is given by

$$\text{cap} = -\frac{\hat{C}\alpha^2 - 2\alpha\beta\hat{B} + \hat{A}\beta^2}{\hat{A}\hat{C} - \hat{B}^2}. \tag{7.48}$$

Now we have two expressions for capacities (7.42) and (7.48). Because of the conformal invariance of the conformal capacity, these expressions must be consistent. By comparing the coefficients of (7.42) and (7.48), estimates for the accessory parameters q_1, q_2, and δ are derived. More precisely,

$$\begin{cases} \dfrac{q_1}{1-\delta^2} = \dfrac{\pi d_1}{8H} \\ \dfrac{2\delta}{1+\delta^2} = \tanh\left[\dfrac{\pi(b-a)}{4H}\right] \\ \dfrac{q_2}{1-\delta^2} = \dfrac{\pi d_2}{8H}. \end{cases} \tag{7.49}$$

Thus, the explicit expressions for these parameters are derived:

$$\begin{cases} \delta = \dfrac{1}{C} - \sqrt{\dfrac{1}{C^2} - 1}, \quad C = \tanh\left[\dfrac{\pi(b-a)}{4H}\right], \\ q_1 = \dfrac{\pi d_1}{8H}(1-\delta^2), \\ q_2 = \dfrac{\pi d_2}{8H}(1-\delta^2). \end{cases} \tag{7.50}$$

In order to check the accuracy of the estimate, the conformal mapping approach described in [40] is used. The accuracy of the expressions can be verified by considering

the logarithmic Cayley map:

$$\chi(\zeta) = \frac{c_\chi}{\pi} \log\left(-\frac{\omega(\zeta,1)}{\omega(\zeta,-1)}\right), \quad c_\chi \in \mathbb{R}. \tag{7.51}$$

This function maps the triply connected domain to the channel with horizontal two slits on the real axis. The parameters c_χ, δ, q_1, and q_2 are obtained by solving the following nonlinear equations such that

$$\begin{cases} \chi(\delta + q_1) = b + d_1, \\ \chi(\delta - q_1) = b - d_1, \\ \chi(-\delta + q_2) = a + d_2, \\ \chi(-\delta - q_2) = a - d_2. \end{cases} \tag{7.52}$$

These parameters can be solved by the nonlinear optimizations such as Newton's method.

The table 7.1 shows the numerical comparison between the matching approach and the conformal mapping methods. These three examples show that the matching approach gives us a good estimate for these parameters.

Table 7.1: Numerical comparison between the matching approach and the conformal mapping method. The values calculated by the matching approach are in the bracket.

	d_1	d_2	$b-a$	δ	q_1	q_2
Case 1	0.1148	0.0758	0.5582	0.4 (0.4123)	0.075 (0.0748)	0.05 (0.0494)
Case 2	0.1950	0.1270	1.1599	0.7 (0.7216)	0.075 (0.0734)	0.05 (0.0478)
Case 3	0.2367	0.1520	0.6169	0.4 (0.4499)	0.15 (0.1483)	0.1 (0.0952)

7.5 Conclusion

By presenting a series of examples and comparing with numerical calculations, this chapter has demonstrated a practical procedure based on asymptotic matching of suitable outer and inner solutions to provide estimates of the capacity associated with multiply connected domains. The estimates show excellent agreement when there is a good separation of scales between the inner and outer regions, a feature on which the matching idea relies [68,146,150]. From the selection of examples explored here, it should be clear that the idea is very general and the approach can be applied to a wide variety of geometries. On a technical note, it is worth remarking that it is usual when using matched asymptotics to introduce a rescaled variable to distinguish the inner region from the outer region and this can be important when doing matching at higher orders in any asymptotic expansions. Here, however, this rescaling has not been introduced explicitly since the estimates for capacity

derived here involve only the leading order asymptotics in each region. In principle, more accurate estimates can be obtained by higher order matching, and then the introduction of suitably scaled inner and outer variables is advised.

As shown in this chapter, the proposed approach has the connection to the isomonodromy approach. The research on the connection between the conformal capacity and tau functions is a future work.

Chapter 8

Summary

In this thesis new methods for the quantification of effective parameters arising in transport theory have been developed. Using the prime function, analytical formulas can be obtained for the calculation of these parameters.

Chapter 1 introduced three important quantities, namely, electrical resistivity, electrical capacity, and slip lengths. This chapter explained that these quantities characterize the properties of electrical performance or fluid flows in channels. It is also mentioned that due to the geometry these flows satisfy mixed boundary conditions in multiply connected domains, which are sometimes difficult to solve.

Chapter 2 followed the book [40] and introduced the prime function. An explanation of the important properties of conformal mappings and three examples of conformal mappings are described. It is explained that the prime function is also used to solve Dirichlet-type boundary value problem by so-called Schwarz integral formulas.

Chapter 3 has developed a natural extension of the Schwarz integral formulas, "generalized Schwarz integral formulas", which can be used to solve mixed boundary value problems in multiply connected domains. This can be done by introducing radial slit maps, which transform mixed boundary value problems into Dirichlet boundary value problems. Using the prime function and the Schwarz integral formulas introduced in Chapter 2, it has been shown that the integrals can calculate the shape of hollow vortex wakes behind a wedge and the longitudinal flow in heat sinks.

Chapter 4 has developed a new resistivity measurement for holey samples. Using the prime function and the cross-ratio identity, i.e., Fay's trisecant identity, a new van der Pauw equation for holey samples is developed and two conjectures proposed by [138] is proven. A new method for measuring the resistivity of holey samples can be obtained by considering the lower envelope's formulas.

Chapter 5 has formulated a new method for calculating electrical capacities of multiply connected domains. This can be done by using the matched asymptotic expansions for

inner solutions and outer solutions. Several numerical results show that the new method gives good estimates for the capacities of multiply connected domains.

In Chapter 6, an analytical formula is proposed for the slip lengths of superhydrophobic channel flow with partially invaded grooves. By using the horizontal slit map introduced in Chapter 2, the boundary value problem can be reduced to a problem on a triply connected domain, which can be solved by the Schwarz integral formulas. The slip lengths of the channel are calculated from the explicit expression for the flow.

Chapter 7 has explained parameter problems in conformal mappings, namely, accessory parameter problems of multiply connected domains. As presented in several examples, the matched asymptotic expansions give good estimates for the accessory parameters associated to conformal mappings for multiply connected domains.

The main purpose of this thesis is to develop new mathematical formulas for the calculation of physical quantities arising in transport theory. The techniques developed here are applicable to the calculation of effective parameters in many areas, so it would be interesting to apply these techniques to the other areas of transport phenomena.

Appendix A

Appendix

A.1 The positiveness of $L(e^{\mathrm{i}\phi})$ for $0 < \phi < 2\pi$

First, we consider the derivative of $L(\zeta)$ defined in (2.15) as follows:

$$M(\zeta) \equiv \zeta \frac{\partial L}{\partial \zeta}. \tag{A.1}$$

Because we have another representation of $L(\mu/\nu) - L(\mu\nu)$ as stated in (4.67), we can consider a limit of each side:

$$\lim_{\nu\to 1} \frac{L(\mu/\nu) - L(\mu\nu)}{1-\nu} = \mu \lim_{\nu\to 1} \left(\frac{1}{\nu} \frac{L(\mu/\nu) - L(\mu)}{\mu/\nu - \mu} + \frac{L(\mu) - L(\mu\nu)}{\mu - \mu\nu} \right) = 2M(\mu). \tag{A.2}$$

The right hand side is, from the definition in (2.11),

$$\lim_{\nu\to 1} \frac{1}{1-\nu} \frac{\hat{P}(1)^2 P(\mu^2) P(\nu^2)}{P(\nu/\mu) P(\mu/\nu) P(\mu\nu)^2} = 2 \frac{\hat{P}(1)^3 P(\mu^2)}{P(1/\mu) P(\mu)^3}. \tag{A.3}$$

We therefore find an alternative representation of $M(\zeta)$:

$$M(\zeta) = \frac{\hat{P}(1)^3 P(\zeta^2)}{P(1/\zeta) P(\zeta)^3}. \tag{A.4}$$

Consequently $M(e^{\mathrm{i}\phi})$ is found to be

$$M(e^{\mathrm{i}\phi}) = \frac{\hat{P}(1)^3 P(e^{2\mathrm{i}\phi})}{P(1/e^{\mathrm{i}\phi}) P(e^{\mathrm{i}\phi})^3} = \frac{\mathrm{i}}{8} C(\phi) \frac{\sin\phi}{\sin^4 \dfrac{\phi}{2}}, \tag{A.5}$$

where

$$C(\phi) = \hat{P}(1)^3 \prod_{n=1}^{\infty} \frac{(1+\rho^{4n}-2\rho^{2n}\cos 2\phi)}{(1+\rho^{4n}-2\rho^{2n}\cos\phi)^4} > 0. \tag{A.6}$$

Therefore, because $\frac{\partial L}{\partial \phi}(e^{\mathrm{i}\phi}) = \mathrm{i}M(e^{\mathrm{i}\phi})$, $L(e^{\mathrm{i}\phi})$ decreases when $0 < \phi < \pi$, and $L(e^{\mathrm{i}\phi})$ increases when $\pi < \phi < 2\pi$. The minimum of $L(e^{\mathrm{i}\phi})$ is $L(e^{\mathrm{i}\pi}) = L(-1)$ where $L(-1)$ can be calculated explicitly to be

$$L(-1) = \frac{1}{4} + 2\sum_{n=1}^{\infty} \frac{\rho^{2n}}{(1+\rho^{2n})^2} > 0. \tag{A.7}$$

Therefore $L(e^{\mathrm{i}\phi})$ is positive over this range of ϕ.

A.2 Proof of the properties of α_θ and β_θ

Here we will prove that for $0 < \theta < \pi$, α_θ is a monotonically increasing function and β_θ is a monotonically decreasing function with respect to θ, that is,

$$\frac{\partial \alpha_\theta}{\partial \theta} > 0, \qquad \frac{\partial \beta_\theta}{\partial \theta} < 0. \tag{A.8}$$

We will prove it using the integrated Fay trisecant identity. From (4.49),

$$\frac{\partial \alpha_\theta}{\partial \theta} X_{0,\pi,\theta} + \frac{\partial \beta_\theta}{\partial \theta} Y_{0,\pi,\theta} = 0, \tag{A.9}$$

which means the sign of $\partial\alpha_\theta/\partial\theta$ is opposite to $\partial\beta_\theta/\partial\theta$. By a log-sum and sum-log inequality,

$$\begin{aligned} &\log[\alpha_{\theta'} X_{0,\pi,\theta} + \beta_{\theta'} Y_{0,\pi,\theta}] \\ &\qquad \geq \frac{1}{2\pi}\int_0^{2\pi} \log[A(0,\theta',\rho e^{\mathrm{i}\phi})X_{0,\pi,\theta} + B(\pi,\theta',\rho e^{\mathrm{i}\phi})Y_{0,\pi,\theta}]d\phi \\ &\qquad = \frac{1}{2\pi}\int_0^{2\pi} \log[A(0,\theta,\rho e^{\mathrm{i}\phi})X_{0,\pi,\theta} + B(\pi,\theta,\rho e^{\mathrm{i}\phi})Y_{0,\pi,\theta}]d\phi = 0, \end{aligned} \tag{A.10}$$

where we used (4.87) and (4.88). This means

$$\alpha_{\theta'} X_{0,\pi,\theta} + \beta_{\theta'} Y_{0,\pi,\theta} \geq 1. \tag{A.11}$$

From the Fay trisecant identity, $\alpha_\theta X_{0,\pi,\theta} + \beta_\theta Y_{0,\pi,\theta} = 1$, so

$$(\alpha_{\theta'} - \alpha_\theta) X_{0,\pi,\theta} + (\beta_{\theta'} - \beta_\theta) Y_{0,\pi,\theta} \geq 0 \tag{A.12}$$

for $0 < \theta' < \pi$. Hence, together with (A.9), we can obtain an inequality for the second derivatives of α_θ and β_θ as follows:

$$\frac{\partial^2 \alpha_\theta}{\partial \theta^2} X_{0,\pi,\theta} + \frac{\partial^2 \beta_\theta}{\partial \theta^2} Y_{0,\pi,\theta} \geq 0. \tag{A.13}$$

When we take the derivative of (A.9) with respect to θ, we get

$$\frac{\partial \alpha_\theta}{\partial \theta}\frac{\partial X_{0,\pi,\theta}}{\partial \theta} + \frac{\partial \beta_\theta}{\partial \theta}\frac{\partial Y_{0,\pi,\theta}}{\partial \theta} + \frac{\partial^2 \alpha_\theta}{\partial \theta^2} X_{0,\pi,\theta} + \frac{\partial^2 \beta_\theta}{\partial \theta^2} Y_{0,\pi,\theta} = 0. \tag{A.14}$$

Thus, from (A.13),

$$\frac{\partial \alpha_\theta}{\partial \theta}\frac{\partial X_{0,\pi,\theta}}{\partial \theta} + \frac{\partial \beta_\theta}{\partial \theta}\frac{\partial Y_{0,\pi,\theta}}{\partial \theta} = -\frac{\partial^2 \alpha_\theta}{\partial \theta^2} X_{0,\pi,\theta} - \frac{\partial^2 \beta_\theta}{\partial \theta^2} Y_{0,\pi,\theta} \leq 0. \tag{A.15}$$

The signs of $\partial X_{0,\pi,\theta}/\partial\theta$ and $\partial Y_{0,\pi,\theta}/\partial\theta$ can be determined for $0 < \theta < \pi$, that is,

$$\begin{aligned} \frac{\partial X_{0,\pi,\theta}}{\partial \theta} &= \mathrm{i} X_{0,\pi,\theta}[K(-e^{\mathrm{i}\theta}) - K(-e^{-\mathrm{i}\theta})] = \mathrm{i} X_{0,\pi,\theta}[2K(-e^{\mathrm{i}\theta}) - 1] < 0, \\ \frac{\partial Y_{0,\pi,\theta}}{\partial \theta} &= \mathrm{i} Y_{0,\pi,\theta}[K(e^{\mathrm{i}\theta}) - K(e^{-\mathrm{i}\theta})] = \mathrm{i} Y_{0,\pi,\theta}[2K(e^{\mathrm{i}\theta}) - 1] > 0. \end{aligned} \tag{A.16}$$

where we used the positiveness of $L(e^{\mathrm{i}\phi})$ to state that the imaginary part of $K(e^{\mathrm{i}\phi})$ is monotonically increasing and $K(e^{\mathrm{i}\pi}) = 1/2$. Because the sign of $\partial\alpha_\theta/\partial\theta$ is opposite to $\partial\beta_\theta/\partial\theta$ as stated in (A.9), we can conclude that

$$\frac{\partial \alpha_\theta}{\partial \theta} > 0, \qquad \frac{\partial \beta_\theta}{\partial \theta} < 0. \tag{A.17}$$

References

[1] M. J. Ablowitz and A. S. Fokas. *Complex variables: introduction and applications*. Cambridge University Press, 2003.

[2] A. Acker. Heat flow inequalities with applications to heat flow optimization problems. *SIAM J. Math. Anal.*, 8(4):604–618, 1977.

[3] L. V. Ahlfors. *Conformal invariants: topics in geometric function theory*, volume 371. Am. Math. Soc., 2010.

[4] A. Ahuja, J. A. Taylor, V. Lifton, A. A. Sidorenko, T. R. Salamon, E. J. Lobaton, P. Kolodner, and T. N. Krupenkin. Nanonails: a simple geometrical approach to electrically tunable superlyophobic surfaces. *Langmuir*, 24(1):9–14, 2008.

[5] G. D. Anderson, M. K. Vamanamurthy, and M. Vuorinen. Conformal invariants, quasiconformal maps, and special functions. In *Quasiconformal space mappings*, pages 1–19. Springer, 1992.

[6] F. P. Andriulli, K. Cools, I. Bogaert, and E. Michielssen. On a well-conditioned electric field integral operator for multiply connected geometries. *IEEE Trans. on Antennas and Propagation*, 61(4):2077–2087, 2012.

[7] T. Anselmo, B. Carneiro da Cunha, R. Nelson, and D. G. Crowdy. Schwarz–Christoffel accessory parameter for quadrilaterals via isomonodromy. *J. Phys. A: Math Theor.*, 53:355201, 2020.

[8] T. Anselmo, R. Nelson, B. C. da Cunha, and D. G. Crowdy. Accessory parameters in conformal mapping: exploiting the isomonodromic tau function for Painlevé VI. *Proc. R. Soc. A*, 474(2216):20180080, 2018.

[9] Applied and Computational Complex Analysis Group. Github website. *https://github.com/ACCA-Imperial*, (ACCA).

[10] Applied and Computational Complex Analysis Group. Github website (philip channel flow). *https://github.com/ACCA-Imperial/Philip_ChannelFlow*, (ACCA).

[11] U. Ausserlechner. The classical hall effect in multiply-connected plane regions part i: Topologies with stream function. *J. Appl. Math. Phys.*, 7(9):1968–1996, 2019.

[12] U. Ausserlechner. Complementary symmetric Hall plates with a hole and four outer extended contacts. *Proc. Royal. Soc. A*, 478(2267):20220433, 2022.

[13] P. J. Baddoo and D. G. Crowdy. Periodic Schwarz–Christoffel mappings with multiple boundaries per period. *Proc. Royal. Soc. A.*, 475:20190225, 2019.

[14] P. J. Baddoo and L. N. Trefethen. Log-lightning computation of capacity and green's function. *Maple Transactions*, 1(1), 2021.

[15] H. F. Baker. *Abelian functions: Abel's theorem and the allied theory of theta functions.* Cambridge University Press, 1995.

[16] G. K. Batchelor. On steady laminar flow with closed streamlines at large Reynolds number. *J. Fluid Mech.*, 1(2):177–190, 1956.

[17] G. K. Batchelor. *An introduction to fluid dynamics.* Cambridge University Press, 2000.

[18] M. Z. Bazant. Conformal mapping of some non-harmonic functions in transport theory. *Proc. Royal Soc. A*, 460(2045):1433–1452, 2004.

[19] G. E. Bell and J. Crank. Influence of imbedded particles on steady-state diffusion. *J. Chem. Soc. Faraday Trans. 2*, 70:1259–1273, 1974.

[20] D. Betsakos, A. Solynin, and M. Vuorinen. Conformal capacity of hedgehogs. *Conform. Geom. Dyn.*, 27(02):55–97, 2023.

[21] T. Biben and L. Joly. Wetting on nanorough surfaces. *Phys. Rev. Lett.*, 100:186103, May 2008.

[22] R. B. Bird. Transport phenomena. *Appl. Mech. Rev.*, 55(1):R1–R4, 2002.

[23] J. B. Campbell. Finite difference techniques for ring capacitors. *J. Eng. Math.*, 9(1):21–28, 1975.

[24] B. Carneiro da Cunha, Nejad S. A., T. Anselmo, Nelson R., and D. G. Crowdy. Zeros of the isomonodromic tau functions in constructive conformal mapping of polycircular arc domains: the n-vertex case. *J. Phys. A: Math Theor.*, 55:025201, 2022.

[25] W. H. Chang. Analytical IC metal-line capacitance formulas. *IEEE Trans. Microw. Theory Tech.*, 24(9):608–611, 1976.

[26] X. Chen, Z. Zhang, S. Yu, and T. G. Zsurzsan. Fringing effect analysis of parallel plate capacitors for capacitive power transfer application. In *2019 IEEE 4th Inter. Future Ener. Electronics Conference (IFEEC)*, pages 1–5. IEEE, 2019.

[27] T. W. Christopher and S. G. Llewellyn Smith. Hollow vortex in a corner. *J. Fluid Mech.*, 908:R2, 2021.

[28] J. L. Cieśliński. Modified van der Pauw method based on formulas solvable by the Banach fixed point method. *Thin Solid Films*, 522:314–317, 2012.

[29] D. G Crowdy. The Schwarz-Christoffel mapping to bounded multiply connected polygonal domains. *Proc. Roy. Soc. A*, 461:2653–2678, 2005.

[30] D. G Crowdy. Schwarz-Christoffel mappings to unbounded multiply connected polygonal regions. *Math. Proc. Camb. Phil. Soc.*, 142:319–339, 2007.

[31] D. G. Crowdy. Geometric function theory: a modern view of a classical subject. *Nonlinearity*, 21(10):T205, 2008.

[32] D. G. Crowdy. The Schwarz problem in multiply connected domains and the Schottky–Klein prime function. *Complex Variables and Elliptic Equations*, 53(3):221–236, 2008.

[33] D. G. Crowdy. Explicit solution of a class of Riemann-Hilbert problems. *Ann. Univ. Paedagog. Crac. Stud. Math.*, 8(1):5–18, 2009.

[34] D. G. Crowdy. A new calculus for two dimensional vortex dynamics. *Theor. Comput. Fluid Dyn.*, 24:9–24, 2010.

[35] D. G. Crowdy. Slip length for longitudinal shear flow over a dilute periodic mattress of protruding bubbles. *Phys. Fluids*, 22(12):121703, 2010.

[36] D. G. Crowdy. Frictional slip lengths and blockage coefficients. *Phys. Fluids*, 23:091703, 2011.

[37] D. G. Crowdy. Analytical formulae for source and sink flows in multiply connected domains. *Theor. Comput. Fluid Dyn.*, 27(1):1–19, 2013.

[38] D. G. Crowdy. Fourier–Mellin transforms for circular domains. *Comput. Methods Funct. Theory.*, 15:655–687, 2015.

[39] D. G. Crowdy. Perturbation analysis of subphase gas and meniscus curvature effects for longitudinal flows over superhydrophobic surfaces. *J. of Fluid Mech.*, 822:307–326, 2017.

[40] D. G. Crowdy. *Solving Problems in Multiply Connected Domains.* CBMS-NSF Regional Conf. Ser. in Appl. Math. SIAM, 2020.

[41] D. G. Crowdy. Slip length formulas for longitudinal shear flow over a superhydrophobic grating with partially filled cavities. *J. Fluid Mech.*, 925, 2021.

[42] D. G. Crowdy. Superhydrophobic annular pipes: a theoretical study. *J. Fluid Mech.*, 906:A15, 2021.

[43] D. G. Crowdy and A. S. Fokas. Conformal mappings to a doubly connected polycircular arc domain. *Proc. R. Soc. A*, 463(2084):1885–1907, 2007.

[44] D. G. Crowdy, A. S. Fokas, and C. C. Green. Conformal mappings to multiply connected polycircular arc domains. *Comput. Methods and Funct. Theory*, 11(2):685–706, 2012.

[45] D. G. Crowdy and C. C. Green. Analytical solutions for von Kármán streets of hollow vortices. *Phys. Fluids*, 23(12):126602, 2011.

[46] D. G. Crowdy, E. H. Kropf, C. C. Green, and M. M. S. Nasser. The Schottky–Klein prime function: a theoretical and computational tool for applications. *IMA J. Appl. Math.*, 81(3):589–628, 2016.

[47] D. G. Crowdy, S. G. Llewellyn Smith, and D. V. Freilich. Translating hollow vortex pairs. *Eur. J. Mech. B Fluids*, 37:180–186, 2013.

[48] D. G. Crowdy and J. S. Marshall. Conformal mappings between canonical multiply connected domains. *Comput. Methods. Funct. Theory*, 6(1):59–76, 2006.

[49] D. G. Crowdy and J. S. Marshall. Computing the Schottky-Klein prime function on the Schottky double of planar domains. *Comput. Methods Funct. Theory*, 7:293–308, 2007.

[50] R. L. M. Dang and N. Shigyo. Coupling capacitances for two-dimensional wires. *IEEE Electron Device Letters*, 2(8):196–197, 1981.

[51] D. T. DiPerna and T. K. Stanton. Sound scattering by cylinders of noncircular cross section: A conformal mapping approach. *J. Acoust. Soc. Am.*, 96(5):3064–3079, 1994.

[52] V. N. Dubinin and N. G. Kruzhilin. *Condenser capacities and symmetrization in geometric function theory.* Springer, 2014.

[53] J. J. Duderstadt and W. R. Martin. Transport theory. *Transport theory*, 1979.

[54] E. A. Ekimov, V. A. Sidorov, E. D. Bauer, N. N. Mel'Nik, N. J. Curro, J. D. Thompson, and S. M. Stishov. Superconductivity in diamond. *Nature*, 428(6982):542–545, 2004.

[55] M. I. Elmasry. Digital MOS integrated circuits. *New York*, 1981.

[56] H. M. Farkas and I. Kra. *Riemann surfaces*. Springer, 1992.

[57] J. D. Fay. *Theta functions on Riemann surfaces*, volume 352. Springer, 2006.

[58] A. S. Fokas and A. A. Kapaev. On a transform method for the laplace equation in a polygon. *IMA J. Appl. Math.*, 68(4):355–408, 2003.

[59] J. B. J. Fourier. *The analytical theory of heat*. Courier Corporation, 2003.

[60] D. Gaier. Capacitance and the conformal module of quadrilaterals. *Journal of mathematical analysis and applications*, 70(1):236–239, 1979.

[61] Z. Ge, H. Holmgren, M. Kronbichler, L. Brandt, and G. Kreiss. Effective slip over partially filled microcavities and its possible failure. *Phys. Rev. Fluids*, 3:054201, May 2018.

[62] C. Green. *Mathematical techniques for free boundary problems with multiple boundaries*. PhD thesis, Imperial College London, 2013.

[63] H. Hakula, M. M. S. Nasser, and M. Vuorinen. Conformal capacity and polycircular domains. *arXiv preprint arXiv:2202.12922*, 2022.

[64] J. C. Hauge and D. G. Crowdy. A new approach to the complex helmholtz equation with applications to diffusion wave fields, impedance spectroscopy and unsteady stokes flow. *IMA J. Appl. Math.*, 86(6):1287–1326, 2021.

[65] D. A. Hejhal. *Theta functions, kernel functions and Abelian integrals*, volume 129. American Mathematical Soc., 1972.

[66] R. Hensel, R. Helbig, S. Aland, H-G Braun, A Voigt, C. Neinhuis, and C. Werner. Wetting resistance at its topographical limit: the benefit of mushroom and Serif T structures. *Langmuir*, 29(4):1100–1112, 2013. PMID: 23278566.

[67] R. Hensel, C. Neinhuis, and C. Werner. The springtail cuticle as a blueprint for omniphobic surfaces. *Chemical Society Reviews*, 45(2):323–341, 2016.

[68] E. J. Hinch. *Perturbation methods*. Cambridge University Press, 1991.

[69] M. H. Hu and Y. P. Chang. Optimization of finned tubes for heat transfer in laminar flow. *Journal of Heat Trans.*, 98:257–261, 1973.

[70] M. Iyengar and A. Bar-Cohen. Design for manufacturability of SISE parallel plate forced convection heat sinks. *IEEE Transactions on Components and Packaging Technologies*, 24(2):150–158, 2001.

[71] M. Jimbo, T. Miwa, and K. Ueno. Monodromy preserving deformation of linear ordinary differential equations with rational coefficients: I. general theory and τ-function. *Physica D: Nonlinear Phenomena*, 2(2):306–352, 1981.

[72] J. Kadoko, G. Karamanis, T. Kirk, and M. Hodes. One-dimensional analysis of gas diffusion-induced cassie to wenzel state transition. *Journal of Heat Transfer*, 139(12), 2017.

[73] G. Karamanis and M. Hodes. Longitudinal-fin heat sink optimization capturing conjugate effects under fully developed conditions. *Jour. Therm. Sci. Eng. Appl.*, 8(4):041011, 2016.

[74] K. M. Kelkar and S. V. Patankar. Numerical prediction of flow and heat transfer in a parallel plate channel with staggered fins. *J. Heat Trans.*, 109/25, 1987.

[75] M. G. Khan and A. Fartaj. A review on microchannel heat exchangers and potential applications. *International journal of energy research*, 35(7):553–582, 2011.

[76] T. L. Kirk. Asymptotic formulae for flow in superhydrophobic channels with longitudinal ridges and protruding menisci. *J. Fluid Mech.*, 839, 2018.

[77] T. L. Kirk, M. Hodes, and D. T. Papageorgiou. Nusselt numbers for Poiseuille flow over isoflux parallel ridges accounting for meniscus curvature. *J. Fluid Mech.*, 811:315–349, 2017.

[78] T. L. Kirk, G. Karamanis, D. G. Crowdy, and M. Hodes. Thermocapillary stress and meniscus curvature effects on slip lengths in ridged microchannels. *J. Fluid Mech.*, 894, 2020.

[79] D. Koon, M. Heřmanová, and J. Náhlík. Electrical conductance sensitivity functions for square and circular cloverleaf van der pauw geometries. *Meas. Sci. Technol.*, 26:115004, 11 2015.

[80] D. W. Koon, Fei W., D. H. Petersen, and Ole H. Sensitivity of resistive and hall measurements to local inhomogeneities: Finite-field, intensity, and area corrections. *J. Appl. Phys*, 116(13):133706, 2014. AIP Publishing LLC.

[81] D. Kramer, S. A. Freunberger, R. Flückiger, I. A. Schneider, A. Wokaun, F. N. Büchi, and G. G. Scherer. Electrochemical diffusimetry of fuel cell gas diffusion layers. *J. Electroanal. Chem.*, 612(1):63–77, 2008.

[82] E. Lauga and H. A. Stone. Effective slip in pressure-driven Stokes flow. *J. Fluid Mech.*, 489:55–77, 2003.

[83] C. Lee, C.H. Choi, and C.J. Kim. Superhydrophobic drag reduction in laminar flows: a critical review. *Exp. Fluids*, 57:176, 2016.

[84] C. Lee and C.J Kim. Maximizing the giant liquid slip on superhydrophobic microstructures by nanostructuring their sidewalls. *Langmuir*, 25(21):12812–12818, 2009. PMID: 19610627.

[85] S. Lee. Optimum design and selection of heat sinks. *IEEE Transactions on Components, Packaging, and Manufacturing Technology: Part A*, 18(4):812–817, 1995.

[86] J. Liesen, M. M. S. Nasser, and O. Sète. Computing the logarithmic capacity of compact sets having (infinitely) many components with the charge simulation method. *arXiv preprint arXiv:2201.10228*, 2022.

[87] A. Lin and L. Landweber. On a solution of the Lavrentiev wake model and its cascade. *J. Fluid Mech.*, 79(4):801–823, 1977.

[88] B. Liu, L. Ristroph, A. Weathers, S. Childress, and J. Zhang. Intrinsic stability of a body hovering in an oscillating airflow. *Phys. Rev. Lett.*, 108(6):068103, 2012.

[89] P. Lv, Y. Xue, Y. Shi, H. Lin, and H. Duan. Metastable states and wetting transition of submerged superhydrophobic structures. *Phys. Rev. Lett.*, 112(19):196101, 2014.

[90] A. Maali and B. Bhushan. Measurement of slip length on superhydrophobic surfaces. *Philos. Trans. Royal Soc. A*, 370(1967):2304–2320, 2012.

[91] A. Maciel, V. Salas, J. F. A. Soltero, J. Guzmán, and O. Manero. On the wall slip of polymer blends. *J. Polym. Sci. B*, 40(4):303–316, 2002.

[92] D. Makow and J. B. Campbell. Circular four electrode capacitors for capacitance standards. *Metrologia*, 8(4):148, 1972.

[93] J. S. Marshall. Exact formulae for the effective slip length of a symmetric superhydrophobic channel with flat or weakly curved menisci. *SIAM Journal on Appl. Math.*, 77(5):1606–1630, 2017.

[94] J. H. Masliyah and K. Nandakumar. Heat transfer in internally finned tubes. *Journal of Heat Trans.*, 95:332–338, 1976.

[95] M. D. Mayer, J. Kadoko, and M. Hodes. Two-dimensional numerical analysis of gas diffusion-induced Cassie to Wenzel state transition. *Journal of Heat Trans.*, 143(10), 2021.

[96] I. Miccoli, F. Edler, H. Pfnür, and C. Tegenkamp. The 100th anniversary of the four-point probe technique: the role of probe geometries in isotropic and anisotropic systems. *J. Phys.: Condens. Matter*, 27:223201, 2015.

[97] H. Miyoshi and D. G. Crowdy. Estimating conformal capacity using asymptotic matching. *IMA Lighthill-Thwaites prize special issue (accepted)*, 2023.

[98] H. Miyoshi and D. G. Crowdy. Generalized Schwarz integral formulae for multiply connected domains. *SIAM Journal of Appl. Math.*, 83(3):966–984, 2023.

[99] H. Miyoshi, D. G. Crowdy, and R. Nelson. Fay meets van der Pauw: the trisecant identity and the resistivity of holey samples. *Proc. Royal Soc. A*, 477(2246):20200796, 2021.

[100] H. Miyoshi, D. G. Crowdy, and R. Nelson. The prime function, the Fay trisecant identity, and the van der Pauw method. *Comput. Methods Funct. Theory*, 21(4):707–736, 2021.

[101] H. Miyoshi, L. T. Kirk, M. Hodes, and D. G. Crowdy. Longitudinal flow through a periodic array of fins: Exact and asymptotic solutions. *J. Fluid Mech.*, (in preparation).

[102] H. Miyoshi, H. Rodriguez-Broadbent, A. Curran, and D. G. Crowdy. Longitudinal flow in superhydrophobic channels with partially invaded grooves. *J. Eng. Math.*, 137(1):1–17, 2022.

[103] J. Náhlík, I. Kaŝpárková, and P. Fitl. Study of quantitative influence of sample defects on measurements of resistivity of thin films using van der pauw method. *Measurement*, 44(10):1968–1979, 2011.

[104] M. M. S. Nasser, O. Rainio, A. Rasila, M. Vuorinen, T. Wallace, H. Yu, and X. Zhang. Polycircular domains, numerical conformal mappings, and moduli of quadrilaterals. *Adv. Comput. Math.*, 48(5):1–34, 2022.

[105] M. M. S. Nasser and M. Vuorinen. Computation of conformal invariants. *Comput. Appl. Math.*, 389:125617, 2021.

[106] C.-L. Navier. Memoire sur les lois du mouvement des fluids. *Mem. Acad. Sci. Inst. Fr.*, 6:389–416, 1823.

[107] Z. Nehari. *Conformal mapping*. Dover Publication, New York., 2012.

[108] C. Neto, D. R. Evans, E. Bonaccurso, H.-J. Butt, and V. S. J. Craig. Boundary slip in newtonian liquids: a review of experimental studies. *Reports on progress in physics*, 68(12):2859, 2005.

[109] C.-O. Ng, H. C. W. Chu, and C. Y. Wang. On the effects of liquid-gas interfacial shear on slip flow through a parallel-plate channel with superhydrophobic grooved walls. *Phys. Fluids*, 22(10):102002, 2010.

[110] C.-O. Ng and C. Y. Wang. Stokes shear flow over a grating: Implications for superhydrophobic slip. *Phys. Fluids*, 21(1):087105, 2009.

[111] M. Nosonovsky and B. Bhushan. *Multiscale dissipative mechanisms and hierarchical surfaces: friction, superhydrophobicity, and biomimetics*. Springer Science & Business Media, 2008.

[112] D. Oh, C. Ahn, M. Kim, E. K. Park, and Y. S. Kim. Application of the van der Pauw method for samples with holes. *Meas. Sci. Technol.*, 27(12), 2016.

[113] H. B. Palmer. The capacitance of a parallel-plate capacitor by the Schwartz-Christoffel transformation. *Electrical Engineering*, 56(3):363–368, 1937.

[114] N. Papamichael. Numerical conformal mapping onto a rectangle with applications to the solution of Laplacian problems. *J. Comput. Appl. Math.*, 28:63–83, 1989.

[115] N. Papamichael and N. Stylianopoulos. *Numerical conformal mapping: Domain decomposition and the mapping of quadrilaterals*. World Scientific, 2010.

[116] S. Parvate, P. Dixit, and S. Chattopadhyay. Superhydrophobic surfaces: insights from theory and experiment. *J. Phys. Chem.*, 124(8):1323–1360, 2020.

[117] L. J. Van Der Pauw. A method of measuring the resistivity and Hall coefficient on lamellae of arbitrary shape. *Philips Tech. Rev.*, 20(8):220–224, 1958.

[118] L. J. Van der Pauw. A method of measuring specific resistivity and Hall effect of discs of arbitrary shape. *Philips Res. Rep*, 13(1):1–9, 1958.

[119] J. R. Philip. Flows satisfying mixed no-slip and no-shear conditions. *Zeitschrift für angewandte Mathematik und Physik ZAMP*, 23(3):353–372, 1972.

[120] G. Pölya and G. Szegö. Isoperimetric inequalities in mathematical physics. *B. Am. Math. Soc.*, 59(6):588–603, 1953.

[121] C. Poor. Fay's trisecant formula and cross-ratios. *Proc. Amer. Math. Soc.*, 114:667–671, 1992.

[122] N. V. Priezjev, A. A. Darhuber, and S. M. Troian. Slip behavior in liquid films on surfaces of patterned wettability: Comparison between continuum and molecular dynamics simulations. *Phys. Rev. E*, 71(4):041608, 2005.

[123] T. Ransford. *Potential theory in the complex plane*. Cambridge University Press, 1995.

[124] J. N. Reddy. *Introduction to the finite element method*. McGraw-Hill Education, 2019.

[125] P. L. Rossiter. *The electrical resistivity of metals and alloys*, volume 6. Cambridge university press, 1991.

[126] J. P. Rothstein. Slip on superhydrophobic surfaces. *Ann. Rev. Fluid Mech.*, 42:89–109, 2010.

[127] A. E. Ruehli and P. A. Brennan. Accurate metallization capacitances for integrated circuits and packages. *IEEE J. Solid-State Circuits*, 8(4):289–290, 1973.

[128] P. G. Saffman and G. R. Baker. Vortex interactions. *Annu. Rev. Fluid Mech.*, 11(1):95–121, 1979.

[129] T. Sakurai and K. Tamaru. Simple formulas for two-and three-dimensional capacitances. *IEEE transactions on electron devices*, 30(2):183–185, 1983.

[130] A. Samouëlian, I. Cousin, A. Tabbagh, A. Bruand, and G. Richard. Electrical resistivity survey in soil science: a review. *Soil and Tillage research*, 83(2):173–193, 2005.

[131] M. Sbragaglia and A. Prosperetti. A note on the effective slip properties for microchannel flows with ultrahydrophobic surfaces. *Phys. Fluids*, 19:043603, 2007.

[132] R. Schinzinger and P. A. A. Laura. *Conformal mapping: methods and applications*. Elsevier, 2012.

[133] J. C. Slattery. *Advanced transport phenomena*. Cambridge University Press, 1999.

[134] E. M. Sparrow, B. R. Baliga, and S. V. Patankar. Forced convection heat transfer from a shrouded fin array with and without tip clearance. *Trans. ASME*, 100, 1978.

[135] Y. Sun, J. Shi, and Q. Meng. Measurement of sheet resistance of cross microareas using a modified van der pauw method. *Semicon. Sci. Tech.*, 11(5):805, 1996.

[136] Z. H. Sun, J. Zhou, X. J. Xia, and D. M. Zhou. Two-dimensional electrostatic model for the Van der Pauw method. *Phys. Lett. A*, 381(27):2144–2148, 2017.

[137] K. Szymański, J. L. Cieśliński, and K. Łapiński. Van der Pauw method on a sample with an isolated hole. *Phys. Lett. A*, 377(8):651–654, 2013.

[138] K. Szymański, K. Łapiński, and J. L. Cieśliński. Determination of the Riemann modulus and sheet resistance of a sample with a hole by the van der Pauw method. *Meas. Sci. Technol.*, 26(5):055003, apr 2015.

[139] K. Szymański, K. Łapiński, J. L. Cieśliński, A. Kobus, P. Zaleski, M. Biernacka, and K. Perzyńska. Determination of the Riemann modulus and sheet resistivity by a six-point generalization of the van der Pauw method. *Meas. Sci. Technol.*, 26(8):1–9, 2015.

[140] K. Szymański, C. J. Walczyk, and J. L. Cieśliński. Determination of topological properties of thin samples by the van der Pauw method. *Measurement*, 145:568–572, 2019.

[141] K. Szymański and P. Zaleski. Precise measurement of inhomogeneity of 2-D system by six-point method. *IEEE Trans. Instrum. Meas.*, PP:1–5, 02 2017.

[142] H. Telib and L. Zannetti. Hollow wakes past arbitrarily shaped obstacles. *Jour. Fluid Mech.*, 669:214–224, 2011.

[143] C. J. Teo and B. C. Khoo. Flow past superhydrophobic surfaces containing longitudinal grooves: effects of interface curvature. *Microfluid. Nanofluid*, 9:499–511, 2010.

[144] J. J. Thomson. *Notes on recent researches in electricity and magnetism: intended as a sequel to Professor Clerk-Maxwell's Treatise on electricity and magnetism.* Clarendon Press, 1893.

[145] R. Truesdell, A. Mammoli, P. Vorobieff, F. van Swol, and C. J. Brinker. Drag reduction on a patterned superhydrophobic surface. *Physical review letters*, 97(4):044504, 2006.

[146] E. O. Tuck. Matching problems involving flow through small holes. *Adv. Appl. Mech.*, 15:89–158, 1975.

[147] A. Tuteja, W. Choi, J. M. Mabry, G. H. McKinley, and R. E. Cohen. Robust omniphobic surfaces. *Proceedings of the National Academy of Sciences*, 105(47):18200–18205, 2008.

[148] L. B. Valdes. Resistivity measurements on germanium for transistors. *Proc. IRE*, 42(2):420–427, 1954.

[149] G. Valiron. *Cours d'Analyse Mathématique, Théorie des fonctions*. Masson et Cie, 1947.

[150] M. Van Dyke. Perturbation methods in fluid mechanics/annotated edition. *NASA STI/Recon Tech. Report A*, 75:46926, 1975.

[151] L. L. Vasiliev. Heat pipes in modern heat exchangers. *Appl. Therm. Eng.*, 25(1):1–19, 2005.

[152] I. N. Vekua. *Generalized analytic functions*. Elsevier, 2014.

[153] A. Weathers, B. Folie, B. Liu, S. Childress, and J. Zhang. Hovering of a rigid pyramid in an oscillatory airflow. *J. Fluid Mech.*, 650:415–425, 2010.

[154] J. G. Webster. *The measurement, instrumentation and sensors handbook*, volume 14. CRC press, 1998.

[155] R. Wegmann, A. H. M. Murid, and M. M. S. Nasser. The Riemann–Hilbert problem and the generalized Neumann kernel. *J. Comput. Appl. Math.*, 182(2):388–415, 2005.

[156] R. Wegmann and M. M. S. Nasser. The Riemann–Hilbert problem and the generalized Neumann kernel on multiply connected regions. *J. Comput. Appl. Math.*, 214(1):36–57, 2008.

[157] F. Wenner. *A method of measuring earth resistivity*. Number 258. US Government Printing Office, 1916.

[158] Z. Wu, L. Z. Deng, M. Gooch, S. Huyan, and C. W. Chu. The retention at ambient of the high-pressure-induced metastable superconducting phases in antimony single crystals. *Materials Today Physics*, 15:100291, 2020.

[159] W. Yang, L. Kasaei, H. Hijazi, S. Rangan, Y.-W. Yeh, R. K. Sah, J. R. Paudel, K. Chen, A. X. Gray, P. Batson, et al. Ultra-thin epitaxial MgB2 on SiC: Substrate surface polarity dependent properties. *arXiv preprint arXiv:2301.01669*, 2023.

[160] Y.-T. Yang and C.-Z. Hwang. Calculation of turbulent flow and heat transfer in a porous-baffled channel. *Int. J. Heat Mass Transf*, 46(5):771–780, 2003.

[161] E. Yariv and D. G. Crowdy. Thermocapillary flow between grooved superhydrophobic surfaces: transverse temperature gradients. *J. Fluid Mech.*, 871:775–798, 2019.

[162] C. P. Yuan and T. N. Trick. A simple formula for the estimation of the capacitance of two-dimensional interconnects in VLSI circuits. *IEEE Elect. Device Lett.*, 3(12):391–393, 1982.

[163] Y. Zou, H. Shin, H. Wei, Y. Fan, B. A. Davidson, E. Guo, Q. Chen, K. Zou, and Z. G. Cheng. Transport behaviors of topological band conduction in KTaO3's two-dimensional electron gases. *NPJ Quantum Materials*, 7(1):1–6, 2022.